

INTERFERENCE-FACILITATED PHOTON PAIR SEPARATION
IN INTEGRATED QUANTUM CIRCUITS

by

Ryan P. Marchildon

A thesis submitted in conformity with the requirements
for the degree of Master of Applied Science
Graduate Department of Edward S. Rogers Sr. Department of Electrical and Computer
Engineering.
University of Toronto

© Copyright 2015 by Ryan P. Marchildon

Abstract

Interference-Facilitated Photon Pair Separation

in Integrated Quantum Circuits

Ryan P. Marchildon

Master of Applied Science

Graduate Department of Edward S. Rogers Sr. Department of Electrical and Computer Engineering.

University of Toronto

2015

The implications of integrated coupler dispersion for interference-facilitated photon pair separation (IFPS) are rigorously explored. A generalized analysis of the second-order spatial correlations is developed for arbitrary input state and coupler attributes. It is found that splitting ratio anti-symmetries can preserve near-perfect separation fidelities as the photon pair non-degeneracy is varied, even though the coupler response may differ greatly from that of an ideal 50:50 splitter. These anti-symmetries are degraded by higher-order coupler dispersion and non-equidistance of the photon pair central wavelengths from the 50:50 splitting wavelength, but can be restored through active coupler tuning. Coupler dispersion is also shown to produce new features such as novel interference visibility behaviour and entanglement-sensitive performance. When only a single input path is utilized, tailoring of spectral correlations in the post-selected output state also becomes possible. A source of path-entangled bunched states based on the Bragg reflection waveguide (BRW) platform is designed for use in IFPS experiments, and a roadmap for testing IFPS behaviour is presented. This work informs the design and characterization of quantum circuits for achieving universal photon pair separation for states with highly tunable spectral and polarization properties.

Acknowledgements

First and foremost, I would like to express my sincere gratitude to my supervisor Professor Amr Helmy, who gave me the opportunity to explore the captivating field of integrated quantum optics. His care, insights, suggestions, and incredible depth of knowledge were tremendously helpful in guiding the development of this dissertation.

I would also like to make special mention of several colleagues whose support I received throughout my work: Dongpeng Kang, for his mentorship in laboratory techniques such as device alignment, and for countless helpful discussions; Nima Zareian, for the many insightful conversations I shared with him and his time spent conducting the electron-beam dose tests for my dual-path photon pair source design; and Rajiv Prinja, for generously taking time out of a busy schedule to fabricate these devices. My appreciation also extends to the rest of the Helmy group, including Steve Rutledge, Herman Wong, and Charles Lin, for making this an enjoyable team to work with.

And finally, for those on the home front, I thank my parents, friends and family for their love and nurturing over the years, as well as my incredible fiancée Jessica, who lifted my spirits and was endless in her patience and support.

Contents

1	Introduction	1
1.1	Integrated Quantum Photonics	2
1.2	Photon Pair Separation	4
1.2.1	Conventional Techniques	4
1.2.2	Non-classical Approach	5
1.3	Thesis Aims and Overview	6
2	Two-Photon Quantum Interference in Integrated Circuits	8
2.1	The Quantum Description of Light	8
2.1.1	Formalism	8
2.1.2	Two-Photon States	11
2.2	Two-Photon Interference in Bulk Optics	16
2.2.1	Photon Coalescence: The Hong-Ou-Mandel Effect	16
2.2.2	Interference as a Which-Path Phenomenon	20
2.2.3	Photon Anti-Coalescence	21
2.3	Light in Integrated Circuits	22
2.3.1	Classical Guided-Wave Optics	22
2.3.2	Directional Couplers	26
2.3.3	On-Chip Quantum Interference	30
3	IFPS with a Dispersive Coupler	33
3.1	Generalized Theoretical Development	33
3.2	Comparison of IFPS to Hong-Ou-Mandel Interference	39
3.3	IFPS Behaviour in the Near-Degeneracy Regime	41
3.3.1	Dimensionless Model	42

3.3.2	Salient Features	44
3.3.3	Photon Polarization Diversity	47
3.3.4	Effect of Photon Bandwidths and Spectral Correlations	48
3.4	Behaviour far from Degeneracy	52
3.4.1	Extrapolation of Near-Degeneracy Behaviour	52
3.4.2	Loss of Splitting Ratio Anti-Symmetry	52
3.5	Impact of IFPS on Entanglement	54
3.5.1	Dichroic Coupler Response	55
3.5.2	Generalized Coupler Response	57
3.6	Conclusions	57
4	IFPS Case Studies	59
4.1	Directional Coupler Design Comparisons	59
4.1.1	Coupling Characteristics	61
4.1.2	Co-Polarized State Performance	63
4.1.3	Cross-Polarized State Performance	68
4.1.4	Summary and Closing Remarks	70
4.2	State Asymmetry	72
4.3	Active Coupler Tuning	73
4.3.1	Mitigating Asymmetries	74
4.3.2	Trajectory Control	77
4.4	Conclusions	79
5	Design of Integrated Devices for IFPS Experiments	80
5.1	Dual-Path BRW Photon Pair Source	80
5.1.1	Background: Phase-Matching in BRWs	81
5.1.2	Design Considerations	83
5.1.3	Width Selection for Restricted PM	85
5.1.4	50:50 Splitter Design	86
5.1.5	Other Considerations	89
5.2	SiON Directional Coupler	90
6	IFPS Experiments	94
6.1	Dual-Path Source Characterization	94

6.1.1	Classical Characterization	95
6.1.2	Non-Classical Characterization	98
6.2	IFPS Characterization Strategy	102
6.3	Summary	106
7	Conclusions and Future Directions	107
7.1	Summary of Contributions	107
7.2	Future Directions	109
7.2.1	Self-Pumped Dual-Path Sources	109
7.2.2	Engineering Higher-Order Correlations	109
A	The Schmidt Decomposition	113
B	Derivation of Coupler Mode Transformations	115
C	Generation of Path Entanglement through Coherent Pumping	117
D	Two-Photon Outcome Probabilities	119
E	Maximal Contour for Cross-Polarized States	121
	Bibliography	122

List of Figures

1.1	(a) Example of pair separation from a bulk nonlinear crystal (BiBO) [1]; conservation of momentum constrains the photons to be found at antipodal points of the conical cross-section, hence placing collection optics at these points guarantees deterministic separation. (b) On-chip pair separation based on lateral mode order, where modal indistinguishability is re-established at the output (figure extracted from Ref. [2]). Generating the photons in two different lateral modes is not always possible.	5
1.2	Seminal implementations of IFPS (a) in fiber and (b) on-chip; the latter was implemented with MMIs instead of a directional coupler. In the fiber implementation, the two interfering paths correspond to the coherently-pumped counter-propagating loop directions. (Figures extracted from Refs. [3] and [4] respectively.)	6
2.1	Radial plots of the first several Laguerre-Gaussian spatial modes, generated using Matlab.	10
2.2	Depictions of two-photon states with various degrees of permutation symmetry: (a) and (b) are left unchanged only for concurrent permutations of all three degrees of freedom $\{\omega, \sigma, j\}$; (c) is invariant under path exchange $\{j\}$; and (d) is invariant under the concurrent exchange of frequency and polarization $\{\omega, \sigma\}$	12
2.3	BPA probability distributions $ \phi(\omega_1, \omega_2) ^2$ showing (a) approximately uncorrelated degenerate, (b) anti-correlated degenerate, and (c) anti-correlated non-degenerate photon pair states generated through on-chip SPDC. The equations from which these plots were generated are detailed in [5].	14
2.4	(a) Two photons incident upon a 50:50 beamsplitter; single-photon detectors monitor the coincidence rate at the output. (b) Output state expansion in terms of observable outcomes; when $\hat{a}^\dagger = \hat{b}^\dagger$ due to photon indistinguishability, the amplitudes associated with anti-bunched outcomes destructively interfere, and the detected coincidence rate drops to zero.	17

2.5	Coincidence count probability versus photon temporal delay τ , plotted for the special case of $\eta = 1/2$. The photon spectra are taken to be gaussian with $\Delta\omega = 1.77 \times 10^{11}$ Hz.	19
2.6	Expansion of the outcome $\hat{a}^{A\dagger}\hat{b}^{B'\dagger}$ in terms of its possible histories ('paths'). Interference between these histories can lead to a non-classical outcome probability.	20
2.7	(a) Photon anti-coalescence with indistinguishable photons in an MZI; (b) photon anti-coalescence with coherently pumped photon pair sources.	22
2.8	(a) Ray-optics illustration of a 1D symmetric slab waveguide. (b) Spatial profiles of the first few TE modes of this waveguide. (c) Visualization of the bound mode solutions for given structural parameters.	23
2.9	(a) Mode evolution in a directional coupler: the input waveguide modes $E_\sigma^{(A)}$ and $E_\sigma^{(B)}$ are projected onto symmetric ($E_\sigma^{(s)}$) and anti-symmetric ($E_\sigma^{(a)}$) modes whose spatial beating determines the waveguide power distribution at the output. (b) Dependence of splitting ratio $\eta_\sigma(\omega)$ on the interaction length z , showing the effect of modal mismatch.	28
2.10	(a) Directional coupler cross-section reported in [6]; GeO ₂ -doping of the cores to a molar fraction of 0.0488 results in a 0.5% index contrast relative to the cladding. (b) Simulated classical splitting performance; the inset shows the effect of modal mismatch due to a waveguide width asymmetry of Δw	30
2.11	Accumulation of additional phase within a directional coupler. Photons begin in waveguide A. The coupling strength is dispersive with $\kappa(\lambda_1) > \kappa(\lambda_2)$. Red circles and black diamonds indicate points where $\eta(\lambda)$ is at a maximum or minimum for wavelengths λ_1 and λ_2 respectively. Depending on the value of $\kappa(\lambda)z$, the mode transformations can acquire an additional factors of $(i)^2$. For example, the factor associated with photons found in waveguide B at point z_0 is $-i\sqrt{1-\eta(\lambda_1)}$ for λ_1 and $+i\sqrt{1-\eta(\lambda_2)}$ for λ_2	32
3.1	(a) Schematic highlighting the bunched and anti-bunched probabilities defined in Equations (3.29)-(3.34), plotted under conditions of perfect path indistinguishability with $\theta = 0$ and a constant splitting ratio of $\eta = 0.276$. (b) Splitting ratio dependence of the IFPS interference visibilities for a constant η ; HOM-equivalents are indicated.	39

3.2	(Left) Calculated IFPS P_S for co-polarized photons degenerate at 1550 nm, produced by Type I SPDC, having gaussian spectra with $\Delta\lambda = 3$ nm. The solid curve is the interference envelope for a perfectly uncorrelated pair (SN = 1), and has a FWHM of $\Delta\tau = 1.67$ ps. The dashed curve shows the same calculation but for a moderately anti-correlated pair with SN = 1.26, and has a width of $\Delta\tau = 3.25$ ps; entanglement was induced by narrowing the pump bandwidth. Rapidly-varying oscillations have been shown only for the uncorrelated pair, and appear aliased at a lower frequency. (Right) Enlarged region showing these oscillations acting as a π phase shift over a 1.26 fs delay time. The oscillation frequency corresponds to that of the 775 nm process pump.	41
3.3	(a) Anti-bunched outcome probability P_S , (b) anti-bunched interference visibility V_S , and (c) bunched interference visibility V_B , as computed for a co-polarized photon pair input state from a typical Type I SPDC process. The value of P_S remains above 95% for $\Delta\xi \in [-0.10, +0.10]$	45
3.4	Visualization of the splitting ratios sampled by the central photon wavelengths (dashed lines) as $\Delta\xi$ and Λ are varied. For $\Delta\xi = 0$, these splitting ratios remain anti-symmetric about the 50:50 point for all values of Λ . The coupler operates as a perfect 50:50 splitter at points i. and iii., and as a perfect wavelength-demultiplexer at ii.	46
3.5	The anti-symmetry condition $\eta^{(1)} + \eta^{(2)} = 1$ is shown to be satisfied for a TE-TE co-polarized state, but broken for other polarizations (e.g. $\eta_{\text{TM}}^{(1)} \neq \eta_{\text{TM}}^{(2)} \neq \eta_{\text{TE}}^{(2)}$) due to coupler birefringence in $\eta_\sigma(\lambda_{\text{deg}})$ and M_σ ; note that $\eta_{\text{TE}}^{(2)} = \eta_{\text{TM}}^{(2)}$ by coincidence only. . . .	48
3.6	Impact of photon bandwidths and spectral entanglement on P_S for various degrees of spectral entanglement. Schmidt numbers are given at degeneracy conditions ($\Lambda = 0$). . .	49

3.7	Mitigation of splitting ratio asymmetries by spectral correlations, shown in frequency space. Let $ \phi^{(j)}(\omega) ^2$ represent the marginal spectrum of photon j , and let these spectra be equidistant from the degeneracy frequency ω_{deg} where $\eta(\omega_{\text{deg}}) = 0.5$. The indices $n \in [-5, 5]$ represent equally-spaced slices of each spectrum (i.e. the $d\omega_j$ in Equations (3.26)-(3.28)), which are labelled relative to the central frequencies. When the photons are perfectly uncorrelated, all permutations of these slices contribute non-vanishingly towards the determination of P_S with varying degrees of splitting ratio asymmetry. Note that the extent of possible asymmetry is reduced when the spectral bandwidths $\Delta\omega_1$ and $\Delta\omega_2$ are made smaller. On the other hand, if the photons are highly anti-correlated, then these slice permutations are restricted to be anti-symmetric. For example, the slice $n = -3$ of spectrum 1 (shaded) only pairs non-vanishingly with the slice $n = +3$ of spectrum 2 (also shaded), for which the splitting ratios are approximately asymmetric with $\Delta\eta^{(1)} \approx \Delta\eta^{(2)}$.	50
3.8	Bandwidth and spectral entanglement dependencies of the IFPS interference visibilities.	51
3.9	Anti-bunched outcome probability P_S and interference visibilities V_B and V_S for all permutations of the photon central wavelength splitting ratios $\eta^{(1)}$ and $\eta^{(2)}$; diagonal lines (dashed) denote the anti-symmetry contour $\eta^{(1)} + \eta^{(2)} = 1$.	53
3.10	Effective evolution of $ \phi(\omega_1, \omega_2) ^2$ to $ \Phi^{AB}(\omega_1, \omega_2) ^2$ for a dichroic coupler response, with a single photon pair source (top) and two coherently-pumped sources (bottom).	56
3.11	Spectral entanglement of the post-selected anti-bunched output. (a) The input state is generated from one photon pair source situated in either path A or path B . (b) The input is generated from two coherently pumped sources, one in each path; fluctuations in SN are attributable to numerical inaccuracies.	57
4.1	(a) Coupler architectures and (b) material systems used in the present case study. (c) Numerical apertures of the material systems; the large variation in confinement for material B is due to a nearby material resonance. The refractive index models for materials A and B were based on Refs. [7] and [8] respectively.	60
4.2	Simulated coupling characteristics for each design, showing: (a) the coupling constant's λ and σ dependence; (b) dimensionless first-order coupler dispersion; and (c) dimensionless second-order coupler dispersion. The waveguides remained single-mode over the wavelength range shown.	62

4.3	Calculated IFPS behaviour: (a)-(b) show the predicted separation probability and visibility; (c)-(d) show the sum and difference of the central-wavelength splitting ratios. States were co-polarized with equal photon bandwidths of $\Delta\lambda = 3$ nm and a pump bandwidth of $\Delta\lambda_P = 1$ nm.	64
4.4	Select IFPS trajectories in $\eta^{(1)}, \eta^{(2)}$ space, showing the associated P_S and V_S behaviour. Each marker represents a $ \lambda_{02} - \lambda_{01} $ step size of approximately 25 nm in (a) and (c), and 5 nm in (b). The diagonal lines in (a) and (c) represent the ideal antisymmetry condition $\eta^{(1)} + \eta^{(2)} = 1$. Contours of the splitting ratio difference $ \eta^{(1)} - \eta^{(2)} $ are perpendicular to those of the sum $\eta^{(1)} + \eta^{(2)}$	65
4.5	Absolute error between the near-degeneracy approximations (NDA) and the true coupler response for (a) P_S and (b) V_S . The near-degeneracy approximations remain accurate to within 1% for nearly 150 nm of non-degeneracy.	66
4.6	(a)-(b) Calculated IFPS bandwidth dependencies; (c)-(d) show the relative error of the NDA for comparison. The inset in (a) shows the Schmidt Number (SN) of the simulated state at each bandwidth.	67
4.7	Calculated cross-polarized performance showing: (a) P_S behaviour; (b) TE-TM and TM-TE central wavelength splitting ratio sums for the birefringent designs; and (c) deviations from the ideal four-dimensional anti-symmetry contour. Points i. and ii. indicate crossovers between designs 1A and 2B, and designs 1B and 2A, respectively. The photons were maximally polarization-entangled and spectrally uncorrelated with 3 nm bandwidths.	69
4.8	IFPS with symmetric versus asymmetric central wavelength tuning, assuming linear coupler dispersion: (a) splitting ratio trajectories, shown in non-degeneracy steps of ~ 10 nm; (b) P_S performance and detuning asymmetry. The calculation inaccuracy near $ \lambda_{02} - \lambda_{01} = 125$ nm is due to high sensitivities occurring when the coupler behaves as a nearly-perfect WD. Computed for spectrally-uncorrelated photons with equal bandwidths of $\Delta\lambda = 3$ nm.	72
4.9	Two well-known methods for tuning the coupling strength in-situ: (a) thermally induced and (b) electro-optically induced changes to the core-cladding index contrast. Index changes are assumed to be identical for both waveguides so that modal mismatch remains negligible.	74
4.10	(a) Coupling characteristics used in the example, with $M = 50$ and $M^{(2)} = 300$. (b) Systematic offsets to the coupling strength cause shifts in the $\eta(\lambda)$ response function, as shown.	74

4.11 (a) Splitting ratio trajectories and (b) IFPS performance of the non-linearly dispersive coupler without active coupler tuning. Photon and pump bandwidths were $\Delta\lambda = 3$ nm and $\Delta\lambda_P = 1$ nm respectively. The trajectory in (a) is plotted with a 2.5 nm non-degeneracy step size; select operating points have been tagged by the letters A through E.	75
4.12 Performance with active coupler tuning: (a) shows the new splitting ratio trajectory (2.5 nm step size); (b) indicates improvements to the separation probability through optimal selection of $\Delta\xi$, and tracks corresponding changes to the 50:50 splitting wavelength; (c) and (d) show the trajectory of the $\Delta\xi$ tuning relative to the global P_S and V_S behaviour (25 nm step size in non-degeneracy).	76
4.13 Trajectory evolution for the coupler described by Fig. 4.10, showing: (a) sample trajectories at various non-degeneracy values, as $\Delta\xi$ increases from 0 to $\pi/4$ in steps of $\pi/40$; (b) relation between global V_S behaviour and the direction of motion along \swarrow or \nearrow ; (c) relation between global P_S behaviour and the direction of motion along \nwarrow or \searrow , which overrides motion along the orthogonal axis when $\Delta\xi$ follows contours of P_S	78
5.1 BRW architecture reported in Refs. [9, 10], which satisfies PM for photon pair generation in the telecom C-band (~ 1550 nm). The Bragg and TIR mode profiles, material index variation, and vertical layer specifications are shown.	83
5.2 Overview of dual-path BRW design (top-down view), showing key design variables discussed in the text. These features will be etched into an existing vertical design (given in Fig. 5.1) to a depth of $D = 3.78$ μm , and will target Type I SPDC near 1550 nm.	84
5.3 Type I SPDC Tuning curves for $W_{\text{In}} = 5.0$ μm and $W_{\text{PM}} = 2.5$ μm , calculated from Equations (5.2)-(5.3) with a monochromatic pump. Waveguide dispersion was simulated using <i>Lumerical</i> . Degeneracy points obtained in this manner are known to be systematically offset from their true values.	86
5.4 Simulated MMI mode evolution at 777 nm for $W_{\text{MMI}} = 10$ μm , showing the injected mode profile at the input (left, $W_{\text{In}} = 5$ μm) and the resultant mode profile at $L_{\text{MMI}} = 220$ μm (right, two-fold image of input).	87

5.5	(a) Refractive indices of SiON and SiO ₂ from the available fabrication recipe, measured via ellipsometry. (b) Ridge-waveguide geometry used in the directional coupler design: H is the core layer thickness; D is the ridge etch depth; W is the waveguide width; and d is the waveguide separation. A SiO ₂ layer thickness of 3 μm prevents mode leakage into the silicon substrate.	91
5.6	Simulated SiON coupler performance as a function of waveguide width and separation. Feature sizes were kept above 1 μm to facilitate easier fabrication. The black arrow indicates a suspected entry into the strong-coupling regime.	92
5.7	(a) Coupling dispersion of the final design; the linear fit has a coefficient of determination (R-squared) of 1.00. (b) Symmetric and (c) anti-symmetric mode profiles within the coupling region.	93
6.1	SEM images of the dual-path sources showing: (a) view of SMF and MMI regions (lengths appear compressed due to the imaging angle); (b) profile of an input waveguide (targeting $W_{\text{In}} = 5 \mu\text{m}$); and (c) profile of an output waveguide in the regions of photon pair generation (targeting $W_{\text{PM}} = 2.5 \mu\text{m}$). Red arrows indicate the abrupt change in ridge sidewall roughness. Images are courtesy of Rajiv Prinja and Nima Zareian.	95
6.2	Simplified experimental setup for SHG and linear loss measurements. Additional mirrors (omitted) are used for alignment. The device orientation was intentionally reversed with respect to the pump, since the SMF region is poorly guiding at 1550 nm. Abbreviations: mirror (M); flip-mounted mirror (FM); beam sampler (S); fiber polarization controller (FPC); fiber coupler (FC); polarizing beamsplitter (PBS); optical spectrum analyzer (OSA); objective lens (Obj).	96
6.3	(a) Nearly path-indistinguishable and (b)-(c) path-distinguishable SHG tuning characteristics measured for three different device specimens. The degeneracy points in (b) and (c) differed between paths by approximately 1.2 nm and 0.8 nm respectively. Data was normalized based on the peak power. The arrow in (a) indicates a possible secondary peak.	97
6.4	A Fabry-Perot transmission spectrum obtained during loss characterization; the data has been fit to Equation 6.1 to extract the corresponding losses.	98
6.5	Simplified schematic depicting the SPDC coincidence count setup. The 1550 nm source is used to align the output collection and single-photon detector optics prior to the injection of the Ti:Sapph pump. New abbreviations: half-wave plate (HWP); beamsplitter (BS); pump rejection filter (PRF); single-photon detector (SPD); multi-mode fiber (MMF).	99

6.6	Sample coincidence histograms from straight waveguides at 1.5 mW input pump power; (a) is taken from the dual-source fabrication; (b) is taken from an earlier fabrication run of straight waveguides with comparable dimensions.	100
6.7	Simplified experimental setup for SPDC tuning curve measurement, where λ_{spec} indicates the spectrometer's transmitted wavelength. SPD-1 monitors the single-photon count rate. The pump and alignment beam are configured as in Figure 6.5. The example SPDC tuning curve is reproduced from Ref. [11].	103
6.8	Simplified schematic for proposed IFPS experiments. Pump conditioning is identical to that of Figure 6.5. The pump rejection filters have been shown as a free-space implementation; in-fiber filters are available, but would require the use of single-mode fibers at the cost of reducing the collection efficiency by a factor of 5 or greater. SPD-1 is free-running, while SPD-2 is gated.	104
7.1	Illustration of a possible waveguide array and source configuration for engineering higher-order photon correlations. An effective index gradient across the array allows Bloch oscillations to be supported. [12].	110
7.2	A three-stage integrated circuit, where the unitary transformation \hat{U} represents a coupled waveguide array. Input correlations and the output selection are chosen with \hat{U} to target the desired output correlations.	112

List of Recurring Abbreviations

AlGaAs	Aluminium Gallium Arsenide
BPA	Biphoton Amplitude
BRW	Bragg Reflection Waveguide
CW	Continuous Wave
DOF	Degree of Freedom
FEA	Finite Element Analysis
FWHM	Full Width at Half-Maximum
HOM	Hong-Ou-Mandel (effect/interference)
IFPS	Interference Facilitated Pair Separation
NA	Numerical Aperture
PM	Phase-Matching
PMF	Polarization-Maintaining Fiber
SFWM	Spontaneous Four-Wave Mixing
SHG	Second Harmonic Generation
SMF	Spatial Mode Filter
SN	Schmidt Number
SPDC	Spontaneous Parametric Downconversion
TE	Transverse-Electric (polarization)
TIR	Total Internal Reflection
TM	Transverse-Magnetic (polarization)
MMF	Multimode Fiber
MMI	Multimode Interferometer
MZI	Mach-Zehnder Interferometer
NDA	Near-Degeneracy Approximations
WD	Wavelength Demultiplexer

Chapter 1

Introduction

During the past three decades, quantum states of light have provided a crucial experimental testbed for fundamental assertions of modern physics. Such states were pivotal in consolidating the non-locality of quantum mechanics [13–16], thereby stimulating intensive research into entanglement and quantum information theory. They have also made important contributions to the understanding of non-classical interference [17–21]. These and related achievements have not only benefited foundational science, but have also motivated efforts to exploit quantum attributes as a resource for practical applications.

Today, a thriving area of research known as quantum photonics seeks to harness the non-classical properties of light to enable optical technologies with new or enhanced capabilities. For example, photon entanglement [22], in which one or more photons form a non-local composite system with joint attributes, can be used to teleport quantum states [23, 24], to access unprecedented resolutions in metrology and microscopy [25–30], to provide pathway selectivity in pump-probe spectroscopy or induce entanglement in matter [31–34], and to image an object without detecting the photons that passed through it [35]. In communications security, photons can be used to exchange an encryption key that cannot be intercepted without heralding the presence of an eavesdropper [36–40]. This is guaranteed in principle by the quantum no-cloning theorem [41] and is driving efforts to establish earth-to-satellite quantum photonic channels [42–44]. ‘Squeezed’ states of light, which exhibit reduced uncertainties in one of their phase-space quadratures [45], have attracted interest as a means of overcoming the classical shot noise limit in certain homodyne-based measurements [46–49]. Quantum states of light also have numerous applications in quantum computing [50, 51] and the simulation of non-classical systems [52, 53].

Most proof-of-concept demonstrations of quantum photonic technology to date have been implemented in free-space using discrete components on an optical bench. However, this bulk-optics approach

faces severe limitations in scalability and practicality. Such setups have large footprints and high costs, require stringent operating environments and careful alignment, and suffer from inherent instabilities that need constant maintenance. For quantum photonic technology to sustain increases in complexity and proliferate beyond the lab, the transition to an integrated on-chip setting has been recognized as essential.

1.1 Integrated Quantum Photonics

All quantum photonic technologies are predicated on three main capabilities: state generation, state manipulation, and state detection. Recent efforts have focused on developing these capabilities in the integrated setting [54], and the results have thus-far been promising.

Quantum states of light can be generated on-chip through two dominant approaches. The first uses the radiative decay of semiconductor quantum dots [55] to produce single photons [56, 57] or entangled photon pairs [58, 59]. This generation process can be on-demand [57] and electrically driven [58, 59], but often necessitates cryogenic cooling and is typically limited to photon wavelengths below 1 micron. The second approach is based on spontaneous parametric downconversion (SPDC) [60, 61] or spontaneous four-wave mixing (SFWM) [62] in integrated nonlinear structures, which have the advantage of operating at room temperature. In both SPDC and SFWM, photons are annihilated from an optical pump to create squeezed states of temporally-correlated photon pairs. Depending on the implementation, these pairs can be entangled in the spectral, spatial or polarization degrees of freedom [63], or can alternatively exist in factorable single-photon states [64, 65]. Pair generation from integrated nonlinear waveguides has been demonstrated in numerous material platforms including AlGaAs [11, 66], silicon [67–69], and lithium niobate [70]. Of these, AlGaAs Bragg reflection waveguides (BRWs) are particularly interesting since they can be monolithically integrated with the pump laser [71, 72]. In addition to their compactness and relative stability, integrated nonlinear sources offer several other advantages over their bulk-optics counterparts. Their state generation rates can be orders of magnitude higher [63], due to the more efficient nonlinear interactions afforded by tight optical confinement. Through dispersion engineering and birefringence management, they can provide unprecedented versatility in tailoring the properties of the quantum state, including the spectral and polarization entanglement [73–75], photon bandwidths [76], and degree of non-degeneracy. Lastly, a single device can be designed to produce a variety of quantum states that are selected through the choice of pump polarization and wavelength. This allows for in-situ toggling between cross- and co-polarized pair generation [77, 78] and can also provide continuous tunability in the photon central wavelengths, from conditions of degeneracy to separations far exceeding

100 nm [11]. Such tunability is not just convenient but essential to certain applications, for instance quantum-enhanced spectroscopy [31–33].

Integrated circuits for manipulating quantum states have also witnessed rapid progress. Early demonstrations were implemented in silica-on-silicon [1, 79–81], but have since expanded to include silicon wire [82], GaAs [83], lithium niobate [84], femtosecond laser-written waveguides in borosilicate [85, 86], and UV-written waveguides in Ge-doped planar silica [87]. The performance of such circuits has generally been benchmarked by their ability to support high-fidelity quantum interference [80] while offering re-configurability through phase-controlled optical components [81]. One of the most ubiquitous integrated devices in these demonstrations is the directional coupler [1, 6, 79–81, 83–86, 88], which serves as the on-chip equivalent of a beamsplitter and can be used to build up more sophisticated components such as Mach-Zehnder Interferometers (MZIs) [83], partially-polarizing beamsplitters (PPBS) [86], and probabilistic quantum gates (e.g. the controlled-not [88]). In some cases the directional coupler is substituted with a multi-mode interferometer (MMI) [82] or X-coupler [87], but this remains less common. Due to their inherently alignment-free nature, integrated quantum circuits have demonstrated superior stability and interference fidelities compared to bulk-optics. They are also advantageous as a means of implementing coupled waveguide arrays for exploring statistical phenomena such as quantum walks [89].

Finally, much work has been done to improve the performance of single photon detectors for on-chip state readout. Detecting the quantum state on-chip has the potential to improve the overall fidelity of quantum photonic technologies by eliminating off-chip coupling losses. Some of the most promising detection efficiencies and temporal resolutions have been obtained using superconducting nanowires [90, 91]. However, this direction precludes room-temperature operation, which other architectures such as single-photon avalanche photodiodes may be able to provide [92].

It is clear that integration is a viable route for quantum photonics, and that its intensive development will continue. However, integration is not without its own unique challenges. Attempts to combine state generation, manipulation and detection into a single monolithic device will inevitably require compromises in the design of each constituent element, since these elements must share a common fabrication process and material system. Furthermore, whereas bulk-optics implementations can easily swap out components as necessary to optimize performance for several situations, integrated circuits are far more restricted in their reconfigurability. Ideally, integrated quantum photonic systems should be made as versatile as possible so that multiple needs can be met with a single design. This aim takes full advantage of the tunability offered by on-chip sources, but means that any key optical components must continue to function over a wide variety of conditions. The performance of integrated quantum circuits under a highly-tunable input state has not previously been addressed, and yet is important

to applications where such tunability is essential or advantageous. Quantum circuit demonstrations to date have generally assumed a single input state; furthermore, on-chip quantum interference has been implemented almost exclusively with degenerate indistinguishable photons.

Increasing the scope of states accommodated by quantum circuits necessarily addresses another key characteristic of the integrated setting, namely that integrated optical components can have highly polarization- and wavelength-dependent behaviour owing to dispersion. Hence, while bulk-optics beam-splitters can provide consistent performance over many tens of nanometers, the same is not necessarily true of their integrated counterpart, the directional coupler. The full implications this has for on-chip quantum interference and other non-classical phenomena are unknown. In order to design quantum photonic circuits for highly-tunable sources, strategies for more universal performance are needed, together with a more complete understanding of how device dispersion impacts non-classical functionalities.

1.2 Photon Pair Separation

One potential bottleneck to improving the versatility of quantum photonic circuits is photon pair separation. Photon pairs are created together but must be separated into different waveguides to allow for independent manipulation. This is generally a straightforward process in bulk optics, since the most common pair generation schemes lead to photons with spatially-divergent and anti-correlated propagation vectors [22, 93, 94]. In such cases the photons can be separated through judicious placement of collection optics, as illustrated in Figure 1.1(a). For integrated sources, however, the restricted spatial modes available for pair production generally overlap and co-propagate, offering no reliable way to separate the photons based on spatial distribution. Separation must therefore be facilitated by an on-chip optical component, but the suitability of a given component to this task can be highly dependent on the quantum state.

1.2.1 Conventional Techniques

Pair separation should ideally be ‘deterministic’ so that the two photons are made to propagate in different waveguides with near-unity probability. One conventional approach is to use a wavelength-demultiplexer or polarization-splitter to classically sort the photons based on a distinguishable degree of freedom. This method clearly fails when the photons are indistinguishable or share significant spectral overlap. Furthermore, it can compromise photon entanglement, since the output path taken by each photon reveals knowledge about the photon’s properties. In such cases it is common to instead separate the photons non-deterministically using a 50:50 mode splitter (e.g. directional coupler); however, this

comes at the cost of post-selection and a 3 dB loss in the number of useful output states produced.

Additional problems arise when the photon polarizations and non-degeneracy are tunable, in which case neither of the aforementioned approaches are suited to handling all possible states. This issue can be sidestepped by counter-propagating generation schemes [95] or through separation based on lateral mode order [2] as seen in Figure 1.1(b), but these represent special cases that are not applicable to most integrated pair sources.

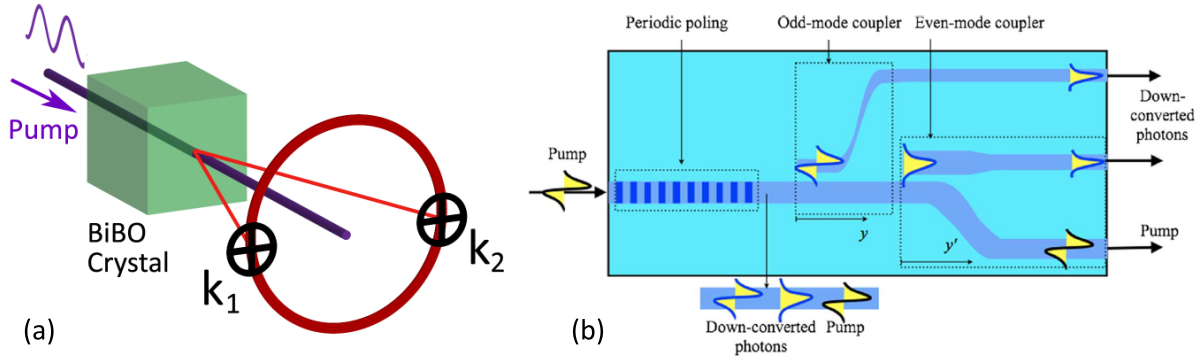


Figure 1.1: (a) Example of pair separation from a bulk nonlinear crystal (BiBO) [1]; conservation of momentum constrains the photons to be found at antipodal points of the conical cross-section, hence placing collection optics at these points guarantees deterministic separation. (b) On-chip pair separation based on lateral mode order, where modal indistinguishability is re-established at the output (figure extracted from Ref. [2]). Generating the photons in two different lateral modes is not always possible.

1.2.2 Non-classical Approach

A more universal solution to pair separation can be achieved by pivoting on the non-classicality of two-photon statistics. The Hong-Ou-Mandel (HOM) effect [17, 96] is perhaps the most familiar example of such non-classicality, and involves the coalescence of an anti-bunched state (where the two photons can only be found in different spatial modes) into a bunched state (where the two photons can only be found in the same spatial mode) through quantum interference. This phenomenon comprises the majority of on-chip quantum interference experiments [1, 6, 79, 81–84, 87, 97]. Under certain conditions, a time-reversed but more general form of the HOM effect can cause bunched states generated by photon pair sources to anti-coalesce into anti-bunched (i.e. separated states).

Such interference-facilitated pair separation (IFPS) was first demonstrated in fiber Sagnac loops [3, 98–100] and later on-chip [4, 101] (e.g. see Figure 1.2) by coherently pumping two identical photon pair sources to produce the path-entangled state $|\Psi\rangle = |\psi\rangle_A |0\rangle_B + |0\rangle_A |\psi\rangle_B$, where A and B label the two sources, $|\psi\rangle$ represents a photon pair, and $|0\rangle$ the vacuum. Interfering these two paths through an ideal 50:50 mode coupler leads to deterministic photon pair separation so long as no which-way

information is available to distinguish $|\psi\rangle_A$ from $|\psi\rangle_B$. Since the interference originates in the path indistinguishability, as opposed to particle indistinguishability, IFPS allows any arbitrary two-photon state $|\psi\rangle$ to be separated into different spatial modes by a single integrated device. Furthermore, spectral and polarization properties remain uncorrelated with the output path, thereby preserving any pre-existing entanglement in these degrees of freedom.

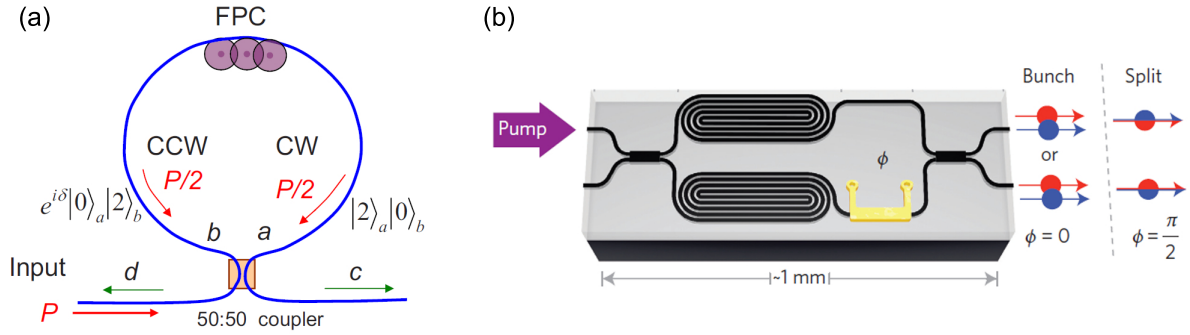


Figure 1.2: Seminal implementations of IFPS (a) in fiber and (b) on-chip; the latter was implemented with MMIs instead of a directional coupler. In the fiber implementation, the two interfering paths correspond to the coherently-pumped counter-propagating loop directions. (Figures extracted from Refs. [3] and [4] respectively.)

IFPS therefore appears to be the superlative approach to photon pair separation in integrated quantum circuits, in principle. Due to the highly dispersive nature integrated optical components, however, the assumption of ideal 50:50 mode coupling is unlikely to be satisfied by all quantum states of interest. On-chip IFPS has been previously demonstrated with indistinguishable [101] and nearly-degenerate [4] co-polarized states, but never in a regime where coupler dispersion becomes a significant consideration, nor with any commentary on the possible effects of coupler dispersion. It is important that the implications of coupler dispersion for IFPS beyond this regime be well-understood, to both anticipate and address any practical limitations to IFPS performance. A comprehensive understanding is also of interest to ascertain whether coupler dispersion leads to novel interference behaviour not encountered in bulk-optics or fiber-based implementations, and to gain insight on how other interference-based functionalities might be affected by coupler dispersion.

1.3 Thesis Aims and Overview

The primary goal of this thesis is to develop a comprehensive understanding of how dispersion impacts on-chip IFPS implemented with a directional coupler. This objective involves the development of a more detailed theoretical treatment of IFPS than what has previously been used. The directional coupler is

given focus not only because of its ubiquity as a quantum circuit component, but also because its function can be more severely affected by dispersion than other mode coupler implementations such as MMIs, X-couplers, and Y-couplers. Any limitations to IFPS performance arising from such dispersion will be identified, and strategies for mitigating such limitations will be discussed. Other details concerning the implementation and characterization of IFPS, not previously reviewed in the context of pair separation, will also be examined, including issues of stability and temporal path walk-off.

The secondary goal is to seek out novel behaviours and capabilities that directional coupler dispersion may enable. This includes the capability of such couplers to serve as versatile tools for quantum state engineering.

Lastly, a route for experimentally testing the predictions of this thesis will be developed. This involves the design of integrated circuits and experiments to implement IFPS for a more diverse range of quantum states than has previously been explored on-chip. Such efforts would leverage the Helmy group's existing expertise in AlGaAs BRW photon pair sources, and are interesting in their own right for assessing the challenges involved in implementing IFPS with the BRW architecture.

The thesis is organized as follows. Chapter 2 introduces the theoretical concepts fundamental to understanding and modelling two-photon on-chip quantum interference, and also reviews in detail the behaviour of conventional HOM-type interference to better place IFPS in context. Chapter 3 develops a detailed theoretical treatment of IFPS from quantum theory. The resulting theoretical model is first used to provide commentary on aspects of IFPS implementation that do not concern coupler dispersion. Then, with dispersive effects included, a dimensionless model is used to analyze IFPS in the near-degeneracy regime, where all on-chip experiments to date have been conducted. Lastly, the insight gained from the near-degeneracy regime is used to understand IFPS behaviour far from degeneracy, and how non-idealities can affect this behaviour. Chapter 4 presents several case studies wherein the effects of higher-order coupler dispersion and quantum state asymmetries are discussed. The capabilities of active coupler tuning for restoring near-perfect performance and tailoring the output state are also explored. Chapter 5 focuses on designing circuits for implementing IFPS based on an existing BRW photon pair source architecture, and will address some practical challenges of using BRWs for this purpose. Chapter 6 presents a experimental roadmap for characterizing the circuits designed in Chapter 5 and for measuring IFPS behaviour. Conclusions and future directions are discussed in Chapter 7.

Chapter 2

Two-Photon Quantum Interference in Integrated Circuits

The aim of this chapter is to establish the key fundamental concepts and formalisms used throughout this thesis. It begins with a review of the quantum description of light and two-photon states, followed by a discussion of the HOM effect and related forms of interference. Concepts are first described in the simpler bulk-optics setting to lay the qualitative foundations for analysing IFPS without the added complications of integration. Finally, the description of light in integrated circuits is briefly reviewed to highlight the origins of coupler dispersion and other factors impacting on-chip IFPS.

2.1 The Quantum Description of Light

This section briefly introduces quantum states of light in free-space and describes how non-classical properties such as entanglement are quantified. Phase-space representations of the field will not be treated in this dissertation.

2.1.1 Formalism

Quantization and Mode Functions

The fundamental description of light is formulated in terms of a quantized field, wherein photons are discrete excitations. Detailed reviews of field quantization are available in Refs. [102–105]. The free-space Hamiltonian of the electromagnetic field takes the form of a simple harmonic oscillator. In quantizing the field, it is mathematically convenient to use a plane-wave basis of mode functions proportional

to $\exp(\mathbf{k}(\omega) \cdot \mathbf{r} - i\omega t)$, where $\mathbf{k}(\omega)$ is the wavevector. However, these modes are unphysical along the directions lateral to $\mathbf{k}(\omega)$ since they extend infinitely throughout space without bound. Physical states of the field can be built up from an orthonormal set of laterally-bounded mode functions $u_{\sigma}^{(j)}(\omega, \mathbf{r})$, where the superscript j denotes the lateral mode and the subscript σ is the polarization degree of freedom. Each lateral mode is associated with a creation and annihilation operator, denoted respectively by $\hat{a}^{j\dagger}(\omega, \mathbf{r})$ and $\hat{a}^j(\omega, \mathbf{r})$. These correspondingly add or remove field quanta from mode j , and obey the commutation relations

$$\left[\hat{a}_{\sigma}^j(\omega, \mathbf{r}), \hat{a}_{\sigma'}^{j'\dagger}(\omega', \mathbf{r}') \right] = \delta_{j,j'} \delta_{\sigma,\sigma'} \delta(\omega - \omega') \delta(\mathbf{r} - \mathbf{r}'), \quad \left[\hat{a}_{\sigma}^j(\omega, \mathbf{r}), \hat{a}_{\sigma'}^{j'}(\omega', \mathbf{r}') \right] = 0. \quad (2.1)$$

The mode operators may also be expressed in their space-time and energy-momenta representations, i.e. $\hat{a}^{j\dagger}(t, \mathbf{r})$ and $\hat{a}^j(\omega, \mathbf{k})$; however, the use of frequency as the scalar four-space coordinate and position as the vector coordinate will be more convenient.

When light is focused into a beam, it is convenient to express the mode operators more compactly as

$$\hat{a}_{\sigma}^j(\omega, z) = \int dx dy u_{\sigma}^{(j)}(\omega, x, y, z) \hat{a}^j(\omega, x, y, z), \quad (2.2)$$

where z designates the position along the beam path. The observables of interest throughout this dissertation are related to correlations of the electric field; hence the general mode functions $u_{\sigma}^{(j)}(\omega, \mathbf{r})$ will correspond to the electric field distributions $\mathbf{E}_{\sigma}^{(j)}(\omega, \mathbf{r})$ obtainable from classical optics. Each such mode has a different lateral structure dependent on the chosen basis. For example, one possible basis for expanding the cross-sectional profile of a beam is given by the Laguerre-Gaussian modes [106]. Several of the lowest-order lateral modes for this basis are illustrated in Figure 2.1. Modal structure is important to quantum interference, as it is a potential source of distinguishability or incomplete amplitude cancellation.

A few brief comments regarding notation are now made. When referring to the same lateral mode but at different positions along the optical path, it is common to use the shorthand notation $\hat{a}_{\sigma}^j(\omega)$, where different coordinates in z are denoted by adding a prime next to the mode order j . For example, the operators $\hat{a}_{\sigma}^j(\omega, z_1)$ and $\hat{a}_{\sigma}^j(\omega, z_2)$ may be written as $\hat{a}_{\sigma}^j(\omega)$ and $\hat{a}_{\sigma}^{j'}$ respectively. In cases where multiple optical paths exist, such as when dealing with a beamsplitter, it is common to use j to signify the path in addition to the mode order. Mode operators that differ in coordinate, path, or mode order may also be delineated through the use of a different letter, i.e. $\hat{b}_{\sigma}^j(\omega)$. It will be clear from context which of these conventions is being used.

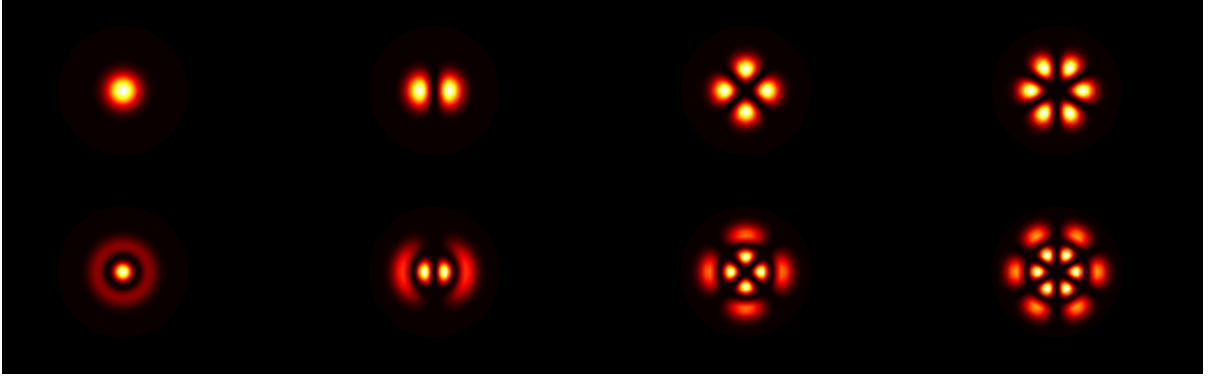


Figure 2.1: Radial plots of the first several Laguerre-Gaussian spatial modes, generated using Matlab.

Fock and Coherent States

Single-mode states containing exactly n photons are called Fock states [102, 103] and given the shorthand notation $|n\rangle$. Using the above formalism, a single excitation of the electromagnetic field is written as

$$\hat{a}_\sigma^{j\dagger}(\omega)|\text{vac}\rangle = |1\rangle_{j,\sigma,\omega}, \quad (2.3)$$

where $|\text{vac}\rangle$ represents the vacuum (zero-point energy) state. States with exactly n photons distributed among several Fock states (e.g. having different frequencies or polarizations) are denoted $|\{n\}\rangle$, and have the completeness relation $\sum_n |\{n\}\rangle \langle\{n\}| = 1$. Operating on a Fock state with a creation or annihilation operator leads to

$$\hat{a}_\sigma^{j\dagger}(\omega)|n\rangle_{j,\sigma,\omega} = \sqrt{n+1}|n+1\rangle_{j,\sigma,\omega}, \quad \hat{a}_\sigma^j(\omega)|n\rangle_{j,\sigma,\omega} = \sqrt{n}|n-1\rangle_{j,\sigma,\omega}. \quad (2.4)$$

States with higher n are built up from the repeated application of $\hat{a}_\sigma^{j\dagger}(\omega)$ on $|\text{vac}\rangle$ and are given by $|n\rangle_{j,\sigma,\omega} = (n!)^{-1/2} (\hat{a}_\sigma^{j\dagger}(\omega))^n |\text{vac}\rangle$. Such states can exhibit highly non-classical behaviour [17, 105, 107] and are therefore a primary resource for quantum photonic technology. Lasers and other common light sources encountered in the lab do not produce Fock states, but rather a Poissonian superposition of photon number states of the form

$$|\alpha\rangle_{j,\sigma,\omega} = e^{(\alpha\hat{a}_\sigma^{j\dagger}(\omega) - \alpha^*\hat{a}_\sigma^j(\omega))} |\text{vac}\rangle = e^{-|\alpha|^2/2} \sum_{n=0}^{\infty} \frac{\alpha^n}{\sqrt{n!}} |n\rangle_{j,\sigma,\omega}, \quad (2.5)$$

where α is a complex amplitude and $|\alpha|^2$ can be thought of as the mean photon number. Such states are called coherent states and tend to behave classically [103].

Single-Photon Amplitudes

All physical states must have finite spectral content so that they are bounded along the direction of propagation. Hence, a single-photon state existing in mode j propagates as a wavepacket described by

$$|\psi\rangle = \sum_{\sigma} \int d\omega \phi_{\sigma}^j(\omega) \hat{a}_{\sigma}^{j\dagger}(\omega) |\text{vac}\rangle, \quad (2.6)$$

where $\phi_{\sigma}^j(\omega)$ represents the photon spectrum and is normalized such that $\langle\psi|\psi\rangle = 1$. The spectrum also determines the coherence properties of the photon; the importance of coherence for quantum interference is described in Section 2.2.1. An equivalent temporal representation of the state is $|\tilde{\psi}\rangle = \sum_{\sigma} \int dt \tilde{\phi}_{\sigma}^j(t) \hat{a}_{\sigma}^{j\dagger}(t) |\text{vac}\rangle$ where $\tilde{\phi}_{\sigma}^j(t)$ is obtained from the Fourier transform $\tilde{\phi}_{\sigma}^j(t) = \int d\omega \phi_{\sigma}^j(\omega) \exp(-i\omega t)$.

The amplitude $\phi_{\sigma}^j(\omega)$ also has a complex phase that changes as the state evolves. For example, evolving the state described in Equation (2.6) over a time interval Δt leads to a phase term of $\exp(-i\omega\Delta t)$. It also is important to note that the amplitude $\phi_{\sigma}^j(\omega)$ is defined relative to the same spatial coordinate as the mode operator $\hat{a}_{\sigma}^{j\dagger}(\omega)$. To translate this definition to a mode operator a distance z away, the amplitude is given a phase of $\exp(ik_z(\omega)z)$. In the wavepacket's spatial representation, these phases lead to the translation and broadening of the wavepacket as it evolves.

2.1.2 Two-Photon States

Two-photon states are an important class of states used in quantum photonic technologies, chiefly because of their ability to provide squeezing, entanglement, or heralded single photons [22, 45, 67]. Assuming that each photon occupies only a single spatial mode, a general two-photon state can be represented as [3, 5, 61]

$$|\psi\rangle = \sum_{\alpha\beta} \int d\omega_1 d\omega_2 \phi_{\alpha\beta}(\omega_1, \omega_2) \hat{a}_{\alpha}^{j_1\dagger}(\omega_1) \hat{a}_{\beta}^{j_2\dagger}(\omega_2) |\text{vac}\rangle, \quad (2.7)$$

where $\phi_{\alpha\beta}(\omega_1, \omega_2)$ is called the biphoton amplitude (BPA). The BPA provides complete information about the polarization and spectral attributes of the state, including entanglement. It is normalized such that $\langle\psi|\psi\rangle = 1$. The properties of such two-photon states will now be discussed.

Permutation Symmetry

Figure 2.2 presents pictorial representations of several distinguishable two-photon states. Under special circumstances, the BPA can be permuted in its frequency and polarization arguments without changing the quantum state [108]. These circumstances arise when the photons are indistinguishable either in spatial mode or in spectral/polarization attributes. To illustrate this, consider the state

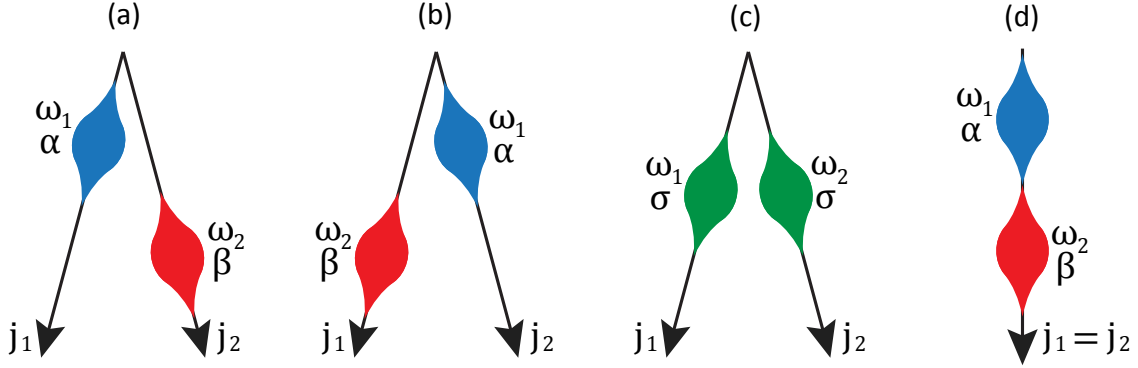


Figure 2.2: Depictions of two-photon states with various degrees of permutation symmetry: (a) and (b) are left unchanged only for concurrent permutations of all three degrees of freedom $\{\omega, \sigma, j\}$; (c) is invariant under path exchange $\{j\}$; and (d) is invariant under the concurrent exchange of frequency and polarization $\{\omega, \sigma\}$.

$|\psi_0\rangle = \sum_{\alpha\beta} \int d\omega_1 d\omega_2 \phi_{\alpha\beta}(\omega_1, \omega_2) |\omega_1, \alpha, j_1\rangle |\omega_2, \beta, j_2\rangle$ under exchange of both the frequency and polarization labels. The resultant state is given by $|\psi_1\rangle = \sum_{\alpha\beta} \int d\omega_1 d\omega_2 \phi_{\beta\alpha}(\omega_2, \omega_1) |\omega_2, \beta, j_1\rangle |\omega_1, \alpha, j_2\rangle$. Several cases are now examined:

- Suppose the labels j_1 and j_2 refer to distinguishable paths, and the photons themselves are also distinguishable in frequency and polarization. In this case, $|\psi_0\rangle$ can be associated with the diagram in Figure 2.2(a), and $|\psi_1\rangle$ with 2.2(b). The total states are clearly distinguishable, and indeed $|\psi_0\rangle \neq |\psi_1\rangle$ unless the path degree of freedom is also exchanged.
- Suppose the labels j_1 and j_2 again refer to distinguishable paths, but that the photons are now indistinguishable in frequency and polarization. The state $|\psi_0\rangle$ now corresponds to Figure 2.2(c), which is invariant under exchange of the ω and σ labels. In this case, $|\psi_0\rangle$ and $|\psi_1\rangle$ are indistinguishable in all degrees of freedom, with $|\psi_0\rangle = |\psi_1\rangle$. This in turn implies that $|\psi_0\rangle$ is invariant under the BPA permutation $\phi_{\alpha\beta}(\omega_1, \omega_2) \rightarrow \phi_{\beta\alpha}(\omega_2, \omega_1)$.
- Finally, suppose the paths are now indistinguishable such that $j_1 = j_2 = j$, but that spectral and polarization distinguishability remains. This also leads to $|\psi_0\rangle = |\psi_1\rangle$, with both states corresponding to Figure 2.2(d). Hence, $|\psi_0\rangle$ is again invariant under the BPA permutation $\phi_{\alpha\beta}(\omega_1, \omega_2) \rightarrow \phi_{\beta\alpha}(\omega_2, \omega_1)$.

In summary, for states in the form of Equation (2.7), the BPA has the effective equivalency $\phi_{\alpha\beta}(\omega_1, \omega_2) = \phi_{\beta\alpha}(\omega_2, \omega_1)$ when either: the photons are indistinguishable in both ω and σ ; or when the photons are indistinguishable in their modal/path degree of freedom. This will have implications for quantum interference.

Two-Photon Entanglement

Two photons are considered entangled if correlations exist between their joint properties, such that measuring an observable for one photon affects the possible values that observable can take for the other [22, 109]. Hence, if entanglement exists in a particular degree of freedom (DOF), the joint probability distribution associated with observables for that DOF cannot be written as a product of independent distributions for each photon. For example, only in the special case of perfectly uncorrelated (i.e. non-entangled) photons can the BPA be written as the factored product $\phi_\alpha^{(1)}(\omega_1)\phi_\beta^{(2)}(\omega_2)$ of individual photon spectra. Entanglement is of interest because of its quintessential role as a quantum photonic resource. Whether coupler dispersion in IFPS adversely affects entanglement is hence an important consideration. Conversely, entanglement may itself influence the degree to which coupler dispersion affects IFPS.

Two of the most common quantifiers of spectral and polarization entanglement are the Schmidt number (SN) [108, 110] and the concurrence (C) [111, 112], respectively. As detailed in Appendix A, the BPA can be decomposed in terms of Schmidt modes $U_{\alpha n}(\omega_1)$ and $V_{\beta n}(\omega_2)$ as

$$\phi_{\alpha\beta}(\omega_1, \omega_2) = \sum_n^\infty \sqrt{p_n} U_{\alpha n}(\omega_1) V_{\beta n}(\omega_2), \quad (2.8)$$

where the p_n are normalized according to $\sum_n p_n = 1$ and are given by the eigenvalues of the matrix

$$\rho_{\alpha\beta}^{\omega\omega'} = \int d\omega'' \phi_{\alpha\beta}(\omega, \omega'') \phi_{\alpha\beta}^*(\omega', \omega''). \quad (2.9)$$

The Schmidt number is then obtained from $\text{SN} = [\sum_n p_n^2]^{-1}$. It is equal to unity for spectrally uncorrelated states, and increases in value with increasing spectral entanglement. For a cross-polarized state, the concurrence can be calculated from [75]

$$C = 2 \left| \int d\omega_1 d\omega_2 \phi_{\beta\alpha}^*(\omega_1, \omega_2) \phi_{\alpha\beta}(\omega_1, \omega_2) \right|. \quad (2.10)$$

The concurrence ranges from $C = 0$ for uncorrelated states to $C = 1$ for maximum polarization entanglement. Maximally polarization-entangled states have the additional BPA permutation symmetry $\phi_{\alpha\beta}(\omega_1, \omega_2) = \phi_{\beta\alpha}(\omega_1, \omega_2)$. The degree of entanglement present in a two-photon state is determined by the photon pair generation process.

When the spectra of two photons are entangled, one may nonetheless define marginal spectra for the individual photons. These are given by $\phi^{(1)}(\omega) = \int d\omega' \phi(\omega, \omega')$ and $\phi^{(2)}(\omega) = \int d\omega' \phi(\omega', \omega)$ for photons 1 and 2 respectively, and represent the possible values of ω one photon can acquire if all information

about the other is discarded. Whenever photon bandwidths are described, it will be in reference to these marginal spectra.

BPA Examples

Figure 2.3 depicts the BPAs of three different co-polarized states generated by SPDC in an integrated nonlinear waveguide. SPDC is only one of several available generation methods [5, 59, 62, 67], but will be the means of photon pair creation in the design and experimental portions of this thesis. In SPDC, a single pump photon is annihilated to produce photon pairs of equivalent total energy. Details of this process are reviewed in Chapter 5.1. The BPA shown in Figure 2.3(a) is of an approximately uncorrelated (SN = 1.121) degenerate photon pair. This represents a special case requiring purpose-specific engineering [64, 65]. More often, the photon pairs will exhibit entanglement as in Figure 2.3(b). The width of the BPA along the diagonal $\omega_1 = \omega_2$ is a significant factor influencing entanglement and is determined predominantly by the pump bandwidth. In the limiting case of a monochromatic pump of frequency ω_p , through energy conservation the BPA becomes constrained to the line $\omega_1 + \omega_2 = \omega_p$, from which knowledge of ω_1 completely determines the value of ω_2 and vice-versa. States where this is a good approximation are described as highly anti-correlated. Finally, Figure 2.3(c) shows a non-degenerate state. The central frequencies of the joint photon spectra follow a tuning curve with respect to the central frequency of the pump (e.g. see [11] or Figure 5.3 in Chapter 5), hence such states can be created by detuning the pump from conditions of degeneracy. Chapter 5.1 discusses tuning characteristics in greater detail.

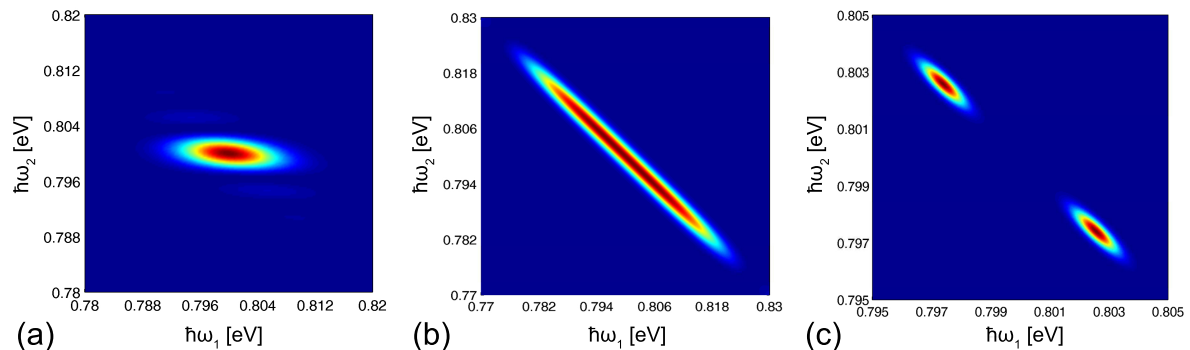


Figure 2.3: BPA probability distributions $|\phi(\omega_1, \omega_2)|^2$ showing (a) approximately uncorrelated degenerate, (b) anti-correlated degenerate, and (c) anti-correlated non-degenerate photon pair states generated through on-chip SPDC. The equations from which these plots were generated are detailed in [5].

Second-Order Spatial Correlations

The manifestations of quantum interference considered in this work affect the joint probability of finding one photon in spatial mode p and the other in spatial mode q . In this case the spatial modes refer to the optical path. Joint probabilities of this kind are measured by placing single-photon detectors in each path and monitoring correlations between detection events at each. For a pure state $|\psi\rangle$, the theoretical probability of the detectors at p and q obtaining detections at times t_1 and t_2 respectively is given by [62, 98, 103, 105]

$$P_{pq}(t_1, t_2) = \sum_{\alpha\beta} \langle \psi | \hat{a}_\alpha^{p\dagger}(t_1) \hat{a}_\beta^{q\dagger}(t_2) \hat{a}_\beta^q(t_2) \hat{a}_\alpha^p(t_1) | \psi \rangle. \quad (2.11)$$

This second-order correlation function is sensitive to the time delay $\tau = t_2 - t_1$ between detection events. One hallmark of two-photon states is the tendency for the detectors to fire in unison when the time delay τ between the arrival of the photons is zero [66]. Such events are called coincidences, and they manifest themselves as a peak in the detection histogram. A number of commercial options for single-photon detection presently exist, including InGaAs/InP avalanche photodiodes and superconducting nanowires. The total theoretical probability R_{pq} for a joint detection in p and q can be obtained by integrating $P_{p,q}(t_1, t_2)$ over the detection times [62]:

$$R_{pq} = \int dt_1 dt_2 P_{pq}(t_1, t_2). \quad (2.12)$$

In practice, several factors such as dark counts and photon losses cause the true detection probability to differ from the theoretical one. These and related non-idealities contribute a noise floor to the observed detection histogram, which is usually subtracted from the true coincidences as a systematic error. This issue is further mitigated by using one detector to electronically gate the other. Another consideration is that the exact form of the state generated by SPDC resembles a coherent state with the odd-number terms removed, given by [61]:

$$|\Psi\rangle = \exp\left(\mu \hat{C}_{II}^\dagger - \mu^* \hat{C}_{II}\right) |\text{vac}\rangle \quad (2.13)$$

where $\hat{C}_{II}^\dagger |\text{vac}\rangle = |\psi\rangle$, with $|\psi\rangle$ given by Equation (2.7). Hence, multiple photon pairs can be generated concurrently by the source. Such higher-order pair production constitutes a source of noise that can alter the count rate R_{pq} from its predicted value. The pair generation probability scales with $|\mu|^2$, which in turn scales with the pump power. Only when μ is sufficiently small does SPDC lead to an approximate

two-photon state:

$$|\Psi\rangle \approx |\text{vac}\rangle + \mu|\psi\rangle + \dots \quad (2.14)$$

This can be enforced by restricting the SPDC process pump to low powers, in which case higher-order pair generation contributes negligibly to the observed detection statistics, at the expense of the single-pair generation rate.

2.2 Two-Photon Interference in Bulk Optics

The bulk-optics setting offers a simple environment for discussing quantum interference before the complications of the integrated setting are introduced. Key features of two-photon interference pertinent to IFPS will be highlighted through a review of the well-known HOM effect. Studying the HOM effect also allows the distinctions of IFPS to be placed in context. For both phenomena, interference is mediated by a beamsplitter coupling two optical paths A and B . The beamsplitter acts as a point-like transformation that maps the mode operators according to [17, 103]

$$\hat{a}_\sigma^{A\dagger}(\omega) \rightarrow \sqrt{\eta}\hat{a}_\sigma^{A'\dagger}(\omega) + i\sqrt{1-\eta}\hat{a}_\sigma^{B'\dagger}(\omega), \quad \hat{a}_\sigma^{B\dagger}(\omega) \rightarrow \sqrt{\eta}\hat{a}_\sigma^{B'\dagger}(\omega) + i\sqrt{1-\eta}\hat{a}_\sigma^{A'\dagger}(\omega), \quad (2.15)$$

where η is the power splitting ratio, taken to be a constant (i.e. dispersionless). This transformation implies that n -photon states become coherent superpositions of the mode operators, which can lead to cases where certain mode operator combinations interfere either constructively or destructively. In contrast, a coherent state $|\alpha\rangle_A|0\rangle_B$ entering the beamsplitter from path A can be shown to evolve into the product state $|\alpha\sqrt{\eta}\rangle_{A'}|i\alpha\sqrt{1-\eta}\rangle_{B'}$, [103], which does not lead to observable non-classical behaviour.

2.2.1 Photon Coalescence: The Hong-Ou-Mandel Effect

Simplified Description: The Hong-Ou-Mandel (HOM) effect is one of the earliest examples of non-classical interference influencing the joint spatial properties of two-photon states [17]. Consider two co-polarized photons arriving simultaneously at a 50:50 beamsplitter ($\eta = 1/2$) from paths A and B as shown in Figure 2.4(a), and for simplicity assume they are monochromatic. The use of two different mode operators here (\hat{a} and \hat{b}) implies that the photons are not necessarily indistinguishable in their

lateral field profiles. The input state is transformed as

$$\begin{aligned} \hat{a}^{A\dagger}\hat{b}^{B\dagger}|\text{vac}\rangle &\rightarrow \left(\frac{1}{\sqrt{2}}\right)^2 \left(\hat{a}^{A'\dagger} + i\hat{a}^{B'\dagger}\right) \left(\hat{b}^{B'\dagger} + i\hat{b}^{A'\dagger}\right)|\text{vac}\rangle \\ &= \frac{1}{2} \left[\hat{a}^{A'\dagger}\hat{b}^{B'\dagger} + i\hat{a}^{A'\dagger}\hat{b}^{A'\dagger} + i\hat{a}^{B'\dagger}\hat{b}^{B'\dagger} - \hat{a}^{B'\dagger}\hat{b}^{A'\dagger} \right] |\text{vac}\rangle. \end{aligned} \quad (2.16)$$

The four possible outcomes in this expansion are illustrated in Figure 2.4(b). Classically, one would expect to observe each of these with equal probability. However, if $\hat{b}^\dagger = \hat{a}^\dagger$, meaning that the photons are indistinguishable in all DOFs aside from optical path, the expansion simplifies to

$$\hat{a}^{A\dagger}\hat{b}^{B\dagger}|\text{vac}\rangle \rightarrow \frac{1}{2} \left[\hat{a}^{A'\dagger}\hat{b}^{A'\dagger} + \hat{a}^{B'\dagger}\hat{b}^{B'\dagger} \right] |\text{vac}\rangle, \quad (2.17)$$

up to a global phase. It is therefore only possible to find the photons emerging from the beamsplitter together in the same optical path. This particular example of interference is called the HOM effect, but more generally the evolution of an anti-bunched state into a bunched state is referred to as coalescence. A factor of $\sqrt{2}$ is introduced during the calculation of outcome probabilities from Equations (2.11)-(2.12) which leads to an appropriately-normalized probability of 1/2 for each bunched outcome. Notably, adding an optical phase shift θ to one of the input paths leads only to an overall global phase factor, i.e. $\exp(i\theta)\hat{a}^{A\dagger}\hat{b}^{B\dagger}|\text{vac}\rangle$, that does not alter the interference, assuming there is no significant change to the photon arrival times. The HOM effect is therefore highly phase-stable, making it relatively easy to implement.

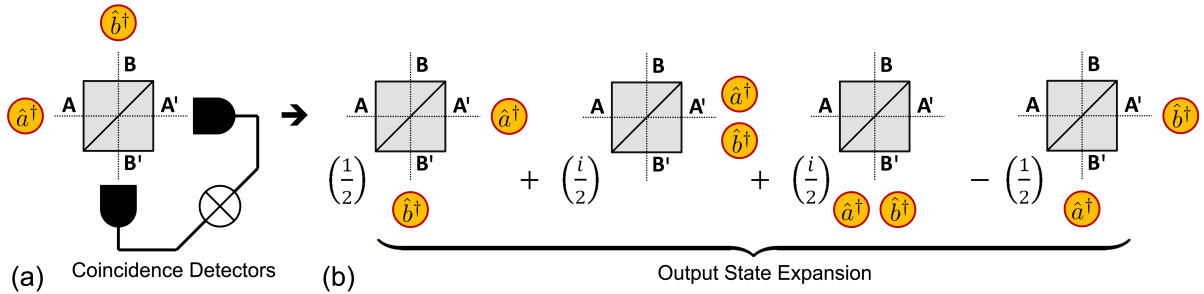


Figure 2.4: (a) Two photons incident upon a 50:50 beamsplitter; single-photon detectors monitor the coincidence rate at the output. (b) Output state expansion in terms of observable outcomes; when $\hat{a}^\dagger = \hat{b}^\dagger$ due to photon indistinguishability, the amplitudes associated with anti-bunched outcomes destructively interfere, and the detected coincidence rate drops to zero.

Note that even if the photons have identical lateral mode structures, the fields must overlap perfectly at the beamsplitter for interference to be maximal. For example, suppose the lateral mode associated with \hat{b}^\dagger is offset relative to that of \hat{a}^\dagger at the beamsplitter, by a distance of ϵ in local x and y coordinates.

Letting z_0 denote the local z-coordinate of the beamsplitter, and using Equation (2.2), this would give

$$\begin{aligned} \hat{a}^{A'\dagger}\hat{b}^{B'\dagger} - \hat{a}^{B'\dagger}\hat{b}^{A'\dagger} &= \int dx_1 dy_1 \int dx_2 dy_2 \left[\mathbf{E}^{*(A')}(\omega, x_1, y_1, z_0) \mathbf{E}^{*(B')}(\omega, x_2 + \epsilon, y_2 + \epsilon, z_0) \right] \\ &\quad \times \hat{a}^\dagger(\omega, x_1, y_1, z_0) \hat{a}^\dagger(\omega, x_2, y_2, z_0) \\ &\quad - \int dx_1 dy_1 \int dx_2 dy_2 \left[\mathbf{E}^{*(A')}(\omega, x_1 + \epsilon, y_1 + \epsilon, z_0) \mathbf{E}^{*(B')}(\omega, x_2, y_2, z_0) \right] \\ &\quad \times \hat{a}^\dagger(\omega, x_1, y_1, z_0) \hat{a}^\dagger(\omega, x_2, y_2, z_0) \\ &\neq 0, \end{aligned}$$

resulting in residual uncanceled anti-bunched amplitudes.

Complete Description: A more complete description of the HOM effect must take into account the finite photon spectra, a general splitting ratio η , and the possibility of a time delay τ between the arrival of the photons. The photon spatial modes are implicitly assumed to overlap perfectly at the beamsplitter. For a co-polarized state where $\phi_{\alpha\beta}(\omega_1, \omega_2) = \phi_{\beta\alpha}(\omega_1, \omega_2) \equiv \phi(\omega_1, \omega_2)$, the total probability of obtaining an anti-bunched output is proportional to [17, 113]

$$R(\tau) \propto \frac{1}{2} \left[1 - \frac{2\eta(1-\eta)}{\eta^2 + (1+\eta)^2} \text{Re} \left\{ \int d\omega_1 d\omega_2 \phi(\omega_1, \omega_2) \phi^*(\omega_2, \omega_1) e^{-i[\omega_2 - \omega_1]\tau} \right\} \right]. \quad (2.18)$$

Note that maximal interference necessitates both $\tau = 0$ and the permutation symmetry $\phi(\omega_1, \omega_2) = \phi(\omega_2, \omega_1)$ [113]. As discussed in Section 2.1.2, the latter requires indistinguishability in the photon spectral properties [114], since the photons begin in distinguishable paths. This is often achieved by placing identical bandpass filters in front of the detectors to ensure the spectra contributing to the measurement are degenerate with equal bandwidths.

Figure 2.5 shows how the anti-bunched probability vanishes when $\tau = 0$ but reverts to its classical value of 1/2 as τ is increased or decreased, tracing out a dip. One way of interpreting this result is that the time delay τ induces distinguishability between the photons and hence interference is lost. Another interpretation is that the photons lose their mutual coherence and hence the phase with which each frequency component (e.g. $d\omega$) sums towards the total probability becomes a random variable, causing the rightmost term in Equation (2.18) to vanish. It can be shown that the width of this dip is related to the spectral properties of the photons. Assuming frequency-uncorrelated photons having individual gaussian spectra of the form $\phi^{(n)}(\omega) \propto \exp(-[\omega_n - \omega_{0n}]^2 / 2\Delta\omega^2)$ where $n \in \{1, 2\}$ and ω_{0n} refers to the

central frequency of photon n , Equation (2.18) becomes

$$R(\tau) \propto \frac{1}{2} \left[1 - \left(\frac{2\eta(1-\eta)}{\eta^2 + (1-\eta)^2} \right) e^{-(\tau\Delta\omega)^2/2} \right]. \quad (2.19)$$

Notably, the dip width is unaffected by the presence of spectral entanglement; for example, enforcing $\omega_1 + \omega_2 = \omega_p$ to make the photon spectra highly anti-correlated leads to the same result. The dip width is therefore often associated with the coherence time of the individual photons. If the interfering photon fields are made non-degenerate before reaching the detectors, for example by using bandpass filters with different central frequencies ω_{01} and ω_{02} , then the interference dip becomes superimposed with sinusoidal oscillations at the frequency difference $\Omega = \omega_{02} - \omega_{01}$ [96]. This example has been illustrated together with the degenerate case in Figure 2.5.

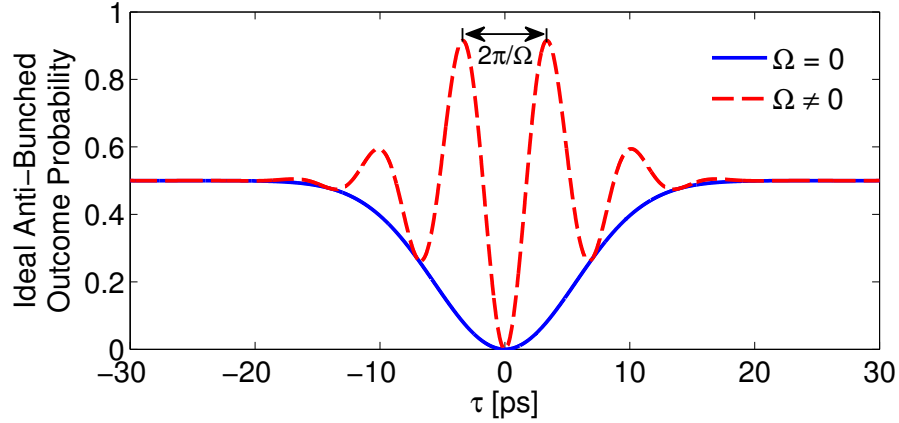


Figure 2.5: Coincidence count probability versus photon temporal delay τ , plotted for the special case of $\eta = 1/2$. The photon spectra are taken to be gaussian with $\Delta\omega = 1.77 \times 10^{11}$ Hz.

Interference Visibilities: One important quantifier of interference is the visibility, defined as the ratio of non-classical to classical contributions to the outcome probability. In the present case, the ideal visibility V_S associated with the anti-bunched (e.g. separated) outcome is equivalent to the dip contrast

$$V_S = \frac{R(\tau \rightarrow \infty) - R(\tau = 0)}{R(\tau \rightarrow \infty)} = \frac{2\eta(1-\eta)}{\eta^2 + (1-\eta)^2}. \quad (2.20)$$

The visibility is bounded by $[0, 1]$ and is maximal when $\eta = 1/2$, since other values of the splitting ratio lead to imperfect amplitude cancellation of the anti-bunched output terms. Deviations from the functional form of Equation (2.20) can also occur due to imperfect modal overlap or other sources of distinguishability not already accounted for. If instead one calculates the visibility associated with the bunched-output probability, V_B , it is found that $V_B = 1$ since both the classical and quantum

contributions to the probability scale identically with η .

2.2.2 Interference as a Which-Path Phenomenon

While implementations of the HOM effect use photons that are perfectly or nearly indistinguishable, photon indistinguishability is not a prerequisite to quantum interference in general. Interference is more fundamentally understood as a Feynman-path phenomenon: so long as two or more possible histories leading up to a measurement outcome are possible, and no ‘which-way’ information exists – even in principle – to causally indicate a particular history has occurred, then the quantum amplitudes ϕ_n associated with each such history add coherently towards the probability of obtaining that outcome [20, 21, 115, 116]. Interference can therefore occur with distinguishable photons provided path indistinguishability exists. The photons need not even arrive at the beamsplitter simultaneously, as long as which-way information is erased through a compensating time delay prior to state measurement [20].

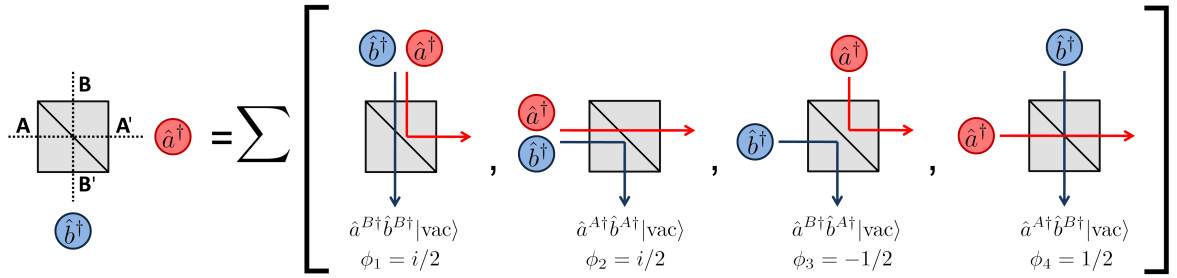


Figure 2.6: Expansion of the outcome $\hat{a}^{A\dagger}\hat{b}^{B\dagger}$ in terms of its possible histories (‘paths’). Interference between these histories can lead to a non-classical outcome probability.

To illustrate path interference, consider the anti-bunched outcome in Figure 2.6, where the photons possess a distinguishable DOF such as wavelength. The outcome has been expanded in terms of the possible histories and corresponding amplitudes that could have produced it, and occurs with a probability proportional to $|\sum_m \phi_m|^2$. If the initial state is known to be anti-bunched, then $\phi_1, \phi_2 \rightarrow 0$. The existence of only one of the remaining histories, either ϕ_3 or ϕ_4 , does not lead to a non-classical probability for the anti-bunched outcome. However, when both histories are present and equally likely, the anti-bunched outcome probability vanishes, leading to photon coalescence. Accomplishing this requires an input state of the form $|\psi\rangle = (2)^{-1/2} [\hat{a}^{A\dagger}\hat{b}^{B\dagger}|\text{vac}\rangle + \hat{a}^{B\dagger}\hat{b}^{A\dagger}|\text{vac}\rangle]$, which is not necessarily straightforward to prepare. On the other hand, both histories are implicitly present in the special case of indistinguishable photons, hence for the HOM effect, path indistinguishability becomes equivalent to photon indistinguishability. Importantly, when the state is written as a superposition of two possible histories, it becomes apparent that the relative phase between the paths plays a role in determining whether the in-

interference is constructive or destructive. For example, $|\psi\rangle = (2)^{-1/2} [\hat{a}^{A\dagger}\hat{b}^{B\dagger}|\text{vac}\rangle + \exp(i\pi)\hat{a}^{B\dagger}\hat{b}^{A\dagger}|\text{vac}\rangle]$ leads to constructive interference between ϕ_3 and ϕ_4 , and destructive interference between the amplitudes contributing to bunched outputs; hence the state remains anti-bunched. If this phase were instead a random variable, the output amplitude averages to the classical result, and interference is not manifested.

2.2.3 Photon Anti-Coalescence

Path interference can also enable anti-coalescence. In this case the possible photon histories must be restricted to bunched states only, and correspond to the path-entangled state

$$|\psi\rangle_{\text{in}} = \frac{1}{\sqrt{2}} [\hat{a}^{A\dagger}\hat{b}^{A\dagger} + \exp(i\theta)\hat{a}^{B\dagger}\hat{b}^{B\dagger}] |\text{vac}\rangle. \quad (2.21)$$

Evolving $|\psi\rangle$ through a beamsplitter when $\theta = 0$ leads to the anti-bunched state

$$|\psi\rangle_{\text{out}} = \frac{1}{\sqrt{2}} [\hat{a}^{A'\dagger}\hat{b}^{B'\dagger} + \hat{a}^{B'\dagger}\hat{b}^{A'\dagger}] |\text{vac}\rangle, \quad (2.22)$$

where the photons are always found to be separated. This is the basic principle behind IFPS. The most straightforward means of observing anti-coalescence is to inject a Mach-Zehnder interferometer (MZI) with an anti-bunched state of indistinguishable photons, as shown in Figure 2.7(a). The first beamsplitter leads to the transformation $|1\rangle_A|1\rangle_B \rightarrow |2\rangle_{A'}|0\rangle_{B'} + |0\rangle_{A'}|2\rangle_{B'}$ through HOM interference, which gives the 2-photon NOON state. The second beamsplitter reverses this process to recover the original state. However, the output statistics are changed if a relative phase shift of θ is present in one of the interferometer arms, in which case the output is given by $|\psi\rangle_{\text{out}} = \cos(\theta)|1\rangle_{A''}|1\rangle_{B''} + \sin(\theta)[|2\rangle_{A''}|0\rangle_{B''} + |0\rangle_{A''}|2\rangle_{B''}]/2$ [3]. Coincidentally, a path-entangled state leading to anti-coalescence can also be created by placing photon pair sources in each arm of the interferometer and pumping them coherently through the input beamsplitter as in Figure 2.7(b), and the presence of interference can be verified by observing changes to the count rate as θ is altered [4]. It is confirmed in Appendix C that although the pump, which is modelled as a coherent state, remains a classically-behaving product state after the input beamsplitter, the concurrent pumping of two photon pair sources does indeed lead to a path-entangled anti-bunched state, which is amenable to anti-coalescence. Equivalently, the output beamsplitter erases all which-way information about the source of origin, hence the two paths interfere as long as they have a stable relative phase.

Perhaps owing to the dominance of indistinguishable-photon manifestations of anti-coalescence due to its straightforward implementation, little in-depth discussion currently exists regarding IFPS with

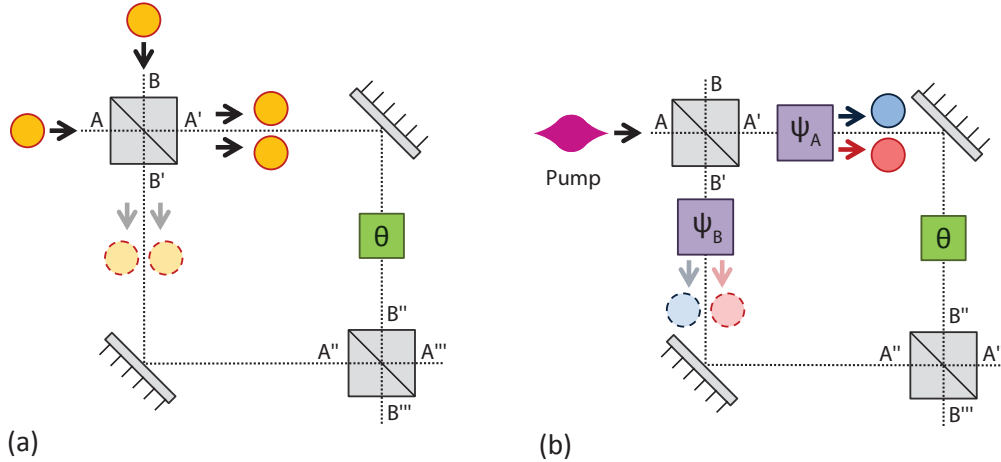


Figure 2.7: (a) Photon anti-coalescence with indistinguishable photons in an MZI; (b) photon anti-coalescence with coherently pumped photon pair sources.

arbitrary photon states. Anti-coalescence with degenerate NOON-states has been studied in the context of metrology [27, 46, 117], but descriptions of arbitrary state separation through IFPS have not progressed beyond the simple formalism presented in this subsection. Studying the full range of IFPS behaviour in the integrated setting requires the full two-photon state formalism of Section 2.1.2 as well as an in-depth understanding of how states of light evolve on-chip.

2.3 Light in Integrated Circuits

2.3.1 Classical Guided-Wave Optics

To understand the design and behaviour of optical components used for mediating on-chip quantum interference, it is first necessary to understand the mechanisms of light propagation in integrated optical structures. Two key concepts have particular importance: firstly, that light propagation is restricted to discrete modes dictated by the structure geometry and composition; and secondly, that these modes have evanescent fields whose properties are likewise dictated by the guiding structure.

Ray Optics Model: The simple ray-optics model of light provides a first look at how light is guided in integrated structures [118]. The fundamental unit of photonic integrated circuits is the optical waveguide, as illustrated in Figure 2.8, which in its most basic implementation consists of a slab ‘core’ with refractive index n_1 surrounded by a cladding with a lower refractive index n_0 . Guiding is provided by total internal reflection (TIR) at the core-cladding interface, which confines light within the core for angles of incidence above the critical angle $\theta_c = \sin^{-1}(n_0/n_1)$. However, for a physical bound state to

exist, every round-trip between the interfaces must lead to a self-consistent optical phase. This condition is satisfied only by a discrete set of incidence angles $\theta_m > \theta_c$ ($m \in \{0, 1, 2, \dots\}$), which define the optical modes supported by the structure. The forward-facing component of the total wavevector for a given θ_m is called the propagation constant (β_m).

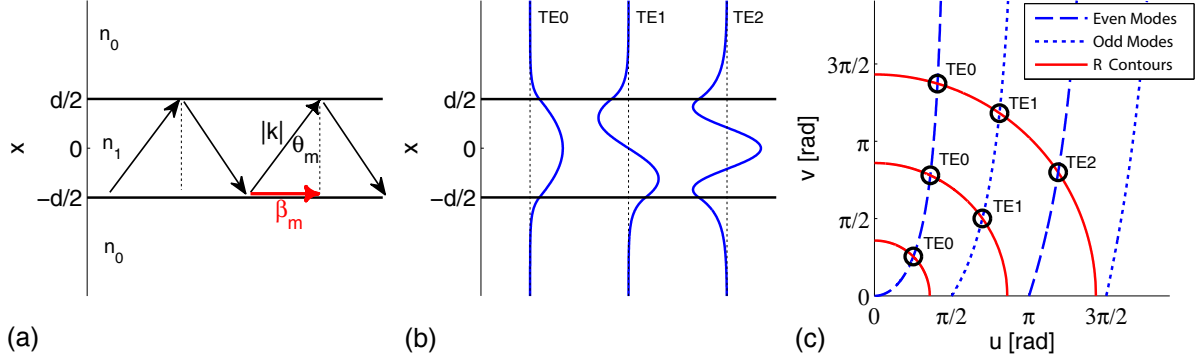


Figure 2.8: (a) Ray-optics illustration of a 1D symmetric slab waveguide. (b) Spatial profiles of the first few TE modes of this waveguide. (c) Visualization of the bound mode solutions for given structural parameters.

Electromagnetic Model: To obtain more complete information about the modes of an integrated structure, such as their spatial profiles, it is necessary to evoke the electromagnetic description of light based on Maxwell's Equations [119, 120]. Solving Maxwell's Equations in the absence of external charges and currents leads to the wave equation

$$\nabla^2 \mathbb{E} - \left(\frac{n_\sigma(\mathbf{r}, \omega)}{c} \right)^2 \frac{\partial^2 \mathbb{E}}{\partial t^2} = 0, \quad (2.23)$$

which describes the electric field in a structure defined by the spatially-varying refractive index $n_\sigma(\mathbf{r}, \omega)$. The subscript σ denotes the polarization degree of freedom, as before. Assuming net propagation in the z -direction, the total field can be expanded as

$$\mathbb{E} = \int d\omega \sum_{\sigma} \sum_m \mathbf{E}_{\sigma}^{(m)}(x, y, \omega) \exp(i\omega t - i\beta_{\sigma, m}(\omega)z), \quad (2.24)$$

in terms of the eigenfunctions of the equation

$$\left[\frac{\partial^2}{\partial x^2} + \frac{\partial^2}{\partial y^2} \right] \mathbf{E}_{\sigma}^{(m)}(x, y, \omega) + \left[\left(\frac{\omega}{c} \right)^2 n^2(\mathbf{r}, \omega) - \beta_{\sigma, m}^2(\omega) \right] \mathbf{E}_{\sigma}^{(m)}(x, y, \omega) = 0. \quad (2.25)$$

The eigenfunctions $\mathbf{E}_{\sigma}^{(m)}(x, y, \omega)$ correspond to the x - y spatial profiles of the supported guided modes, with eigenvalues related to the corresponding propagation constant $\beta_{\sigma, m}(\omega)$. These modes form an

orthogonal basis for constructing the general solutions of Equation (2.24).

Bound State Solutions: For the symmetric 1D slab waveguide of thickness d illustrated in Figure 2.8(a), Equation (2.25) can be solved analytically by applying the appropriate boundary conditions at each material interface [119, 120]. Note that these boundary conditions depend on polarization, which naturally leads to the definition of the polarization basis in terms of transverse-electric (TE) and transverse-magnetic (TM) components. The TE polarization includes only the E_y , B_x , and B_z electric and magnetic field components, whereas TM includes only E_x , E_z , and B_y . If x is associated with the vertical direction, then TE and TM are equivalent to the free-space horizontal (H) and vertical (V) polarizations, respectively. It is found that the spatial profile of the m -th TE mode is given by

$$E_{TE}^{(m)}(x, \omega) = \begin{cases} Ae^{-qx} & \text{if } x \geq d/2 \\ Be^{ihx} + Ce^{-ihx} & \text{if } -d/2 < x < d/2, \\ De^{qx} & \text{if } x \leq -d/2 \end{cases}, \quad (2.26)$$

where $h^2 \equiv (n_1\omega/c)^2 - \beta_{TE,m}^2(\omega)$, $q^2 \equiv \beta_{TE,m}^2(\omega) - (n_0\omega/c)^2$, and $\beta_{TE,m}(\omega)$ satisfies the transcendental equation

$$\tan(hd + m\pi) - \left[\frac{2hq}{h^2 - q^2} \right] = 0. \quad (2.27)$$

The coefficients A-D are solved by applying continuity conditions at each interface. Figure 2.8(b) shows typical TE field profiles for the first few bound modes of the structure. The modes of the TM polarization can be found in a similar way. A well-known method of visualizing the bound mode solutions [119] is to define the coordinates $u = hd/2$ and $v = qd/2$, in which case the allowed TE modes are given by the intersection of the circle $u^2 + v^2 = R^2$ of radius

$$R = \frac{d}{2} \left(\frac{\omega}{c} \right) \sqrt{n_1^2(\omega) - n_0^2(\omega)} = \frac{d\pi}{\lambda} \sqrt{n_1^2(\omega) - n_0^2(\omega)}, \quad (2.28)$$

with the curves $u \tan(u) = v$ for even values of m , and $-u \cot(u) = v$ for odd values of m . These graphic solutions are shown in Figure 2.8(c) for different values of R . It is seen through R that the highest mode order m supported by the structure is determined by the index difference $n_1^2(\omega) - n_0^2(\omega)$, the core thickness d , and the vacuum wavelength λ . In general, more modes are permitted for thicker cores and smaller wavelengths. One common metric for comparing confinement for different materials or wavelengths is the numerical aperture (NA) [118], defined as

$$\text{NA} = \sqrt{n_1^2 - n_0^2}, \quad (2.29)$$

where a larger NA indicates stronger confinement.

Single-Mode Waveguides: It is often desirable to limit waveguiding to only the fundamental TE and TM modes through appropriate design. This is done to establish better control over the field evolution. The presence of multiple guided modes can lead to spatial beating, which is detrimental to components such as Y-couplers or MMIs that rely on a well-conditioned input field profile. As will be described in the upcoming subsection, directional couplers require their constituent waveguides to be single-mode so that exactly two modes exist in the coupling region for each polarization. Furthermore, scattering and other perturbations can lead to power transfer between the waveguide modes, which in turn leads to phase noise since the phase of each mode accumulates at a different rate and the relative time spent in each mode is a random variable. This is detrimental to phase-sensitive processes such as IFPS.

Dispersion: A key characteristic of the integrated setting is the presence of dispersion, which refers to the wavelength dependence of the propagation constant and other guided-mode attributes. When this originates from the material properties, namely the material refractive index $n_\sigma(\mathbf{r}, \omega)$, it is referred to as chromatic dispersion. The wavelength dependence of $n_\sigma(\mathbf{r}, \omega)$ is determined largely by atomic resonances in the material composition. Wavelength dependence arising instead through the structure geometry is called waveguide dispersion. To better understand dispersion, it is useful to define $n_{\text{eff}}^{\sigma,m}(\omega) = \beta_{\sigma,m}(\omega)c/\omega$ as the effective index. The effective index of a TIR-guided mode is bounded by the waveguide material indices at a given polarization according to $n_0(\omega) < n_{\text{eff}}^{\sigma,m}(\omega) < n_1(\omega)$, and gives a qualitative indication of the average refractive index experienced by the field profile. Broadly speaking, the closer an effective index is to the core index n_1 , the better confined the mode is to the waveguide core. Conversely, lower values of $n_{\text{eff}}^{\sigma,m}(\omega) < n_1(\omega)$ means that more of the field exists as an exponential tail in the cladding regions. In the 1D slab waveguide example, Equation (2.28) was used to relate structural parameters to the number of supported modes. These same parameters are likewise related to how well-confined the supported modes are. For the 1D slab, waveguide dispersion originates from the choice of core thickness d and index difference $n_1^2(\omega) - n_0^2(\omega)$ which scale the wavelength dependence of R . Similarly, the contribution of chromatic dispersion enters through the dependence of this refractive index contrast on the frequency. Dispersion has two main implications for IFPS. Firstly, dispersion in the propagation constant $\beta_{\sigma,m}(\omega)$ results in wavepacket broadening that can be a source of path distinguishability. This is usually dealt with through appropriate design. More importantly, wavelength dependence in the modal confinement results splitting-ratio dispersion for directional couplers. This point is elaborated upon in Section 2.3.2 .

3D Structures: Simple 1D slab waveguides are seldom used. Typical waveguiding structures provide

confinement in both the vertical and horizontal dimensions, and can be defined via lithographic etching, laser-writing, or dopant diffusion [67, 85, 118]. Note that lateral confinement does not necessarily require the mode to be completely surrounded by cladding. Ridge waveguides (e.g. see Figures 4.1(a) in Chapter 4 and 5.1 in Chapter 5) provide one such example. So long as part of the mode is latitudinal with the ridge sidewalls, lateral guiding is still provided, although the mode may leak substantially into the surrounding slab if the etch depth is too shallow. Obtaining modal properties for 2D and 3D structures requires the use of numerical finite element analysis (FEA) tools. Etch depths and core widths can play a significant role in determining the dispersion. These dependencies are case-specific, but typically become more pronounced as the waveguide approaches sub-micron dimensions [76].

2.3.2 Directional Couplers

Directional couplers operate on the basis of field coupling between two waveguides in close vicinity. They have been used since the 1970s to manipulate first-order electric field intensities through the classical interference of coupled optical modes [120, 121]. Their use as a quantum-interference mediator has only occurred within the past six years [1, 79–81, 83, 85–87]. This section connects the classical performance of directional couplers to the concepts of dispersion introduced in Section 2.3.1. The extent of splitting ratio variation due to coupler dispersion is then placed in context by simulating the classical performance of a previously reported design used in quantum photonics circuits.

Coupled-Mode Theory and Origins of Coupler Dispersion

Two waveguides in close vicinity can become coupled due to overlap of their evanescent modal fields. Consider the simple directional coupler shown in Figure 2.9(a) consisting of two single-mode waveguides. Polarizations are assumed to remain uncoupled. For a given frequency, the total field in the coupling region can be expressed as a z -dependent superposition of the fundamental modes $m \in \{A, B\}$ of each constituent waveguide, given by

$$\mathbb{E} = \sum_{\sigma} \left[A_{\sigma}(z) \mathbf{E}_{\sigma}^{(A)}(x, y, \omega) e^{i\omega t - i\beta_{\sigma,A}(\omega)z} + B_{\sigma}(z) \mathbf{E}_{\sigma}^{(B)}(x, y, \omega) e^{i\omega t - i\beta_{\sigma,B}(\omega)z} \right], \quad (2.30)$$

where $A_{\sigma}(z)$ and $B_{\sigma}(z)$ are the position-dependent expansion coefficients. Let $n_{\sigma,A}(\mathbf{r}, \omega)$ and $n_{\sigma,B}(\mathbf{r}, \omega)$ represent the waveguide index profiles that result in the modes $\mathbf{E}_{\sigma}^{(A)}(x, y, \omega)$ and $\mathbf{E}_{\sigma}^{(B)}(x, y, \omega)$ respectively. Substituting Equation (2.30) into (2.23) and using Equation (2.25) to eliminate the partial

derivatives in x and y leads to

$$\sum_{\sigma} \sum_j \mathbf{E}_{\sigma}^{(j)}(x, y, \omega) e^{-i\beta_{\sigma,j}(\omega)z} \left[2i\beta_{\sigma,j}(\omega) \frac{dj_{\sigma}(z)}{dz} - \left(\frac{\omega}{c}\right)^2 (n_{\sigma}^2(\mathbf{r}, \omega) - n_{\sigma,j}^2(\mathbf{r}, \omega)) j_{\sigma}(z) \right] = 0, \quad (2.31)$$

$j \in \{A, B\}$, under the slowly-varying envelope approximation $d^2j_{\sigma}(z)/dz^2 \ll \beta_{\sigma,j}(\omega) dj_{\sigma}(z)/dz$. Multiplying this equation by terms of the form $\int dx dy \mathbf{E}_{\sigma}^{(j)*}(x, y, \omega)$ and making use of the mode orthogonality leads to the coupled-mode equations

$$\frac{d}{dz} \begin{bmatrix} A_{\sigma}(z) \\ B_{\sigma}(z) \end{bmatrix} = \begin{bmatrix} -i\kappa_{\sigma}^{AA}(\omega) & -i\kappa_{\sigma}^{AB}(\omega) e^{-i(\beta_{\sigma,B}(\omega) - \beta_{\sigma,A}(\omega))z} \\ -i\kappa_{\sigma}^{BA}(\omega) e^{i(\beta_{\sigma,B}(\omega) - \beta_{\sigma,A}(\omega))z} & -i\kappa_{\sigma}^{BB}(\omega) \end{bmatrix} \begin{bmatrix} A_{\sigma}(z) \\ B_{\sigma}(z) \end{bmatrix}, \quad (2.32)$$

where

$$\kappa_{\sigma}^{AA}(\omega) \propto \omega \int dx dy \mathbf{E}_{\sigma}^{(A)*}(x, y, \omega) \mathbf{E}_{\sigma}^{(A)}(x, y, \omega) (n_{\sigma}^2(\mathbf{r}, \omega) - n_{\sigma,A}^2(\mathbf{r}, \omega)), \quad (2.33)$$

$$\kappa_{\sigma}^{AB}(\omega) \propto \omega \int dx dy \mathbf{E}_{\sigma}^{(A)*}(x, y, \omega) \mathbf{E}_{\sigma}^{(B)}(x, y, \omega) (n_{\sigma}^2(\mathbf{r}, \omega) - n_{\sigma,B}^2(\mathbf{r}, \omega)), \quad (2.34)$$

$$\kappa_{\sigma}^{BA}(\omega) \propto \omega \int dx dy \mathbf{E}_{\sigma}^{(B)*}(x, y, \omega) \mathbf{E}_{\sigma}^{(A)}(x, y, \omega) (n_{\sigma}^2(\mathbf{r}, \omega) - n_{\sigma,A}^2(\mathbf{r}, \omega)), \quad (2.35)$$

$$\kappa_{\sigma}^{BB}(\omega) \propto \omega \int dx dy \mathbf{E}_{\sigma}^{(B)*}(x, y, \omega) \mathbf{E}_{\sigma}^{(B)}(x, y, \omega) (n_{\sigma}^2(\mathbf{r}, \omega) - n_{\sigma,B}^2(\mathbf{r}, \omega)). \quad (2.36)$$

The functions $\kappa_{\sigma}^{AB}(\omega)$ and $\kappa_{\sigma}^{BA}(\omega)$ represent the strength of the cross-coupling between the two waveguides, while $\kappa_{\sigma}^{AA}(\omega)$ and $\kappa_{\sigma}^{BB}(\omega)$ are perturbative correction terms to the propagation constant of the original waveguide modes. It is often convenient to lump the correction terms together with the spatial envelope functions by defining $A'_{\sigma}(z) = A_{\sigma}(z) \exp(i\kappa_{\sigma}^{AA}(\omega)z)$ and $B'_{\sigma}(z) = B_{\sigma}(z) \exp(i\kappa_{\sigma}^{BB}(\omega)z)$, in which case the coupled-mode equations simplify to

$$\frac{d}{dz} \begin{bmatrix} A'_{\sigma}(z) \\ B'_{\sigma}(z) \end{bmatrix} = \begin{bmatrix} 0 & -i\kappa_{\sigma}^{AB} e^{-i2\Delta(\omega)z} \\ -i\kappa_{\sigma}^{BA} e^{i2\Delta(\omega)z} & 0 \end{bmatrix} \begin{bmatrix} A'_{\sigma}(z) \\ B'_{\sigma}(z) \end{bmatrix}, \quad (2.37)$$

where $\Delta_{\sigma}(\omega)$ is the modal mismatch and is defined as

$$\Delta_{\sigma}(\omega) = [(\beta_{\sigma,B}(\omega) + \kappa_{\sigma}^{BB}(\omega)) - (\beta_{\sigma,A}(\omega) + \kappa_{\sigma}^{AA}(\omega))] / 2. \quad (2.38)$$

Both polarizations obey coupled-mode equations of this form. The polarization DOF is now re-introduced.

Splitting Ratio and Coupler Dispersion: To obtain the power-splitting ratio $\eta_{\sigma}(\omega)$ at any

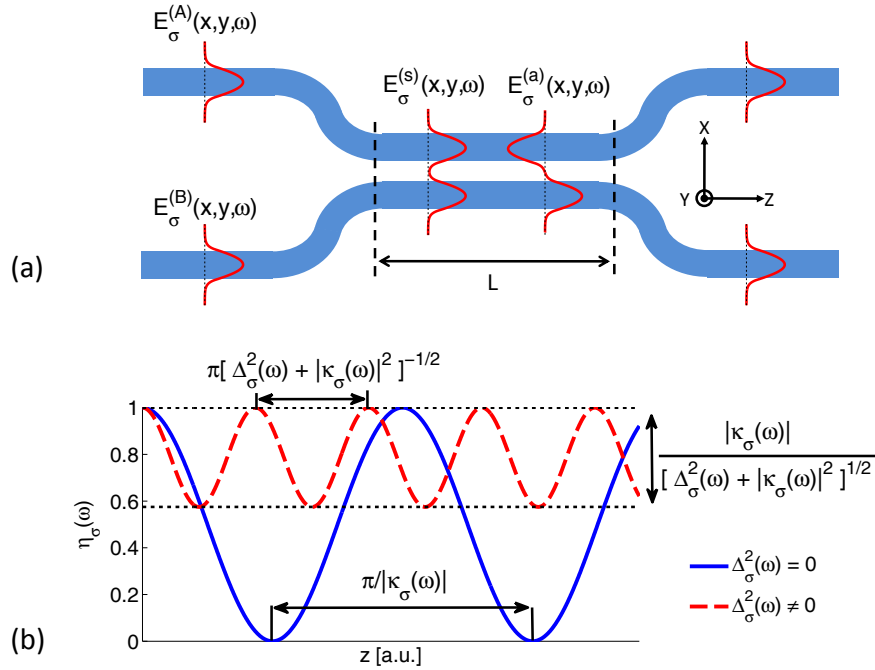


Figure 2.9: (a) Mode evolution in a directional coupler: the input waveguide modes $E_{\sigma}^{(A)}$ and $E_{\sigma}^{(B)}$ are projected onto symmetric ($E_{\sigma}^{(s)}$) and anti-symmetric ($E_{\sigma}^{(a)}$) modes whose spatial beating determines the waveguide power distribution at the output. (b) Dependence of splitting ratio $\eta_{\sigma}(\omega)$ on the interaction length z , showing the effect of modal mismatch.

given length along the coupling region, the coupled-mode equations are solved for the initial conditions $A'_{\sigma}(0) = A_{\sigma,0}$ and $B'_{\sigma}(0) = 0$, leading to

$$\eta_{\sigma}(\omega) \equiv \frac{|A'_{\sigma}(z)|^2}{|A'_{\sigma}(0)|^2} = 1 - \left(\frac{|\kappa_{\sigma}(\omega)|^2}{\Delta_{\sigma}^2(\omega) + |\kappa_{\sigma}(\omega)|^2} \right) \sin^2 \left(L \sqrt{\Delta_{\sigma}^2(\omega) + |\kappa_{\sigma}(\omega)|^2} \right), \quad (2.39)$$

where $|\kappa_{\sigma}(\omega)| \equiv |\kappa_{\sigma}^{AB}(\omega)| = |\kappa_{\sigma}^{BA}(\omega)|$ results from energy conservation [121]. Note that, as defined, $\eta_{\sigma}(\omega) = 1$ corresponds to zero waveguide power transfer. Equations (2.34)-(2.35) show that the wavelength dependence of the splitting ratio originates from both chromatic and waveguide dispersion. The overlap between the waveguide modes will invariably increase as each mode becomes less confined. Since confinement generally decreases at larger wavelengths as implied by Equation (2.28), $d|\kappa|/d\lambda$ is expected to be a positive value. The behaviour of $|\kappa_{\sigma}(\omega)|$ thus depends heavily on the coupler implementation, including the waveguide geometry and choice of material system. The z -dependence of the splitting ratio for a given coupling strength is shown in Figure 2.9(b). Also shown is the effect of modal mismatch which leads to incomplete power transfer. Directional couplers requiring broadband performance are designed with symmetric waveguides so that ideally $\Delta_{\sigma}(\omega) \rightarrow 0$. In practice, however, non-zero mode mismatch can arise through imperfections in fabrication, such as lithographic over/under-exposures and

stochastic sidewall roughness. Whether this might play a significant role in performance is discussed in the following subsections. It is apparent that these terms are polarization-dependent as well, which has implications for IFPS when the state is cross-polarized.

Symmetric and Anti-Symmetric Modes: It is also possible to express the field in the coupling region in terms of modes that diagonalize Equation (2.37). As shown in Figure 2.9(a), the corresponding mode profiles resemble symmetric and anti-symmetric linear combinations of the original waveguide modes. These profiles can be obtained through numerical tools. The propagation constants of the symmetric and anti-symmetric modes are given respectively by

$$\beta_{\sigma}^s(\omega) = [\beta_{\sigma,A}(\omega) + \beta_{\sigma,B}(\omega)]/2 + |\kappa_{\sigma}(\omega)|, \quad (2.40)$$

$$\beta_{\sigma}^a(\omega) = [\beta_{\sigma,A}(\omega) + \beta_{\sigma,B}(\omega)]/2 - |\kappa_{\sigma}(\omega)|, \quad (2.41)$$

Directional coupler operation can then be understood as follows: the input modes arriving at the coupling region are projected onto the symmetric and anti-symmetric modes in the coupling region, which spatially beat along z with a beat frequency determined by the difference in their phase accumulation. The spatial profile at point $z = L$ is then projected back onto the original waveguide modes, which for $\Delta_{\sigma}(\omega) = 0$ results in a splitting ratio of

$$\eta_{\sigma}(\omega) = \cos^2(L|\kappa_{\sigma}(\omega)|) = \cos^2(L[\beta_{\sigma}^s(\omega) - \beta_{\sigma}^a(\omega)]/2). \quad (2.42)$$

This highlights the importance of the constituent waveguides being single-mode. Multimoded waveguides would lead to additional modes in the interaction region that contribute to the beating and hence influence the splitting ratio. Even if these additional modes are accommodated in theoretical predictions, the splitting ratio would nonetheless be highly sensitive to the field profiles at the input, which would not be well-controlled.

Illustrative Example

The $\kappa_{\sigma}(\omega)$ and $\Delta_{\sigma}(\omega)$ dependencies are now placed in perspective with an illustrative example. Using commercial FEA software (*Lumerical Mode Solutions*), the classical splitting performance of the silicon-on-silicon directional coupler reported in [6] has been simulated. This device was used in several early demonstrations of on-chip quantum interference with indistinguishable photons (see [1, 79–81, 87]). Figure 2.10(a) shows a cross-section of the device, which was designed to provide 50:50 splitting at a wavelength of 780 nm for a coupling length of $L = 2.5$ mm. The material was modelled with an intrinsic

birefringence of 5×10^{-4} ($n_{\text{TM}} - n_{\text{TE}}$), which is typical for this architecture in the absence of stress-relieving measures [122]. To explore the influence of modal mismatch, an asymmetric perturbation of one of the waveguide widths by Δw was introduced. The results are shown in Figure 2.10(b).

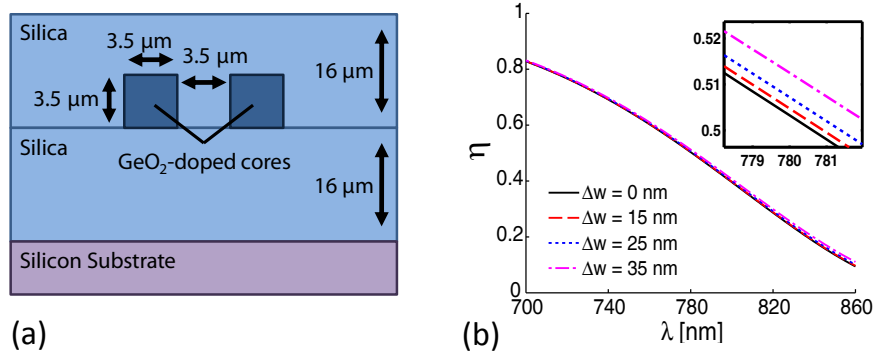


Figure 2.10: (a) Directional coupler cross-section reported in [6]; GeO_2 -doping of the cores to a molar fraction of 0.0488 results in a 0.5% index contrast relative to the cladding. (b) Simulated classical splitting performance; the inset shows the effect of modal mismatch due to a waveguide width asymmetry of Δw .

Despite the high material birefringence, this device was found to have a polarization-independent splitting ratio, largely due to the vertical-horizontal symmetry in the waveguide design. In general, however, polarization-dependence can be significant, especially if complex vertical structures are present. The device's splitting ratio is found to change by $\sim 5\%$ within 10 nm of the 780 nm design wavelength, which underscores the inadequacy of assuming a constant splitting ratio even for small deviations from degeneracy. This stands in contrast to typical bulk-optics beamsplitters, which effectively retain a constant splitting ratio over hundreds of nanometers. For the same coupler geometry, the coupling strength's λ -dependence could vary significantly between material systems due to chromatic dispersion, especially in the vicinity of material resonances. Modal mismatch is found not to have a significant effect. Up to a 1% (35 nm) asymmetric width perturbation, the splitting ratio is found to change by less than 0.5%. Since unintentional asymmetry arising during fabrication is typically much less for two waveguides in such close vicinity, modal mismatch for a symmetrically-designed coupler will play a negligible role in determining the classical performance and can safely be neglected.

2.3.3 On-Chip Quantum Interference

Having discussed the classical aspects of how light behaves in relevant integrated structures, additional details pertaining to on-chip interference are now discussed. In the quantum description, the mode operators $\hat{a}_\sigma^j(\omega)$ now become associated with discrete bound modes, given by the classical solutions to Maxwell's equations as described in Section 2.3.1. The spatial evolution of these mode operators is given

by

$$\hat{a}_\sigma^j(\omega, z) = \hat{a}_\sigma^j(\omega, 0)e^{i\beta_{\sigma,j}(\omega)z}, \quad (2.43)$$

in the Heisenberg picture, which can lead to pulse broadening of the wavepackets as determined by the frequency-dependence of $\beta_{\sigma,j}(\omega)$. Wavepacket broadening is a potential source of distinguishability between two interfering paths, but can generally be accommodated through symmetric device design. It is therefore not a focus of this dissertation; nonetheless, wavepacket broadening may be an important consideration in more sophisticated circuits that route states from several on-chip sources, where the routing paths are not necessarily symmetric.

The formal description of a directional coupler, in the absence of mode mismatch, is given in terms of the interaction Hamiltonian [105, 123]

$$\hat{\mathcal{H}}_{\text{int}} = \hbar \sum_{\sigma} \int d\omega J_{\sigma}(\omega) [\hat{a}_{\sigma}^{A\dagger}(\omega)\hat{a}_{\sigma}^B(\omega) + \hat{a}_{\sigma}^{B\dagger}(\omega)\hat{a}_{\sigma}^A(\omega)], \quad (2.44)$$

where $J_{\sigma}(\omega)$ is a generic coupling strength. This system can be solved in the Heisenberg picture (see Appendix B) to yield the following mode operator transformation

$$\begin{bmatrix} \hat{b}_{\sigma}^{A\dagger}(\omega) \\ \hat{b}_{\sigma}^{B\dagger}(\omega) \end{bmatrix} = \begin{bmatrix} \sqrt{\eta_{\sigma}(\omega)} & i\sqrt{1-\eta_{\sigma}(\omega)} \\ i\sqrt{1-\eta_{\sigma}(\omega)} & \sqrt{\eta_{\sigma}(\omega)} \end{bmatrix} \begin{bmatrix} \hat{a}_{\sigma}^{A\dagger}(\omega) \\ \hat{a}_{\sigma}^{B\dagger}(\omega) \end{bmatrix}. \quad (2.45)$$

The mode operators at the output have been labelled $\hat{b}_{\sigma}(\omega)$ to emphasize that, unlike the point-like beamsplitter transformation, the directional coupler transformation occurs over a finite distance during which pulse broadening can occur.

The transformation given by Equation (2.45) has been written in terms of the power splitting ratio $\eta_{\sigma}(\omega)$, and is similar to that of a beamsplitter. This thesis will focus on how the wavelength dependence of $\eta_{\sigma}(\omega)$ impacts IFPS performance, gives rise to new behaviours, or enables new functionalities. It is noted that the mode operators can acquire an additional phase of π (a factor of i^2), depending on the value of $\kappa_{\sigma}(\omega)L$. This has been illustrated in Figure 2.11, and is a consequence of the original sinusoidal form of the transformation matrix elements (see Appendix B). Such additional phase factors can be treated as a relative phase shift between the interfering paths (e.g. $\exp(-i\theta)$), and are not explored within this work.

There are some additional distinctions between integrated circuits and bulk-optics in how quantum interference is implemented which warrant discussion. In bulk optics, a spatial mode mismatch at the

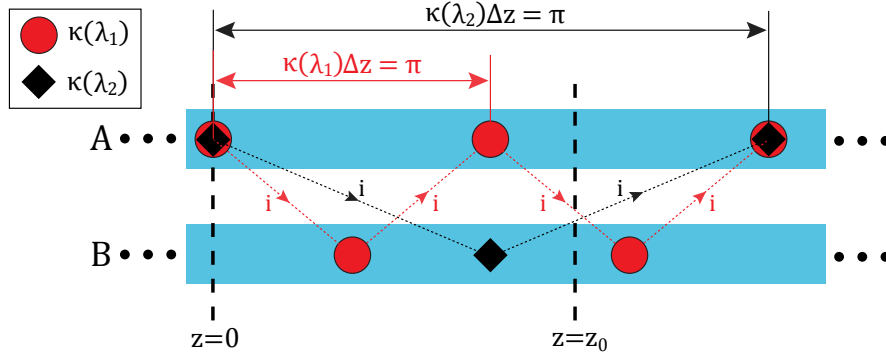


Figure 2.11: Accumulation of additional phase within a directional coupler. Photons begin in waveguide A. The coupling strength is dispersive with $\kappa(\lambda_1) > \kappa(\lambda_2)$. Red circles and black diamonds indicate points where $\eta(\lambda)$ is at a maximum or minimum for wavelengths λ_1 and λ_2 respectively. Depending on the value of $\kappa(\lambda)z$, the mode transformations can acquire an additional factors of $(i)^2$. For example, the factor associated with photons found in waveguide B at point z_0 is $-i\sqrt{1-\eta(\lambda_1)}$ for λ_1 and $+i\sqrt{1-\eta(\lambda_2)}$ for λ_2 .

beamsplitter's silvered mirror can occur due to misalignment or dissimilar beam waists. This can lead to the presence of which-way information at the output, since there will be regions of the output field profile that can be traced back to the input path due to misalignment. Furthermore, since the beam waist and other modal features are in part determined by the spectral properties of the light, such which-way information can also compromise entanglement. In contrast, since waveguides are usually restricted to be single-mode, directional couplers are inherently alignment free, and modal mismatch due to waveguide asymmetry does not lead to which-way information at the output. This is because any which-way information existing within the coupler region (e.g. in the symmetric and anti-symmetric modes) is subsequently projected onto the supported waveguide modes at the output, determining the relative weighting of the output mode amplitudes (i.e. the splitting ratio). Hence, although a subtle point, degradation to interference from modal mismatch arises solely from an unequal weighting of indistinguishable path amplitudes, not from distinguishing path information.

Chapter 3

IFPS with a Dispersive Coupler

The aim of this chapter is to develop a generalized understanding of on-chip IFPS and how its behaviour is influenced by coupler dispersion. This requires IFPS to be described and analyzed at a higher level of detail than what presently exists in the literature. A general theoretical description of IFPS will be developed to predict its performance for arbitrary anti-bunched photon pair states. Using this model, a qualitative comparison between IFPS and the more-familiar HOM effect will be made to highlight key differences in their implementation and characterization. The implications of coupler dispersion will then be studied in detail.

3.1 Generalized Theoretical Development

What follows is a detailed derivation of generalized IFPS behaviour. Since IFPS is equivalent to time-reversed HOM interference in the special case of indistinguishable photons, its theoretical treatment is similar [17, 96]. It will be shown, however, that distinct differences do arise. Photon losses will be neglected.

Consider two waveguides, denoted A and B , that are single-mode over the bandwidths of interest and converge at a mode coupler having a classical power splitting ratio of $\eta_\sigma(\omega)$. Let $\hat{a}_\sigma^j(\omega)$ and $\hat{b}_\sigma^j(\omega)$ represent the mode operators for waveguide j at the input and output of the coupler, respectively. Modal mismatch is assumed to be negligible, so that these mode operators are related by Equation (2.45). Suppose now that each waveguide is coupled to an integrated source of photon pairs which co-propagate towards the coupler inputs. If these sources are coherently pumped, the resultant quantum state can be

expressed as

$$|\Psi\rangle = \sum_{\alpha\beta} \int d\omega_1 d\omega_2 \left[e^{i\theta} \phi_{\alpha\beta}^A(\omega_1, \omega_2) \hat{a}_{\alpha}^{A\dagger}(\omega_1) \hat{a}_{\beta}^{A\dagger}(\omega_2) + e^{-i[\omega_1 + \omega_2]\tau} \phi_{\alpha\beta}^B(\omega_1, \omega_2) \hat{a}_{\alpha}^{B\dagger}(\omega_1) \hat{a}_{\beta}^{B\dagger}(\omega_2) \right] |\text{vac}\rangle, \quad (3.1)$$

assuming the sources are pumped with equal strength and higher-order photon pair production is negligible. The variable τ represents a temporal delay between the two generation paths, while θ represents an ideal relative phase shift. The biphoton amplitudes (BPAs) $\phi_{\alpha\beta}^j(\omega_1, \omega_2)$ are normalized such that

$$\langle\Psi|\Psi\rangle = \sum_j \sum_{\alpha\beta} \int d\omega_1 d\omega_2 |\phi_{\alpha\beta}^j(\omega_1, \omega_2)|^2 = 1, \quad (3.2)$$

and are defined relative to the same spatial coordinates as the mode operators $\hat{a}_{\sigma}^j(\omega)$. As such, their description includes any wavepacket broadening or intra-pair temporal walk-off that has occurred en-route to the coupler. Note that for each path j , the BPA refers to photons in the same spatial mode, hence permutation symmetry permits $\phi_{\alpha\beta}^j(\omega_1, \omega_2)$ to be swapped with $\phi_{\beta\alpha}^j(\omega_2, \omega_1)$ in these equations.

The values of interest will be the anti-bunched outcome probability P_S , representing the fidelity with which the coupler separates a given photon pair, and the interference visibilities V_B and V_S associated with the bunched and anti-bunched outcomes. Adopting Equation (2.11), the joint probability of finding one photon exiting the coupler from waveguide A and the other from waveguide B at times t_1 and t_2 respectively is given by

$$P_{AB}(t_1, t_2) = \sum_{\alpha\beta} \langle\Psi| \hat{b}_{\alpha}^{A\dagger}(t_1) \hat{b}_{\beta}^{B\dagger}(t_2) \hat{b}_{\beta}^B(t_2) \hat{b}_{\alpha}^A(t_1) |\Psi\rangle. \quad (3.3)$$

Note that the photon pair is assumed to remain in a pure state. In practice, interactions with the environment can cause $|\Psi\rangle$ to become a mixed state [150], which must be represented by the density matrix $\rho = |\Psi\rangle\langle\Psi|$. The joint probability is then instead calculated using

$$P_{AB}(t_1, t_2) = \sum_{\alpha\beta} \text{Tr} \left\{ \hat{b}_{\alpha}^{A\dagger}(t_1) \hat{b}_{\beta}^{B\dagger}(t_2) \hat{b}_{\beta}^B(t_2) \hat{b}_{\alpha}^A(t_1) \rho \right\}, \quad (3.4)$$

where $\text{Tr}\{ \}$ represents the trace operator. The implications of state impurity for IFPS are not examined in this thesis.

Equation (3.3) can be simplified using the Fock Space completeness relation $\sum_n |\{n\}\rangle\langle\{n\}| = 1$,

leading to

$$P_{AB}(t_1, t_2) = \sum_n \sum_{\alpha\beta} \langle \Psi | \hat{b}_\alpha^{A\dagger}(t_1) \hat{b}_\beta^{B\dagger}(t_2) | \{n\} \rangle \langle \{n\} | \hat{b}_\beta^B(t_2) \hat{b}_\alpha^A(t_1) | \Psi \rangle, \quad (3.5)$$

$$= \sum_n \sum_{\alpha\beta} \left| \langle \{n\} | \hat{b}_\beta^B(t_2) \hat{b}_\alpha^A(t_1) | \Psi \rangle \right|^2, \quad (3.6)$$

$$= \sum_{\alpha\beta} \left| \langle \text{vac} | \hat{b}_\beta^B(t_2) \hat{b}_\alpha^A(t_1) | \Psi \rangle \right|^2. \quad (3.7)$$

Here, the second line is obtained by recognizing that the two matrix elements are Hermitian conjugates of one another. The third line has retained only the non-vanishing matrix elements; since $|\Psi\rangle$ contains exactly two photons and is operated upon by exactly two annihilation operators, it can be reasoned from Equations (2.4) that the resultant ket must be the vacuum state $|\text{vac}\rangle$, hence only the $n = 0$ term in the projection leads to non-zero contributions towards the probability. Employing Equation (2.45) and making a Fourier Transform allows the mode operators to be expanded as

$$\hat{b}_\alpha^A(t_1) = \int d\omega_1 \hat{b}_\alpha^A(\omega_1) e^{-i\omega_1 t_1} = \int d\omega_1 \left[\sqrt{\eta_\alpha(\omega_1)} \hat{a}_\alpha^A(\omega_1) - i\sqrt{1-\eta_\alpha(\omega_1)} \hat{a}_\alpha^B(\omega_1) \right] e^{-i\omega_1 t_1}, \quad (3.8)$$

$$\hat{b}_\beta^B(t_2) = \int d\omega_2 \hat{b}_\beta^B(\omega_2) e^{-i\omega_2 t_2} = \int d\omega_2 \left[\sqrt{\eta_\beta(\omega_2)} \hat{a}_\beta^B(\omega_2) - i\sqrt{1-\eta_\beta(\omega_2)} \hat{a}_\beta^A(\omega_2) \right] e^{-i\omega_2 t_2}, \quad (3.9)$$

Utilizing Equation (3.1) and retaining only the non-vanishing matrix elements as before, the joint probability becomes

$$P_{AB}(t_1, t_2) = \sum_{\alpha\beta} \left| (-i) \int d\omega_1 d\omega_2 d\omega'_1 d\omega'_2 \sum_{\alpha'\beta'} \left[e^{i\theta} \sqrt{\eta_\alpha(\omega_1)} [1 - \eta_\beta(\omega_2)] \phi_{\alpha'\beta'}^A(\omega'_1, \omega'_2) M^A e^{-i\omega_1 t_1} e^{-i\omega_1 t_2} \right. \right. \\ \left. \left. + e^{-i[\omega'_1 + \omega'_2] \tau} \sqrt{[1 - \eta_\alpha(\omega_1)] \eta_\beta(\omega_2)} \phi_{\alpha'\beta'}^B(\omega'_1, \omega'_2) M^B e^{-i\omega_1 t_1} e^{-i\omega_2 t_2} \right] \right|^2, \quad (3.10)$$

where $M^j \equiv \langle \text{vac} | \hat{a}_\beta^j(\omega_2) \hat{a}_\alpha^j(\omega_1) \hat{a}_{\alpha'}^{j\dagger}(\omega'_1) \hat{a}_{\beta'}^{j\dagger}(\omega'_2) | \text{vac} \rangle$. From the mode operator commutation relations

and Equation (2.4), the matrix elements can be written as

$$\begin{aligned} & \phi_{\alpha'\beta'}^j(\omega'_1, \omega'_2) M^j \\ &= \delta(\omega_1 - \omega'_1) \delta(\omega_2 - \omega'_2) \delta_{\alpha\alpha'} \delta_{\beta\beta'} \langle \text{vac} | \hat{a}_\beta^j(\omega_2) \hat{a}_\alpha^j(\omega_1) \left[\phi_{\alpha\beta}^j(\omega_1, \omega_2) \hat{a}_\alpha^{j\dagger}(\omega_1) \hat{a}_\beta^{j\dagger}(\omega_2) | \text{vac} \rangle \right] \\ &+ \delta(\omega_1 - \omega'_2) \delta(\omega_2 - \omega'_1) \delta_{\alpha\beta'} \delta_{\beta\alpha'} \langle \text{vac} | \hat{a}_\beta^j(\omega_2) \hat{a}_\alpha^j(\omega_1) \left[\phi_{\beta\alpha}^j(\omega_2, \omega_1) \hat{a}_\beta^{j\dagger}(\omega_2) \hat{a}_\alpha^{j\dagger}(\omega_1) | \text{vac} \rangle \right] \end{aligned} \quad (3.11)$$

$$\begin{aligned} &= \phi_{\alpha\beta}^j(\omega_1, \omega_2) \langle \text{vac} | \hat{a}_\beta^j(\omega_2) \hat{a}_\alpha^j(\omega_1) \hat{a}_\alpha^{j\dagger}(\omega_1) \hat{a}_\beta^{j\dagger}(\omega_2) | \text{vac} \rangle \\ &\times [\delta(\omega_1 - \omega'_1) \delta(\omega_2 - \omega'_2) \delta_{\alpha\alpha'} \delta_{\beta\beta'} + \delta(\omega_1 - \omega'_2) \delta(\omega_2 - \omega'_1) \delta_{\alpha\beta'} \delta_{\beta\alpha'}] \end{aligned} \quad (3.12)$$

$$= \phi_{\alpha\beta}^j(\omega_1, \omega_2) [\delta(\omega_1 - \omega'_1) \delta(\omega_2 - \omega'_2) \delta_{\alpha\alpha'} \delta_{\beta\beta'} + \delta(\omega_1 - \omega'_2) \delta(\omega_2 - \omega'_1) \delta_{\alpha\beta'} \delta_{\beta\alpha'}]. \quad (3.13)$$

Permutation symmetry was used to equate $\phi_{\beta\alpha}^j(\omega_2, \omega_1) \hat{a}_\beta^{j\dagger}(\omega_2) \hat{a}_\alpha^{j\dagger}(\omega_1) | \text{vac} \rangle = \phi_{\alpha\beta}^j(\omega_1, \omega_2) \hat{a}_\alpha^{j\dagger}(\omega_1) \hat{a}_\beta^{j\dagger}(\omega_2) | \text{vac} \rangle$, since both creation operators are indistinguishable in path/spatial mode. Note that the remaining matrix elements appearing in Equation (3.12) are all equal to unity, except for the special case of $\alpha = \beta$ and $\omega_1 = \omega_2$ which instead contribute a factor of two. However, because only a small fraction of the total parameter space (i.e. the line $\omega_1 = \omega_2$) can satisfy this special case, these matrix elements can be approximated as unity for all ω_1, ω_2 permutations. Dropping all common factors, which can later be amalgamated into a normalization constant, Equation (3.10) then simplifies to

$$\begin{aligned} P_{AB}(t_1, t_2) &= \sum_{\alpha\beta} \left| \int d\omega_1 d\omega_2 e^{i\theta} \phi_{\alpha\beta}^A(\omega_1, \omega_2) \sqrt{\eta_\alpha(\omega_1) [1 - \eta_\beta(\omega_2)]} e^{-i\omega_1 t_1} e^{-i\omega_2 t_2} \right. \\ &\quad \left. + \int d\omega_1 d\omega_2 \phi_{\alpha\beta}^B(\omega_1, \omega_2) \sqrt{[1 - \eta_\alpha(\omega_1)] \eta_\beta(\omega_2)} e^{-i\omega_1(t_1+\tau)} e^{-i\omega_2(t_2+\tau)} \right|^2. \end{aligned} \quad (3.14)$$

The following convenient definitions are made: the amplitude contributed by source j towards finding photons 1 and 2 in waveguides p and q respectively,

$$\Phi_{\alpha\beta}^{j \rightarrow pq}(\omega_1, \omega_2) = \phi_{\alpha\beta}^j(\omega_1, \omega_2) G_\alpha^{j \rightarrow p}(\omega_1) G_\beta^{j \rightarrow q}(\omega_2), \quad (3.15)$$

where

$$G_\sigma^{j \rightarrow q}(\omega) = \begin{cases} \sqrt{\eta_\sigma(\omega)}, & \text{if } j = q \\ \sqrt{1 - \eta_\sigma(\omega)}, & \text{if } j \neq q \end{cases}, \quad (3.16)$$

and the associated set of Fourier transforms

$$F_{\alpha\beta}^{j \rightarrow pq}(t_1, t_2) = \int d\omega_1 d\omega_2 \Phi_{\alpha\beta}^{j \rightarrow pq}(\omega_1, \omega_2) e^{-i\omega_1 t_1} e^{-i\omega_2 t_2}. \quad (3.17)$$

The joint probability can then be written as

$$P_{AB}(t_1, t_2) = \sum_{\alpha\beta} \left| F_{\alpha\beta}^{A \rightarrow AB}(t_1, t_2) + e^{-i\theta} F_{\alpha\beta}^{B \rightarrow AB}(t_1 + \tau, t_2 + \tau) \right|^2, \quad (3.18)$$

explicitly showing the probability as a coherent sum of amplitudes contributed from the two possible histories. Expanding the square by multiplying its argument by its complex conjugate leads to

$$P_{AB}(t_1, t_2) = \sum_{\alpha\beta} \left[\left| F_{\alpha\beta}^{A \rightarrow AB}(t_1, t_2) \right|^2 + \left| F_{\alpha\beta}^{B \rightarrow AB}(t_1 + \tau, t_2 + \tau) \right|^2 + 2\text{Re} \left\{ e^{-i\theta} F_{\alpha\beta}^{B \rightarrow AB}(t_1 + \tau, t_2 + \tau) F_{\alpha\beta}^{*A \rightarrow AB}(t_1, t_2) \right\} \right] \quad (3.19)$$

which uses the identity for complex number c : $c + c^* = 2\text{Re}\{c\}$. The total probability is now obtained by integrating over time in accordance with Equation (2.12). For the first term, this leads to

$$\int dt_1 dt_2 \left| F_{\alpha\beta}^{A \rightarrow AB}(t_1, t_2) \right|^2 \quad (3.20)$$

$$= \int dt_1 dt_2 \left[\int d\omega_1 d\omega_2 \Phi_{\alpha\beta}^{A \rightarrow AB}(\omega_1, \omega_2) e^{-i\omega_1 t_1} e^{-i\omega_2 t_2} \right] \left[\int d\omega'_1 d\omega'_2 \Phi_{\alpha\beta}^{*A \rightarrow AB}(\omega'_1, \omega'_2) e^{i\omega'_1 t_1} e^{i\omega'_2 t_2} \right] \quad (3.21)$$

$$= \int d\omega_1 d\omega_2 \int d\omega'_1 d\omega'_2 \Phi_{\alpha\beta}^{A \rightarrow AB}(\omega_1, \omega_2) \Phi_{\alpha\beta}^{*A \rightarrow AB}(\omega'_1, \omega'_2) \left[\int dt_1 e^{i[\omega'_1 - \omega_1]t_1} \right] \left[\int dt_2 e^{i[\omega'_2 - \omega_2]t_2} \right] \quad (3.22)$$

$$= \int d\omega_1 d\omega_2 \int d\omega'_1 d\omega'_2 \Phi_{\alpha\beta}^{A \rightarrow AB}(\omega_1, \omega_2) \Phi_{\alpha\beta}^{*A \rightarrow AB}(\omega'_1, \omega'_2) [2\pi\delta(\omega'_1 - \omega_1)] [2\pi\delta(\omega'_2 - \omega_2)] \quad (3.23)$$

$$= 4\pi^2 \int d\omega_1 d\omega_2 \left| \Phi_{\alpha\beta}^{A \rightarrow AB}(\omega_1, \omega_2) \right|^2. \quad (3.24)$$

The other terms are similarly calculated to give a total probability of

$$R_{AB}(\theta, \tau) = N \sum_{\alpha\beta} \int d\omega_1 d\omega_2 \left[\left| \Phi_{\alpha\beta}^{A \rightarrow AB}(\omega_1, \omega_2) \right|^2 + \left| \Phi_{\alpha\beta}^{B \rightarrow AB}(\omega_1, \omega_2) \right|^2 + 2\text{Re} \left\{ e^{-i\theta} \Phi_{\alpha\beta}^{B \rightarrow AB}(\omega_1, \omega_2) \Phi_{\alpha\beta}^{*A \rightarrow AB}(\omega_1, \omega_2) e^{-i[\omega_1 + \omega_2]\tau} \right\} \right], \quad (3.25)$$

where N is a normalization constant. The other R_{pq} can be found in the same way, and must be normalized such that $\sum_{pq} R_{pq}(\theta, \tau) = 1$. For reference, the full equations for all four permutations are given in Appendix D, where normalization is shown to be satisfied for $N = 1$.

The complete set of outcome probabilities can be written more compactly as

$$R_{pq}(\theta, \tau) = R_{pq}^0 + \cos(\pi\delta_{pq})R_{pq}^I(\theta, \tau), \quad (3.26)$$

where

$$R_{pq}^0 = \sum_{\alpha\beta} \int d\omega_1 d\omega_2 \left(|\Phi_{\alpha\beta}^{A \rightarrow pq}(\omega_1, \omega_2)|^2 + |\Phi_{\alpha\beta}^{B \rightarrow pq}(\omega_1, \omega_2)|^2 \right), \quad (3.27)$$

represents the classical probability contributions from sources A and B in the absence of interference, and

$$R_{pq}^I(\theta, \tau) = \sum_{\alpha\beta} \int d\omega_1 d\omega_2 2\text{Re} \left\{ e^{-i\theta} \Phi_{\alpha\beta}^{B \rightarrow pq}(\omega_1, \omega_2) \Phi_{\alpha\beta}^{*A \rightarrow pq}(\omega_1, \omega_2) e^{-i(\omega_1 + \omega_2)\tau} \right\}, \quad (3.28)$$

describes the non-classical influence of path interference. These in turn are related to the total anti-bunched and bunched outcome probabilities, given respectively by

$$P_S(\theta, \tau) = R_{AB}(\theta, \tau) + R_{BA}(\theta, \tau) = P_S^0 + P_S^I(\theta, \tau) \quad (3.29)$$

and

$$P_B(\theta, \tau) = R_{AA}(\theta, \tau) + R_{BB}(\theta, \tau) = P_B^0 - P_B^I(\theta, \tau). \quad (3.30)$$

which have similarly been subdivided into classical and non-classical contributions:

$$P_S^0 = R_{AB}^0 + R_{BA}^0, \quad (3.31)$$

$$P_S^I(\theta, \tau) = R_{AB}^I(\theta, \tau) + R_{BA}^I(\theta, \tau), \quad (3.32)$$

$$P_B^0 = R_{AA}^0 + R_{BB}^0, \quad (3.33)$$

$$P_B^I(\theta, \tau) = R_{AA}^I(\theta, \tau) + R_{BB}^I(\theta, \tau). \quad (3.34)$$

Normalization imposes $P_S(\theta, \tau) + P_B(\theta, \tau) = 1$. It can be shown that the classical contributions are similarly constrained by $P_S^0 + P_B^0 = 1$, while the non-classical contributions must obey the equality $|P_S^I(\theta, \tau)| = |P_B^I(\theta, \tau)|$. The latter implies that constructive interference of the anti-bunched amplitudes is always balanced by destructive interference of the bunched amplitudes, and vice-versa. These relations have been illustrated in Figure 3.1(a). When the source BPAs are path-symmetric, i.e. $\phi_{\alpha\beta}^A(\omega_1, \omega_2) = \phi_{\alpha\beta}^B(\omega_1, \omega_2)$, the expressions for R_{pq} also become symmetric such that $R_{AB} = R_{BA}$ and $R_{AA} = R_{BB}$. This means the anti-bunched probability could also be calculated from the amplitude of the $|A, B\rangle$ outcome alone, i.e. by taking the squared modulus of $\Phi_{\alpha\beta}^{A \rightarrow AB}(\omega_1, \omega_2) + \Phi_{\alpha\beta}^{B \rightarrow AB}(\omega_1, \omega_2)$.

Non-classical contributions are maximized when all frequency components of the overlap integral interfere in-phase. This has two requirements: that the BPAs are perfectly indistinguishable ($\Phi_{\alpha\beta}^{A \rightarrow pq}(\omega_1, \omega_2) = \Phi_{\alpha\beta}^{B \rightarrow pq}(\omega_1, \omega_2)$); and that the time delay τ is zero so that the phase $\exp(-i[\omega_1 + \omega_2]\tau)$ becomes unity. The ideal interference visibilities are defined as

$$V_S = \frac{|P_S^I(\theta = 0, \tau = 0)|}{P_S^0}, \quad V_B = \frac{|P_B^I(\theta = 0, \tau = 0)|}{P_B^0}, \quad (3.35)$$

and quantify the ratio of non-classical to classical contributions for each total probability. Both visibilities are bounded by $[0, 1]$.

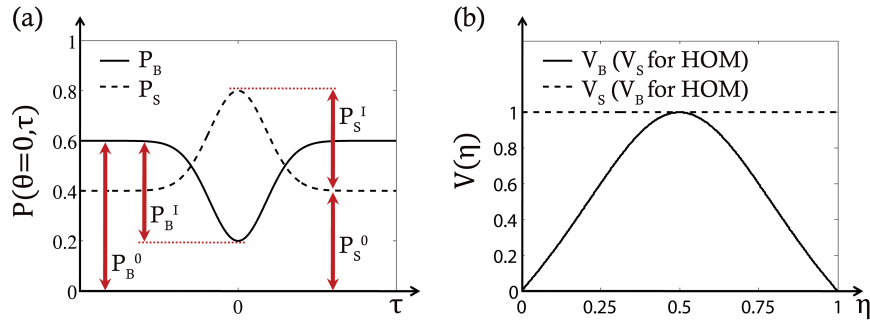


Figure 3.1: (a) Schematic highlighting the bunched and anti-bunched probabilities defined in Equations (3.29)-(3.34), plotted under conditions of perfect path indistinguishability with $\theta = 0$ and a constant splitting ratio of $\eta = 0.276$. (b) Splitting ratio dependence of the IFPS interference visibilities for a constant η ; HOM-equivalents are indicated.

Note that while all expressions in this section have been derived in terms of frequency, it is often convenient to discuss photon and coupler attributes in terms of wavelength λ . In subsequent sections, frequency and wavelength will be used interchangeably as variables; however, all calculations of P_S , V_S and V_B are carried out in the frequency space representation.

3.2 Comparison of IFPS to Hong-Ou-Mandel Interference

The HOM effect serves as a useful reference because it is the most commonly-implemented form of two-photon interference, appearing ubiquitously throughout the integrated quantum photonics literature. Before discussing the implications of coupler dispersion, several fundamental distinctions between IFPS and HOM interference will first be highlighted. These distinctions are important to the implementation and characterization of IFPS. One such difference is in the relation of the interference visibilities to a non-dispersive (i.e. constant) splitting ratio η . Whereas in HOM interference the anti-bunched visibility V_S

scales according to Equation (2.20) and the bunched visibility V_B remains invariant, these η -dependencies are reversed for IFPS, as can be shown from Equations (3.26)-(3.35). Figure 3.1(b) illustrates this distinction.

Another distinction concerns the BPAs for which perfect interference can be achieved. While perfect IFPS places no fundamental restrictions on the BPA, perfect HOM interference requires the BPA to be symmetric in its frequency arguments [113]. This can be seen through comparison of the overlap integrals in Equations (2.18) and (3.28), reaffirming the fact that IFPS may be applied to any arbitrary two-photon state so long as the BPAs contributed from paths A and B are identical. This lack of restriction on the internal details of the BPA also extends to the temporal domain, with important ramifications for cross-polarized states. Unlike the HOM effect where the delay of one photon relative to the other causes interference to degrade, IFPS is immune to *intra*-pair photon walk-off, and is hence not fundamentally limited by system birefringence (aside from its impact on the coupler's splitting ratio).

Important distinctions also exist in the τ -dependence of both phenomena. In HOM interference, τ is effectively an *intra*-pair delay scaled by the frequency difference $\omega_2 - \omega_1$. As discussed in Chapter 2, this leads to the modulation of P_S by a slowly-varying envelope determined primarily by the two-photon coherence time τ_c [17]. Additional oscillations at the beat frequency $\Omega = \omega_{02} - \omega_{01}$ are only present in the case of non-degenerate central frequencies. For IFPS on the other hand, τ is effectively an *inter*-pair delay that is scaled instead by the frequency sum $\omega_2 + \omega_1$, leading to rapidly-varying oscillations even at degeneracy. This sensitivity of the interference to τ can be orders of magnitude greater than that of the HOM effect, posing a practical challenge for stability. For example, consider a pair of photons degenerate at 1550 nm whose marginal spectra have a FWHM intensity bandwidth of $\Delta\lambda = 3$ nm. Assuming gaussian spectra, the HOM dip for such a pair has a FWHM of $\Delta\tau = 1.67$ ps, equivalent to a free-space path difference of 500.6 μm . Hence, path instability on the order of tens of microns can occur without severely affecting the result. However, if these same photons are subjected to IFPS, an optical delay of merely $\tau = 1.29$ fs (or 0.387 μm in path) is manifested as a π phase shift that can switch the output between the extremes of perfect anti-bunching ($P_S = 1$) and perfect bunching ($P_S = 0$). This example has been illustrated in Figure 3.2. While such stability issues are mitigated by monolithic integration, they remain a serious concern when pair generation and quantum interference occur on two separate chips that must be fiber-coupled.

Finally, HOM interference visibilities are commonly obtained by tracing over the entire interference envelope and comparing conditions of maximal interference ($\tau = 0$) to the classical count rate ($|\tau| > |\tau_c|$); however, the practicality of obtaining such a trace for IFPS is limited not only by the aforementioned oscillations, which demand extreme precision in τ , but also by differences in the two-photon coherence

times manifested by $\exp(-i[\omega_2 + \omega_1]\tau)$. HOM coherence times are generally associated with the photon bandwidths and do not depend on frequency entanglement, whereas for anti-coalescence the degree of spectral correlations can have a pronounced effect. This is exemplified by Figure 3.2, where a moderately anti-correlated state with Schmidt number $\text{SN} = 1.26$ yields an interference envelope nearly twice as wide in τ as that of its perfectly uncorrelated counterpart. In order to better appreciate this point, consider SPDC in the limiting case of a continuous-wave (CW) monochromatic pump, where the photon frequencies are perfectly anti-correlated. Since in this case the sum $\omega_1 + \omega_2$ can be replaced by the monochromatic pump frequency ω_p , a non-zero τ contributes a frequency-independent phase factor that does not degrade the coherence of the path superposition in $|\Psi\rangle$, hence the interference visibility never decays and the temporal width of the interference envelope approaches infinity. Realistic pump bandwidths remove the perfect anti-correlation and therefore limit the actual envelope width; however only in the limit of perfectly uncorrelated photons does this width approach its HOM equivalent.

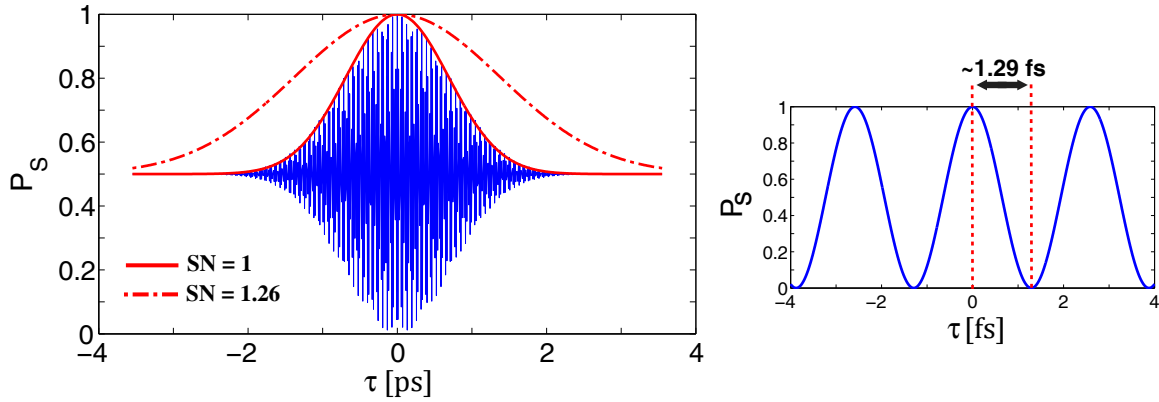


Figure 3.2: (Left) Calculated IFPS P_S for co-polarized photons degenerate at 1550 nm, produced by Type I SPDC, having gaussian spectra with $\Delta\lambda = 3$ nm. The solid curve is the interference envelope for a perfectly uncorrelated pair ($\text{SN} = 1$), and has a FWHM of $\Delta\tau = 1.67$ ps. The dashed curve shows the same calculation but for a moderately anti-correlated pair with $\text{SN} = 1.26$, and has a width of $\Delta\tau = 3.25$ ps; entanglement was induced by narrowing the pump bandwidth. Rapidly-varying oscillations have been shown only for the uncorrelated pair, and appear aliased at a lower frequency. (Right) Enlarged region showing these oscillations acting as a π phase shift over a 1.26 fs delay time. The oscillation frequency corresponds to that of the 775 nm process pump.

3.3 IFPS Behaviour in the Near-Degeneracy Regime

The dependence of IFPS on coupler dispersion is now considered. For simplicity, all requirements for perfect deterministic separation unrelated to the coupler performance are assumed to be satisfied, i.e.

$\phi_{\alpha\beta}^A(\omega_1, \omega_2) = \phi_{\alpha\beta}^B(\omega_1, \omega_2)$, $\tau = 0$, and $\theta = 0$. It will prove convenient to first study IFPS near conditions

of degeneracy.

When the photons are nearly degenerate, two simplifying approximations can be made: first, that the photon central wavelengths (denoted λ_{01} and λ_{02}) are equidistant from the photon degeneracy wavelength λ_{deg} ; and second, that the coupling strength $\kappa_\sigma(\lambda)$ can be locally described as a linear function in λ . These conditions define what will be referred to as the near-degeneracy regime. Although virtually all on-chip interference experiments have been conducted near degeneracy, the study of this regime can nonetheless provide useful insight into the impact of coupler dispersion on IFPS in general. Furthermore, a much larger parameter space (e.g. photon bandwidths, coupler dispersions, etc.) will be explored than what has previously been visited by experiment.

3.3.1 Dimensionless Model

To provide a comprehensive yet generic overview of this regime, it is useful to introduce simple dimensionless parameters that allow calculations to be mapped to any specific combination of twin-photon state and coupler characteristics. The quantum state will be described in terms of a dimensionless non-degeneracy $\Lambda = |\lambda_{02} - \lambda_{01}|/\lambda_{\text{deg}}$, as well as dimensionless photon bandwidths $\Delta\lambda/\lambda_{\text{deg}}$, with $\Delta\lambda$ referring to the full-width at half-maximum (FWHM) intensity of the marginal spectrum. When required, state entanglement will be quantified by the Schmidt number. To explore changes to IFPS performance as these parameters are swept, it is also convenient to construct the BPA directly from a set of specified photon bandwidths and central wavelengths, rather than having to search algorithmically for waveguide mode dispersion parameters that reproduce the desired state properties. For Type I SPDC, where the photons are co-polarized at generation, this is achieved by defining the BPA as

$$\phi_{\sigma\sigma}(\omega_1, \omega_2) = \phi^{(P)}(\omega_1 + \omega_2) \left[\phi_\sigma^{(1)}(\omega_1)\phi_\sigma^{(2)}(\omega_2) + \phi_\sigma^{(1)}(\omega_2)\phi_\sigma^{(2)}(\omega_1) \right] / \sqrt{2}. \quad (3.36)$$

The $\phi_\sigma^{(j)}(\omega)$ are the marginal photon spectra, which replace a sinc function in the original theoretical equation (assuming a constant-width nonlinear waveguide), while $\phi^{(P)}(\omega_1 + \omega_2)$ is the pump spectrum, which enforces the necessary energy conservation. All bandwidths are taken to be gaussian, and the BPA obeys the usual permutation symmetries.

Since $\kappa_\sigma(\lambda)$ is assumed to be a linear function in the near-degeneracy regime, the directional coupler splitting ratio in the absence of mode mismatch can be expressed as $\eta_\sigma(\lambda) = \cos^2(\xi_\sigma(\lambda; \lambda_{\text{deg}}))$ by introducing the dimensionless variable

$$\xi_\sigma(\lambda; \lambda_{\text{deg}}) = \xi^0 + \Delta\xi_\sigma + [\lambda/\lambda_{\text{deg}} - 1] M_\sigma, \quad (3.37)$$

where $\xi^0 = \pi/4 + m\pi$ (m an integer) is the ideal value of $\xi_\sigma(\lambda = \lambda_{\text{deg}}; \lambda_{\text{deg}})$ for a perfect 50:50 split at the degeneracy wavelength λ_{deg} ,

$$\Delta\xi_\sigma = [L\kappa_\sigma(\lambda_{\text{deg}}) - \pi/4, \text{ mod } \pi] \quad (3.38)$$

is a systematic offset defining the true splitting ratio at λ_{deg} , and

$$M_\sigma \equiv \lambda_{\text{deg}} L \left[\left. \frac{d\kappa_\sigma(\lambda)}{d\lambda} \right|_{\lambda_{\text{deg}}} \right] \quad (3.39)$$

characterizes the local first-order coupler dispersion. The oscillation period of $\eta_\sigma(\lambda)$ is given in terms of these parameters by $T_\lambda = \pi\lambda_{\text{deg}}/M_\sigma$. As a quantitative example, consider a directional coupler having a local coupling strength described by $\kappa_\sigma(\lambda) = 1.053871 \times 10^{10}\lambda - 9217 \text{ m}^{-1}$ in the vicinity of $\lambda_{\text{deg}} = 1550 \text{ nm}$ over an interaction length of $L = 1 \text{ mm}$, giving a degeneracy splitting ratio of $\eta_\sigma(\lambda_{\text{deg}}) = 0.4507$. Such a coupler would correspond to $\Delta\xi_\sigma = 0.0494$, $M_\sigma = 16.335$, and $T_\lambda = 298 \text{ nm}$.

With the above definitions, the parameter space of the near-degeneracy is generated by the following variables:

- (i) $\Delta\xi_\sigma$, the dimensionless coupling offset, which can account for intentional or unintentional (i.e. fabrication-related) detunings of the 50:50 split point from λ_{deg} ; note that this has the effect of shifting the $\eta_\sigma(\omega)$ sinusoid.
- (ii) $M_\sigma\Lambda$, the product of the dimensionless first-order coupler dispersion with the dimensionless photon non-degeneracy, which is equivalent to the absolute difference in the total coupling experienced at the two photon central wavelengths, i.e. $|L\kappa_\sigma(\lambda_{02}) - L\kappa_\sigma(\lambda_{01})|$, and is independent of λ_{deg} ;
- (iii) The polarizations of the twin photons (subscripts α, β);
- (iv) $M_\sigma\Delta\lambda/\lambda_{\text{deg}}$, the product of the dimensionless first-order coupler dispersion with the dimensionless photon bandwidths, which is equivalent to the absolute difference in the total coupling ($L\kappa_\sigma(\lambda)$) over the bandwidth interval $\Delta\lambda$, and also is independent of λ_{deg} .

The aim of the following sections is to assess how IFPS behaves as each of these parameters is varied. For brevity, polarization subscripts will be dropped when only a single polarization is being considered, and the splitting ratio at the photon central wavelengths will be written in shorthand as $\eta_\sigma^{(j)} \equiv \eta_\sigma(\lambda_{0j})$, with $j \in \{1, 2\}$.

3.3.2 Salient Features

The main implications of coupler dispersion for IFPS are revealed through the dependence of the anti-bunched outcome probability P_S , as well as the interference visibilities V_S and V_B , on the parameter $M\sigma\Lambda$. Figure 3.3 illustrates these dependencies as calculated for a co-polarized state (e.g. generated through Type I SPDC) having dimensionless pump and twin-photon bandwidths of $\Delta\lambda_P/\lambda_{\text{deg}} = 1.282 \times 10^{-4}$ and $\Delta\lambda_1/\lambda_{\text{deg}} = \Delta\lambda_2/\lambda_{\text{deg}} = 3.205 \times 10^{-4}$ (corresponding, for example, to $\Delta\lambda_P = 0.1$ nm and $\Delta\lambda_{1(2)} = 0.25$ nm at $\lambda_{\text{deg}} = 780$ nm) respectively. The influence of a non-zero $\Delta\xi_\sigma$ is also shown, as it is complementary to understanding the predicted behaviour. Equations (3.26)-(3.35) and (3.36) have been used in the calculation. The plotted span $\Delta\xi \in [-\pi/4, \pi/4]$ maps directly to degeneracy splitting ratios $\eta(\lambda_{\text{deg}}) \in [0, 1]$, while the span $M\Lambda \in [0, \pi/2]$ covers all allowed permutations of the splitting ratio difference $|\eta^{(2)} - \eta^{(1)}| \in [0, 1]$ for each $\Delta\xi$. All three functions P_S , V_S and V_B are continuous and periodic beyond these axis limits.

The line $M\Lambda = 0$ shows behaviour that is already well-known from previous work. On one hand, it describes all IFPS experiments in which the photons are degenerate ($\Lambda = 0$); on the other, it describes IFPS under conditions of vanishing coupler dispersion, and is therefore the only slice of the parameter space accessible using bulk-optics beamsplitters. As expected, a perfect 50:50 splitting ratio at the degeneracy point ($\Delta\xi = 0$) is seen to yield perfect deterministic pair separation ($P_S=1$). As η is detuned from 1/2 (i.e. $\Delta\xi \neq 0$), P_S and V_B degrade through imperfect cancellation of the interfering bunched-state amplitudes, with changes to V_B in agreement with Equation (2.20). The anti-bunched visibility V_S remains invariant.

New behaviour emerges when both coupler dispersion and non-degeneracy are present so that $M\Lambda$ is non-vanishing. The anti-bunched visibility V_S is no longer invariant and acquires dependencies on both $\Delta\xi$ and $M\Lambda$. The $\Delta\xi$ -dependence of the bunched visibility V_B also changes as a function of $M\Lambda$. Perhaps most remarkably, for a coupling offset of $\Delta\xi = 0$, P_S remains at unity for all $M\Lambda$. This implies that perfect deterministic separation occurs even if the splitting ratios $\eta^{(1)}$ and $\eta^{(2)}$ at the photon central wavelengths deviate from 50:50 conditions and from one-another, so long as the splitting ratio is the ideal 50:50 at the degeneracy wavelength λ_{deg} and the assumptions of the near-degeneracy regime remain valid.

To understand this behaviour, first consider the two extreme cases along the line $\Delta\xi = 0$. When $M\Lambda = 0$, the coupler behaves as an ideal 50:50 splitter at both photon central frequencies, i.e. $\eta^{(1)} = \eta^{(2)} = \eta(\lambda_{\text{deg}}) = 1/2$, and the non-classical enhancement of P_S is maximal. In contrast, $M\Lambda = \pi/2$ corresponds to conditions of $|\eta^{(2)} - \eta^{(1)}| = 1$, such that the coupler behaves as an ideal wavelength

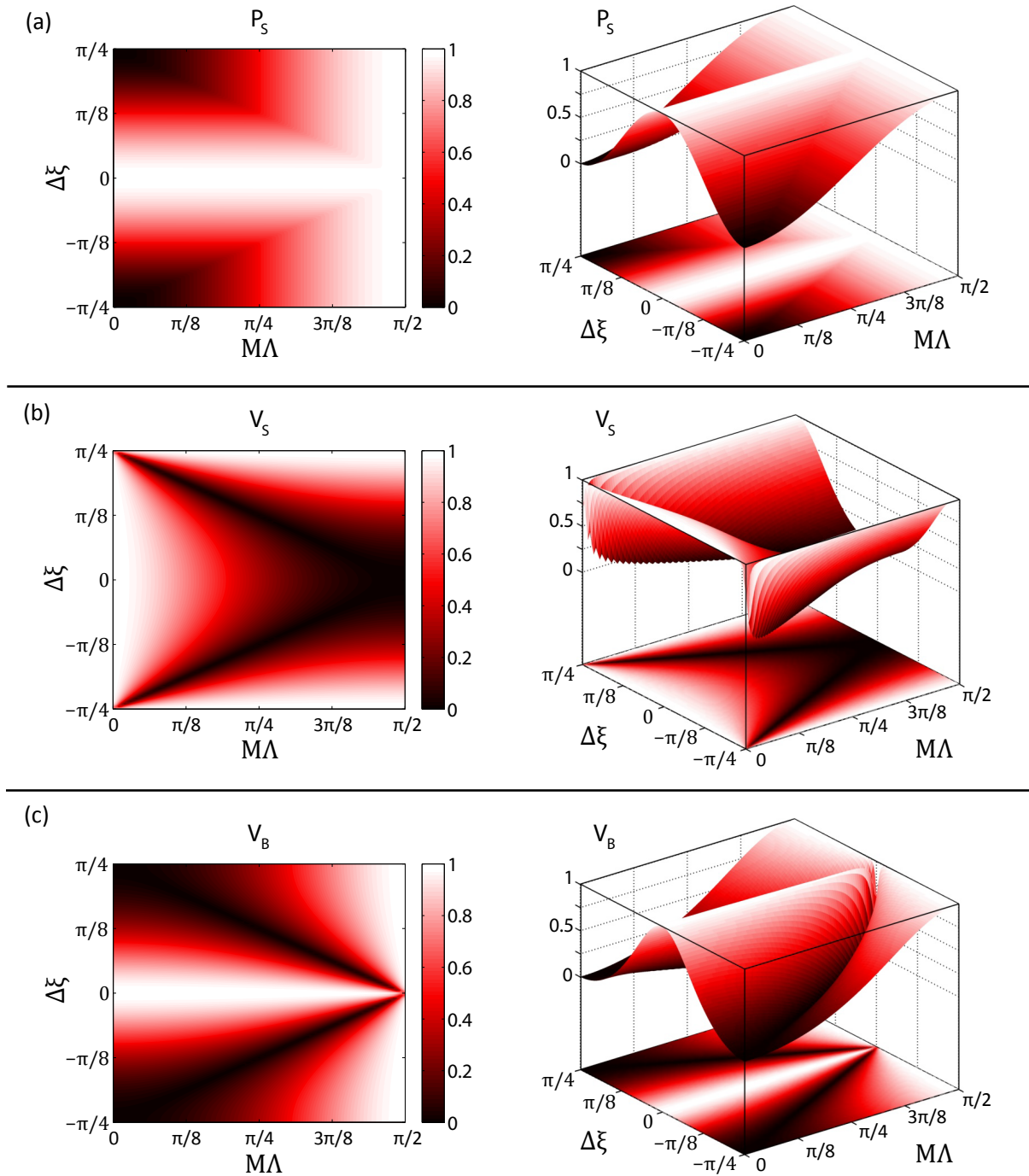


Figure 3.3: (a) Anti-bunched outcome probability P_S , (b) anti-bunched interference visibility V_S , and (c) bunched interference visibility V_B , as computed for a co-polarized photon pair input state from a typical Type I SPDC process. The value of P_S remains above 95% for $\Delta\xi \in [-0.10, +0.10]$.

demultiplexer (WD). Separation of the photons is then entirely classical, with interference contributions P_S^I and P_B^I both vanishing. This leads to $V_S = 0$ and $V_B = \lim_{x,y \rightarrow 0} \frac{x}{y}$ in accordance with Equation (3.35), with the latter no longer being well-defined.

The transition from an ideal 50:50 splitter to an ideal WD occurs gradually along the interval $M\Lambda = [0, \pi/2]$ in such a manner that reduction in P_S^I due to loss of quantum interference is balanced by increases in P_S^0 from classical WD-induced splitting. That these combined quantum and classical effects perfectly balance to preserve $P_S = P_S^0 + P_S^I = 1$ along the entire interval is related to anti-symmetry in the central wavelength splitting ratios. Whenever the condition $\eta^{(1)} + \eta^{(2)} = 1$ is satisfied, perfect deterministic separation is found to occur. Figure 3.4 presents a visualization of how the $\eta^{(j)}$ change as a function of $\Delta\xi$ and $M\Lambda$. For $\Delta\xi = 0$, it can be seen that $\eta^{(1)} + \eta^{(2)} = 1$ is in fact a constraint imposed by the assumptions of linear coupling strength (i.e. chirp-free $\eta(\lambda)$) and central wavelength equidistance from λ_{deg} , both of which were the defining assumptions of the near-degeneracy regime.

Perfect separation fidelity is also possible for non-zero $\Delta\xi$ along the line $M\Lambda = \pi/2$. At this value of $M\Lambda$, the central wavelengths are spaced by exactly half the splitting ratio oscillation period, i.e. $|\lambda_{02} - \lambda_{01}| = T_\lambda/2$. Figure 3.4 illustrates how this leads the coupler to transition from an ideal WD response at $\Delta\xi = 0$ back to an ideal 50:50 splitter response at $\Delta\xi = \pm\pi/4$. During this transition, the condition $\eta^{(1)} + \eta^{(2)} = 1$ is satisfied, leading to perfect balancing between the magnitudes of P_S^0 and P_S^I as before; however, since this special case only occurs for a specific non-degeneracy, it is of little practical value for addressing highly-tunable input states.

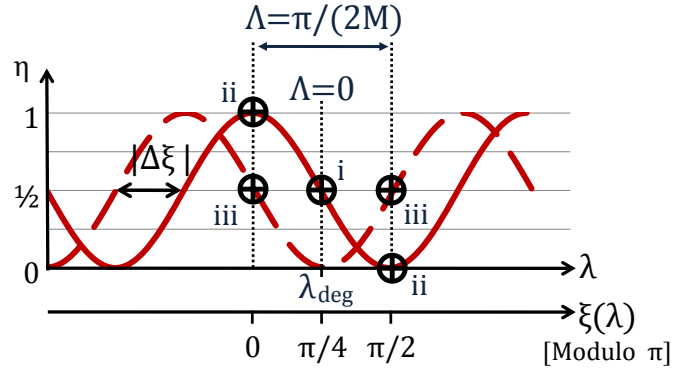


Figure 3.4: Visualization of the splitting ratios sampled by the central photon wavelengths (dashed lines) as $\Delta\xi$ and Λ are varied. For $\Delta\xi = 0$, these splitting ratios remain anti-symmetric about the 50:50 point for all values of Λ . The coupler operates as a perfect 50:50 splitter at points i. and iii., and as a perfect wavelength-demultiplexer at ii.

Changes to the anti-bunched interference visibility V_S are also of interest because they have no analogue in dispersion-free systems. A non-vanishing visibility implies, by definition, the existence of

non-classical contributions to the outcome probability. However, changes in quantum interference are not the only factor causing variation in V_S , since at $\Lambda = 0$ the visibility remains equal to unity for values of $\Delta\xi$ at which interference is clearly imperfect. Yet V_S in Figure 3.3(b) is seen to degrade as $\eta^{(1)}$ and $\eta^{(2)}$ become dissimilar, hence its behaviour is a consequence of the splitting ratio dispersion. Neither fiber-based [3, 98–100] nor chip-based [4, 101] implementations of IFPS have reported such dispersion-derived visibility behaviour, likely because the combined coupler dispersion and photon non-degeneracy have not been high enough. This is also true of on-chip quantum interference in general [1, 79–81, 83, 85–87].

The dispersion-dependence of V_B makes it a useful tool for tracking the coupler’s transition from 50:50 splitting to WD behaviour, particularly at $\Delta\xi = 0$ where it may be regarded as a measure of the relative balance between non-classical and classical contributions to the separation fidelity. Equivalently, V_B can be used to characterize the coupler’s ability to sustain quantum interference over a range of non-degeneracies.

In contrast, the bunched visibility V_B does respond to changes in interference along the line $\Lambda = 0$, but not along the line $\Delta\xi = 0$. On the other hand, the value of V_B provides a qualitative indication of how closely the $\eta^{(1)} + \eta^{(2)} = 1$ condition is being met, albeit this use is limited since V_B becomes undefined at the intersection of $M\Lambda = \pi/2$ and $\Delta\xi = 0$.

3.3.3 Photon Polarization Diversity

It is necessary to consider how IFPS performance changes if additional polarizations are introduced, since many on-chip sources generate cross-polarized photon pairs [77, 78], while others are capable of toggling between TE-TE and TM-TM states or producing both of these co-polarized states concurrently [75]. Such polarization diversity leads to two main complications. Firstly, the polarization dependence of the coupling strength, and thereby the splitting ratio, becomes a potential source of asymmetry that can break the $\eta^{(1)} + \eta^{(2)} = 1$ constraint needed for perfect separation fidelity. This asymmetry has been illustrated in Figure 3.5 and results from both an absolute offset, $\eta_{TE}(\lambda_{deg}) \neq \eta_{TM}(\lambda_{deg})$, and birefringence in the first-order coupler dispersion, $M_{TE} \neq M_{TM}$. Secondly, when polarization entanglement is present but not maximal, the non-degeneracy of the TE-TM state may differ from that of the TM-TE state. In such cases, the pair generation process admits two distinct tuning curves determining the photon wavelengths, one for each polarization (e.g. see Fig. 2 in [11]), with the degeneracy point λ_{deg} occurring at their intersection. The two aforementioned complications can be mitigated to some extent by appropriate design, as will be further discussed in Chapter 4.

On-chip IFPS involving more than a single polarization has not yet been demonstrated [4, 101]. Other

forms of on-chip interference involving anti-bunched states have explored polarization diversity [85], but avoided these challenges through the use of laser-written low-birefringence waveguides and bulk-optics sources of maximally polarization-entangled photons.

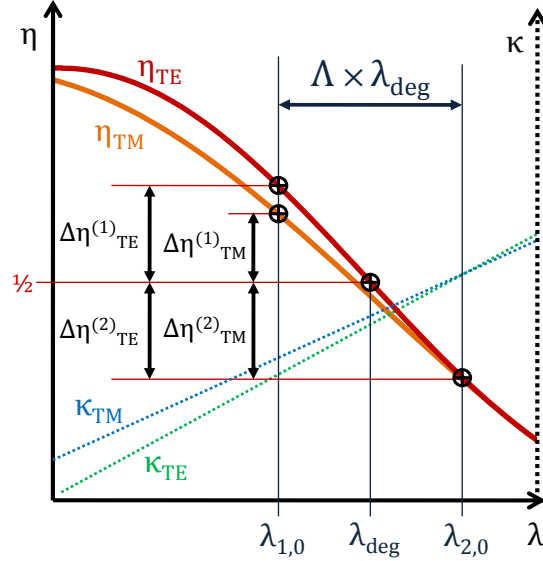


Figure 3.5: The anti-symmetry condition $\eta^{(1)} + \eta^{(2)} = 1$ is shown to be satisfied for a TE-TE co-polarized state, but broken for other polarizations (e.g. $\eta_{\text{TM}}^{(1)} \neq \eta_{\text{TM}}^{(2)} \neq \eta_{\text{TE}}^{(2)}$) due to coupler birefringence in $\eta_{\sigma}(\lambda_{\text{deg}})$ and M_{σ} ; note that $\eta_{\text{TE}}^{(2)} = \eta_{\text{TM}}^{(2)}$ by coincidence only.

3.3.4 Effect of Photon Bandwidths and Spectral Correlations

The previous two subsections assumed a single photon bandwidth, concentrating primarily on how IFPS is influenced by the coupler response at the photon central wavelengths. Photon bandwidth affects IFPS as well, but its influence is comparatively weak except in extreme or special cases. Interestingly, spectral correlations also play a role in determining the bandwidth dependence.

Figure 3.6 shows the calculated dependence of $P_{\mathfrak{S}}$ on both $M\Delta\lambda/\lambda_{\text{deg}}$ and $M\Lambda$ for co-polarized states constructed from Equation (3.36). The splitting ratio offset has been set to $\Delta\xi = 0$, and the bandwidths of the twin-photon marginal spectra are equal ($\Delta\lambda_1 = \Delta\lambda_2 \equiv \Delta\lambda$). The upper bound on the plot range, $M\Delta\lambda/\lambda_{\text{deg}} = \pi$, occurs when the photon bandwidth spans one full oscillation in $\eta(\lambda)$, i.e. $\Delta\lambda = T_{\lambda}$. The states represented in Figure 3.6(a) are perfectly uncorrelated at degeneracy, having Schmidt numbers of $\text{SN} = 1$ for $\Lambda = 0$, whereas the states in Figure 3.6(b) are moderately correlated with $1 < \text{SN} \leq 2.60$. Large photon bandwidths combined with large splitting ratio dispersion are shown to degrade the separation fidelity, but the extent of degradation appears to be mitigated by entanglement. The relationship between $P_{\mathfrak{S}}$ and SN has been calculated explicitly in Figure 3.6(c) for various values of

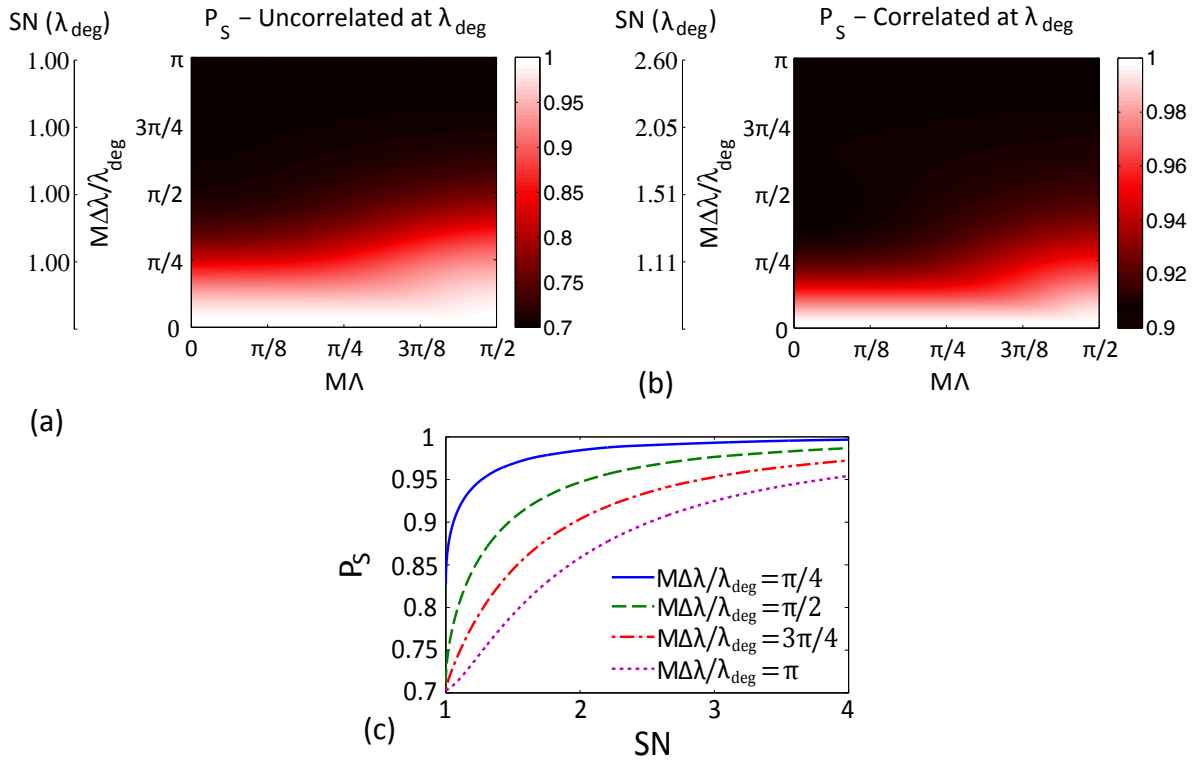


Figure 3.6: Impact of photon bandwidths and spectral entanglement on P_S for various degrees of spectral entanglement. Schmidt numbers are given at degeneracy conditions ($\Lambda = 0$).

$M\Delta\lambda/\lambda_{\text{deg}}$ at degeneracy, revealing a general tendency for P_S to asymptotically approach unity as the photon anti-correlation increases. This suggests opportunities for entanglement-sensitive detection.

To understand this behaviour, recall from Equations (3.26)-(3.28) that the total anti-bunched outcome probability represented by P_S is a sum over all possible combinations of frequencies $\omega_1 = 2\pi c/\lambda_1$ and $\omega_2 = 2\pi c/\lambda_2$ weighted by the BPA. As illustrated in Figure 3.7, when the state is spectrally uncorrelated, the λ_1, λ_2 combinations contributing to this sum are not necessarily equidistant from degeneracy and hence deviate from the $\eta(\lambda_1) + \eta(\lambda_2) = 1$ condition required for perfect separation fidelity. Only in the limit of $\Delta\lambda \rightarrow 0$ is this splitting ratio anti-symmetry condition strictly enforced. Larger photon bandwidths therefore degrade P_S because they allow more λ_1, λ_2 combinations violating this anti-symmetry to contribute towards the total outcome probability. However, when the photon spectra are highly anti-correlated, the BPA restricts the contributing λ_1, λ_2 combinations to be approximately equidistant from λ_{deg} , effectively restoring the splitting ratio antisymmetry even when the bandwidths are large. It is important to note that this restoration is imperfect because frequency does not monotonically map to wavelength. Equidistant anti-correlations in ω will only be approximately equidistant in λ ; likewise, a

coupling strength that is linear in λ will not be perfectly linear in ω .

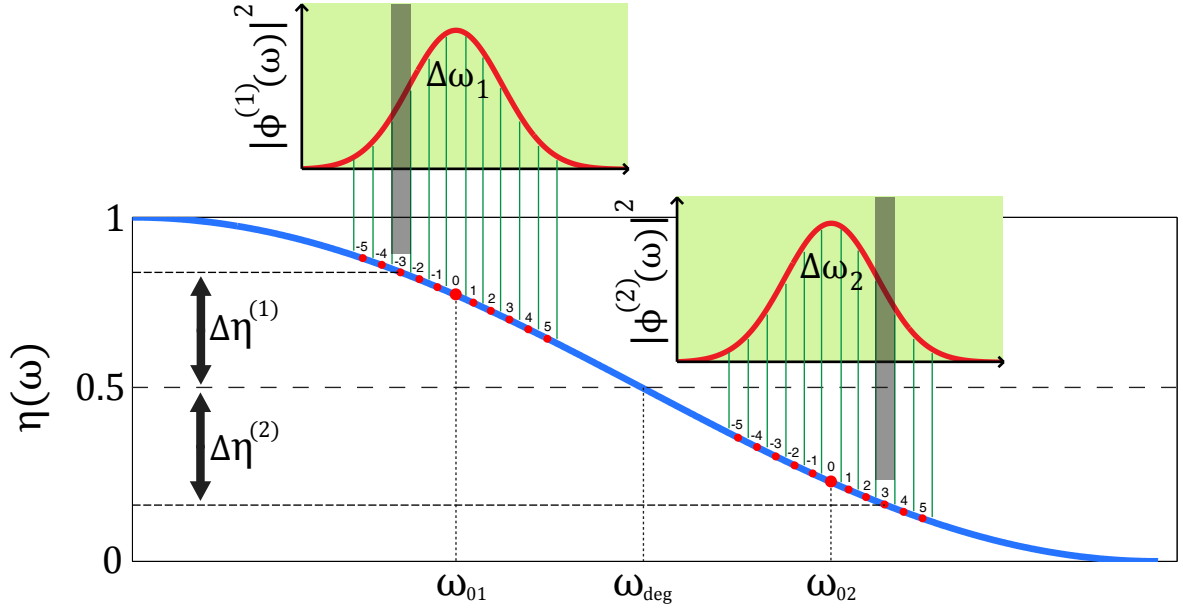


Figure 3.7: Mitigation of splitting ratio asymmetries by spectral correlations, shown in frequency space. Let $|\phi^{(j)}(\omega)|^2$ represent the marginal spectrum of photon j , and let these spectra be equidistant from the degeneracy frequency ω_{deg} where $\eta(\omega_{\text{deg}}) = 0.5$. The indices $n \in [-5, 5]$ represent equally-spaced slices of each spectrum (i.e. the $d\omega_j$ in Equations (3.26)-(3.28)), which are labelled relative to the central frequencies. When the photons are perfectly uncorrelated, all permutations of these slices contribute non-vanishingly towards the determination of P_S with varying degrees of splitting ratio asymmetry. Note that the extent of possible asymmetry is reduced when the spectral bandwidths $\Delta\omega_1$ and $\Delta\omega_2$ are made smaller. On the other hand, if the photons are highly anti-correlated, then these slice permutations are restricted to be anti-symmetric. For example, the slice $n = -3$ of spectrum 1 (shaded) only pairs non-vanishingly with the slice $n = +3$ of spectrum 2 (also shaded), for which the splitting ratios are approximately asymmetric with $\Delta\eta^{(1)} \approx \Delta\eta^{(2)}$.

The interference visibilities V_S and V_B are also influenced by the photon bandwidths as shown in Figure 3.8. As $M\Delta\lambda/\lambda_{\text{deg}}$ increases, V_S is shown to lose much of its Λ -dependence, eventually assuming a nearly constant value in the range of 0.3-0.4 at all non-degeneracies. This is a result of the bandwidths becoming large enough that both the 50:50 splitter and WD regimes of the coupler's response are straddled; beyond $M\Delta\lambda/\lambda_{\text{deg}} = \pi/2$ the bandwidth extends over all possible permutations of $|\eta(\lambda_2) - \eta(\lambda_1)| \in [0, 1]$ such that the classical and non-classical contributions to the anti-bunched outcome acquire a steady relative weighting. The influence of spectral correlations on this behaviour are seen to be minimal. The bunched visibility V_B exhibits similar behaviour, but with two differences. First, it acquires an approximately Λ -independent value when the bandwidth extends over all possible permutations of the *sum* (rather than difference) $|\eta(\lambda_2) + \eta(\lambda_1)| \in [0, 1]$. Secondly, unlike V_S , V_B does depend significantly on spectral entanglement, since greater anti-correlations restrict the contributing

wavelengths to approximately satisfy $\eta(\lambda_2) + \eta(\lambda_1) = 1$ as previously discussed.

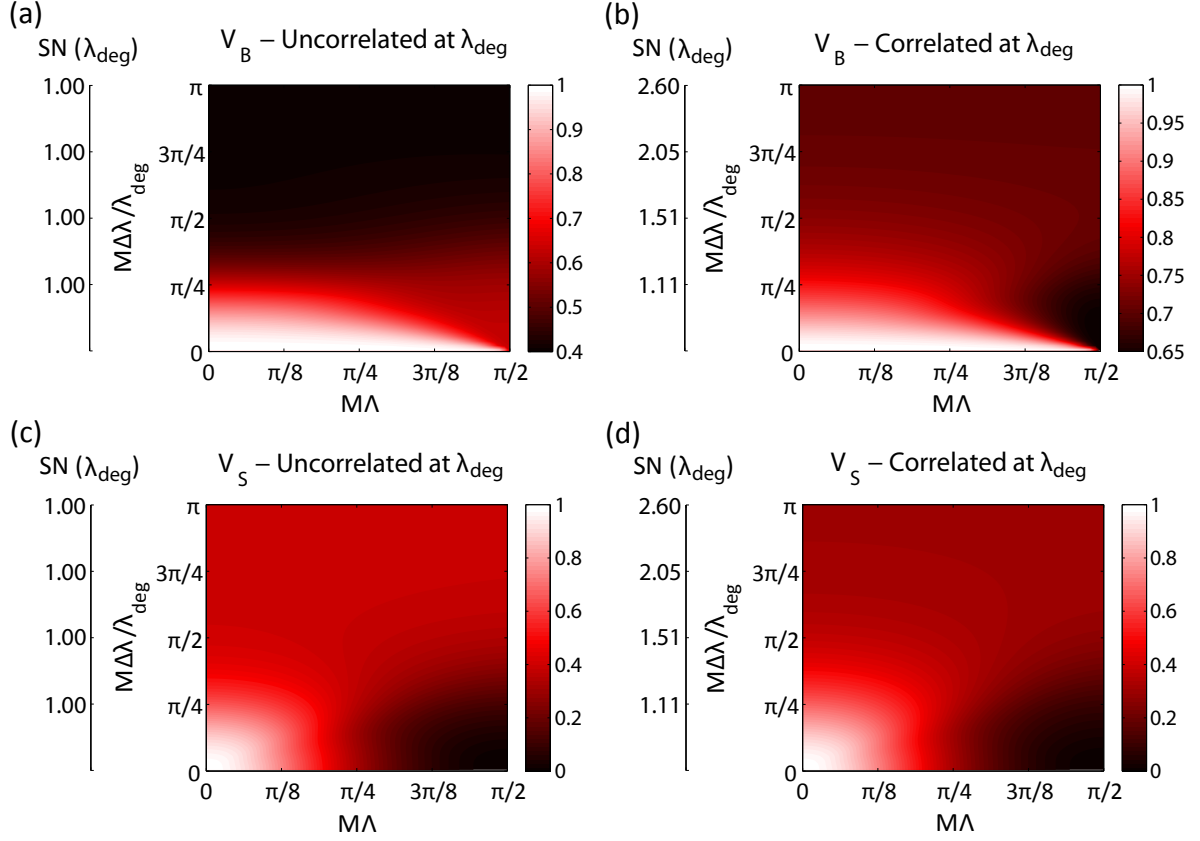


Figure 3.8: Bandwidth and spectral entanglement dependencies of the IFPS interference visibilities.

Although P_S , V_S and V_B are all influenced by photon bandwidth in principle, $M\Delta\lambda/\lambda_{\text{deg}}$ in typical circumstances will not be large enough to make these effects appreciable. For example, consider a photon bandwidth of $\Delta\lambda = 3$ nm, which is thus-far the largest bandwidth used in an on-chip HOM interference experiment. To reach $M\Delta\lambda/\lambda_{\text{deg}} = \pi/4$ with this bandwidth at the common degeneracy point $\lambda_{\text{deg}} = 1550$ nm, a coupler dispersion of $M = 405.8$ ($T_\lambda = 12$ nm) is needed. Since this coupler dispersion is extreme, it is unsurprising that bandwidth has not appeared to be a performance-limiting factor for on-chip interference. In applications where large bandwidths are essential, IFPS will generally be sufficiently aided by spectral correlations. While $P_S \approx 0.83$ for perfectly uncorrelated photons at $M\Delta\lambda/\lambda_{\text{deg}} = \pi/4$, it is far more common for some spectral entanglement to be present, and a Schmidt number as low as 1.25 can increase the separation probability to $P_S \approx 0.95$ and higher.

3.4 Behaviour far from Degeneracy

The study of the near-degeneracy regime has provided key insights about how IFPS performs in the presence of coupler dispersion. It was seen that splitting ratio antisymmetry at the photon wavelengths led to the preservation of near-perfect separation fidelities even when interference was lost. However, this antisymmetry assumed a linear coupling strength and equidistant central wavelength separations from degeneracy. It is important to consider IFPS performance far from degeneracy, where these assumptions may no longer be valid.

3.4.1 Extrapolation of Near-Degeneracy Behaviour

Even when far from degeneracy, the predictions of the near-degeneracy regime may nonetheless be a suitable approximation of IFPS behaviour. This ultimately depends on both the coupler and the tuning characteristics of the photon pair generation process. As an example, consider the silica-on-silicon coupler discussed in Chapter 2. The simulated TE coupling strength of this device was well-described by $\kappa_{\text{TE}}(\lambda) = 3.805 \times 10^{15} \lambda^2 - 3.853 \times 10^9 \lambda + 1003$ for wavelengths in the range $700 \text{ nm} \leq \lambda \leq 860 \text{ nm}$. However, the higher-order coupler dispersion is sufficiently small that $\kappa_{\text{TE}}(\lambda)$ can be well-approximated by a linear function, having a goodness-of-fit R-squared of 0.9987. For $\lambda_{\text{deg}} = 780 \text{ nm}$, the coupler can then be described using Equations (3.37)-(3.39) by $\Delta\xi_{\text{TE}} \approx 0$ and $M_{\text{TE}} = 4.0716$. Suppose this coupler is used to apply IFPS to a TE-TE co-polarized state created from Type I SPDC with a non-degeneracy of 80 nm. The central wavelength equidistance assumption is generally a good approximation for SPDC at non-degeneracies below 100 nm (see Chapter 5), hence the dimensionless non-degeneracy $\Lambda = 80 \text{ nm}/780 \text{ nm} \approx 10\%$ may be used, giving $M_{\text{TE}}\Lambda = 0.133\pi \approx \pi/8$. Using these parameter values, the contour calculations of Figure 3.3 predict $P_{\text{S}} = 1$ and $V_{\text{S}} = 0.7169$, which closely match the values of $P_{\text{S}} = 0.9989$ and $V_{\text{S}} = 0.7171$ computed from Equations (3.26)-(3.35) using the true polynomial expression for $\kappa_{\text{TE}}(\lambda)$. The near-degeneracy predictions can thus remain a useful guide even at large non-degeneracies. Chapter 4 examines this in greater detail through several case studies.

3.4.2 Loss of Splitting Ratio Anti-Symmetry

In principle, the near-degeneracy regime assumptions may nonetheless break down completely when the non-degeneracy becomes large enough. Although the coupler dispersion may be locally linear, higher-order dispersion may dominate the global coupler behaviour and significantly chirp the splitting ratio's wavelength dependence. Furthermore, as the central wavelengths λ_{01} and λ_{02} follow the phase-matching tuning curve, they will eventually become asymmetric about λ_{deg} . Together, these non-idealities break

the $\eta^{(1)} + \eta^{(2)} = 1$ antisymmetry, with the consequence that classical WD behaviour no longer perfectly compensates P_S when quantum interference is lost. This leads to degradation of the IFPS separation fidelity, as will be examined in Chapter 4.

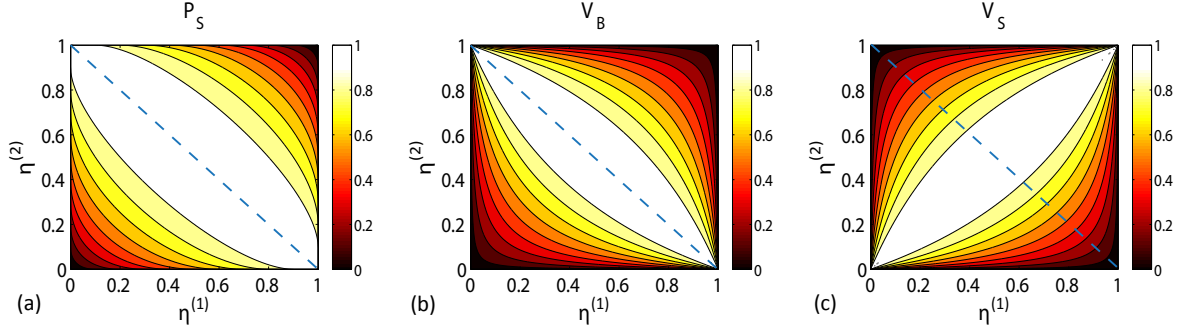


Figure 3.9: Anti-bunched outcome probability P_S and interference visibilities V_B and V_S for all permutations of the photon central wavelength splitting ratios $\eta^{(1)}$ and $\eta^{(2)}$; diagonal lines (dashed) denote the anti-symmetry contour $\eta^{(1)} + \eta^{(2)} = 1$.

In the absence of symmetry, a generic set of dimensionless variables spanning all parameter space can no longer be constructed. Predictions can be made on a case-by-case basis using Equations (3.26)-(3.35). However, it is possible to comment generically on how the central wavelength splitting ratios $\eta^{(1)}$ and $\eta^{(2)}$ determine the IFPS behaviour, without accounting for bandwidth or correlation effects. For co-polarized states, the substitution $\phi^j(\omega_{01}, \omega_{02}) = \delta(\omega_1)\delta(\omega_2)$ leads to the simplified expressions

$$P_S = \eta^{(1)} [1 - \eta^{(2)}] + [1 - \eta^{(1)}] \eta^{(2)} + 2\sqrt{\eta^{(1)}\eta^{(2)} [1 - \eta^{(1)}] [1 - \eta^{(2)}]}, \quad (3.40)$$

$$V_S = \frac{2\sqrt{\eta^{(1)}\eta^{(2)} [1 - \eta^{(1)}] [1 - \eta^{(2)}]}}{\eta^{(1)} [1 - \eta^{(2)}] + [1 - \eta^{(1)}] \eta^{(2)}}, \quad (3.41)$$

$$V_B = \frac{2\sqrt{\eta^{(1)}\eta^{(2)} [1 - \eta^{(1)}] [1 - \eta^{(2)}]}}{\eta^{(1)}\eta^{(2)} + [1 - \eta^{(1)}] [1 - \eta^{(2)}]}, \quad (3.42)$$

which have been plotted in Figure 3.9. A similar approach for cross-polarized states is discussed in Chapter 4. Such plots will be used to visualize and interpret the evolution of IFPS behaviour as the state or coupler properties are tuned.

It is seen that high separation fidelities ($P_S > 0.9$) remain achievable so long as $\eta^{(1)}$ and $\eta^{(2)}$ are on opposing sides of the 50:50 split point, corresponding to the top-left and bottom-right quadrants of Figure 3.9(a). This can generally be satisfied when λ_{01} and λ_{02} span no more than a single cycle in $\eta(\lambda)$, provided $\eta(\lambda_{\text{deg}}) \approx 1/2$. Beyond one cycle it is possible to find $\eta^{(1)}$ and $\eta^{(2)}$ either both above or both below $\eta = 1/2$, with a net effect similar to a Λ -dependent non-zero $\Delta\xi$ in the near-degeneracy regime.

Note that P_S is least sensitive to deviations from the $\eta^{(1)} + \eta^{(2)} = 1$ contour near the 50:50 split point, suggesting that separation provided through quantum interference is more robust against non-idealities than purely classical separation.

3.5 Impact of IFPS on Entanglement

Earlier in this chapter, input state spectral correlations were found to influence the bandwidth dependence of IFPS. This section now investigates whether IFPS can in turn influence the entanglement properties of the output state. For simplicity, only co-polarized states are discussed. First consider the most simplistic expression for the input state, expressed solely in terms of the photon central wavelengths and path DOF:

$$|\Psi\rangle_{in} = |\lambda_{01}, A\rangle|\lambda_{02}, A\rangle + |\lambda_{01}, B\rangle|\lambda_{02}, B\rangle. \quad (3.43)$$

For a perfect 50:50 coupler response, spectral correlations remain intact since evolution through the coupler does not depend on ω ; hence, the Schmidt number of the input state equals that of the output state. Consider also perfect WD operation, where separation is entirely classical. Supposing $\eta(\lambda_{01}) = 1$ and $\eta(\lambda_{02}) = 0$, the state maps to

$$|\Psi\rangle_{out} = |\lambda_{01}, A\rangle|\lambda_{02}, B\rangle + |\lambda_{01}, B\rangle|\lambda_{02}, A\rangle. \quad (3.44)$$

Although the coupler has pivoted on distinguishability in the photon spectral properties to provide separation, the output state nonetheless remains spectrally entangled, since the wavelength of a given photon cannot be identified by the waveguide it exits from. This preservation of spectral entanglement is a direct consequence of the path entanglement at the input.

In general, however, it cannot be assumed that entanglement is similarly preserved in other regimes of operation, such as when $M_\sigma\Lambda \neq 0$. Examining these cases requires the full expression for the output state after evolution through the coupler. Using Equations (3.15)-(3.16), this can be written as

$$|\Psi\rangle_{out} = \sum_{pq} \int d\omega_1 d\omega_2 \Phi^{pq}(\omega_1, \omega_2) |\omega_1, p\rangle |\omega_2, q\rangle \quad (3.45)$$

where $\Phi^{pq}(\omega_1, \omega_2) = (-i)^{[\delta_{pB} + \delta_{qB}]} \Phi^{A \rightarrow pq}(\omega_1, \omega_2) + (-i)^{[\delta_{pA} + \delta_{qA}]} \Phi^{B \rightarrow pq}(\omega_1, \omega_2)$ has been defined, and $|\omega, j\rangle \equiv \hat{b}^{j\dagger}(\omega)|\text{vac}\rangle$. Of particular interest is the SN of the anti-bunched (i.e. separated) outcome, as this is often post-selected so that only separated photons contribute to the experiment or quantum photonic application at hand.

3.5.1 Dichroic Coupler Response

It is instructive to first consider a step-like $\eta(\omega)$ response. This emulates the familiar scenario in free-space where non-degenerate photons in a common path are separated using a ‘dichroic’ mirror (e.g. see Ref [11]). The dichroic mirror reflects all frequencies $\leq \omega_0$ and transmits all higher frequencies. The equivalent coupler response is

$$\eta(\omega) = \begin{cases} 0, & \text{if } \omega \leq \omega_0 \\ 1, & \text{if } \omega > \omega_0 \end{cases}. \quad (3.46)$$

Although $\eta(\omega)$ is sinusoidal for linearly dispersive couplers, this step-like response can be approximated when the photon bandwidths are sufficiently narrow. For the purposes of this discussion, Equation (3.46) will be imposed directly, without restricting the bandwidth.

Let ‘1’ label the photon emerging from path A , and ‘2’ label the photon emerging from path B . The outcome thus being considered is associated with $|\omega_1, A\rangle|\omega_2, B\rangle$, and the corresponding state is

$$|\Psi\rangle_{AB} = \int_0^\infty d\omega_1 \int_0^\infty d\omega_2 \Phi^{AB}(\omega_1, \omega_2) |\omega_1, A\rangle |\omega_2, B\rangle. \quad (3.47)$$

The SN of this state is calculated by substituting $\phi(\omega_1, \omega_2)$ with $\Phi^{AB}(\omega_1, \omega_2)$ in Equation 2.9. The output is assumed to remain in a pure state. In practice, the photon pairs may interact with the environment, resulting in the loss of quantum information and leading to a mixed state [109, 150]. This could be caused, for example, by system resonances in the vicinity of the photon pair’s joint spectra. While the implications of state impurity are not examined in this thesis, a brief discussion of how it can be accounted for is included in Appendix A.

Note that the $G^{j \rightarrow pq}$ contained within the definitions of the $\Phi^{j \rightarrow pq}$ are effectively transfer functions on the BPAs. The $G^{j \rightarrow pq}$ were defined in Equation (3.16). For single input source, e.g. $\phi^A(\omega_1, \omega_2) \neq 0$ and $\phi^B(\omega_1, \omega_2) = 0$, the joint spectral intensity of the output can be written as $|\Phi^{AB}(\omega_1, \omega_2)|^2 = |\phi(\omega_1, \omega_2)|^2 |G^{A \rightarrow AB}(\omega_1, \omega_2)|^2$, where the superscript on the input BPA has been dropped. Similarly, for two symmetric sources (where $\phi^A(\omega_1, \omega_2) = \phi^B(\omega_1, \omega_2)$), this can be written as $|\Phi^{AB}(\omega_1, \omega_2)|^2 = |\phi(\omega_1, \omega_2)|^2 |G^{A \rightarrow AB}(\omega_1, \omega_2) + G^{B \rightarrow AB}(\omega_1, \omega_2)|^2$. In either case, the total transfer function on $|\phi(\omega_1, \omega_2)|^2$ will be denoted $|G^{AB}(\omega_1, \omega_2)|^2$.

Suppose there is only a single source of photon pairs, located at the input of path A . The state simplifies to

$$|\Psi\rangle_{AB} = \int_{\omega_0}^\infty d\omega_1 \int_0^{\omega_0} d\omega_2 \phi^A(\omega_1, \omega_2) |\omega_1, A\rangle |\omega_2, B\rangle, \quad (3.48)$$

which takes the same form as in the analogous free-space situation (see Eqn. 8 in Ref. [75] or Eqn. 10 in

Ref. [73]). As an example, suppose the input state is described by $\lambda_{\text{deg}} = 1550$ nm, $|\lambda_{02} - \lambda_{01}| = 6$ nm, $\Delta\lambda = 3$ nm, and $\Delta\lambda_P = 0.25$ nm, modelled using Equation (3.36). The value of ω_0 will be taken as the degeneracy frequency, i.e. $\omega_0 = 2\pi c/\lambda_{\text{deg}}$. Entanglement in the input state is calculated to be $\text{SN} = 4.62$, and the central wavelengths are highly anti-correlated.

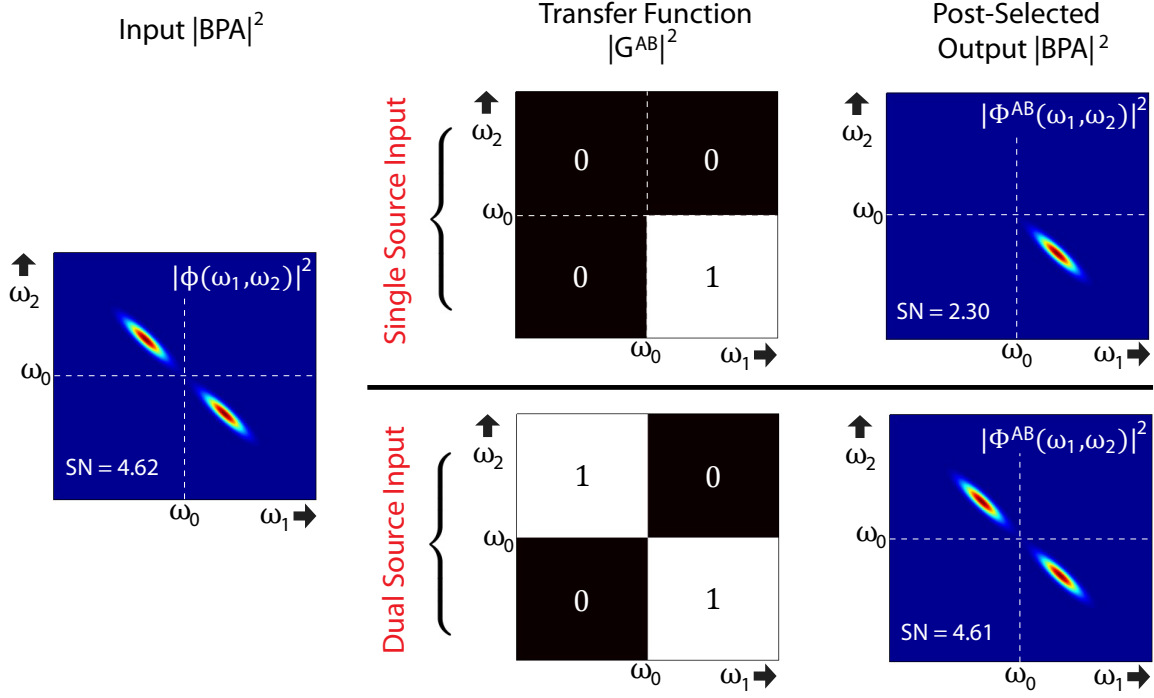


Figure 3.10: Effective evolution of $|\phi(\omega_1, \omega_2)|^2$ to $|\Phi^{AB}(\omega_1, \omega_2)|^2$ for a dichroic coupler response, with a single photon pair source (top) and two coherently-pumped sources (bottom).

Figure 3.10 shows the evolution of this input state to the $|A, B\rangle$ output state. Since the photons are non-degenerate, it is known a-priori that the photon of higher frequency will emerge from path A . This results in a decrease of the Schmidt number to $\text{SN} = 2.30$ at the output. Note that some entanglement remains due to correlations between the photon bandwidths. These residual correlations would disappear as $\Delta\lambda$ approaches zero. For example, if the photon bandwidth is changed to $\Delta\lambda = 0.5$ nm, the Schmidt number is calculated to be $\text{SN} = 2.04$ at the input and $\text{SN} = 1.02$ at the output. In either case, entanglement of the photon central wavelengths has been lost. On the other hand, if the input consists of two path-entangled sources such as in IFPS, then the effective transfer function leaves the BPA invariant as seen in Figure 3.10, with the result that all spectral correlations are conserved. In the dichroic mirror analogy, a photon found in output path A could have been either transmitted or reflected, and hence its central wavelength is not pre-determined. With $\Delta\lambda = 3$ nm, the output state is found to have $\text{SN} = 4.61$, which equals the input SN to within numerical inaccuracy.

3.5.2 Generalized Coupler Response

Having looked at the familiar dichroic mirror analogy, the full parameter space of the coupler response is explored. Near-degeneracy conditions (linearity in κ ; λ_{01} and λ_{02} equidistance with respect to λ_{deg}) are assumed. The output SN is computed from $\Phi^{AB}(\omega_1, \omega_2)$ as before, but as a function of $M\Lambda$ and $\Delta\xi$. The states used in these calculations have $\lambda_{\text{deg}} = 1550$ nm, $|\lambda_{02} - \lambda_{01}| = 10$ nm, $\Delta\lambda = 1$ nm, and $\Delta\lambda_p = 0.25$ nm, with $\text{SN} = 2.31$ at the input. Figure 3.11(a) shows the results for only a single source in waveguide A , while 3.11(b) is computed using two identical coherently pumped sources.

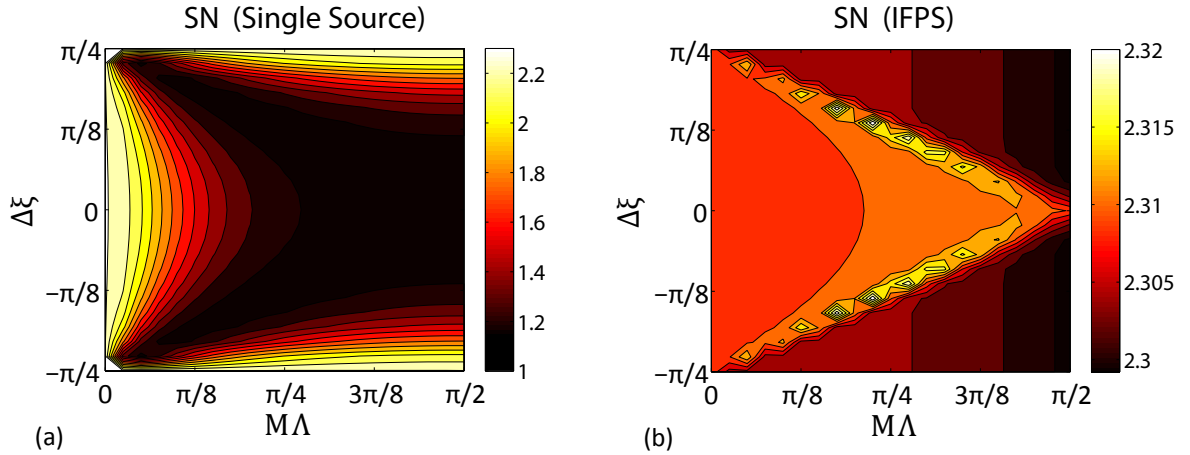


Figure 3.11: Spectral entanglement of the post-selected anti-bunched output. (a) The input state is generated from one photon pair source situated in either path A or path B . (b) The input is generated from two coherently pumped sources, one in each path; fluctuations in SN are attributable to numerical inaccuracies.

With only a single source, the Schmidt number exhibits similar behaviour to the anti-bunched interference visibility V_S of IFPS. Entanglement is invariant for $M\Lambda = 0$, but is nearly eliminated at the coordinate $[M\Lambda = \pi/2, \Delta\xi = 0]$, where the coupler exhibits perfect WD behaviour. Interestingly, these results indicate the possibility of tailoring the post-selected state entanglement by tuning the coupler properties, for example by changing the offset $\Delta\xi$ at $M\Lambda = \pi/2$. This can provide an in-situ tool for quantum state engineering; the topic of active coupler tuning is discussed in Chapter 4.3. On the other hand, no significant change in SN is seen with two coherently pumped sources, indicating that IFPS continues to preserve entanglement throughout the entire parameter space.

3.6 Conclusions

Coupler dispersion has been shown to influence two-photon quantum interference in ways the beamsplitter of bulk optics does not. To sum up the results of this chapter, as the photon pair state deviates from

degeneracy, dispersion in $\eta_\sigma(\lambda)$ leads to a reduction in interference, but antisymmetry in $\eta_\sigma(\lambda)$ about λ_{deg} can restore the anti-bunched outcome probability P_S to unity through wavelength-demultiplexing effects, with the visibility V_S revealing the balance between classical WD and quantum interference. This visibility behaviour is unique to dispersive couplers and has not been experimentally demonstrated. Non-trivial reduction in P_S by large photon bandwidths can occur but is naturally suppressed by spectral entanglement and requires severe coupler dispersion to take place. The spectral entanglement of the output state is preserved by IFPS, but can be tailored by tuning the coupler properties if only one photon pair source is used at the input. At larger non-degeneracies, asymmetries can cause deviations from ideal performance, and make it useful to describe IFPS behaviour in terms of the central-wavelength splitting ratios $\eta^{(1)}$ and $\eta^{(2)}$.

If integrated mode couplers completely lacked dispersion and birefringence such that $\eta = 1/2$ indefinitely, interference-facilitated deterministic separation could be provided for any arbitrary two-photon state generated on-chip. The realities of dispersion in integrated systems makes this goal subject to the coupler design and performance. While it has been shown that this same dispersion can nonetheless restore perfect splitting performance through WD effects, ensuring that such compensation is retained requires a linear coupler response and symmetry in the central wavelengths relative to degeneracy. The consequences of relaxing these idealities is explored in Chapter 4, along with an approach for mitigating splitting ratio asymmetry.

Chapter 4

IFPS Case Studies

The present chapter provides physical examples of IFPS with integrated directional couplers, to complement the generalized discussions of Chapter 3. It also explores the consequences of relaxing the near-degeneracy approximations (NDAs), and how resultant degradation to separation performance can be mitigated. Section 4.1 studies and contrasts various aspects of IFPS in four different directional coupler designs, under the assumption of symmetric quantum state detuning from degeneracy. Section 4.2 provides an example of IFPS with realistic asymmetric state detuning. Lastly, Section 4.3 presents active coupler tuning as useful route for mitigating asymmetries, and as a tool for state engineering.

4.1 Directional Coupler Design Comparisons

This section considers the IFPS performance of four different straight-waveguide directional coupler designs, as an illustrative complement to the more generalized discussion of Chapter 3. It also provides insight into how physical coupler attributes may impact IFPS, with a focus on: (i) a symmetric vs. asymmetric waveguide profiles, and (ii) high vs. low material refractive index dispersion. The examples are based on existing designs, but in some cases unorthodox modifications have been made to allow for more direct comparison of the two aforementioned attributes. Performance will be investigated for a degeneracy point of $\lambda_{\text{deg}} = 800$ nm, which is in the vicinity of several common photon pair sources such as potassium-diphosphate (KDP) [87] and bismuth borate (BBO) crystal [81].

Architectures: Figure 4.1(a) shows two common architectures for implementing directional couplers. In the first (design 1), the waveguide cores are completely surrounded by the cladding. This configuration is typical of many dielectric material systems, such as the silica-on-silicon coupler introduced in Chapter 2.3.2, which saw extensive use in on-chip quantum interference-based demonstrations

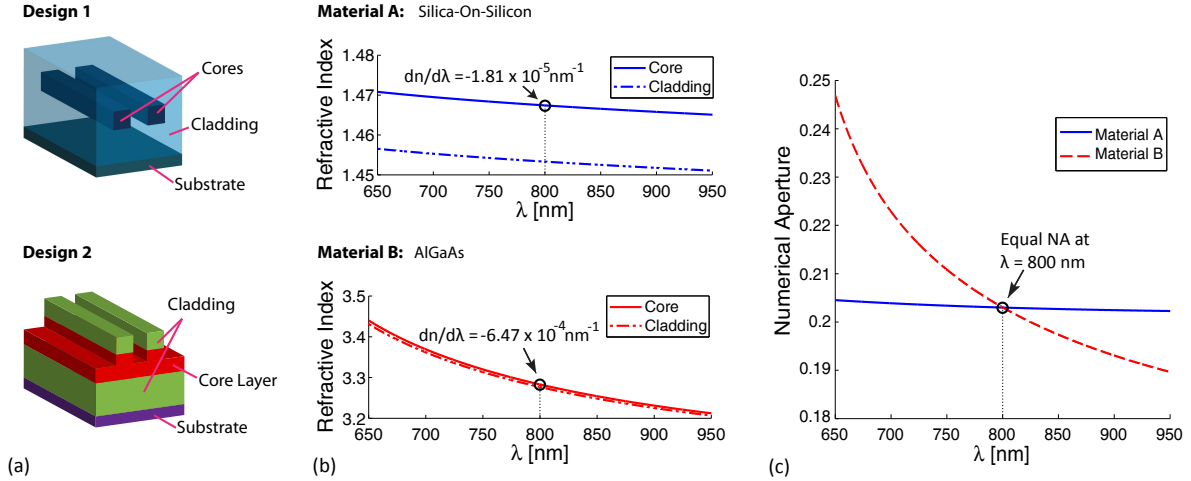


Figure 4.1: (a) Coupler architectures and (b) material systems used in the present case study. (c) Numerical apertures of the material systems; the large variation in confinement for material B is due to a nearby material resonance. The refractive index models for materials A and B were based on Refs. [7] and [8] respectively.

[1, 6, 79–81, 87]. The second architecture (design 2) employs ridge waveguides for guiding and coupling, and is often seen with semiconductor materials. A recent example using AlGaAs is reported in Ref. [83], where high-visibility on-chip HOM interference was observed. Table 4.1 gives the design specifications used in this study. The waveguides have been given similar dimensions, to better compare the two architectures. The cladding layers are treated as infinite in extent (i.e. their thickness is much larger than the evanescent tails of the modes), hence their specifications are omitted. Note that the etch depth specification for design 2 refers to the depth below the surface of the topmost core-cladding interface.

Table 4.1: Directional Coupler Design Specifications

Property	Design 1	Design 2
Waveguide Architecture	Buried Wire	Ridge
Core Layer Thickness	2.5 μm	2.5 μm
Core Layer Etch Depth	N/A	1.25 μm
Waveguide Width	2.5 μm	2.5 μm
Waveguide Separation	2.0 μm	2.0 μm

Materials: The two material systems considered are GeO_2 -doped silica (material A; a dielectric) and AlGaAs (material B; a semiconductor). The refractive index of these systems is shown in Figure 4.1(b); further details are summarized in Table 4.2 (note: ‘x’ refers to the molar fraction of the dopant). The material dispersion of the AlGaAs system is more than an order of magnitude larger than that of the dielectric, since the core layer of the former has a nearby bandgap at 571 nm. To facilitate a more equal

comparison, the core-cladding numerical apertures (NAs) of these systems, and thereby their relative confinement, have been made equal at 800 nm, as seen in Figure 4.1(c). Note that this made the AlGaAs core-cladding specifications unrealistic compared to conventional designs, which typically have far greater confinement (e.g. Ref. [83] uses GaAs as the core, and $\text{Al}_{0.30}\text{Ga}_{0.70}\text{As}$ as the cladding, with $\text{NA} \simeq 1$ at 800 nm). Furthermore, such a system would not likely be operated near its bandgap, since absorption losses would restrict the range of useful operation. The specifications given to the AlGaAs system nonetheless serve to highlight the effects of high material dispersion in these examples. The GeO_2 -doped silica specifications, on the other hand, closely resemble those used in real devices [6]. Both AlGaAs and silica lack intrinsic material birefringence [124]. Although birefringence can be induced by wafer stresses [122], this is not considered here. Any birefringence in the coupler performance will be the result of polarization-dependent waveguide dispersion.

Table 4.2: Material System Design Specifications

Property	Material A	Material B
Substrate	Silicon	GaAs
Core Composition	GeO_2 -doped Silica ($x = 0.0942$)	$\text{Al}_{0.50}\text{Ga}_{0.50}\text{As}$
Cladding Composition	Undoped Silica	$\text{Al}_{0.51}\text{Ga}_{0.49}\text{As}$
Numerical Aperture at 800 nm	0.203	0.203
$dn_{\text{core}}/d\lambda$ at 800 nm	$-1.81 \times 10^{-5} \text{ nm}^{-1}$	$-6.47 \times 10^{-4} \text{ nm}^{-1}$
Nearest Material Resonance	118 nm	571 nm

4.1.1 Coupling Characteristics

The four designs considered in this case study are formed from permutations of the above architectures and material systems, where ‘1A’ refers to architecture design 1 combined with material system A, etc. Coupling characteristics were numerically simulated using commercial software (*Lumerical Mode Solutions*), and have been plotted in Figure 4.2. Key values at 800 nm are summarized in Table 4.3, and the coupling constants are given in Fig. 4.2(a). Coupler birefringence was present only in designs 2A and 2B. Despite identical numerical apertures at 800 nm, the coupling strength of designs with material A are more than a factor of two larger than those with material B. A likely explanation is that the evanescent tails in material A extend farther and therefore have greater overlap compared to those of material B, since the in-material wavelength (λ/n) is roughly twice as large in the former than the latter.

To compare coupler dispersions, it is important to note that the splitting ratio dispersion scales as $d\eta_\sigma(\lambda)/d\lambda \propto L[d\kappa\sigma(\lambda)/d\lambda]$, where L is the coupler interaction length. This length is taken to be $L = L_0 = (\pi/4)[\kappa_{\text{TE}}(\lambda = 800 \text{ nm})]^{-1}$, where L_0 is the smallest possible length for which 50:50

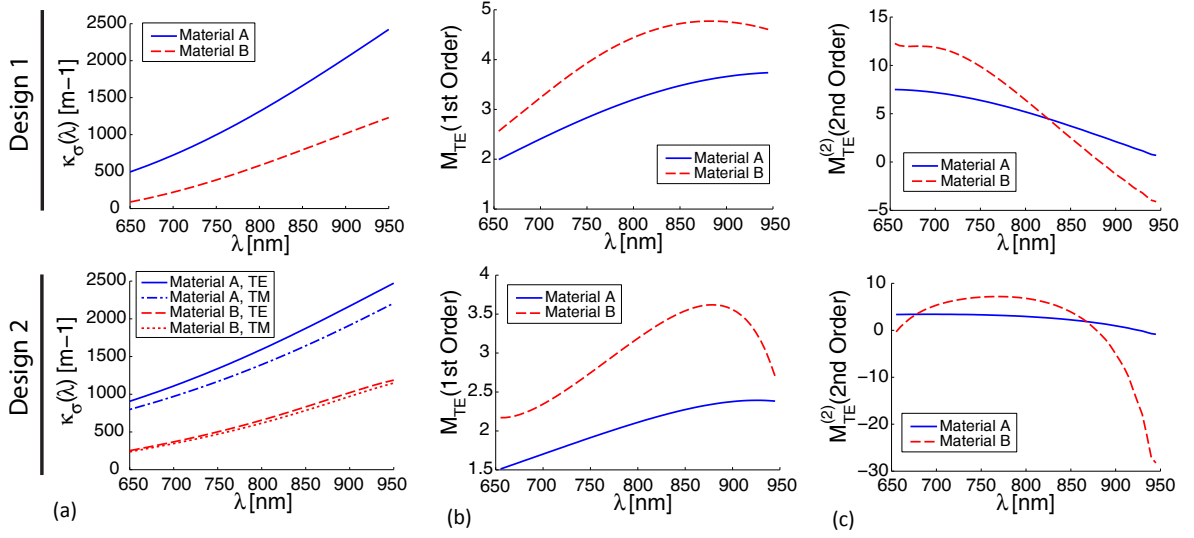


Figure 4.2: Simulated coupling characteristics for each design, showing: (a) the coupling constant's λ and σ dependence; (b) dimensionless first-order coupler dispersion; and (c) dimensionless second-order coupler dispersion. The waveguides remained single-mode over the wavelength range shown.

TE splitting is satisfied at 800 nm. Note that any $L = n \times L_0$ where n is an odd integer will also satisfy 50:50 splitting, but the dispersion will be multiplied by a factor of n . For convenience, the first order coupler dispersion has been written in terms of the dimensionless parameter M_σ defined in Equation 3.39 (but evaluated at the local λ rather than λ_{deg}). To compare higher-order dispersion, which will be responsible for deviations from the near-degeneracy approximations (NDA) of Chapter 3.3.1, a second-order dimensionless dispersion may likewise be defined as

$$M_\sigma^{(2)} = \lambda_{deg}^2 L \left[\frac{d^2 \kappa_\sigma(\lambda)}{d\lambda^2} \right]. \quad (4.1)$$

The first- and second-order coupler dispersion are shown in Fig. 4.2(b)-(c).

Table 4.3: Coupling Characteristics at 800 nm

Parameter	Design 1A		Design 1B		Design 2A		Design 2B	
	TE	TM	TE	TM	TE	TM	TE	TM
κ_σ [m ⁻¹]	1312.5	1312.5	580.7	580.7	1594.7	1392.9	656.5	616.3
L_0 ($\eta_{TE} = 1/2$) [μ m]	598	–	1352	–	492	–	1196	–
M_σ	3.197	3.197	4.442	4.442	2.110	1.865	3.190	3.022
$M_\sigma^{(2)}$	5.186	5.186	6.420	6.420	2.944	3.264	6.798	7.209

Comparison between architectures: The buried-wire architecture (design 1) exhibits marginally higher levels of dispersion than the ridge waveguide structure (design 2) over most of the wavelength range; however, the dispersions of both architectures are well within the same order of magnitude.

Neither poses a markedly significant advantage in linearity. Although not investigated here, differences in the dispersion characteristics could become more apparent if the waveguide geometries were decreased to sub-micron dimensions, where the effects of waveguide dispersion are amplified (e.g. see [76]). The most apparent difference is that coupler birefringence exists only for design 2.

Comparison between materials: The two material systems also exhibit similar coupler characteristics, with the dispersion of material B (AlGaAs) being only a factor of two higher than that of material A (silica). That these fall within the same order of magnitude is non-intuitive, since the material dispersion of material B (AlGaAs) is roughly 35 times that of material A (silica). The large material dispersion of material B manifests most strongly in $M_\sigma^{(2)}$ of design 1, particularly at the lower end of the wavelength range, where changes in the NA (and hence confinement) are most rapid.

Curiously, $M_\sigma^{(2)}$ at the lower wavelengths appears suppressed in design 2. This is presumably cancellation due to waveguide dispersion of opposite sign. This suggests that in principle, the AlGaAs layer properties could be optimized (i.e. by changing the Aluminium concentration to shift the bandgap) to provide cancellation of $M_\sigma^{(2)}$ over a greater range. The decrease in $M_\sigma^{(2)}$ between architectures is more significant for AlGaAs than for silica. This could be attributed to the fact that waveguide dispersion is not completely decoupled from the material dispersion, as noted in Section 2.3.1. A sharp increase in $M_\sigma^{(2)}$ is seen beyond 875 nm, which may be due to the onset of field leakage when the AlGaAs waveguide numerical aperture (i.e. field confinement) drops to its lowest values.

4.1.2 Co-Polarized State Performance

The IFPS performance for co-polarized TE-TE photon pair states is now examined, utilizing the simulated coupler characteristics of each design. Equations (3.26)-(3.34) as well as the idealized Type I BPA model of Equation (3.36) are used in the calculations. Equidistance in the central photon wavelengths (λ_{01} and λ_{02}) from λ_{deg} is enforced, so that deviations from ideal performance result from the coupler characteristics only, and not asymmetries in the quantum state.

Variable Non-Degeneracy

The results for the separated (anti-bunched) probability P_S and separated interference visibility V_S as a function of the absolute non-degeneracy $|\lambda_{02} - \lambda_{01}|$ are shown in Figures 4.3(a)-(b). Figures 4.3(c)-(d) track the corresponding sum and difference of the photon central wavelength splitting ratios $\eta^{(1)} = \eta_{\text{TE}}(\lambda_{01})$ and $\eta^{(2)} = \eta_{\text{TE}}(\lambda_{02})$. As recalled from Chapter 3, the condition $\eta^{(1)} + \eta^{(2)} = 1$ corresponds to perfect splitting ratio antisymmetry and maximal P_S , while the difference $|\eta^{(1)} - \eta^{(2)}|$ indicates that the

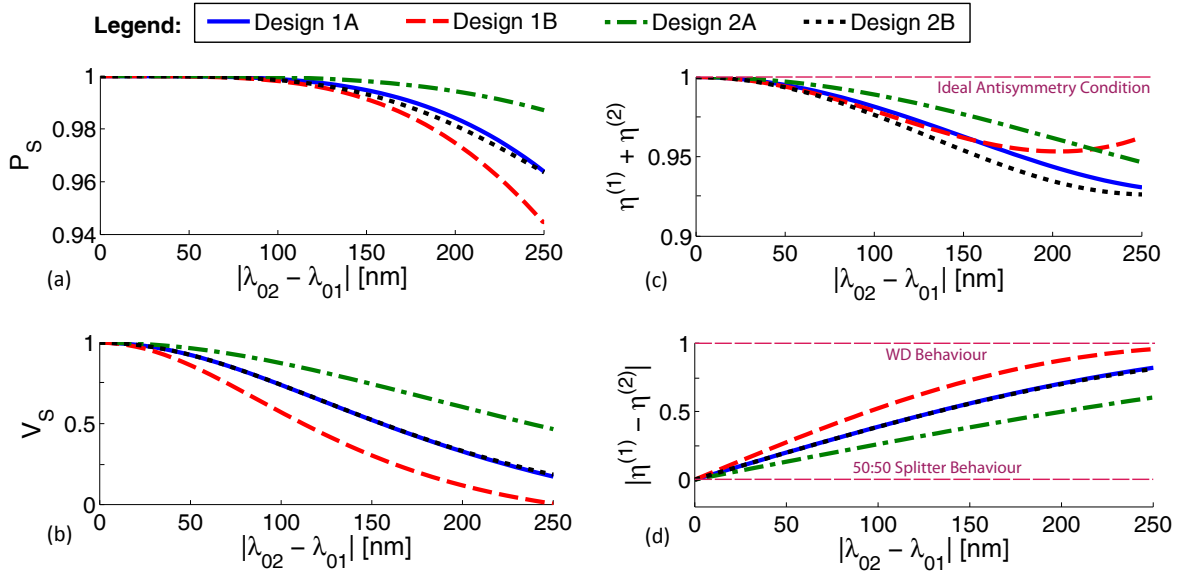


Figure 4.3: Calculated IFPS behaviour: (a)-(b) show the predicted separation probability and visibility; (c)-(d) show the sum and difference of the central-wavelength splitting ratios. States were co-polarized with equal photon bandwidths of $\Delta\lambda = 3$ nm and a pump bandwidth of $\Delta\lambda_P = 1$ nm.

coupler is operating as a 50:50 splitter for values near 0, or a wavelength demultiplexer (WD) for values near 1. The trajectories of the designs in $\eta^{(1)}, \eta^{(2)}$ parameter space have also been plotted in Figure 4.4, against the corresponding P_S and V_S behaviour (see Section 3.4.2 and Figure 3.9).

Up to 250 nm of central wavelength separation, high separation probabilities in excess of 94% were maintained by all four designs. Figure 4.3(b) and (d) show clearly that this occurs even as the coupler response to the quantum state changes from 50:50 splitting behaviour to WD behaviour. Recall that V_S decreases as WD behaviour is approached because non-classical contributions to P_S from quantum interference are gradually replaced by classical contributions from WD. The predicted V_S behaviour agrees with this assertion. The relative rate at which V_S decreases for each design matches well with the ranking of their first-order coupler dispersion M_{TE} at $\lambda_{deg} = 800$ nm (given in Table 4.3). The trajectory in Figure 4.4(c) is shown for the least and most linearly dispersive coupler designs, where the distance between steps increases with increasing M_{TE} , as would be expected.

Comments on Design Performance: Designs employing material B (AlGaAs) are seen to have consistently lower P_S values at high non-degeneracy compared to material A (silica). This is due to first and second order coupler dispersion being higher in the former than the latter. However, the performance difference in P_S is less than 5%. For the same material, coupler design 2 (ridge waveguides) presented higher P_S values than design 1 (wire waveguides), albeit the P_S performances also differed by less than 5%

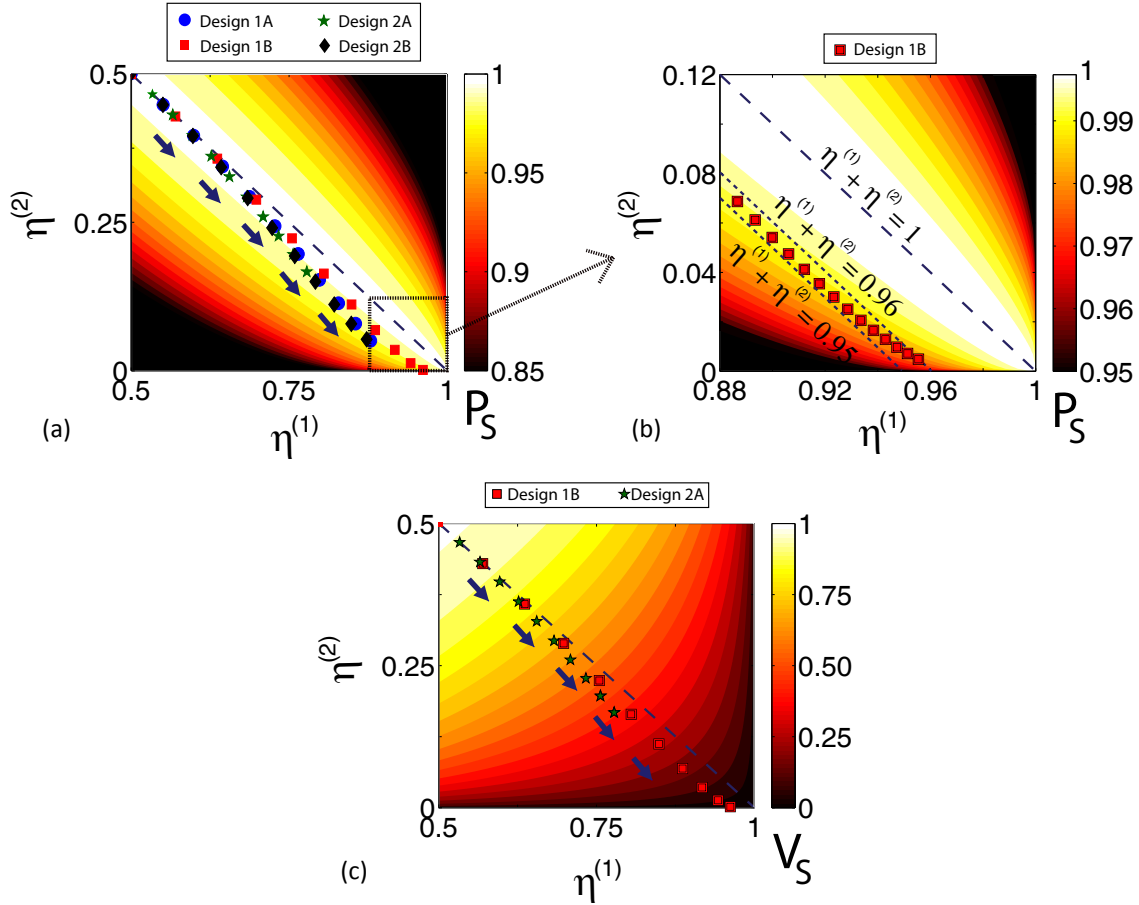


Figure 4.4: Select IFPS trajectories in $\eta^{(1)}, \eta^{(2)}$ space, showing the associated P_S and V_S behaviour. Each marker represents a $|\lambda_{02} - \lambda_{01}|$ step size of approximately 25 nm in (a) and (c), and 5 nm in (b). The diagonal lines in (a) and (c) represent the ideal antisymmetry condition $\eta^{(1)} + \eta^{(2)} = 1$. Contours of the splitting ratio difference $|\eta^{(1)} - \eta^{(2)}|$ are perpendicular to those of the sum $\eta^{(1)} + \eta^{(2)}$.

Sensitivity of P_S to Splitting Ratio Asymmetry: Notably, the design with the highest second-order coupler dispersion is not necessarily the worst-performing at $|\lambda_{02} - \lambda_{01}| = 250$ nm, even though larger $M_{TE}^{(2)}$ allows for greater deviation from the ideal $\eta^{(1)} + \eta^{(2)} = 1$ contour. For example, design 2B has the highest such dispersion ($M_{TE}^{(2)} = 6.798$), but design 1B (with $M_{TE}^{(2)} = 6.420$) exhibits the lowest P_S . Furthermore, this occurs even though design 1B is closer to the ideal splitting ratio symmetry than design 2B, as seen in Figure 4.3(c). The reason is that P_S becomes more sensitive to deviations from $\eta^{(1)} + \eta^{(2)} = 1$ when the coupler is behaving as a WD. As shown in the trajectory plots of Figures 4.4(a)-(b), the P_S contours curve towards the $\eta^{(1)} + \eta^{(2)} = 1$ line as $|\eta^{(1)} - \eta^{(2)}| \rightarrow 1$ (i.e. as WD operation is approached). Hence, the greatest sensitivity of P_S to splitting ratio asymmetry occurs at $|\eta^{(1)} - \eta^{(2)}| = 1$ (perfect WD behaviour), whereas $|\eta^{(1)} - \eta^{(2)}| = 0$ (perfect 50:50 splitter behaviour) has the least sensitivity. Since design 1B has the largest first-order dispersion, it approaches WD behaviour

more rapidly, which results in lower P_S values for any given value of $\eta^{(1)} + \eta^{(2)}$. Hence, low $M_{TE}^{(2)}$ cannot be treated as the sole comparative criteria for anticipating the relative P_S performance for a set of coupler designs; the linear dispersion M_{TE} can be equally important. Note also that this increase in sensitivity near WD operation explains why P_S for design 1B continues to decrease even though the splitting ratio symmetry improves beyond $\simeq 200$ nm of non-degeneracy: the P_S contours curve more rapidly towards $\eta^{(1)} + \eta^{(2)} = 1$ than the coupler's IFPS trajectory. This behaviour has been detailed in Figure 4.4(b).

Comparison to the Near-Degneracy Approximations: In Chapter 3, the general characteristics of IFPS were studied via a dimensionless model that made two key assumptions: linearity of $\kappa_\sigma(\lambda)$ near λ_{deg} , and equidistance in the central photon wavelengths from λ_{deg} . The latter has already been enforced, but it is of interest to see how well the linear approximation predicts the behaviour of the coupler designs studied here. Figure 4.5 gives the absolute difference between the P_S and V_S values calculated using the true coupler response, from those obtained after enforcing the near-degeneracy approximation (NDA) in its entirety. Calculated values at 250 nm of non-degeneracy are shown in Table 4.4. The discrepancy in P_S remains less than 1% for the first 150 nm of non-degeneracy, and at 250 nm the largest discrepancy is $\sim 5.5\%$. Differences in the calculated V_S are even lower, remaining below 1.5%. This demonstrates that, for many conventional coupler designs, the assumption of linear $\kappa_\sigma(\lambda)$ can remain quite accurate even at large non-degeneracies, permitting extrapolation of the generic dimensionless model for near-degeneracy IFPS developed in Chapter 3.

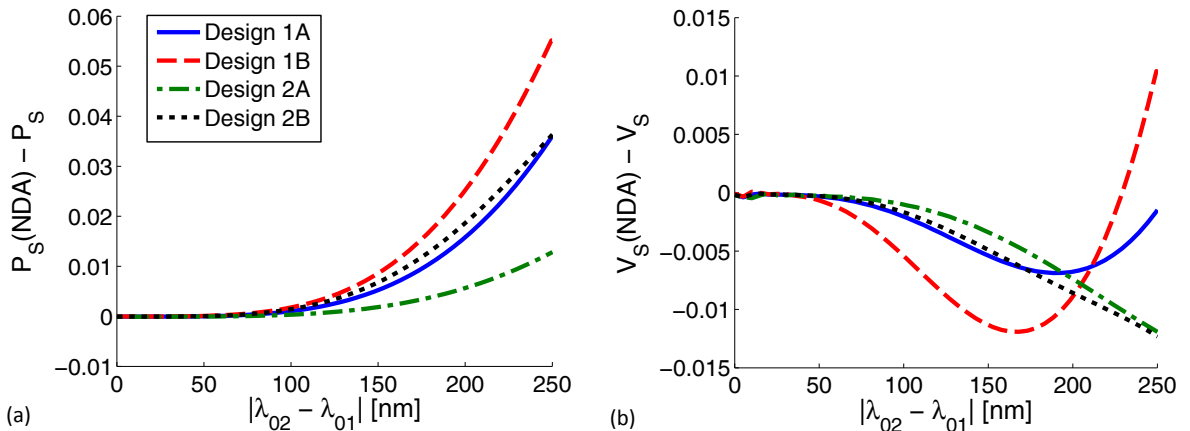


Figure 4.5: Absolute error between the near-degeneracy approximations (NDA) and the true coupler response for (a) P_S and (b) V_S . The near-degeneracy approximations remain accurate to within 1% for nearly 150 nm of non-degeneracy.

Table 4.4: Calculated IFPS Behaviour at $|\lambda_{02} - \lambda_{01}| = 250$ nm

Property	Design			
	1A	1B	2A	2B
$\Delta\xi_{\text{TE}}$	0	0	0	0
$M_{\text{TE}}\Lambda$	0.318π	0.442π	0.210π	0.317π
P_S	0.9639	0.9447	0.9871	0.9636
P_S (ND Approx)	1.0	1.0	1.0	1.0
V_S	0.1730	0.0063	0.4661	0.1853
V_S (ND Approx)	0.1715	0.0168	0.4542	0.1730

Variable Bandwidth

As discussed in Chapter 3, on-chip quantum interference experiments have typically restricted photon bandwidths to 3 nm or smaller; however, many sources can provide photon pairs with large bandwidths of hundreds of nm [76]. Hence, the IFPS bandwidth dependence for these designs is also investigated, and likewise compared to predictions made using the NDAs. The results are shown in Figure 4.6 for the best- and worst-performing designs, where $\Delta\lambda$ is the FWHM intensity bandwidths of the marginal photon spectra (made equal for both photons). The pump bandwidth was fixed at 1 nm, and the central wavelengths of the twin photons are kept at λ_{deg} . The asymmetry-mitigating effect of spectral

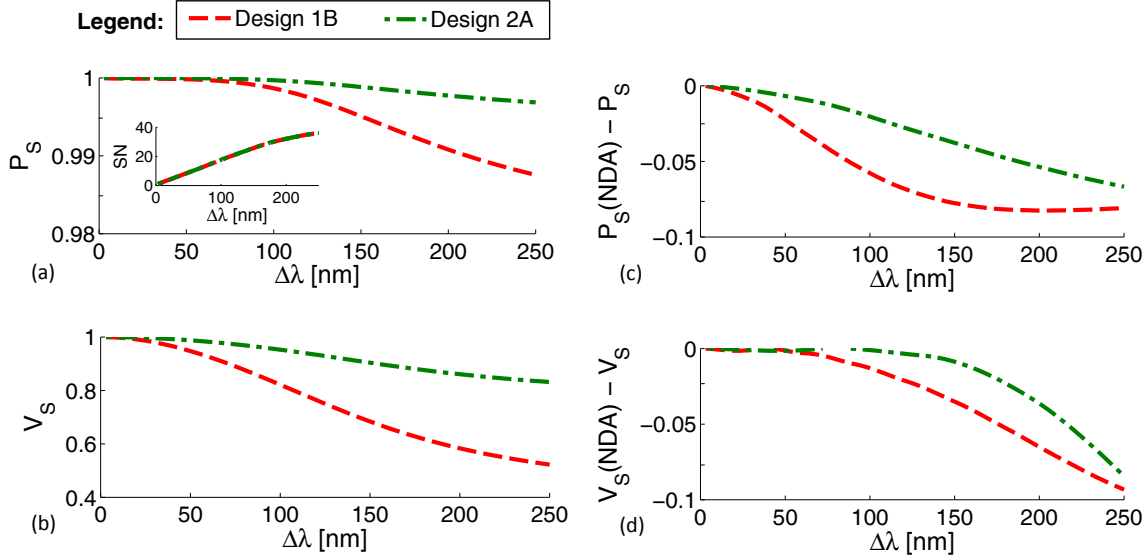


Figure 4.6: (a)-(b) Calculated IFPS bandwidth dependencies; (c)-(d) show the relative error of the NDA for comparison. The inset in (a) shows the Schmidt Number (SN) of the simulated state at each bandwidth.

entanglement results in higher values of P_S than those obtained during the $|\lambda_{02} - \lambda_{01}|$ sweeps. Note that the NDA results have a much larger discrepancy than in Figure 4.5, of up to $\sim 10\%$ at the highest

bandwidth values. The error remains less than 1% only for $\Delta\lambda \leq 40$ nm. While less accurate at large bandwidths, the near-degeneracy model nonetheless continues to provide a rough approximation of the IFPS behaviour.

4.1.3 Cross-Polarized State Performance

Finally, the cross-polarized state performance of each design is considered. This is examined for the special case of a maximally polarization-entangled state, where $\phi_{\alpha\beta}(\omega_1, \omega_2) = \phi_{\beta\alpha}(\omega_1, \omega_2)$, allowing the BPA to be calculated using Equation (3.36).

Performance at Degeneracy: Performance at the degeneracy point has been summarized in Table 4.5. All TE splitting ratios were 50:50 at $\lambda_{\text{deg}} = 800$ nm. Also shown are the predictions of Equation (3.40), based solely on the central wavelength splitting ratios. This approximation provides close agreement with the full IFPS calculations to within 0.1%. Note that despite a splitting ratio birefringence as high as $\eta_{\text{TE}} - \eta_{\text{TM}} = 0.10$ (for design 2A), separation fidelities remained above 99%. IFPS performance is thus highly resilient against birefringence when the coupler is near its 50:50 operating point, where non-classical contributions to P_S are largest. This can be contrasted against the more sensitive performance near WD operation. For a hypothetical birefringence of $\eta_{\text{TE}} - \eta_{\text{TM}} = 0.10$ with $\eta_{\text{TE}} = 0$, Equation (3.40) predicts a separation probability $P_S = 0.90$, which is roughly 9% lower than near the 50:50 operating point, and entirely classical in origin. The case where $\eta_{\text{TE}} = 0.5$ while $\eta_{\text{TM}} = 0$ or 1 gives $P_S = 0.50$, and is also an entirely classical result.

Table 4.5: Cross-Polarized Performance at Degeneracy ($\lambda_{\text{deg}} = 800$ nm)

Property	Design			
	1A	1B	2A	2B
η_{TM}	0.50	0.50	0.60	0.55
P_S (Full IFPS Calc)	0.9999	0.9999	0.9901	0.9976
P_S (Eq. 3.40 Approx)	1.0000	1.0000	0.9899	0.9975

Non-Degenerate Behaviour: Figure 4.7(a) shows the separation performance of each design plotted over a range of non-degeneracies. Designs 1A and 1B lacked coupler birefringence, and hence their cross-polarized state performance remains unchanged from the co-polarized performance studied in Section 4.1.2. Interestingly, in the birefringent designs 2A and 2B, P_S is seen to improve at certain non-degeneracies, relative to performance at degeneracy. Furthermore, at the highest plotted non-degeneracies, the calculated P_S values exceed those of the non-birefringent designs. This can be attributed to the non-equal coupler dispersions associated with each polarization, which cause the TE-TM splitting ratios to more closely approach the ideal anti-symmetry conditions with increasing $|\lambda_{02} - \lambda_{01}|$,

as seen in Figure 4.7(b). The cross-polarized V_S curves for these designs were nearly identical (within 5%) to their co-polarized counterparts shown earlier in Figure 4.3(b).

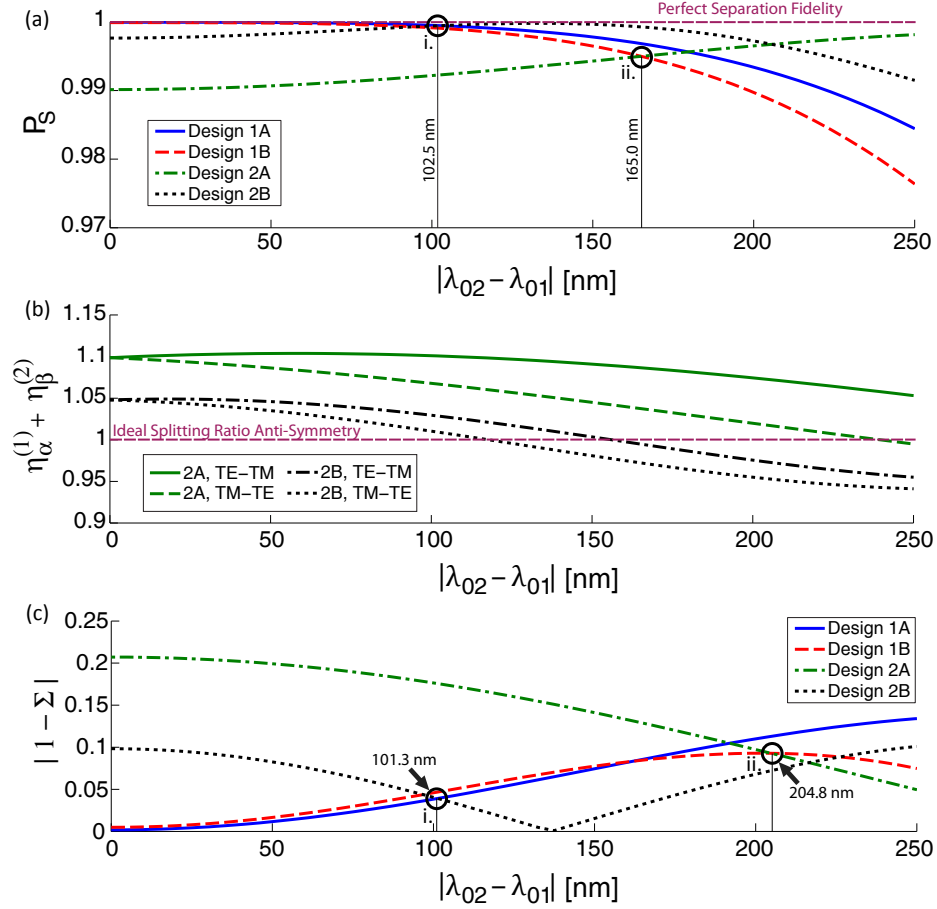


Figure 4.7: Calculated cross-polarized performance showing: (a) P_S behaviour; (b) TE-TM and TM-TE central wavelength splitting ratio sums for the birefringent designs; and (c) deviations from the ideal four-dimensional anti-symmetry contour. Points i. and ii. indicate crossovers between designs 1A and 2B, and designs 1B and 2A, respectively. The photons were maximally polarization-entangled and spectrally uncorrelated with 3 nm bandwidths.

Since there are now four distinct central wavelength splitting ratios to consider (i.e. $\eta_\sigma^{(j)}$ for permutations of $j \in \{1, 2\}$ and $\sigma \in \{\text{TE}, \text{TM}\}$), the two-dimensional contour $\eta^{(1)} + \eta^{(2)} = 1$ no longer suffices as the condition for maximal P_S . A four-dimensional analogue of this contour would be a useful metric for relating cross-polarized IFPS performance to the overall splitting ratio antisymmetry, and for qualitative comparison between designs. As shown in Appendix E, the ideal contour for maximally polarization-entangled states becomes $\Sigma = 1$ with Σ defined as

$$\Sigma = \frac{1}{2} [\eta_{\text{TE}}^{(1)} + \eta_{\text{TM}}^{(2)}]^2 + \frac{1}{2} [\eta_{\text{TM}}^{(1)} + \eta_{\text{TE}}^{(2)}]^2. \quad (4.2)$$

Absolute deviations from the ideal contour, given by $|\Sigma - 1|$, have been plotted in Figure 4.7(c). This metric is now used to compare some of the P_S crossover points seen in Figure 4.7(a). Designs 1A and 2B are examined first, since these exhibited nearly identical V_S curves, and therefore have similar P_S sensitivities to splitting ratio asymmetry at each non-degeneracy. Equal P_S values are obtained at approximately $|\lambda_{02} - \lambda_{01}| = 102.5$ nm, which compares well with the $|\Sigma - 1|$ crossover point at $|\lambda_{02} - \lambda_{01}| = 101.3$ nm. Designs 1B and 2A are examined next, since these had the most dissimilar V_S curves. In this case, the P_S crossover occurs at $|\lambda_{02} - \lambda_{01}| = 165.0$ nm, while the $|\Sigma - 1|$ cross-over is at $|\lambda_{02} - \lambda_{01}| = 204.8$ nm. Nonetheless, $|\Sigma - 1|$ does predict that design 2A eventually overtakes 1B in P_S performance. Hence, as was the case with co-polarized states, strict quantitative comparisons using the ideal anti-symmetry contour require similar V_S behaviour, albeit qualitative comparisons still offer a useful guide.

Remarks on Mitigating Birefringence: In principle, severe cases of coupling birefringence could be mitigated through judicious choice of the coupling length L . For a given wavelength, the TE and TM splitting ratios acquire equal values for a beat-length of $L = m\pi/|\kappa_{TE} - \kappa_{TM}|$, where m is an integer. However, the necessary interaction lengths are generally not practical — for example, the η_{TE}, η_{TM} beat length of design 2A at degeneracy is 15.56 mm. One might also consider the changes to η_{TM} when the interaction length is increased by an odd-integer multiple. For design 2A, the splitting ratio acquires the degeneracy values $\eta_{TM} = [0.60, 0.22, 0.91, 0.01, 0.99, 0.10]$ for lengths $L = [1, 3, 5, 7, 9, 11] \times L_0$, none of which improve upon the original birefringence (η_{TE} remains unchanged). Birefringence is therefore best mitigated through the design of the waveguide geometry itself, e.g. by employing vertical-horizontal symmetry as in architecture 1.

4.1.4 Summary and Closing Remarks

The theoretical IFPS performance of several hypothetical straight-waveguide directional couplers was investigated. Several notable observations were made:

- (i) Wire and ridge waveguide architectures provide similar co-polarized IFPS performance (to within 5%), with neither architecture presenting a fundamental advantage. The main distinction in their characteristics is the coupler birefringence resulting from horizontal-vertical asymmetry in the ridge structure.
- (ii) High material dispersion does not necessarily translate into high coupler dispersion and degraded P_S performance. The material systems studied differed in $dn/d\lambda$ by a factor of 35.7, but differences in M and $M^{(2)}$ were less than a factor of 1.75 and 2.5, respectively.

- (iii) The NDAs can provide reasonable estimations of IFPS performance at large non-degeneracies even when the assumptions of linear $\kappa_\sigma(\lambda)$ are relaxed. Predicted dependencies on $|\lambda_{02} - \lambda_{01}|$ showed less than 5% discrepancy from calculations using the true coupler response, for non-degeneracies of up to 250 nm. Bandwidth dependencies were predicted with less than 10% discrepancy for up to $\Delta\lambda = 250$ nm.
- (iv) The probability P_S is less sensitive to splitting ratio asymmetries when the separation mechanism is non-classical (i.e. when the coupler behaves as a 50:50 splitter). Regimes of classical operation (i.e. WD coupler behaviour) produce comparatively lower values of P_S for any given value of $\eta^{(1)} + \eta^{(2)} \neq 1$. Hence, when higher-order coupler dispersion is present, linear coupler dispersion also becomes an important factor influencing P_S performance, since it dictates the non-degeneracies for which the coupler exhibits WD behaviour.
- (v) IFPS remains remarkably robust to coupler birefringence in the non-classical operating regime. For a splitting ratio difference of $|\eta_{TE}(\lambda_{deg}) - \eta_{TM}(\lambda_{deg})| = 10\%$, the separation probability P_S is still 99%.
- (vi) For cross-polarized states and birefringent couplers, differences in coupler dispersion between polarizations can cause P_S to improve at higher non-degeneracies, compared to degenerate performance.

In addition to the above, a new metric was introduced in Equation 4.2 for quantifying the splitting ratio asymmetry when the photons are cross-polarized and maximally polarization-entangled. This metric accurately predicted the relative P_S performance for two designs (1A and 2B) with similar V_S behaviour.

Notably, all physical designs considered in this section performed well ($P_S \geq 94\%$) over the investigated parameter space. This parameter space was ultimately limited by the single-mode waveguide requirement and field leakage occurring at higher wavelengths. Single-mode requirements, as well as the balance between field coupling and leakage, may in fact be the limiting factors in implementing IFPS at large non-degeneracies with directional couplers. Higher order coupler dispersion did not pose a significant problem for these designs. Although the straight-waveguide couplers studied here were based on common implementations, other designs wherein the waveguides are tapered or asymmetric along the propagation direction are also possible [125]. These present greater diversity in their coupler response, and may provide interesting environments for IFPS or related state engineering that pivots on such dispersion.

4.2 State Asymmetry

In the previous section, degradation to P_S was caused by asymmetries arising from higher-order coupler dispersion, while the quantum state was assumed to be perfectly symmetric about λ_{deg} . This brief section explores the consequences of introducing asymmetry in the central wavelengths of the quantum state itself, while assuming linear coupler characteristics. This effectively relaxes the second of the near-degeneracy assumptions. Such asymmetry is normally present at large non-degeneracies due to energy and momentum conservation in the photon pair generation process, the details of which are covered in Chapter 5.1.

As an example, consider the tuning characteristics of the photon pair source designed in Chapter 5, where the theoretical values of λ_{01} and λ_{02} relative to λ_{deg} for a given non-degeneracy are shown in Figure 5.3. The detuning of λ_{01} and λ_{02} from λ_{deg} will be calculated from the same characteristics, but with the absolute values of the propagation constants adjusted so that the degeneracy point is at exactly 1550 nm. The directional coupler is given the dispersion characteristics $M = 19.48$ and $M^{(2)} = 0$ at $\lambda_{\text{deg}} = 1550$ nm. This choice of linear dispersion gives a splitting ratio oscillation period of $T_\lambda = 250$ nm, so that all possible values of the $\eta(\lambda)$ response are sampled over the plotted range of non-degeneracies seen in Figure 4.8. The lack of higher-order coupler dispersion ensures that deviation from the ideal P_S results only from the state asymmetry.

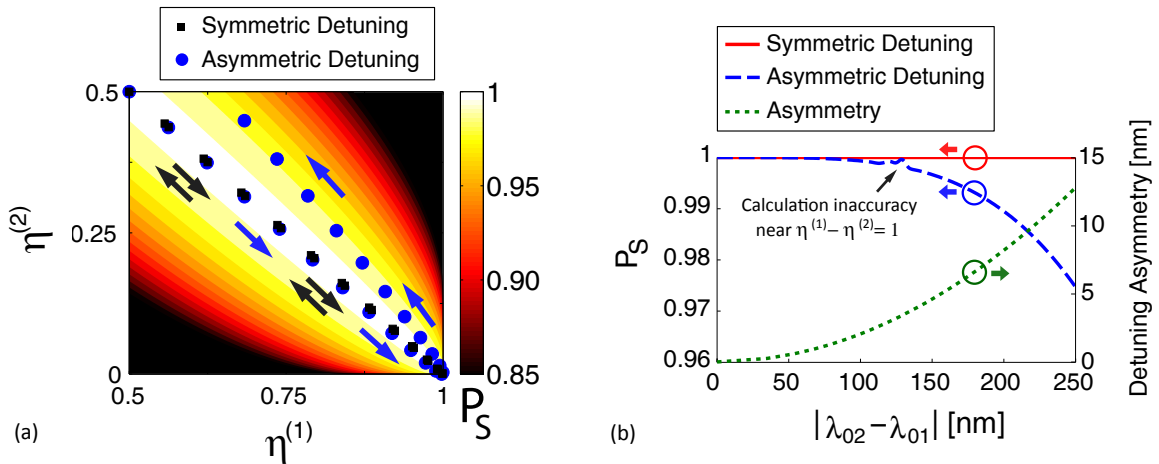


Figure 4.8: IFPS with symmetric versus asymmetric central wavelength tuning, assuming linear coupler dispersion: (a) splitting ratio trajectories, shown in non-degeneracy steps of ~ 10 nm; (b) P_S performance and detuning asymmetry. The calculation inaccuracy near $|\lambda_{02} - \lambda_{01}| = 125$ nm is due to high sensitivities occurring when the coupler behaves as a nearly-perfect WD. Computed for spectrally-uncorrelated photons with equal bandwidths of $\Delta\lambda = 3$ nm.

Figures 4.8(a) and 4.8(b) respectively show the central wavelength splitting ratio trajectories and the P_S performance calculated with an ideal symmetric state (i.e. equidistance of λ_{01} and λ_{02} from

λ_{deg}) compared to a realistic asymmetric state following the aforementioned tuning characteristics. The former maintains perfect deterministic separation with $P_S = 1$, while the latter sees this decrease to $P_S = 0.9751$ at 250 nm of non-degeneracy, where the detuning asymmetry attains a value of $|\lambda_{02} - \lambda_{\text{deg}}| - |\lambda_{01} - \lambda_{\text{deg}}| = 12.6$ nm.

This example highlights two assertions. First, the central wavelength asymmetries relative to λ_{deg} produces consequences qualitatively similar to those of higher-order coupler dispersion. Secondly, even when the state symmetry assumption is supplanted with realistic tuning characteristics, high separation fidelities (>95%) can nonetheless be maintained at large non-degeneracies. This last point also reaffirms the ability of the near-degeneracy assumptions provide reasonable approximations at large non-degeneracies.

4.3 Active Coupler Tuning

Discussions up to this point have focused on fixed coupler characteristics. This section provides a first look at the opportunities afforded by tuning the directional coupler characteristics in-situ. As will be shown, active coupler tuning can mitigate non-idealities in IFPS performance, and allow the $\eta^{(1)}, \eta^{(2)}$ trajectories to be dynamically modified. Previous explorations of in-situ quantum circuit tuning have been implemented through control of the relative path phase θ [4, 81, 83, 101], but never by tuning the properties of the coupler itself.

The most basic means of adjusting the coupler characteristics is to systematically offset the coupling strength $\kappa(\lambda)$ by an amount $\Delta\kappa$, thereby altering $\eta(\lambda_{\text{deg}})$. For a dispersive coupler, this also shifts the wavelength at which 50:50 splitting occurs. The coupling strength can be offset by modifying the core-cladding index contrast, to either increase or decrease the mode confinement, which in turn alters the extent of evanescent overlap between the waveguides. Two methods of achieving this are illustrated in Figure 4.9. The first exploits the temperature-dependence of the material refractive indices, using resistive heaters to raise the temperature of the waveguide cores relative to the cladding (or air gap) between the coupled waveguides. The second pivots on the amenability of certain materials to the electro-optic effect [126], whereby an applied DC electric field results in a refractive index change. Coupling is tuned by changing the applied voltage. In what follows, it is assumed the refractive index changes are applied symmetrically to both waveguides, so that no modal mismatch develops.

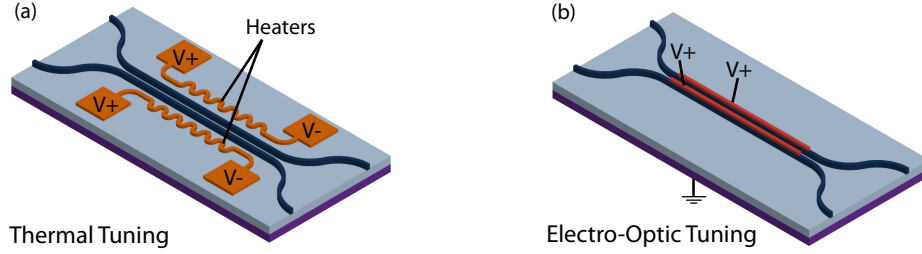


Figure 4.9: Two well-known methods for tuning the coupling strength in-situ: (a) thermally induced and (b) electro-optically induced changes to the core-cladding index contrast. Index changes are assumed to be identical for both waveguides so that modal mismatch remains negligible.

4.3.1 Mitigating Asymmetries

The effect of coupler tuning was briefly examined in Chapter 3, but in the context of a fixed dimensionless detuning $\Delta\xi$ from the ideal 50:50 splitting condition at λ_{deg} . This is related to a systematic change in coupling strength by $\Delta\xi = L\Delta\kappa$, where L is the coupling length, and $\Delta\kappa$ is assumed to be uniform across all wavelengths. Under the near-degeneracy approximations, P_S was maximal and independent of the non-degeneracy when $\Delta\xi = 0$. An obvious practical advantage of in-situ coupler tuning is that unintentional cases of $\Delta\xi \neq 0$ arising from fabrication error can be corrected. However, more interestingly, non-zero $\Delta\xi$ can be used to restore conditions of splitting ratio anti-symmetry (i.e. $\eta^{(1)} + \eta^{(2)} = 1$) and thereby maximal P_S in situations where higher-order coupler dispersion or central-wavelength state asymmetry are present.

Consider a highly dispersive directional coupler of length $L = 2$ mm having $M = 50$ and $M^{(2)} = 300$, far exceeding the levels of coupler dispersion studied in previous examples. The coupling strength of this device is depicted in Figure 4.10(a), together with the corresponding $\eta(\lambda)$. The splitting ratio

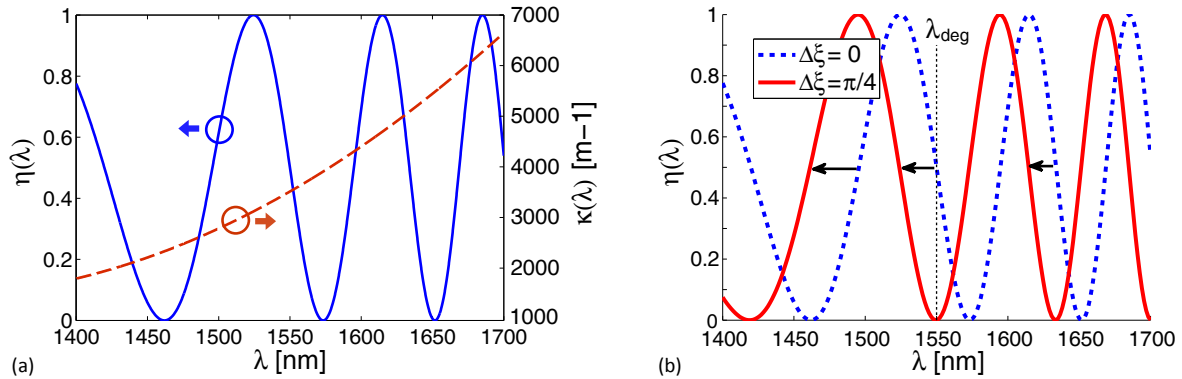


Figure 4.10: (a) Coupling characteristics used in the example, with $M = 50$ and $M^{(2)} = 300$. (b) Systematic offsets to the coupling strength cause shifts in the $\eta(\lambda)$ response function, as shown.

is highly chirped in wavelength, with detrimental implications for successful pair separation. Suppose, however, that active tuning of the coupling strength $\kappa(\lambda)$ is possible, allowing $\Delta\xi$ to be varied as desired. Changes to $\Delta\xi$ cause $\eta(\lambda)$ to shift in wavelength, as shown in Figure 4.10(b). The IFPS performance of this coupler with and without active tuning will now be examined.

Figure 4.11 shows the IFPS separation performance and splitting ratio trajectories for a co-polarized state without coupler tuning ($\Delta\xi = 0$). The degeneracy point is taken to be $\lambda_{\text{deg}} = 1550$ nm, with the coupling length L chosen such that $\eta(\lambda_{\text{deg}}) = 0.5$. Equal central wavelength separation from λ_{deg} is assumed for convenience, but could also be considered in an equivalent manner as the $\eta(\lambda)$ chirping. Without coupler tuning, the separation probability P_S for this coupler reaches a minimum of less than 10% near 200 nm of non-degeneracy. To investigate if active coupler tuning could improve upon this, IFPS performance was then recalculated as a function of both $|\lambda_{02} - \lambda_{01}|$ and $\Delta\xi \in [-\pi/2, \pi/2]$. The value of $\Delta\xi$ for optimal P_S at each non-degeneracy was identified.

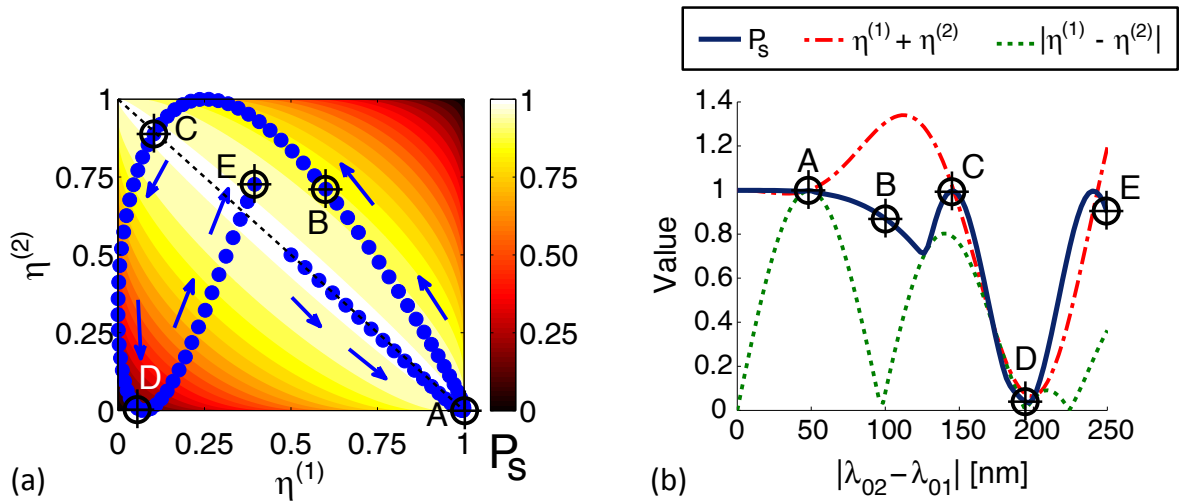


Figure 4.11: (a) Splitting ratio trajectories and (b) IFPS performance of the non-linearly dispersive coupler without active coupler tuning. Photon and pump bandwidths were $\Delta\lambda = 3$ nm and $\Delta\lambda_P = 1$ nm respectively. The trajectory in (a) is plotted with a 2.5 nm non-degeneracy step size; select operating points have been tagged by the letters A through E.

Figures 4.12(a)-(b) show that near-perfect separation fidelities and splitting ratio anti-symmetry can be restored through optimal choice of $\Delta\xi$. Coupler tuning corresponded to a continuous transition of the 50:50 split point from 1550 nm to 1582 nm. The small deviations from the $\eta^{(1)} + \eta^{(2)} = 1$ contour result from the finite resolution of the $\Delta\xi$ sweep, which used a step size of $\sim \pi/160$. Figures 4.12(c)-(d) show the corresponding values of optimal $\Delta\xi$ used to plot (a)-(b), as a trajectory relative to the global P_S and V_S dependencies. These contour plots possess similar features as those produced under the near-degeneracy approximations in Chapter 3 (see Figure 3.3), but are skewed as a result of the second-order

coupler dispersion. Note that more than one optimal $\Delta\xi$ path is possible because of the approximate periodicity.

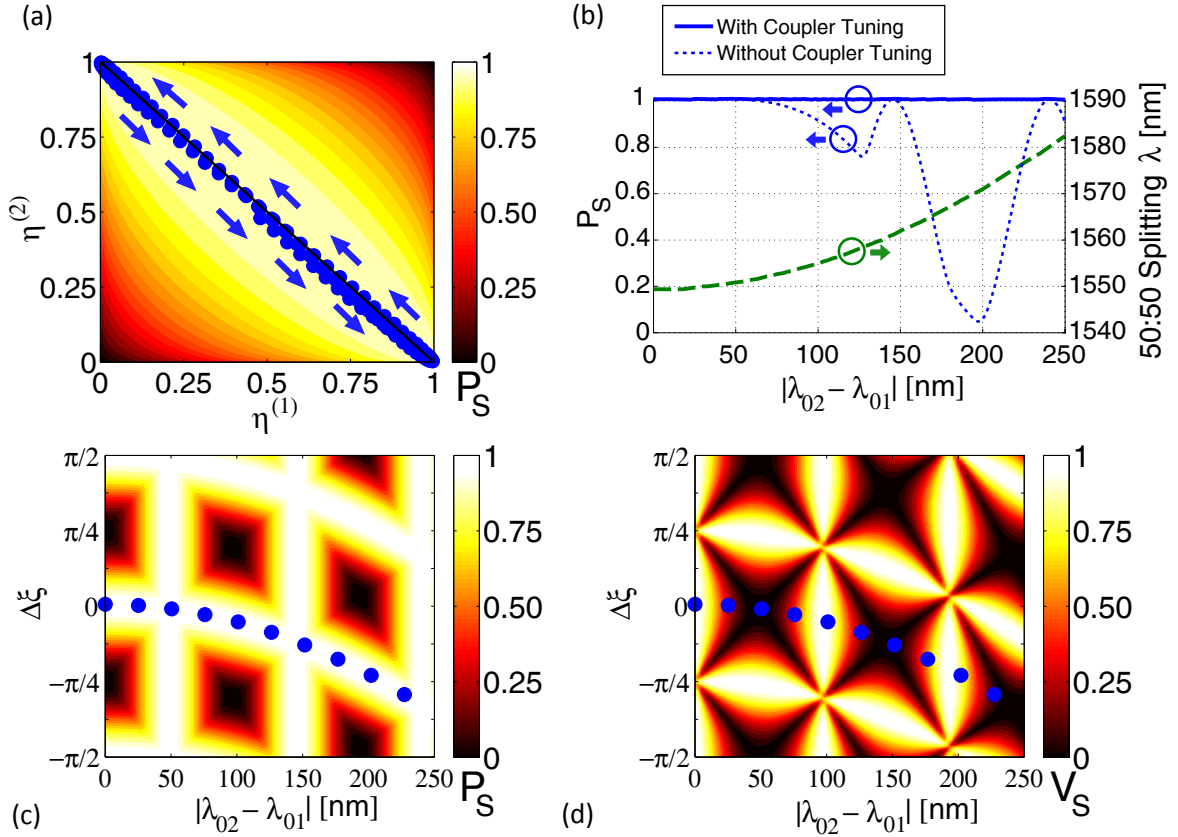


Figure 4.12: Performance with active coupler tuning: (a) shows the new splitting ratio trajectory (2.5 nm step size); (b) indicates improvements to the separation probability through optimal selection of $\Delta\xi$, and tracks corresponding changes to the 50:50 splitting wavelength; (c) and (d) show the trajectory of the $\Delta\xi$ tuning relative to the global P_S and V_S behaviour (25 nm step size in non-degeneracy).

It has thus been shown that active coupler tuning can restore near-perfect separation fidelities in the presence of higher-order coupler dispersion. Coupler tuning can similarly mitigate the effects of asymmetric central wavelength separations. For example, in the case of a perfectly linear $\kappa(\lambda)$, P_S is maximized by tuning the 50:50 splitting wavelength to bisect the central wavelength separation (i.e. $\lambda_{50:50} \rightarrow [\lambda_{01} + \lambda_{02}]/2$), which restores the splitting ratio anti-symmetry. Hence, active coupler tuning offers a simple yet effective means of addressing deviations from ideal performance at large non-degeneracies.

4.3.2 Trajectory Control

Active coupler tuning can also be utilized to operate at a different point in the $\eta^{(1)}, \eta^{(2)}$ space – for example, away from conditions of splitting ratio anti-symmetry. As such, coupler tuning provides a tool for quantum state engineering, to create arbitrary superpositions of the bunched and anti-bunched outcomes with arbitrary visibilities. In addition, with only one photon pair source at the input, this could be used to modify the Schmidt number of the post-selected output state as discussed in Chapter 3.5. It is therefore useful to understand how $\Delta\xi$ can be used to navigate the $\eta^{(1)}, \eta^{(2)}$ space. Figure 4.13(a) shows several trajectories at various non-degeneracy values for the coupler examined in Figure 4.11. Each trajectory corresponds to $\Delta\xi$ increasing from 0 to $\pi/4$ in steps of $\pi/40$. The directions and general behaviours of these trajectories can be related to the global behaviour of P_S and V_S shown in Figures 4.13(b)-(c), as will now be discussed. Trajectory evolution will be described in terms of two orthogonal axes corresponding to the diagonals of the $\eta^{(1)}, \eta^{(2)}$ space, i.e. (\swarrow , \nearrow) and (\nwarrow , \searrow), which describe contours of the sum $\eta^{(1)} + \eta^{(2)}$ and the difference $\eta^{(1)} - \eta^{(2)}$ respectively.

First consider the trajectory behaviour at non-degeneracies of 100 nm and 200 nm, where the evolution is primarily in the \nearrow and \swarrow directions. The direction of evolution is determined largely by ‘domains’ in the global V_S behaviour, as indicated in Figure 4.13(b). The ‘domain’ boundaries correspond to the minima of V_S along the $|\lambda_{02} - \lambda_{01}|$ axis, and the maxima of V_S along the $\Delta\xi$ axis. Following the line $|\lambda_{02} - \lambda_{01}| = 100$ nm in this figure, increasing $\Delta\xi$ from zero causes the trajectory’s $\eta^{(1)}, \eta^{(2)}$ coordinate to move in the \nearrow direction until the domain boundary is crossed near $3\pi/16$, where the direction reverses to \swarrow . Similarly, the trajectory at $|\lambda_{02} - \lambda_{01}| = 200$ nm begins in the \swarrow direction but then reverses to \nearrow near $3\pi/80$.

Next consider trajectory evolution in the directions \nwarrow and \searrow . Such behaviour is exhibited with increasing $\Delta\xi$ at non-degeneracies of 50 nm and 150 nm. Movement in these directions are special cases occurring when the global behaviour of P_S follows a contour aligned with the $\Delta\xi$ -axis. Such contours appear at periodic intervals as seen in Figure 4.13(c), but can be skewed by higher-order coupler dispersion. The contours around each local maximum of P_S are associated with a particular trajectory direction, which alternates every period. Hence, at 50 nm of non-degeneracy, the trajectory moves in the \nwarrow direction, whereas at 150 nm (falling within the adjacent period) movement is in the \searrow direction. Note that the $\Delta\xi$ -axis does not align with P_S contours at the non-degeneracies of 100 nm nor 200 nm, where evolution was instead observed in the \nearrow and \swarrow directions. Although not shown within the plotted range, the trajectory directions in Figure 4.13(c) also undergo periodic reversal as a function of $\Delta\xi$, at intervals of approximately $\pi/4 + m\pi/2$, where m is an integer.

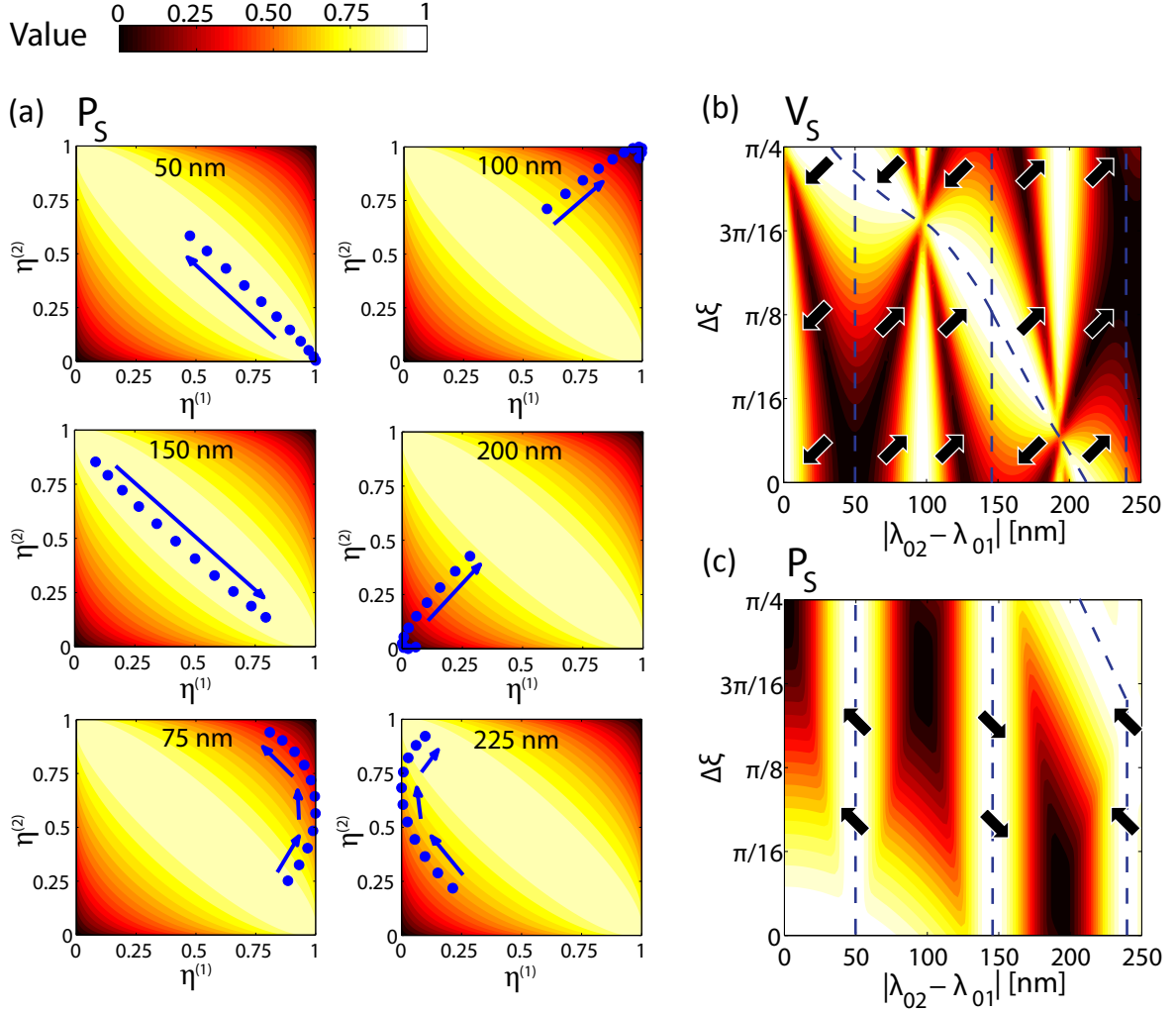


Figure 4.13: Trajectory evolution for the coupler described by Fig. 4.10, showing: (a) sample trajectories at various non-degeneracy values, as $\Delta\xi$ increases from 0 to $\pi/4$ in steps of $\pi/40$; (b) relation between global V_S behaviour and the direction of motion along \nearrow or \nwarrow ; (c) relation between global P_S behaviour and the direction of motion along \swarrow or \searrow , which overrides motion along the orthogonal axis when $\Delta\xi$ follows contours of P_S .

Finally, examples of evolution along both trajectory axes are described. At 75 nm non-degeneracy, as $\Delta\xi$ is first increased from 0, the P_S contours are not aligned with the $\Delta\xi$ -axis, and hence the trajectory evolution is in the \nearrow direction as per the local domain in V_S . However, in the vicinity of $\Delta\xi = \pi/8$, the P_S contours do become aligned with the $\Delta\xi$ -axis, and motion in the \swarrow direction results. On the other hand, at 225 nm of nondegeneracy, the P_S contour alignment already exists at $\Delta\xi = 0$, and motion begins in the \swarrow direction. However, near $3\pi/16$, the skewing of P_S abruptly misaligns the contours with respect to the $\Delta\xi$ -axis, and the local V_S then determines that the \nearrow direction ensues.

The above provides a framework for intuitively predicting $\Delta\xi$ -dependent trajectory evolution from the global P_S and V_S behaviour. Other means of tailoring the trajectories are also possible. For example,

active tuning of the photon pair source can systematically shift λ_{deg} with respect to the coupler's 50:50 splitting wavelength. This has a similar effect as tuning $\Delta\xi$. Narrow-bandwidth photons, such as those required for quantum memories [127], may also present opportunities for modulating the coupler response within the photon coherence time.

4.4 Conclusions

This chapter provided specific examples of IFPS performance in a variety of scenarios. First, directional coupler designs using common waveguide architectures and material systems were explored under assumptions of central wavelength equidistance from degeneracy (i.e. state symmetry). Secondly, the impact of asymmetric central wavelength tuning was investigated. Finally, active coupler tuning was proposed and investigated as an effective means of restoring near-unity P_S in the presence of coupler and state asymmetries.

The results reaffirmed the generalized formulation of Chapter 3 while providing further insight about the sensitivity of separation performance to coupler birefringence and higher-order dispersion. For the same degree of splitting ratio asymmetry, the non-classical IFPS regime near 50:50 coupler operation exhibited greater immunity against these non-idealities than the classical regime near WD operation. Extrapolation of the near-degeneracy assumptions was found to reasonably approximate the true IFPS behaviour. Limitations to IFPS in conventional directional coupler designs will likely come from single-mode requirements rather than from coupler dispersion.

Chapter 5

Design of Integrated Devices for IFPS Experiments

Experimentally testing the key predictions of Chapter 3 requires a highly-tunable photon pair source having two coherent indistinguishable paths, and an integrated directional coupler exhibiting large splitting ratio dispersion. The present chapter highlights the design of these devices. The dual-path photon pair source will be designed in an AlGaAs Bragg reflection waveguide (BRW) architecture. This represents a novel effort because BRWs have not been previously used to directly generate path-entangled states nor to construct integrated quantum circuits involving passive optical components. Due to architecture-specific challenges such as high propagation losses, the presence of higher-order lateral modes, and sensitive lateral mode confinement, the design considerations involved differ significantly from those of silicon wires and other implementations. Establishing IFPS as a viable capability for the BRW architecture is itself a worthy pursuit, given the ability of BRWs to be monolithically integrated with a pump laser and provide highly-tunable quantum states [11, 72, 77]. For the directional coupler design, the objective is to obtain a large enough dispersion that all possible values of the anti-bunched visibility V_S can be visited within the non-degeneracy limitations of the photon pair source. This coupler will be implemented in the silicon oxynitride (SiON) material system for practical reasons described later.

5.1 Dual-Path BRW Photon Pair Source

This section describes the design of a novel BRW-based source that generates photon pairs in the path-entangled state $|\Psi\rangle = [|\psi\rangle_A|0\rangle_B + |0\rangle_A|\psi\rangle_B]/\sqrt{2}$ required for subsequent IFPS. An existing BRW

vertical structure will serve as the basis of the design, but will require judicious tailoring of its horizontal structure, including the design of passive optical devices, to fulfil its intended purpose. Focus will be given to co-polarized pair generation, although cross-polarized generation can also be supported by BRWs. Before discussing the design, a brief review of pair production in BRWs is necessary.

5.1.1 Background: Phase-Matching in BRWs

Photon pairs in BRWs are created through a second-order nonlinear process known as spontaneous parametric downconversion (SPDC). In SPDC, the optical nonlinearity mediates the conversion of a pump photon at frequency ω_p into two lower-energy photons at frequencies ω_1 and ω_2 . This process occurs over a finite interaction length and can be analyzed in terms of coupled-wave equations [10], similar to the formalism used to describe directional couplers in Chapter 2. The corresponding interaction Hamiltonian is given by [61]

$$\hat{H} = \sum_{\alpha\beta\gamma} \int d\omega_1 d\omega_2 d\omega_p S_{\alpha\beta\gamma}(\omega_1, \omega_1, \omega_p) \hat{a}_{\alpha}^{d1\dagger}(\omega_1) \hat{a}_{\beta}^{d2\dagger}(\omega_2) \hat{a}_{\gamma}^p(\omega_p) + \text{H.c.}, \quad (5.1)$$

where p and γ denote the guided mode and polarization of the pump photon respectively, while $\alpha(\beta)$ and $d1(d2)$ denote those of the downconverted photons. For SPDC to be efficient, i.e. have a non-vanishing $S_{\alpha\beta\gamma}(\omega_1, \omega_1, \omega_p)$, it can be shown that the phase evolution of the interacting fields must allow the amplitudes of the generated photons to sum constructively over the interaction length. This requires the propagation constants of the pump and downconverted photons to obey $k_{\gamma,p}(\omega_p) = k_{\alpha,d1}(\omega_1) + k_{\beta,d2}(\omega_2)$, which is known as the phase-matching (PM) condition. The propagation constants have been written as ‘ k ’ rather than the usual ‘ β ’ to avoid confusion with the polarization subscripts. For a rectangular nonlinear waveguide of length ℓ , the resultant biphoton amplitude $\phi_{\alpha\beta}(\omega_1, \omega_2)$ acquires the proportionality [5, 61]

$$\phi_{\alpha\beta}(\omega_1, \omega_2) \propto \phi_P(\omega_p) \text{sinc}(\Delta k \ell / 2), \quad (5.2)$$

where $\phi_P(\omega)$ is the pump spectrum, $\omega_p = \omega_1 + \omega_2$, and Δk is the phase mismatch, defined as

$$\Delta k = k_{\gamma,p}(\omega_p) - k_{\alpha,d1}(\omega_1) - k_{\beta,d2}(\omega_2). \quad (5.3)$$

Hence, Δk restricts the frequencies and polarizations for which photon pair production will be significant. Pair generation rates generally increase with ℓ but are eventually limited by corresponding increases in propagation loss. Since the propagation constants are typically on the order of $\sim 10^6$ and are subject to

material and waveguide dispersion as well as birefringence, the $\text{sinc}(\Delta k\ell/2)$ term is only non-vanishing for a small subset of the total parameter space. Achieving PM in a nonlinear waveguide for a desired set of frequencies and polarizations therefore requires deliberate engineering of the modal properties, which can be achieved through careful selection of the waveguide material and geometric parameters. It is often convenient to re-express the phase mismatch in terms of the modal effective indices as

$$\Delta k = 2\pi \left[\frac{n_{\text{eff}}^{\gamma,p}(\omega_p)}{\lambda_p} - \frac{n_{\text{eff}}^{\alpha,d1}(\omega_1)}{\lambda_1} - \frac{n_{\text{eff}}^{\beta,d2}(\omega_2)}{\lambda_2} \right]. \quad (5.4)$$

This can help elucidate some of the challenges of phase matching. Suppose the objective is to produce co-polarized degenerate photon pairs at $\lambda_{\text{deg}} = 1550$ nm, both within the fundamental TIR-guided mode (d). Energy conservation requires the pump wavelength to be 775 nm, which simplifies the PM condition to $n_{\text{eff}}^{\gamma,p}(\lambda_{\text{deg}}/2) = n_{\text{eff}}^{\alpha,d}(\lambda_{\text{deg}})$. Satisfying this condition in conventional nonlinear waveguides can be difficult, especially when one of the wavelengths is close to a material resonance. For example, aluminium gallium arsenide (AlGaAs) exhibits a high intrinsic nonlinearity, but has a bandgap in the vicinity of 775 nm that causes $n_{\text{eff}}^{\gamma,p}(\lambda_{\text{deg}}/2)$ to be significantly higher than $n_{\text{eff}}^{\alpha,d}(\lambda_{\text{deg}})$. The value of $n_{\text{eff}}^{\gamma,p}(\lambda_{\text{deg}}/2)$ can be lowered by pumping from a higher-order (i.e. less-confined) mode, but such modes are difficult to populate selectively and have poorer overlap with the downconverted photon modes, which can make the process less efficient by orders of magnitude. Other methods such as quasi-phase matching [128, 129] can compensate for the effective index difference, but these too are inefficient.

Bragg reflection waveguides (BRWs) present an alternative approach, wherein the pump is guided not by total internal reflection, but by the photonic bandgap effect [130]. Such modes are called Bragg modes, and unlike TIR modes, their effective indices are not bounded by the core and cladding refractive indices, and can in fact be lower than any material index within the waveguide structure [124, 131]. BRWs therefore offer a viable route for achieving perfect phase matching when it is difficult to satisfy PM with TIR modes alone, and can indeed obtain $n_{\text{eff}}^{\gamma,p}(\lambda_{\text{deg}}/2) = n_{\text{eff}}^{\alpha,d}(\lambda_{\text{deg}})$ for efficient degenerate SPDC in AlGaAs at 1550 nm. Figure 5.1 illustrates an existing $\text{Al}_x\text{Ga}_{1-x}\text{As}$ BRW structure that was designed for PM at this wavelength [9]. The material index of each layer can be tuned by changing the aluminum molar fraction x . A one-dimensional photonic bandgap is achieved in the vertical direction by surrounding the waveguide core with Bragg reflectors, formed from periodic layers of alternating material index. This periodic variation gives rise to an optical stopband that forms bound modes between the reflectors. When the Bragg reflectors satisfy the quarter-wave (QtW) condition [132], the fundamental Bragg mode is maximally confined, and its modal effective index depends only on the operating wavelength and core composition, not on the Bragg reflector properties. This allows the PM

conditions to be tuned through the core design [133]. Matching layers (ML) [9] flanking the core provide additional tailoring of the modal properties while retaining the QtW condition. Further to the vertical layer design, the waveguide width and etch depth also modify the modal properties, offering another set of engineering controls on PM [124]. This can be used to restrict PM to desired regions of a larger integrated circuit formed from the same vertical structure, which will be important in the design of a dual-path source.

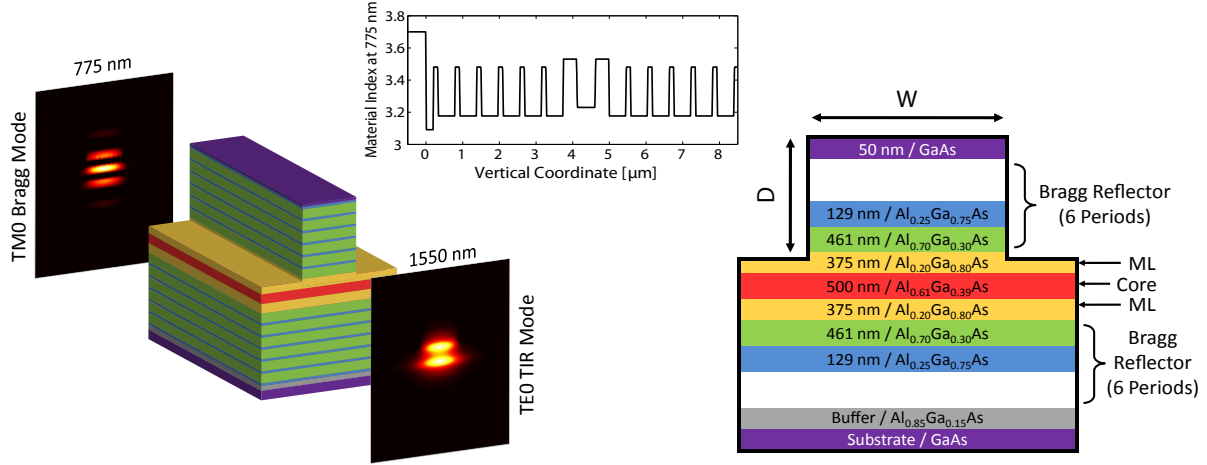


Figure 5.1: BRW architecture reported in Refs. [9, 10], which satisfies PM for photon pair generation in the telecom C-band (~ 1550 nm). The Bragg and TIR mode profiles, material index variation, and vertical layer specifications are shown.

Three types of SPDC phase matching can be supported by BRWs, which differ in the polarizations of the photons [5]. Type 0 and Type I SPDC involve a TM-polarized pump, with the downconverted photons being TM co-polarized in the former, and TE co-polarized in the latter. In Type II SPDC, a TE pump is downconverted into orthogonally-polarized TE-TM photon pairs, which can exhibit polarization entanglement [11]. Existing efforts in quantum photonic BRW design have aimed at achieving one [66] or several [134] of these processes with high pair generation rates. Other designs have targeted integration with a pump laser [71, 72], hyper-entangled states [77], and maximally polarization-entangled states without the need for dispersion-compensating optics [73]. In all of these cases, the BRW photon source has consisted of a single waveguide segment, without any additional integrated devices.

5.1.2 Design Considerations

Vertical Structure and Generation Process: The device will be based on the vertical structure described in Figure 5.1, and will target Type I SPDC near 1550 nm. Phase-matching takes place with the pump in the TM0 Bragg mode, and the downconverted photons both in the TIR-guided TE0 mode.

Based on prior experience, it is assumed this architecture will allow photon non-degeneracies of at least $|\lambda_{02} - \lambda_{01}| = 50 \text{ nm}$ to be achieved with sufficient brightness for the IFPS experiment. Figure 5.2 illustrates the design concept. Pair generation is to occur within the waveguides of width W_{PM} , which ideally will be the only regions where PM is satisfied over the range of operating pump wavelengths. To construct a ‘dual-path’ BRW source for IFPS, it is necessary not only to add an integrated on-chip splitter, but also to deliberately modify the PM properties across the device.

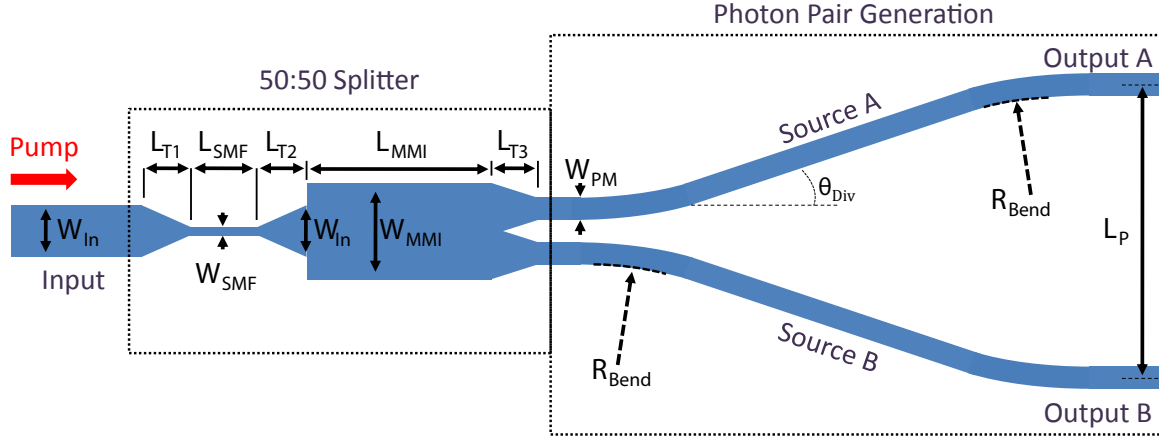


Figure 5.2: Overview of dual-path BRW design (top-down view), showing key design variables discussed in the text. These features will be etched into an existing vertical design (given in Fig. 5.1) to a depth of $D = 3.78 \mu\text{m}$, and will target Type I SPDC near 1550 nm .

Source Symmetry and Pumping: A number of reasons exist for splitting the pump on-chip. Owing to the realities of fabrication, device characteristics will vary across the wafer; hence if two different waveguides are to form the two interfering paths, they should be located as close together as possible to facilitate their indistinguishability. This poses a problem for off-chip splitting because high-magnification objective lenses are required for coupling into the Bragg mode (fiber does not suffice), and the size of these bulk components makes it difficult to couple into two close waveguides without introducing an impractical device layout or footprint. Furthermore, due to the presence of multiple supported modes and the vicissitudes of alignment quality in general, it would be challenging to guarantee that both paths are pumped with equal strength. Finally, as discussed in Chapter 3, stability of the inter-path time delay τ is also an issue. Coherent pumping of the paths is therefore best achieved by injecting from a single objective lens into an integrated 50:50 mode coupler.

Restricted Pair Generation: Varying the PM properties across the device is necessary to suppress pair generation within the splitter and the input waveguide preceding it. Pairs generated in these regions of the circuit would not form a path-entangled output state, and therefore constitute a source of noise.

Accomplishing this for a single vertical structure and etch depth requires the waveguide width W of each component to be carefully selected, so that over a suitable range of pump wavelengths, the PM conditions will only be satisfied within the two waveguides at the splitter output.

Architecture-Specific Challenges: Photon losses are also a significant factor in selecting the waveguide widths and other aspects of the design, since propagation losses in the Bragg mode can be high (on the order of 40 cm^{-1}) [10]. Device lengths must therefore be kept short compared to other architectures such as silicon wire [67]. These losses are thought to be largely due to scattering from waveguide sidewall imperfections, which worsens as the waveguide width is decreased, and as the ridge etch depth approaches the core of the device. On the other hand, too shallow an etch depth can lead to high guiding losses, especially within waveguide bends, because lateral confinement is weak. Based on both simulation and past experience, a ridge etch depth of $D = 3.78 \text{ }\mu\text{m}$ (reaching approximately to the middle of the topmost ML) was selected to provide a suitable compromise.

Lastly, the design must also contend with the presence of multiple lateral modes. This is in contrast to silicon-nanowire based sources [4], where single-mode conditions occur together with the targeted PM requirements, and photon losses are less severe. Multi-modedness presents challenges for the 50:50 splitter implementation, and is also a concern for phase stability. The following sections discuss each aspect of the dual-path design in greater detail.

5.1.3 Width Selection for Restricted PM

Each waveguide geometry is associated with a tuning curve, giving the downconverted photon wavelengths $\lambda_{1(2)}$ at which PM occurs as a function of pump wavelength λ_P . These curves are parabolic as shown in Figure 5.3, and have a maximum λ_P beyond which PM can no longer be satisfied. Due to waveguide dispersion, the curves shift rightwards as the waveguide width is decreased. This implies a narrow waveguide can support PM over a range of λ_P where PM is absent at wider widths.

Tuning curves were calculated for $D = 3.78 \text{ }\mu\text{m}$ at several waveguide widths using simulated dispersion characteristics. Two of these curves, corresponding to selected widths of $W_{\text{In}} = 5.0 \text{ }\mu\text{m}$ and $W_{\text{PM}} = 2.5 \text{ }\mu\text{m}$, are given in Figure 5.3. This selection is predicted to allow for more than 220 nm of photon non-degeneracy in W_{PM} prior to the onset of PM in W_{In} . Since only 50 nm of non-degeneracy is expected to be used, this provides a suitable safety margin. The following considerations were also in mind: W_{In} is large enough to facilitate stable and suitably-efficient injection of the Bragg mode pump; W_{PM} better mitigates photon losses compared to a narrower width; at the same time, both W_{In} and W_{PM} are small enough to facilitate reasonable dimensions for the 50:50 mode splitter (see next section).

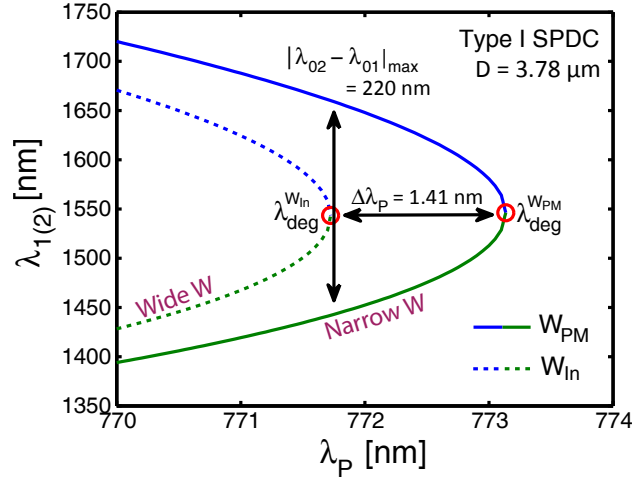


Figure 5.3: Type I SPDC Tuning curves for $W_{\text{In}} = 5.0 \mu\text{m}$ and $W_{\text{PM}} = 2.5 \mu\text{m}$, calculated from Equations (5.2)-(5.3) with a monochromatic pump. Waveguide dispersion was simulated using *Lumerical*. Degeneracy points obtained in this manner are known to be systematically offset from their true values.

The 50:50 splitter design will determine the other waveguide widths indicated in Figure 5.2; however, their selection will account for compatibility with W_{In} and W_{PM} .

The degeneracy points predicted in Figure 5.3 are $\lambda_{\text{deg}} = 1543.5 \text{ nm}$ for W_{In} and $\lambda_{\text{deg}} = 1546.3 \text{ nm}$ for W_{PM} . Numerical simulations give reasonable estimations of relative differences between degeneracy points (i.e. at different widths), but are known to be systematically offset from their true values. The experimental value of λ_{deg} at $W_{\text{In}} = 5 \mu\text{m}$ for this vertical structure is in the vicinity of 1552 nm [10]. The true value of λ_{deg} at W_{PM} is thus expected to be in the vicinity of 1554.5 nm, with a corresponding pump wavelength of approximately 777 nm.

5.1.4 50:50 Splitter Design

Numerous approaches are available for coherently splitting the pump on-chip, including Y-junctions and directional couplers. Y-junctions were explored, but are challenging to compactly implement for this BRW structure without incurring large guiding losses. A sufficiently short, low-dispersion directional coupler is also challenging, in part because the lateral confinement of ridge-guided Bragg modes is highly sensitive to small variations in the etch depth. A suitable design choice for the BRW dual-source is a 1 x 2 port multimode interferometer (MMI). The uni-directional geometry of MMIs reduces the number of waveguide bends needed, helping keep losses low. Furthermore, the inherent symmetry of a 1 x 2 MMI mitigates the effects of splitting-ratio dispersion, and does not add a relative phase shift between the paths that would otherwise require correction before IFPS can be implemented [4].

Optimal MMI Length

The general layout of the MMI was shown in Figure 5.2. A 50:50 splitting ratio results from the spatial beating of lateral modes, which forms a two-fold image of the fundamental mode at a propagation length of

$$L_{\text{MMI}} = \frac{3\pi}{16(k_1 - k_0)} = \frac{3\lambda}{32\Delta n_{\text{eff}}}, \quad (5.5)$$

where k_n is the propagation constant of the n th mode, and Δn_{eff} is the effective index difference of the first two lateral modes [135]. In general, L_{MMI} can be decreased by a factor of two through a four-fold decrease in W_{MMI} . However, the MMI dimensions are ultimately constrained by W_{PM} . Smaller-footprint MMIs are also have less tolerance for imperfections in fabrication. An MMI width of $W_{\text{MMI}} = 10 \mu\text{m} = 2W_{\text{In}}$ was chosen, giving a theoretical optimal 50:50 splitting length of $L_{\text{MMI}} \simeq 220 \mu\text{m}$. The simulated mode evolution of this design is plotted in Figure 5.4. The net power transmission was found to be 0.486 in both output waveguides (relative to the input), indicating equal power splitting. The 2.8% power loss arises from minor modal mismatch, but does not account for guiding or scattering losses, and is therefore not an accurate prediction of the true MMI insertion loss. Dispersion is not an issue for this MMI, because the pump is tuned at most by 2-3 nm, and any wavelength dependence of L_{MMI} changes only the effective insertion loss and not the relative power balance at the outputs, owing to the lateral symmetry of the field evolution.

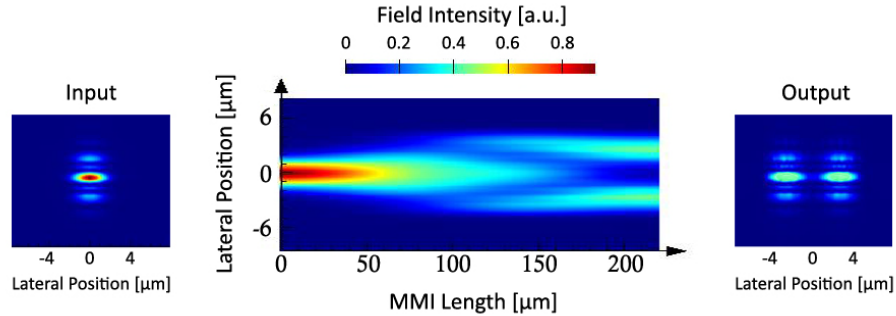


Figure 5.4: Simulated MMI mode evolution at 777 nm for $W_{\text{MMI}} = 10 \mu\text{m}$, showing the injected mode profile at the input (left, $W_{\text{In}} = 5 \mu\text{m}$) and the resultant mode profile at $L_{\text{MMI}} = 220 \mu\text{m}$ (right, two-fold image of input).

Spatial Mode Filter

For the spatial profile to evolve as intended, the input power must be entirely within the fundamental mode. This can only be satisfied for the present design through the use of a spatial mode filter (SMF), which introduces a narrow waveguide width wherein all higher-order modes are deliberately unguided

and therefore eliminated.

SMF Width: At the chosen etch depth of $D = 3.78 \mu\text{m}$, simulations predict single-mode TM operation at 777 nm for widths below $W = 1.2 \mu\text{m}$. The TM0 mode remains guided for widths down to $W = 0.7 \mu\text{m}$. An SMF width of $W_{\text{SMF}} = 1.0 \mu\text{m}$ is therefore suitable. Although W_{SMF} is more narrow than W_{PM} and can therefore generate pairs at the operating pump wavelengths, photons generated in the SMF are expected to contribute negligibly to the total detected photon pair flux. There are several reasons for this: the interaction length is small compared to that of the W_{PM} sections; photons created in the SMF undergo far greater total losses, especially since the MMI is not designed for 1550 nm and will have high insertion losses at that wavelength; lastly, these photons will already be highly non-degenerate at the λ_{P} where W_{PM} is phase-matched, and will be detected less efficiently (the single-photon detectors are most efficient at 1550 nm – see Chapter 6).

SMF Length: To determine a suitable SMF length for higher-order mode suppression, the simulated loss of the TM1 mode in the vicinity of cutoff was used [136]. The imaginary part of the TM1 mode propagation constant was found through FEA to be $\beta_{\text{im}} = 8.607 \times 10^{-4} \text{ m}^{-1}$ at $W = 1.3 \mu\text{m}$, corresponding to 7476 dB/cm of attenuation. Power within this mode decays as $\exp(-2\beta_{\text{im}}z)$, and decreases below 1% of its initial value for a propagation length of $z = 5/2\beta_{\text{im}} \simeq 29.05 \mu\text{m}$. This length was doubled to provide a conservative safety margin, giving $L_{\text{SMF}} = 60 \mu\text{m}$.

Waveguide Tapering

Waveguide tapering is used to minimize mode mismatch losses between waveguides of dissimilar width, as well as to facilitate adiabatic expansion of the TM0 mode from the SMF to the MMI input so that power remains within the fundamental mode. To ensure adiabatic expansion, increases in the waveguide width must occur more slowly than the lateral diffraction of the mode [137]. This happens when the taper angle satisfies $\theta < \lambda/2Wn_{\text{eff}}$, where θ is the local taper angle, W is the local waveguide width, and n_{eff} is the local effective index of the fundamental mode. This same design rule also ensures efficient modal compression to narrower waveguide widths [138]. Table 5.1 summarizes the maximum permissible taper angle for the three pertinent waveguide widths, where $\theta_{\text{max}} = \lambda/2Wn_{\text{eff}}$.

Table 5.1: Maximum Local Adiabatic Taper Angles at $\lambda = 775 \text{ nm}$

W [μm]	n_{eff}	θ_{max} [$^\circ$]
1	3.1331	7.10
2.5	3.1420	2.83
5	3.1440	1.42

Since a local waveguide width of $W = 5 \mu\text{m}$ is present in all tapers, $\theta_{\text{max}} = 7.10^\circ$ determines that the minimum taper lengths be $L_{T1} = L_{T2} = 80 \mu\text{m}$ and $L_{T3} = 50 \mu\text{m}$. Note that θ_{max} decreases at smaller widths. The taper lengths can thus be made smaller by tapering the widths parabolically rather than linearly, so that the local taper angle always matches the local θ_{max} . However, the linear taper will be retained to provide a safety margin for the majority of the taper length. For example, the angle of the SMF tapers are more than a factor of two smaller than the average local θ_{max} predicted by the design rule.

Pairs generated in these tapers are expected to have a negligible effect on the measured photon statistics, due to both higher losses and smaller interaction lengths. Field coupling between the two tapered waveguides at the MMI output was found to be negligible.

5.1.5 Other Considerations

Waveguide Divergence

As elaborated upon in Section 5.2, the directional coupler will be implemented on a separate chip. It is therefore necessary to couple the output of the dual-path BRW source to the input of the dispersive coupler using a fiber array (e.g. see Figure 6.8). The fiber array used for this purpose has a waveguide pitch of $L_P = 127 \mu\text{m}$. Due to the poor lateral confinement, it is preferable to minimize waveguide bending. Waveguide bends of radius $R_{\text{Bend}} = 500 \mu\text{m}$ were kept short by bringing the output waveguides to a divergence angle of $\theta_{\text{Div}} = 6^\circ$, and then using straight waveguide sections to reach the required pitch. The resultant total propagation length of each pair generation path (beyond the MMI) is approximately $650 \mu\text{m}$. To facilitate device cleaving, an additional $300 \mu\text{m}$ of waveguide length must be added to both ends of the device. With these additions, the total nominal device length is approximately $1600 \mu\text{m}$. Key design specifications have been summarized in Table 5.2.

Table 5.2: Final Design Specifications for BRW Dual-Path Source

Parameter	Value	Parameter	Value	Parameter	Value
W_{In}	$5 \mu\text{m}$	L_P	$127 \mu\text{m}$	L_{T2}	$80 \mu\text{m}$
W_{SMF}	$1 \mu\text{m}$	L_{SMF}	$60 \mu\text{m}$	L_{T3}	$50 \mu\text{m}$
W_{MMI}	$10 \mu\text{m}$	L_{MMI}	$220 \mu\text{m}$	R_{Bend}	$500 \mu\text{m}$
W_{PM}	$5 \mu\text{m}$	L_{T1}	$80 \mu\text{m}$	θ_{Div}	6°

Potential Impact of Multi-Modedness

The potential impact of the device's multi-modedness on the quality of quantum interference is discussed.

Power Transfer and Spatial Beating: Since SPDC is the only significant source of light at ~ 1550 nm in this device, all power at 1550 nm will initially begin in the TE₀ TIR-guided mode, and spatial beating will not occur unless there is power transfer into higher-order lateral modes. Such power transfer is theoretically negligible under the ideal field evolution. For example, the mode mismatch between the first two lateral TE modes at the W_{PM} width is $|k_1 - k_0| = 14828 \text{ m}^{-1}$, which together with the mode overlap leads to a power transfer of less than 1% per 1000 μm of propagation. However, scattering from sidewall imperfections can contribute an effective k-vector that compensates for the mode mismatch. The amount of power thus scattered into the higher order modes is difficult to predict. Nonetheless, power in these modes is expected to rapidly dissipate due to their poorer confinement and correspondingly higher propagation loss. Even if the downconverted photons enter into a superposition of lateral modes, spatial beating en route to the directional coupler is not expected to have adverse effects, since any resultant distinguishability will subsequently be projected back into the indistinguishable fundamental modes at the single-mode directional coupler waveguides (see next section). The possible exception is the relative path brightness, which can depend on the waveguide-to-fiber and waveguide-to-waveguide coupling efficiency of the field's total spatial profile.

Phase Stability: Of greater concern are the implications for the relative path phase stability. If the downconverted photons propagate in a superposition of guided modes, then their optical phase upon reaching the directional coupler is no longer a well-defined variable. In the extreme case of an entirely random phase θ in Equation (3.26), the observed count rate averages out to give the classical result. Phase variation is anticipated to be far less severe for the present dual-path design, and may perhaps be negligible. However, its potential effect on IFPS performance should be noted, and may become especially important for more complex circuit designs based on the BRW architecture, or indeed any architecture where the waveguides are not single-mode.

5.2 SiON Directional Coupler

The objective of this section is to design a highly-dispersive directional coupler with a TE splitting ratio of 50:50 occurring at 1554.5 nm. Since the dual-path BRW source is expected to attain at least 50 nm of non-degeneracy around $\lambda_{\text{deg}} \approx 1554.5$ nm ($\Lambda \approx 0.032$), a dimensionless linear coupler dispersion of $M = 50$ or greater is therefore sufficient to reach $M\Lambda = \pi/2$ and observe all possible values of V_S indicated in Figure 3.3.

Choice of Architecture: The high propagation losses of the AlGaAs BRW platform pose practical challenges for implementing a directional coupler on the same chip, since long interaction lengths are

required to reach this level of dispersion. Furthermore, monolithically integrating the devices would make it difficult to experimentally measure the source performance independent of the coupler performance, which is essential for testing the predictions of Chapter 3. Obtaining monolithic devices where both the source and the coupler are performing optimally would also be more challenging than selecting these devices independently. For the above reasons, the directional coupler is therefore designed as a separate chip that will be fiber-coupled to the dual-path BRW device.

The SiON material system is an attractive choice for this design because of its decreased potential for sidewall scattering losses (due to a lower core-cladding index contrast), as well as the availability of existing recipes for on-campus fabrication. Material dispersion curves for the SiON core and silicon oxide (SiO₂) cladding grown by these recipes are shown in Figure 5.5(a). Both curves are nearly flat in the vicinity of 1550 nm, indicating low material dispersion near the targeted 50:50 splitting wavelength. Coupler dispersion must therefore come predominately from waveguide dispersion, which can be enhanced by selecting narrow waveguide features.

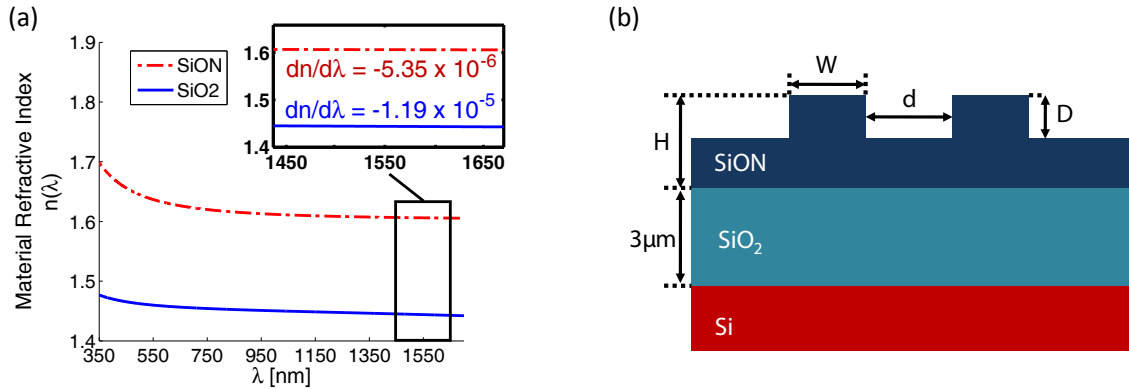


Figure 5.5: (a) Refractive indices of SiON and SiO₂ from the available fabrication recipe, measured via ellipsometry. (b) Ridge-waveguide geometry used in the directional coupler design: H is the core layer thickness; D is the ridge etch depth; W is the waveguide width; and d is the waveguide separation. A SiO₂ layer thickness of $3\mu\text{m}$ prevents mode leakage into the silicon substrate.

Increasing the Dispersion: In general, wavelength-dependent changes to modal confinement have a greater impact on the coupling strength $\kappa_\sigma(\lambda)$ when the modal overlap between waveguides is already large. This suggests the design should aim for maximized coupling. Furthermore, for a given $d\kappa_\sigma(\lambda)/d\lambda$, the dimensionless linear coupling dispersion (M) defined in Equation (3.39) increases with the total coupling length L . Rather than using the minimum interaction length L_0 at which 50:50 splitting occurs for a particular design, an odd-valued integer multiple of L_0 will correspondingly multiply the associated dispersion. However, photon losses still place a practical limit on how large L can be. An appropriate

design strategy is to maximize the waveguide coupling to minimize L_0 , and then multiply L_0 only until the desired M is achieved.

Selection of Coupler Geometry: The ridge waveguide geometry shown in Figure 5.5(b) was chosen for its straightforward fabrication. For a given index contrast, ridges provide lateral confinement that is less localized than in other waveguide structures, allowing the modes to extend well beyond the waveguide sidewalls. This in turn leads to greater field overlap between adjacent waveguides, enhancing the coupling strength. For the directional coupler to operate as intended, the waveguide geometry must support only the fundamental guided modes. Single-mode conditions are met in the vertical direction for a SiON layer thickness of $H = 1 \mu\text{m}$. For this layer thickness, an etch depth of $D = 500 \text{ nm}$ provides a reasonable compromise between the lateral mode extent and guiding losses. The waveguide then remains laterally single-mode for waveguide widths below $4 \mu\text{m}$.

Device performance was simulated using commercial software (*Lumerical Mode Solutions*) over a range of waveguide widths W and separations d . The extracted linear coupler dispersion at 1554.5 nm is shown in Figure 5.6(a). For comparative purposes, this has been normalized by the minimum required 50:50 splitting length L_0 shown in Figure 5.6(b), since smaller device lengths are favourable. Curiously, the computed values of M/L_0 are found to sharply decrease at waveguide widths below $1.4 \mu\text{m}$.

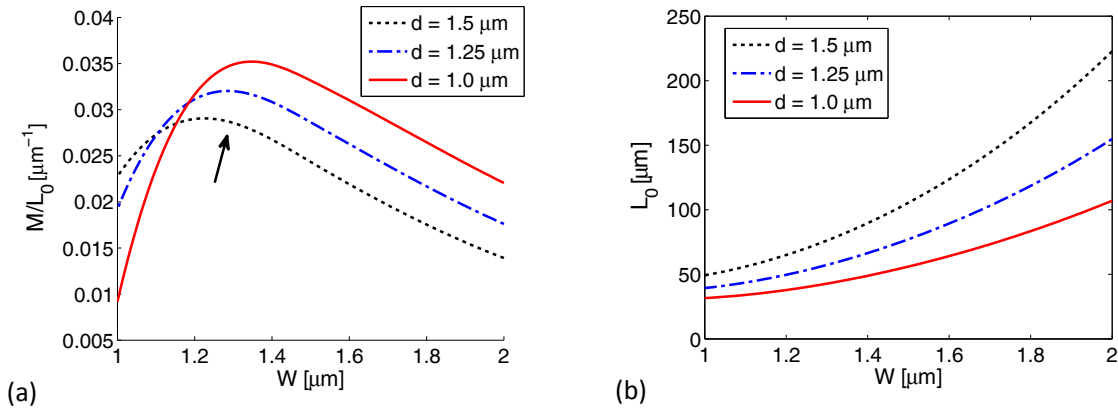


Figure 5.6: Simulated SiON coupler performance as a function of waveguide width and separation. Feature sizes were kept above $1 \mu\text{m}$ to facilitate easier fabrication. The black arrow indicates a suspected entry into the strong-coupling regime.

Although not rigorously investigated, it is suspected this may indicate entry into the strong-coupling regime, where the d^2/dz^2 terms of the mode evolution can no longer be neglected (see Chapter 2.3.2). This is analogous to the breakdown of the rotating wave approximation for a driven two-level electron, where strong driving can lead to an effective shift of the resonance frequency, known as the Bloch-Siegert shift [139]. For the case of a directional coupler, the analogous result is an effective modal mismatch,

which can cause the true L_0 to be shorter than the L_0 values calculated in Fig. 5.6(b). This would lead to erroneously low values of M/L_0 . Investigating this phenomenon further is beyond the scope of this thesis. It suffices to restrict the design to parameters where M/L_0 is well-behaved.

The best-performing design that avoids the suspected strong-coupling regime is given by $W = 1.5 \mu\text{m}$ and $d = 1 \mu\text{m}$, where $M/L_0 = 0.03316 \mu\text{m}^{-1}$ and $L_0 = 56 \mu\text{m}$. To reach the targeted dispersion of $M \geq 50$, L_0 must be multiplied by a factor of 27, giving a total dispersion of $M \geq 50.14$ for an interaction length of $L = 1512 \mu\text{m}$. An s-bend radius of $400 \mu\text{m}$ was selected to bring the waveguides to the required $127 \mu\text{m}$ pitch at the coupler inputs/outputs, based on a compromise between bend losses and the total added propagation length. To correct for waveguide coupling within the s-bend regions, $11 \mu\text{m}$ was subtracted from the interaction length. An additional $600 \mu\text{m}$ of waveguide length was added to provide sufficient tolerance for device cleaving. The final device specifications are summarized in Table 5.3. Figure 5.7 shows the coupling dispersion and mode profiles of the final design. The coupling strength is found to be linear from 1500-1600 nm. Hence the near-degeneracy approximations are expected to provide a good description of the observed IFPS behaviour.

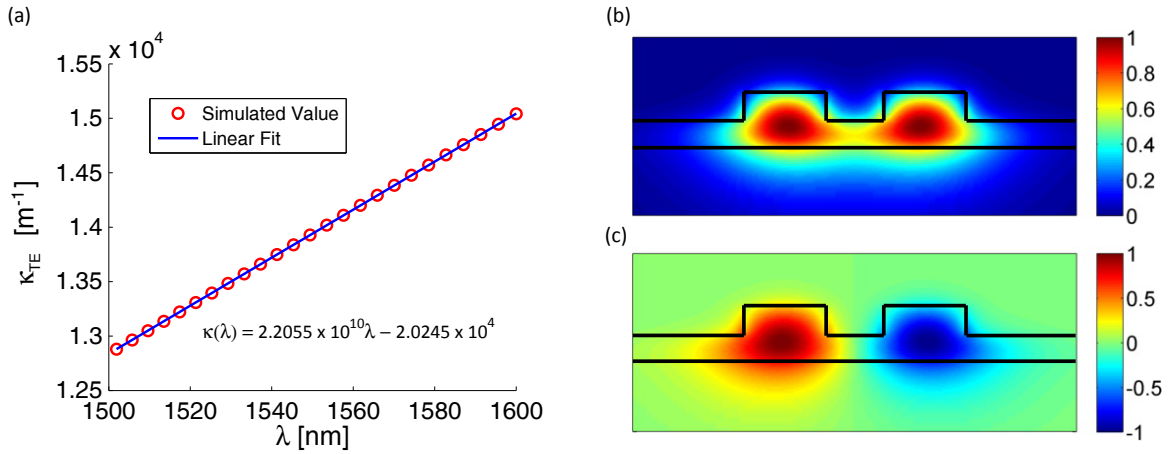


Figure 5.7: (a) Coupling dispersion of the final design; the linear fit has a coefficient of determination (R-squared) of 1.00. (b) Symmetric and (c) anti-symmetric mode profiles within the coupling region.

Table 5.3: SiON Directional Coupler Specifications (at 1554.5 nm)

Parameter	Value	Parameter	Value
H	$1 \mu\text{m}$	L_0	$56 \mu\text{m}$
D	$0.5 \mu\text{m}$	M/L_0	$0.03316 \mu\text{m}^{-1}$
W	$1.5 \mu\text{m}$	L	$1512 \mu\text{m}$
d	$1 \mu\text{m}$	M	50.14

Chapter 6

IFPS Experiments

This chapter details an experimental roadmap for investigating IFPS behaviour using the dual-path source and dispersive coupler designed in Chapter 5, and discusses some early device characterization results. The end goal of these efforts is to test the following central predictions about IFPS:

- that near-perfect deterministic separation can be provided over a large range of non-degeneracies in spite of high coupler dispersion;
- that the anti-bunched interference visibility changes as a consequence of dispersion even while the outcome probabilities remain approximately invariant.

6.1 Dual-Path Source Characterization

Device characterization not only provides useful feedback about the source design, but is also an essential step in determining device specimens having performance suitable for IFPS experiments. Due to limitations in control over the fabrication process, variations in device performance can be considerable. Ideally, sources selected for use in IFPS should exhibit photon pair tuning properties and generation efficiencies that are identical for both paths. This section details initial efforts to identify sources with these attributes from the first batch of fabricated devices.

The dual-path sources were fabricated from existing recipes at the Toronto Nanofabrication Centre (St. George campus). Wafer areas of 1cm-by-1cm were processed and cleaved into bars containing approximately 15-25 devices each. Straight waveguides of widths W_{In} and W_{PM} were included on either side of each dual-path device. Scanning electron microscope (SEM) images of several device samples are shown in Figure 6.1. The waveguide width features seen in these and other SEMs were roughly 0.5 μm

smaller than their targeted values, possibly due to overexposure during electron-beam lithography of the etch mask. In addition, the slab regions adjacent to the waveguide ridge sidewalls are slightly tapered in height, resulting in a shallower etch depth than the target depth of $3.78\ \mu\text{m}$; however, excluding this tapering, profilometer measurements indicated an etch depth of $3.75\ \mu\text{m}$. Midway down the ridge sidewalls, the sidewall roughness abruptly worsens, which is not typical and will increase the device propagation losses.

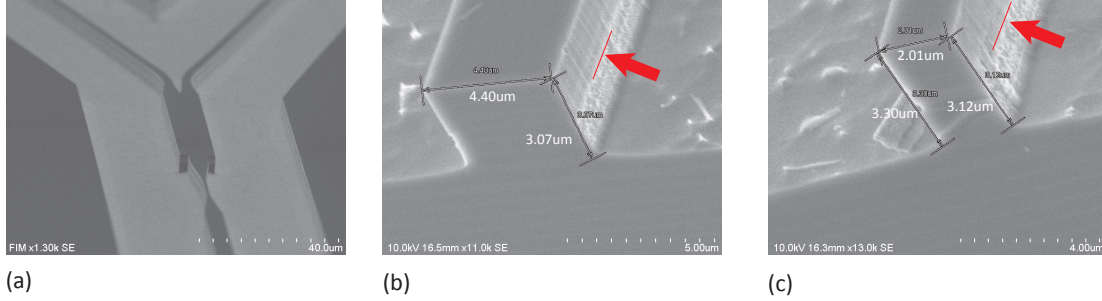


Figure 6.1: SEM images of the dual-path sources showing: (a) view of SMF and MMI regions (lengths appear compressed due to the imaging angle); (b) profile of an input waveguide (targeting $W_{\text{In}} = 5\ \mu\text{m}$); and (c) profile of an output waveguide in the regions of photon pair generation (targeting $W_{\text{PM}} = 2.5\ \mu\text{m}$). Red arrows indicate the abrupt change in ridge sidewall roughness. Images are courtesy of Rajiv Prinja and Nima Zareian.

6.1.1 Classical Characterization

SHG Measurements

Measurements of the classical second-harmonic generation (SHG) process are used to identify the degeneracy points of the dual paths and compare their distinguishability. SHG is equivalent to time-reversed SPDC, but is a stimulated rather than spontaneous process, making it several orders of magnitude more efficient and thus easier to observe [5, 124]. Like SPDC, SHG has Type I and Type II processes defined by the polarizations of the interacting fields. The Type I process is selected by ensuring that the pump is TE-polarized while the collected SHG power is TM-polarized.

The experimental setup used to measure the generated SHG power as a function of the input pump wavelength is depicted in Figure 6.2. Light was coupled into and out of the device using objective lenses. Both objective lenses and the device were mounted on a micro-manipulator stage for alignment with the pump beam. A CCD camera was used to view the modes on a monitor, aiding the alignment process. Pumping was provided by a mode-locked tunable C-band source (PriTel femtosecond fiber laser; 10 MHz pulse repetition, 3 nm FWHM bandwidth), which was swept over the wavelength interval

1540-1560 nm. The pump central wavelength and relative peak power were tracked using an optical spectrum analyzer (Agilent 86146B). The peak power, as well as the average input power monitored by a Germanium detector (Newport 818-IR), remained approximately constant over this span. SHG power was monitored using a Silicon detector (Newport 818-SL), which is only sensitive to wavelengths below 1100 nm, making it unnecessary to spectrally filter the pump. The peak of the measured SHG response corresponds to the photon pair degeneracy point λ_{deg} .

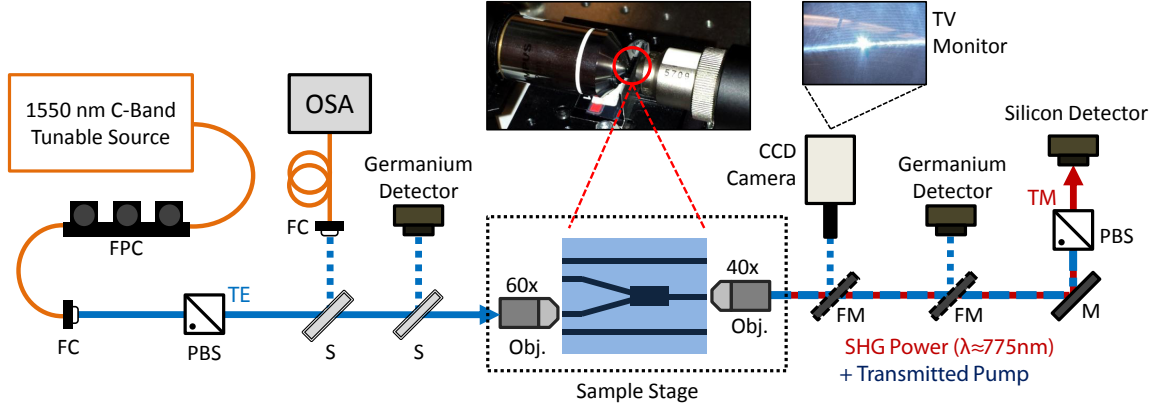


Figure 6.2: Simplified experimental setup for SHG and linear loss measurements. Additional mirrors (omitted) are used for alignment. The device orientation was intentionally reversed with respect to the pump, since the SMF region is poorly guiding at 1550 nm. Abbreviations: mirror (M); flip-mounted mirror (FM); beam sampler (S); fiber polarization controller (FPC); fiber coupler (FC); polarizing beam-splitter (PBS); optical spectrum analyzer (OSA); objective lens (Obj).

Figure 6.3 shows the SHG tuning characteristics for three different specimens, and demonstrates the importance of conducting these initial SHG experiments to screen out poor performers. The SHG tuning curves in Figure 6.3(a) are nearly identical for both paths, indicating a device with reasonable path indistinguishability. On the other hand, the curves shown in Figures 6.3(b)-(c) indicate path distinguishability due to differing degeneracy points. The majority of the tested devices exhibited such distinguishability. This can be partly attributed to uncontrollable variations in the fabricated waveguide widths. However, the tuning curve simulations conducted in Chapter 5 indicate that for widths near 2.5 μm , a large $\pm 0.25 \mu\text{m}$ width variation should lead at most to a degeneracy difference of only 0.23 nm, whereas many of the observed degeneracy differences were closer to 1 nm. Minor variations in etch depth, to which the Bragg mode dispersion is very sensitive, may also be a contributing factor.

Note that Figure 6.3(a) shows a possible secondary peak near 1555 nm. Since the PM degeneracy point was anticipated to be near 1554.4 nm, it is possible that this secondary peak is the true phase-matching peak for the output waveguides, while the dominant peak near 1550 nm could originate from the MMI or input waveguide regions. This could be better resolved by using a narrowband continuous

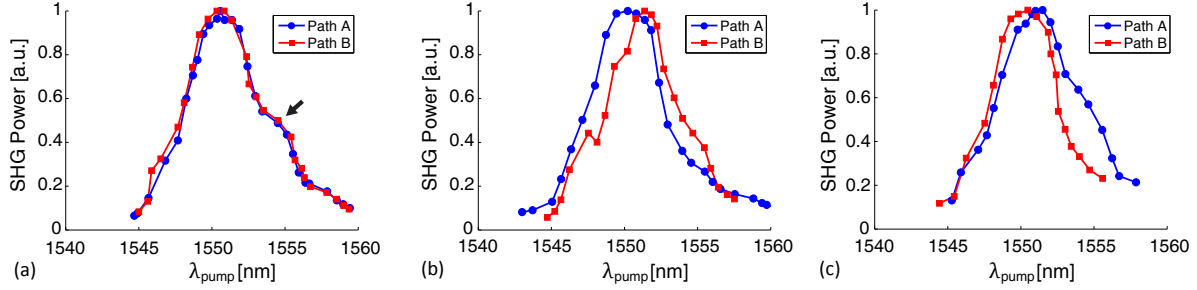


Figure 6.3: (a) Nearly path-indistinguishable and (b)-(c) path-distinguishable SHG tuning characteristics measured for three different device specimens. The degeneracy points in (b) and (c) differed between paths by approximately 1.2 nm and 0.8 nm respectively. Data was normalized based on the peak power. The arrow in (a) indicates a possible secondary peak.

wave (CW) source rather than a mode-locked laser. However, initial efforts using a CW pump failed to observe any detectable SHG power. SHG is easier to detect with mode-locked pumping because the SHG power scales quadratically with the peak power [10, 124]. With the mode-locked laser, the collected SHG powers were on the order of nW for a time-averaged pump input power of 1.5 mW. SHG powers measured from straight-section waveguides surrounding the dual-paths were generally an order of magnitude higher.

Loss Measurements

Photon propagation losses will affect the rate of successful pair generation and the signal-to-noise ratio in coincidence count measurements. Ascertaining these losses is useful in understanding the device performance. A common technique for measuring the propagation loss of a straight optical waveguide is based on Fabry-Perot transmission fringes [140–142]. Fresnel reflection at the input and output facets of the waveguide lead to Fabry-Perot resonances that modulate the waveguide transmission T according to

$$T(\lambda) = A \left[\frac{B}{1 + B^2 - 2B \cos(D/\lambda)} \right], \quad (6.1)$$

where $A = (1 - R)^2/R$, $B = R \exp(-\alpha L)$, and $D = 4\pi n_{\text{eff}}L$. The variable α refers to the propagation loss coefficient, L is the waveguide length, n_{eff} is the mode effective index, and R is the facet Fresnel reflectance, given by

$$R = \left| \frac{n_{\text{eff}} - 1}{n_{\text{eff}} + 1} \right|^2. \quad (6.2)$$

Losses can be extracted by measuring the transmitted power of the waveguide over a range of wavelengths and then fitting the data to Equation (6.1). This can be accomplished using the same setup depicted in Figure 6.2 with a narrow-band CW laser (HP-8168F tunable laser source).

While this technique cannot be applied to the dual-path devices, measuring the losses of the adjacent straight waveguides can provide a benchmark for comparison with similar devices from previous fabrication runs. The propagation loss of a straight waveguide having a targeted width of $W_{\text{In}} = 5 \mu\text{m}$ was measured using this technique and found to be approximately $\alpha = 4.1 \text{ cm}^{-1}$. This compares to loss values in the vicinity of $\alpha = 2.5 \text{ cm}^{-1}$ measured for waveguides of similar geometry fabricated earlier from the same vertical wafer structure. A sample Fabry-perot transmission spectrum, measured from the latter, is shown in Figure 6.4. Losses in the dual-sources may thus indeed be higher than usual due to the aforementioned ridge sidewall roughness. However, additional waveguides must be characterized before such a conclusion is drawn.

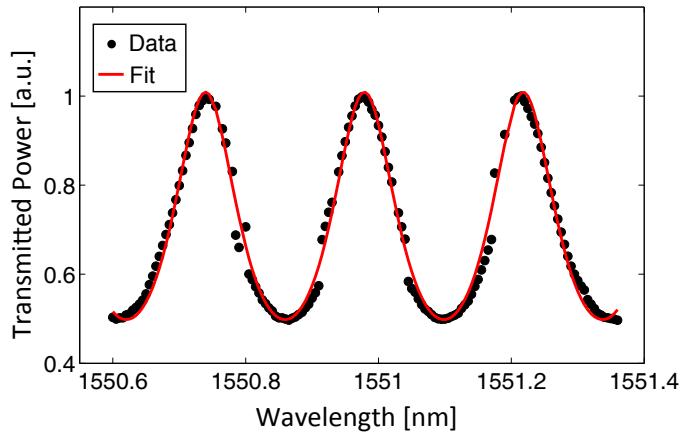


Figure 6.4: A Fabry-Perot transmission spectrum obtained during loss characterization; the data has been fit to Equation 6.1 to extract the corresponding losses.

6.1.2 Non-Classical Characterization

SPDC Measurements

After devices with path-indistinguishable SHG tuning characteristics are identified, the next step is to assess their SPDC performance. This is achieved by pumping the source at a wavelength of $\lambda_{\text{deg}}/2$ for degenerate pair production, distributing the output between two single-photon detector modules using a 50:50 beamsplitter, and measuring detection coincidences.

The setup used in this experiment is detailed in Figure 6.5. Pumping was provided by a CW titanium-sapphire (Ti:Sapph) laser (Coherent MBR-110). The output of the Ti:Sapph was first conditioned by transmitting it through a single-mode fiber to improve its spatial mode characteristics. Past experience has shown this leads to better coupling into the Bragg mode, but it comes at the cost of limiting the maximum achievable input power. In this case, the maximum available power for injection was

6 mW. Detector SPD-1 (idQuantique id220) was operated in free-running mode, while detector SPD-2 (idQuantique id800) was gated with a 20- μ s window upon a detection event at SPD-1. A fiber delay is added to the path of SPD-2 to allow sufficient time for the detector’s electronic arming. The detectors have quantum efficiencies of 20% and 25% respectively, with dead times of 20- μ s. Pump photons are removed from the output through a series of three filters (Newport FSR-RG1000, Thorlabs FEL1450, and Thorlabs FEL1200) with more than 120 dB of rejection at the pump wavelength.

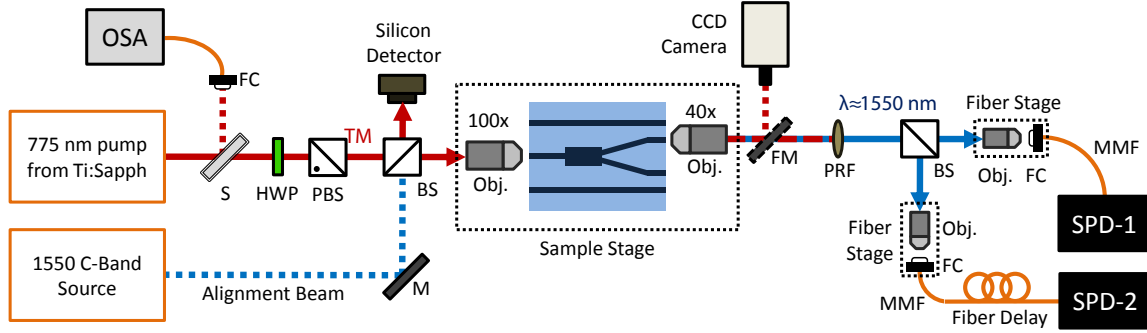


Figure 6.5: Simplified schematic depicting the SPDC coincidence count setup. The 1550 nm source is used to align the output collection and single-photon detector optics prior to the injection of the Ti:Sapph pump. New abbreviations: half-wave plate (HWP); beamsplitter (BS); pump rejection filter (PRF); single-photon detector (SPD); multi-mode fiber (MMF).

A key signature of photon pair generation is the tendency for detection events to occur in unison around a particular value of the relative time delay between detections. Figure 6.6 shows two detection histograms wherein photon pair coincidence peaks are visible. The coincidence count rate can be corrected for the detector dead time by monitoring the single-photon count rate at the free-running detector and using

$$\text{True Count Rate} = \frac{\text{Measured Count Rate}}{1 - \text{Dead Time} \times \text{Single Count Rate}} \quad (6.3)$$

The ratio of the coincidence peak (after summing over all relevant time bins) relative to the average number of counts elsewhere (summed over the same number of time bins) is called the coincidence-to-accidental ratio (CAR) and gives a measure of the signal-to-noise ratio of the coincidence measurement [97]. The CAR provides a means of contrasting the performance of different devices, since its value decreases with increasing photon loss. It can also be used to determine the input pump power for which the signal-to-noise ratio is maximized. The histograms in Figure 6.6 compare the SPDC performance of two straight waveguides for 1.5 mW of injected pump power. The CAR of the waveguide from the dual-source fabrication batch is roughly a factor of 3.3 lower than that of an earlier fabrication run for a waveguide of similar dimensions. This further suggests that the losses of this dual-source batch are

atypically large.

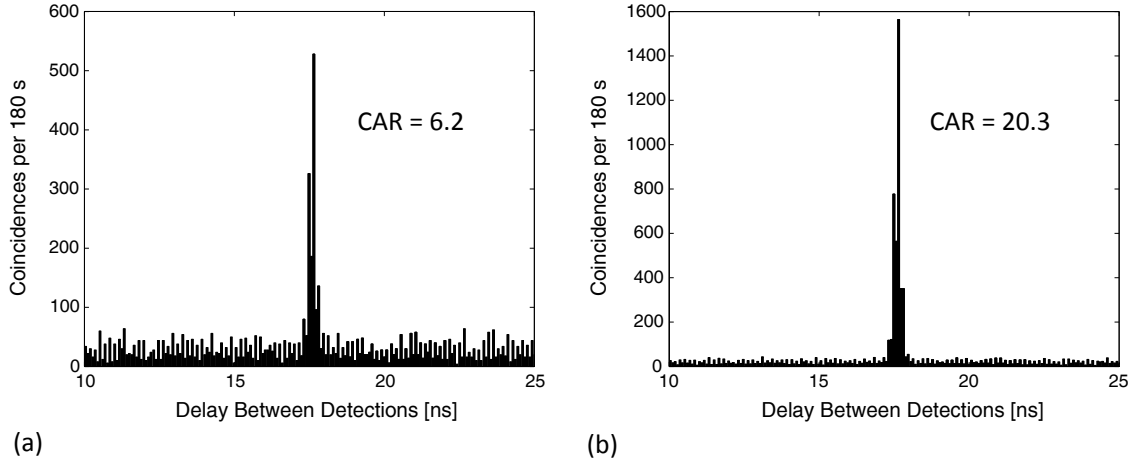


Figure 6.6: Sample coincidence histograms from straight waveguides at 1.5 mW input pump power; (a) is taken from the dual-source fabrication; (b) is taken from an earlier fabrication run of straight waveguides with comparable dimensions.

When the pump is aligned with the dual-source input, the coincidence count rates can be measured for both of the dual-source output paths to determine their relative brightness. Coincidence rates will ideally be identical to within measurement uncertainty for both paths, which corresponds to equal weighting of the BPAs $\phi_{\alpha\beta}^A(\omega_1, \omega_2)$ and $\phi_{\alpha\beta}^B(\omega_1, \omega_2)$ in Equation 3.1. Initial attempts to record coincidences from the dual-path outputs were unsuccessful, albeit weak coincidence peaks have been seen but were subsequently lost during the optimization process. This partly due to the difficulty of the alignment, but could also be attributed to high losses in the Bragg mode, especially within the waveguide bends. Higher pump powers could be accessed by coupling the Ti:Sapph beam directly to the input objective instead of first spatially filtering it through the single-mode fiber. However, poorer Bragg mode coupling and high pump powers in general may increase noise contributions to the histograms through substrate fluorescence or absorption/re-emission processes occurring near the AlGaAs bandgap. A more optimal solution may be to use a pulsed Ti:Sapph source with high peak power but low average power.

Loss Extraction from Photon Pairs

Conventional non-destructive loss measurements are based on the transmission of an externally-injected source through a waveguide, and are ill-suited for circuits containing multiple optical components. Coincidence counts, on the other hand, may enable a convenient route for selectively measuring only the propagation losses experienced by the photon pairs, without requiring additional sources. This technique involves the comparison of single count rates to the coincidence count rates, and is similar to existing

methods for absolute detector calibration [143, 144].

Let ϵ_A and ϵ_B represent the total detection efficiencies in the paths leading from the beamsplitter to the single-photon detectors. These include the beamsplitter insertion loss, fiber collection efficiencies, and detector quantum efficiency. Let ζ represent the probability that an SPDC photon generated within the device survives to reach the beamsplitter. This accounts for losses due to facet reflectance, the output objective collection efficiency and transmission, as well as the pump rejection filter. It can be shown that the theoretical coincidence count rate is related to these parameters by

$$C = \frac{1}{2}\zeta^2|\mu|^2\epsilon_A\epsilon_B, \quad (6.4)$$

where $|\mu|^2$ represents a per-unit-time photon pair generation probability. This can be derived from the density matrix formalism, but can also be rationalized as follows: the probability of a coincidence is proportional to the probability that the photons are generated ($|\mu|^2$), both survive to reach the beamsplitter (ζ^2), and emerge non-deterministically from different beamsplitter ports ($1/2$), multiplied by the probability that both photons are successfully detected ($\epsilon_A\epsilon_B$). Similarly, an expression for the single-photon count rate at detector SPD-1 can be derived as

$$S_A = |\mu|^2 \left(\zeta^2 \left[\frac{1}{2}\epsilon_A + \frac{1}{4}\epsilon_A^{(2)} \right] + \zeta(1 - \zeta)\epsilon_A \right) \quad (6.5)$$

where $\epsilon_A^{(2)} = 1 - (1 - \epsilon_A)^2$ represents the probability of obtaining a successful detection from two incident photons. The terms in this expression can be rationalized as follows:

- all detection events are proportional to the probability of successful pair generation ($|\mu|^2$);
- the first two terms correspond to both photons surviving to reach the beamsplitter (ζ^2);
 - the first represents the probability that the beamsplitter sends only one of these to SPD-1 ($1/2$) and that it is successfully detected (ϵ_A);
 - the second represents the probability that both are sent to SPD-1 ($1/4$) and that at least one successful detection results from the incidence of two photons $\epsilon_A^{(2)}$;
- the third term corresponds to the probability that only one photon reaches the beamsplitter ($\zeta(1 - \zeta)$), that it is sent by the beamsplitter to SPD-1 ($1/2$), and that it is successfully detected (ϵ_A); however, there are two ways in which this may occur (one for each photon), so the probability is multiplied by two

Solving this system recovers a simple expression for ζ in terms of measurable parameters:

$$\zeta = \left[\frac{\epsilon_B}{2} \left(\frac{S_A}{C} \right) - \frac{\epsilon_A^{(2)}}{4\epsilon_A} + \frac{1}{2} \right]^{-1}. \quad (6.6)$$

Estimates of the facet reflectance and output objective collection then allow the propagation loss coefficient α to be calculated from ζ . To the best of the author's knowledge, the use of this technique specifically for waveguide loss measurements has not been reported. It would be interesting to explore its accuracy and compare it against conventional methods for straight waveguides. If reliable, it would then enable the dual-path photon pair losses to be obtained, and could be used to characterize losses in quantum circuits of even greater complexity.

6.2 IFPS Characterization Strategy

This section describes planned experiments for testing core IFPS predictions, following the identification of suitable dual-path source specimens. Measurements of the anti-bunched outcome probability P_S and interference visibility V_S are required over a range of input state non-degeneracies. A strategy for obtaining these quantities and comparing them to the theoretical predictions of Equations (3.15)-(3.35) is detailed.

Dual-Path Tuning Curves

The photon pair non-degeneracy is tuned through the central pump wavelength (λ_{pump}). An SPDC tuning curve, such as that of Figure 5.3, must be experimentally measured to determine the corresponding non-degeneracy $|\lambda_{02} - \lambda_{01}|$. One way to achieve this is to pass the downconverted photons through a spectrometer (Horiba iHR320) while monitoring the single-photon count rate at the output, as illustrated in Figure 6.7. The spectrometer acts as a narrow pass-band filter (with central wavelength λ_{spec}) that can be tuned over the downconverted photon spectra. The accumulated count rate as a function of λ_{pump} and λ_{spec} then gives the SPDC tuning curve, with λ_{01} and λ_{02} determined from the count rate peaks at each λ_{pump} .

Directional Coupler Characterization

The directional coupler designed in Chapter 5 will be fabricated with a spread of coupling lengths about the design value (within the span of $\pm 0.5L_0$) to maximize the likelihood of obtaining a device with perfect 50:50 splitting at the source degeneracy wavelength. Devices will be tested through simple

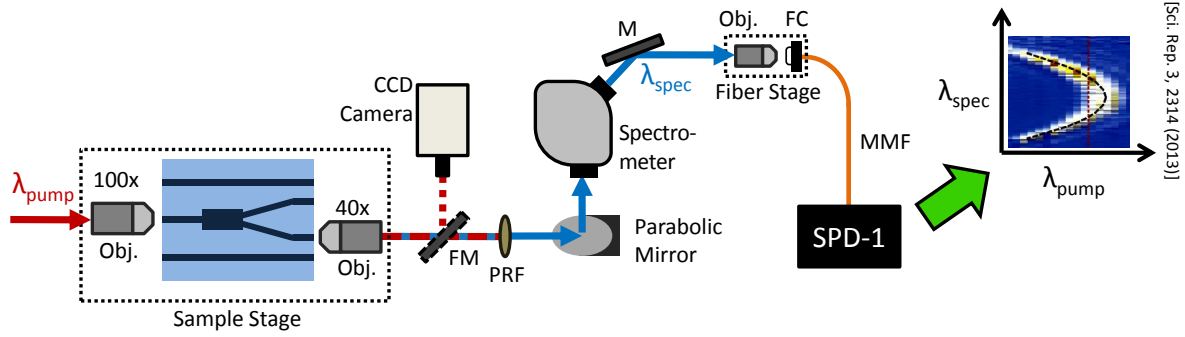


Figure 6.7: Simplified experimental setup for SPDC tuning curve measurement, where λ_{spec} indicates the spectrometer’s transmitted wavelength. SPD-1 monitors the single-photon count rate. The pump and alignment beam are configured as in Figure 6.5. The example SPDC tuning curve is reproduced from Ref. [11].

transmission-based measurements that compare relative powers at the output facets as a function of λ , using a setup similar to that of Figure 6.2. This in turn provides the $\eta(\lambda)$ response of the coupler, which will be required for comparing the IFPS measurements against theoretical predictions. Specimens exhibiting $\eta(\lambda_{\text{deg}} \approx 0.5)$ will be selected to proceed with the IFPS experiment.

Measuring IFPS Behaviour

To implement IFPS, the output of the dual-path source will be injected into the directional coupler using polarization-maintaining fiber (PMF) arrays. These consist of a solid ‘chip’ of polished fiber facets with a 127 μm pitch, and a short (3 ft) fiber ribbon which terminates in an FC-connectorized fanout. PMFs are used because polarization rotations occurring within ordinary fiber would degrade the path indistinguishability. A third array, comprised of multimode fiber (MMF)s, is used to collect the directional coupler output. A schematic highlighting the key features of the proposed setup is shown in Figure 6.8.

Alignment: The source is first aligned for free-space transmission to maximize the SPDC efficiency; its output is then aligned to the PMF array by connecting the fiber fanout to a power meter and maximizing the transmitted pump power. This is later fine-tuned to optimize the photon pair collection. The directional coupler can be aligned by injecting light into the PMF array and maximizing the power collected by the MMF array; adjacent straight waveguides matching the array pitch have been added to the coupler design to make this more convenient.

Path Selection: Most conventional interference experiments use either a variable temporal delay (τ) or relative phase shift (θ) to delineate classical from non-classical contributions in the output coincidence count rate (e.g. Ref. [4]). The sensitivity of IFPS to τ (discussed in Chapter 3.2) makes the former

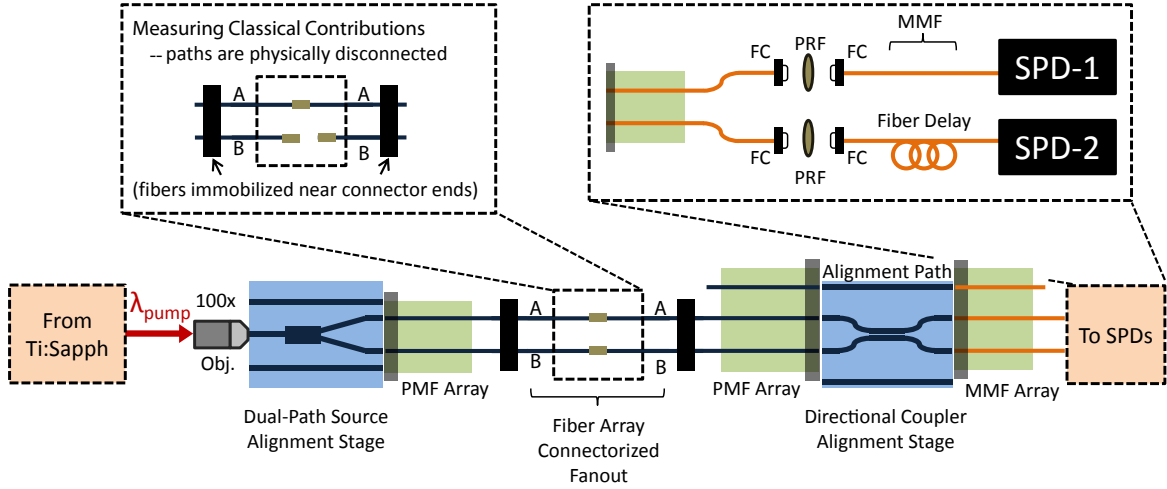


Figure 6.8: Simplified schematic for proposed IFPS experiments. Pump conditioning is identical to that of Figure 6.5. The pump rejection filters have been shown as a free-space implementation; in-fiber filters are available, but would require the use of single-mode fibers at the cost of reducing the collection efficiency by a factor of 5 or greater. SPD-1 is free-running, while SPD-2 is gated.

challenging, while the latter requires additional equipment that is typically designed for non-polarization-maintaining single-mode fiber. In the present setup, the quantum and classical count rates can instead be contrasted by physically disconnecting the PMF arrays in one of the two paths (A or B).

Count Rates: Let C_{AB} denote the coincidence count rate when both paths are connected. Similarly, let C_A and C_B denote the coincidence rates when only path A or path B is connected, respectively. These are proportional to the IFPS separation probability according to

$$P_S \propto C_{AB}, \quad (6.7)$$

$$P_S^0 \propto C_A + C_B, \quad (6.8)$$

$$P_S^I \propto C_{AB} - C_A - C_B, \quad (6.9)$$

where P_S^0 and P_S^I are the classical and non-classical contributions to the IFPS separation probability, given by Equations (3.31) and (3.32) respectively, and P_S is the total separation probability given by Equation (3.29).

Initial Optimization: With both dual-source output paths (A and B) connected to the directional coupler inputs, the pump wavelength is set to the degeneracy point. Alignment and pump power are adjusted to maximize the CAR of the observed coincidence peaks. Additional adjustments can then be made to optimize the ratio $C_{AB}/(C_A + C_B) = P_S/P_S^0$, which attains a value of 2 for perfect deterministic separation. This depends not only on the quality of alignment which affects the relative path amplitudes

and distinguishability, but also on the rate of higher-order pair production. The latter does not obey the predicted two-photon correlations, but can be mitigated by using low pump powers.

Visibility Measurements: The visibility V_S can be measured as a function of $|\lambda_{02} - \lambda_{01}|$ by recording C_{AB} , C_A , and C_B at each λ_{pump} . Writing Equation (3.35) in terms of Equations (6.8) and (6.9), this can be calculated from

$$V_S = \frac{C_{AB} - C_A - C_B}{C_A + C_B}, \quad (6.10)$$

where the denominator and numerator respectively give the classical and non-classical count rate contributions.

Separation Probability Measurements: Let C_A^0 and C_B^0 represent the single-path coincidence count rates at the degeneracy point. Assuming perfect 50:50 splitting at degeneracy, the total flux of degenerate photon pairs passing through the directional coupler is equal to $2(C_A^0 + C_B^0)$, hence the separation probability is simply $P_S = C_{AB}/2(C_A^0 + C_B^0)$. However, away from degeneracy, the total photon pair generation rate may decrease as SPDC becomes less efficient. To account for this, the count rates must be normalized relative to the total photon flux at a given pump wavelength. Let S_A and S_B represent the single-photon count rates of the detectors in paths A and B respectively when operating in free-running mode, and let S_A^0 and S_B^0 represent these values at degeneracy. The separation probability can then be calculated from

$$P_S = \frac{C_{AB}}{2(C_A^0 + C_B^0)} \left[\frac{S_A^0 + S_B^0}{S_A + S_B} \right]. \quad (6.11)$$

Comparison with Theory: At each value of $|\lambda_{02} - \lambda_{01}|$, theoretical predictions for P_S and V_S can be calculated from Equations (3.15)-(3.16) and (3.26)-(3.35) using the splitting ratios $\eta(\lambda)$ measured during the coupler characterization. The BPAs can be approximated by the photon central wavelengths according to $\phi^j(\omega_1, \omega_2) \rightarrow \delta(2\pi c/\lambda_{01})\delta(2\pi c/\lambda_{02})$, where λ_{01} and λ_{02} are given by the SPDC tuning curve. Note that this omits the influence of photon bandwidth and spectral entanglement. Alternatively, the $\phi^j(\omega_1, \omega_2)$ can be directly measured through quantum state tomography; for example, using the technique described in Ref. [145].

Stability Challenges: The efficiency of SPDC in BRW waveguides is highly sensitive to alignment. This alignment can drift considerably over timescales of 10-20 minutes, which places a practical limit on the total duration of the experiment before re-alignment is required. In principle, changes in the pair generation rate due to alignment drift can be accounted for through renormalization of the data by the single-photon count rates, as in Equation 6.11. However, misalignment will worsen the signal-to-noise ratio in the coincidence histograms. Instabilities in the time delay τ may also pose challenges for the experiment, despite the use of fiber arrays. While the close vicinity of the fibers helps ensure

temperature- and strain-induced variations in optical path length are symmetric for both paths, the stability of τ is far from guaranteed; furthermore, even if τ is stable, it may be a non-zero value that does not yield maximal interference. Should these prove problematic, improvement may be possible by packaging select devices with polarization-maintaining fiber pigtails. Some control over τ could also be provided through careful strain or temperature tuning of the connecting fibers.

6.3 Summary

In summation, this chapter discussed experimental techniques for characterizing the BRW dual-path sources and obtaining measurements of P_S and V_S in an IFPS experiment. These techniques included SHG characterization, Fabry-Perot loss measurements, and conventional coincidence count experiments, for which some early device results were presented. Also discussed, though not yet demonstrated, was a technique for extracting photon losses directly from coincidence count experiments. An experiment for obtaining the tuning curves of suitable dual-source specimens was outlined. Lastly, a setup for testing IFPS behaviour was proposed, and the method for measuring P_S and V_S was described.

Future work will continue with a rigorous characterization of the dual-path sources, including the discrimination of SPDC originating from different regions of the device (i.e. input waveguide, MMI, output waveguides). The best devices will then be used to implement the IFPS experiments proposed in Section 6.2.

Chapter 7

Conclusions and Future Directions

7.1 Summary of Contributions

Prior to this dissertation, studies of on-chip quantum interference involving two-photon states had always approximated the interference-mediating coupler's splitting ratio as a constant, even though integrated couplers can exhibit considerable wavelength dependencies. Interference-facilitated pair separation was highlighted as an important task where this approximation is no longer suitable and the implications of coupler dispersion are unknown. By fully accounting for coupler dispersion, this thesis has shown that integrated couplers can not only provide robust and near-universal deterministic pair separation despite high dispersion, but they can also benefit from the dispersion to exhibit novel features such as entanglement-sensitive performance and serve as a versatile tool for quantum state engineering.

General expressions for predicting IFPS behaviour with arbitrary NOON-type states were derived and placed in context with the more familiar Hong-Ou-Mandel interference. A dimensionless model was then constructed for studying state evolution in the near-degeneracy regime, as influenced by the coupler and quantum state properties. This led to the result that perfect separation fidelity can be maintained even as the coupler's response to the input state transitions from 50:50 splitter to wavelength-demultiplexer operation. The conditions for maximal separation performance are linearity in the coupling strength $\kappa(\lambda)$ and equidistance of the photon central wavelengths from the 50:50 splitting wavelength (usually made equal to the degeneracy wavelength). This was explained as the result of anti-symmetry in the central wavelength splitting ratios $\eta^{(1)}$ and $\eta^{(2)}$. When these sum to unity, classical WD-based contributions to the separation probability always increase to compensate decreases in the non-classical contributions, and vice-versa. Dispersion also leads to new interference visibility behaviour, where the visibility depends

on the difference of the central wavelength splitting ratios, rather than their vicinity to 50:50 splitting conditions.

The role of photon bandwidth and spectral entanglement was also studied. Separation performance can decrease at large bandwidths, but this was found to be mitigated by the presence of spectral entanglement. This presents the possibility of discerning the Schmidt number from an ensemble of photon pairs if other spectral properties such as the photon marginal spectra are known. The influence of IFPS on post-selected output states was also investigated. Entanglement was shown to be invariant when the input is path-entangled. However, if only one of the coupler input paths is injected with photon pairs, then coupler dispersion enables tailoring of the output state spectral correlations by tuning coupler properties such as the coupling strength.

Several case studies were presented to provide specific examples of how coupler design influences IFPS performance over large non-degeneracies. The consequences of higher-order coupler dispersion and quantum state asymmetry were also explored. Separation performance was found to be most robust against such asymmetries when the separation enhancement was mainly non-classical (i.e. 50:50 coupler operation), while the greatest sensitivities occurred when separation was entirely classical (i.e. WD coupler operation). Predictions of P_S and V_S based on the near-degeneracy assumptions of the dimensionless model remained accurate to within 5% for non-degeneracies as high as 250 nm, when the downconverted bandwidths were below 3 nm. Cross-polarized photon states were also discussed, and a four-dimensional splitting ratio anti-symmetry metric was created for making qualitative predictions about the P_S performance.

In situations where asymmetries severely compromised the separation performance, active coupler tuning was presented as a viable route for restoring near-perfect separation fidelities. The effect of coupler tuning on the $\eta^{(1)}, \eta^{(2)}$ values associated with the state was also explored as a potential quantum state engineering tool to obtain arbitrary values of P_S and V_S for a given quantum state.

The thesis then focused on the design of integrated devices for testing IFPS behaviour under the influence of coupler dispersion. This included the design of the first path-entangled photon pair source based on the BRW architecture. It was shown how the waveguide widths could be selected to restrict phase-matching to only a specific region of the device. A simple implementation of a highly-dispersive directional coupler was also detailed. Lastly, an experimental roadmap was created for investigating IFPS with these devices.

7.2 Future Directions

Future work will seek to complete the source characterization and IFPS experiments detailed in Chapter 6. Several related research directions are now discussed.

7.2.1 Self-Pumped Dual-Path Sources

The ability of the BRW platform to be self-pumped leads naturally to the generation of bunched states in a superposition of the two counter-propagating directions of the laser cavity. Similar to the case of contra-directionally pumped Sagnac loops [3], pairs in both paths are generated within the same waveguide [72], and hence naturally meet the IFPS requirements for indistinguishability and coherent pumping. Furthermore, SPDC in such sources is alignment-free. This makes the BRW platform poised to become a highly practical source for implementing IFPS. Future work may target the design of a self-pumped monolithic source of deterministically-separated photon pairs.

7.2.2 Engineering Higher-Order Correlations

This dissertation assumed that the quantum states contained exactly two photons. However, for photon pair sources based on SPDC and other nonlinear processes, this is only an approximation, since terms corresponding to the concurrent generation of multiple photon pairs also exist (see Equation (2.13)). These higher-order terms are generally unwanted because they degrade the fidelity of two-photon measurements, such as those involving interference. Higher-order pair production becomes increasingly significant as the pump power is increased, thereby limiting the maximum single-pair flux for which the source remains useful.

A route for mitigating higher order pair production may exist through the engineering of higher-order spatial correlations of the output state. Consider an array of N coupled waveguides, and let \hat{a}_n and \hat{b}_n represent the input and output mode operators for waveguide n . Expanding upon Equation 2.11 but using a simplified notation, the spatial correlations can be expressed as

$$\Gamma_{m,n}^{(2)} = \langle \Psi | \hat{a}_m^\dagger \hat{a}_n^\dagger \hat{a}_n \hat{a}_m | \Psi \rangle, \quad (7.1)$$

$$\Gamma_{m,n,p}^{(3)} = \langle \Psi | \hat{a}_m^\dagger \hat{a}_n^\dagger \hat{a}_p^\dagger \hat{a}_p \hat{a}_n \hat{a}_m | \Psi \rangle, \quad (7.2)$$

$$\Gamma_{m,n,p,q}^{(4)} = \langle \Psi | \hat{a}_m^\dagger \hat{a}_n^\dagger \hat{a}_p^\dagger \hat{a}_q^\dagger \hat{a}_q \hat{a}_p \hat{a}_n \hat{a}_m | \Psi \rangle, \quad (7.3)$$

\vdots

where $|\Psi\rangle$ is the total quantum state given by Equation(2.13), including the higher order pair production

terms. Going beyond two-port directional couplers, an N -waveguide array may allow higher order correlations to be engineered so as to suppress the probability of obtaining more than two photons from a given pair of output waveguides, even if higher order pair production is present. For example, if obtaining a photon in waveguide n is highly correlated with obtaining a second photon in a different waveguide m , a situation where $\Gamma_{m,n,n}^{(3)}$, $\Gamma_{m,n,m}^{(3)}$, $\Gamma_{m,n,m,n}^{(4)}$, $\Gamma_{m,n,n,m}^{(4)}$, $\Gamma_{m,n,m,m}^{(4)}$, and $\Gamma_{m,n,n,n}^{(4)}$ all approach zero would effectively filter higher-order terms from anti-bunched output states taken from these waveguides.

As with IFPS, the judicious use of path-entangled states at the input can help tailor the output correlations towards their desired values through quantum interference. This can pivot on the dual-path source designed in this dissertation, which can serve as a building block for N -path sources as seen in Figure 7.1. Furthermore, the waveguide array itself has several degrees of freedom over how it transforms the input state; for example, the interaction length L , the effective index mismatch Δn_{eff} , and variability in the waveguide pitch. Together with the ability to alter the relative phase between input paths, these provide a diverse set of tools for engineering the output state correlations. Figure 7.1 presents an example of what such a waveguide array/source combination may look like. Recent work

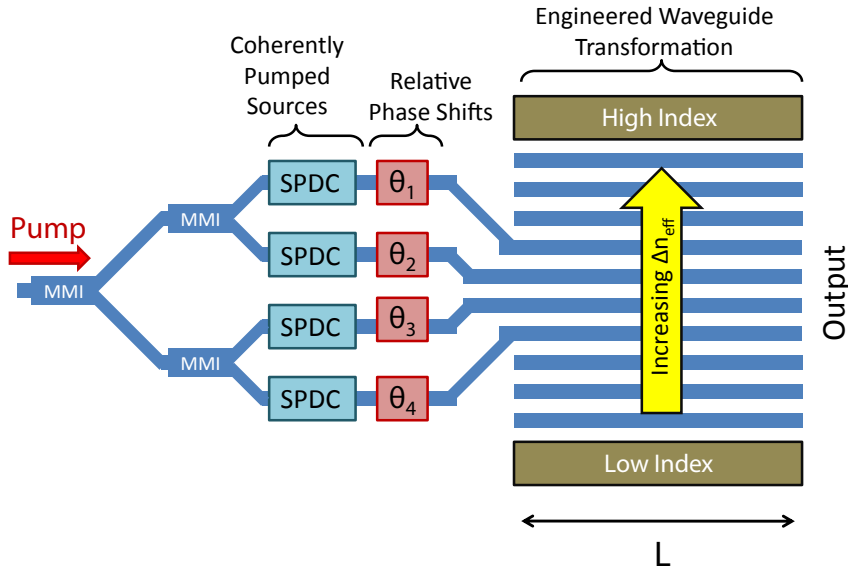


Figure 7.1: Illustration of a possible waveguide array and source configuration for engineering higher-order photon correlations. An effective index gradient across the array allows Bloch oscillations to be supported. [12].

has shown that arrays supporting Bloch oscillations exhibit transitions from bunching to anti-bunching behaviour over length scales that depend on the photon number of the initial state as well as the relative location of the input paths [12, 146–148]. Since this evolution is sensitive to the phase acquired by the photons, which scales with the number of photons in the state, differences in evolution between the

single-pair and multi-pair terms could be advantageous. Phase-controlled photonic transport [149] is another interesting concept with potential uses for correlation engineering.

Appropriate parameters for achieving desired correlations can be guided through standard numerical optimization. Assuming nearest-neighbour coupling and applying periodic boundary conditions, the input and output mode operators can be related by [105, 149]

$$\hat{b}_n = \sum_m G_{n,m}(z) \hat{a}_m \quad (7.4)$$

where the $G_{n,m}(z)$ are Greens functions obeying

$$\frac{dG_{n,m}(z)}{dz} = -i\beta_n G_{n,m}(z) - iJ(G_{n+1,m}(z) + G_{n-1,m}(z)), \quad (7.5)$$

with J representing the coupling strength. The above expression comes from Heisenberg's equations using an interaction Hamiltonian describing the waveguide array [149], and admits analytic solutions to the state evolution. Solving for the Greens functions provides a convenient way of relating input and output correlations using transfer functions, i.e.

$$\Gamma_{n,m}^{(2)} = \langle \hat{b}_m^\dagger \hat{b}_n^\dagger \hat{b}_n \hat{b}_m \rangle = \sum_{pqlr} G_{m,p}^*(L) G_{n,q}^*(L) G_{m,l}(L) G_{n,r}(L) \langle \hat{a}_p^\dagger \hat{a}_q^\dagger \hat{a}_l \hat{a}_r \rangle \quad (7.6)$$

Using the above formulation, the tailoring of the output correlations can be reduced to the generic problem of designing a unitary evolution \hat{U} that transforms the input correlations into the desired output correlations. Figure 7.2 depicts a lumped-element representation of the corresponding circuit. The input correlations themselves are also treated as a design variable, and additional output processing (such as a 50:50 directional coupler) may be required. Once a suitable combination of these parameters has been identified, a physical source and waveguide array can be designed to implement them. It is worth investigating whether such a design approach can lead to the creation of a 'correlation filter' that curbs the effects of higher order pair production to allow increased photon pair generation rates to be utilized.

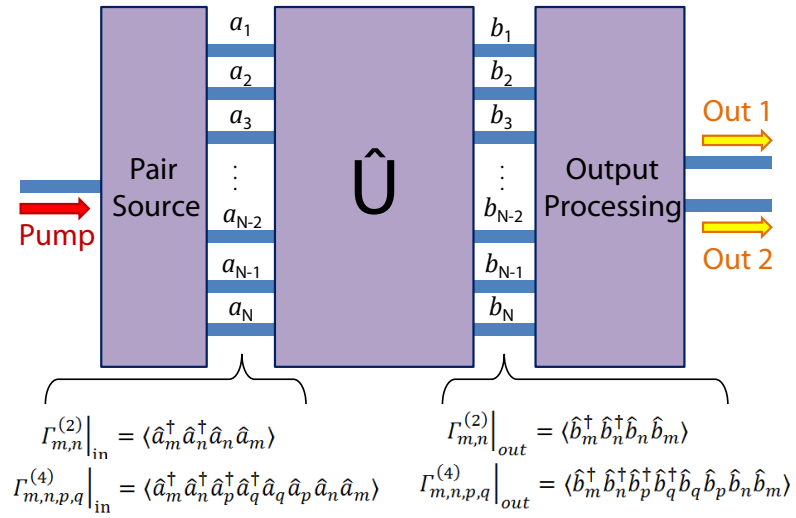


Figure 7.2: A three-stage integrated circuit, where the unitary transformation \hat{U} represents a coupled waveguide array. Input correlations and the output selection are chosen with \hat{U} to target the desired output correlations.

Appendix A

The Schmidt Decomposition

Consider a bipartite system comprised of two Hilbert spaces $H_{(1)} \otimes H_{(2)}$ of equal dimension, and let $|\psi\rangle$ be a pure state of this system. There exist orthonormal states $|i\rangle_{(1)}$ and $|i\rangle_{(2)}$ of the two subsystems such that [150]

$$|\psi\rangle = \sum_i \sqrt{p_i} |i\rangle_{(1)} \otimes |i\rangle_{(2)}. \quad (\text{A.1})$$

The states $|i\rangle_{(1)}$ and $|i\rangle_{(2)}$ are eigenstates of the subsystems only if the composite density matrix is separable as $\rho = \rho^{(1)} \otimes \rho^{(2)}$, i.e. no entanglement exists between the subsystems. Let $|j\rangle$ and $|k\rangle$ be the eigenstates of the individual subsystems. A general expression for the total state is given by

$$|\psi\rangle = \sum_{jk} A_{jk} |j\rangle |k\rangle. \quad (\text{A.2})$$

The matrix A_{jk} includes any correlations between the subsystems, and has a singular value decomposition of the form

$$A_{jk} = \sum_i U_{ji} d_{ii} V_{ik}, \quad (\text{A.3})$$

where U_{ji} and V_{ik} are unitary matrices, and d_{ii} is a non-negative diagonal matrix. The total state can then be written in the form of Equation (A.1) by defining $|i\rangle_{(1)} = \sum_j U_{ji} |j\rangle$, $|i\rangle_{(2)} = \sum_k V_{ik} |k\rangle$, and $\sqrt{p_i} = d_{ii}$. For a two-photon state described by

$$|\psi\rangle = \int d\omega_1 d\omega_2 \phi(\omega_1, \omega_2) |\omega_1\rangle_{(1)} |\omega_2\rangle_{(2)}, \quad (\text{A.4})$$

the BPA $\phi(\omega_1, \omega_2)$ takes the place of A_{jk} and can be written as

$$\phi(\omega_1, \omega_2) = \sum_n \sqrt{p_n} U_n(\omega_1) V_n(\omega_2), \quad (\text{A.5})$$

where $U_n(\omega)$ and $V_n(\omega)$ are the Schmidt modes.

The p_n are given by the eigenvalues of Equation (2.9), which is obtained by taking a partial trace of the bipartite density matrix ρ over one of the composite systems. When the quantum state is expressed in more than one degree of freedom, the appropriate density matrix can be obtained by first tracing over all other degrees of freedom (e.g., polarization, path) so that only the Hilbert spaces for frequency remain.

To account for state impurity, the density matrix formalism is used and an additional subspace corresponding to a quantum bath is introduced. The interaction can then be represented as a unitary transformation that leads to the entanglement of the photon pair and quantum bath subspaces [150]. Tracing out the latter yields the mixed-state density matrix $\tilde{\rho}$. Then, after tracing out all other degrees of freedom and taking the partial trace over one of the frequencies, the Schmidt number can be calculated from the eigenvalues of the resultant matrix elements.

Appendix B

Derivation of Coupler Mode Transformations

The coupling of modes between two optical waveguides can be described in terms of the interaction Hamiltonian [105]

$$\hat{\mathcal{H}}_{\text{int}} = \hbar \sum_{\sigma} \int d\omega J_{\sigma}(\omega) [\hat{a}_{\sigma}^{A\dagger}(\omega) \hat{a}_{\sigma}^B(\omega) + \hat{a}_{\sigma}^{B\dagger}(\omega) \hat{a}_{\sigma}^A(\omega)]. \quad (\text{B.1})$$

where $J_{\sigma}(\omega)$ represents a generic coupling strength. The total Hamiltonian for the system is then

$$\hat{\mathcal{H}} = \sum_{\sigma} \int d\omega \hbar\omega [\hat{a}_{\sigma}^{A\dagger}(\omega) \hat{a}_{\sigma}^A(\omega) + \hat{a}_{\sigma}^{B\dagger}(\omega) \hat{a}_{\sigma}^B(\omega)] + \hat{\mathcal{H}}_{\text{int}}. \quad (\text{B.2})$$

To obtain the mode operator evolution in the Heisenberg picture, one must solve the Heisenberg equations of motion for each $j \in \{A, B\}$, given by

$$i\hbar \frac{d}{dt} \hat{a}_{\alpha}^j(\omega) = [\hat{a}_{\alpha}^j(\omega), \hat{\mathcal{H}}]. \quad (\text{B.3})$$

This leads to coupled mode operator equations

$$\frac{d}{dt} \hat{a}_{\alpha}^A(\omega) = -i\omega \hat{a}_{\alpha}^A(\omega) - iJ_{\sigma}(\omega) \hat{a}_{\alpha}^B(\omega), \quad (\text{B.4})$$

$$\frac{d}{dt} \hat{a}_{\alpha}^B(\omega) = -i\omega \hat{a}_{\alpha}^B(\omega) - iJ_{\sigma}(\omega) \hat{a}_{\alpha}^A(\omega). \quad (\text{B.5})$$

$$(\text{B.6})$$

The solution to these equations, obtainable through Laplace transform techniques, is

$$\hat{a}_\alpha^A(\omega; t) = \cos(J_\sigma(\omega)t)\hat{a}_\alpha^A(\omega; 0)e^{-i\omega t} - i \sin(J_\sigma(\omega)t)\hat{a}_\alpha^B(\omega; 0)e^{-i\omega t} \quad (\text{B.7})$$

$$\hat{a}_\alpha^B(\omega; t) = \cos(J_\sigma(\omega)t)\hat{a}_\alpha^B(\omega; 0)e^{-i\omega t} - i \sin(J_\sigma(\omega)t)\hat{a}_\alpha^A(\omega; 0)e^{-i\omega t} \quad (\text{B.8})$$

For symmetric waveguides without modal mismatch (i.e. identical propagation constants), these can be re-expressed using $\sqrt{\eta_\sigma(\omega)} = \cos(J_\sigma(\omega)t)$ and $\sqrt{1 - \eta_\sigma(\omega)} = \sin(J_\sigma(\omega)t)$. Any pulse broadening occurring over the interaction length will be approximately independent of the input path taken, hence the phase evolution can be rewritten using $\omega t = \beta_\sigma(\omega)z$ and grouped with the output mode operators to define $\hat{b}_\sigma^j(\omega) = \hat{a}_\sigma^j(\omega; t)e^{i\beta_\sigma(\omega)z}$. This phase shift in z accounts for the change in spatial coordinates of the mode operator relative to those of the input. The mode transformation equations then become

$$\begin{bmatrix} \hat{b}_\sigma^A(\omega) \\ \hat{b}_\sigma^B(\omega) \end{bmatrix} = \begin{bmatrix} \sqrt{\eta_\sigma(\omega)} & -i\sqrt{1 - \eta_\sigma(\omega)} \\ -i\sqrt{1 - \eta_\sigma(\omega)} & \sqrt{\eta_\sigma(\omega)} \end{bmatrix} \begin{bmatrix} \hat{a}_\sigma^A(\omega) \\ \hat{a}_\sigma^B(\omega) \end{bmatrix}. \quad (\text{B.9})$$

for the annihilation operators, and similarly

$$\begin{bmatrix} \hat{b}_\sigma^{A\dagger}(\omega) \\ \hat{b}_\sigma^{B\dagger}(\omega) \end{bmatrix} = \begin{bmatrix} \sqrt{\eta_\sigma(\omega)} & i\sqrt{1 - \eta_\sigma(\omega)} \\ i\sqrt{1 - \eta_\sigma(\omega)} & \sqrt{\eta_\sigma(\omega)} \end{bmatrix} \begin{bmatrix} \hat{a}_\sigma^{A\dagger}(\omega) \\ \hat{a}_\sigma^{B\dagger}(\omega) \end{bmatrix}. \quad (\text{B.10})$$

for the mode creation operators.

Appendix C

Generation of Path Entanglement through Coherent Pumping

A completely quantum formalism is utilized to show that coherent pumping of two nonlinear waveguides leads to a path-entangled anti-bunched output state. Consider a pump represented by the coherent state

$$|\Gamma_0\rangle_{I,\sigma,\omega} = \exp\left(\Gamma_0\hat{A}^{I\dagger} - h.c.\right)|\text{vac}\rangle, \quad (\text{C.1})$$

where I denotes the input waveguide, $h.c.$ refers to the Hermitian conjugate, and $\hat{A}^{j\dagger} = \int d\omega \phi_P(\omega)\hat{a}_\sigma^{j\dagger}(\omega)$, with $\phi_P(\omega)$ giving the pump spectrum. Suppose this state is evolved through a 50:50 splitter such as an MMI or directional coupler. It is reasonable to approximate the splitter response as frequency-independent since the pump wavelength will change at most by a few nanometers to tune the photon pair non-degeneracy, and typical pump bandwidths are also on the order of a few nanometers or less. The mode operators then transform according to $\hat{a}_\sigma^{I\dagger}(\omega) \rightarrow [\hat{a}^{A\dagger}(\omega) + z\hat{a}^{B\dagger}(\omega)]/\sqrt{2}$, where z is a complex phase factor that is equal to unity for a 1-by-2 port MMI, and equal to $(-i)$ for a 2-by-2 port directional coupler. The total quantum state becomes

$$\begin{aligned} |\Psi\rangle &= \exp\left((\Gamma_0/\sqrt{2})\hat{A}^{A\dagger} + z(\Gamma_0/\sqrt{2})\hat{A}^{B\dagger} - h.c.\right)|\text{vac}\rangle, \\ &= \exp\left((\Gamma_0/\sqrt{2})\hat{A}^{A\dagger} - h.c.\right) \exp\left((z\Gamma_0/\sqrt{2})\hat{A}^{B\dagger} - h.c.\right)|\text{vac}\rangle, \\ &= \left|\frac{\Gamma_0}{\sqrt{2}}\right\rangle_{A,\sigma,\omega} \left|\frac{z\Gamma_0}{\sqrt{2}}\right\rangle_{B,\sigma,\omega}. \end{aligned} \quad (\text{C.2})$$

Suppose now that each path contains a nonlinear waveguide that supports SPDC. The resultant state after the nonlinear interaction can be obtained using the Backwards Heisenberg Picture approach [61], which is one of the only derivations for the generated SPDC state that retains fully quantum expressions for the pump without approximating it by a classical field. Using the un-depleted pump approximation, Ref. [61] shows that each term in the above product state maps as

$$\begin{aligned} |z\Gamma_j\rangle &\rightarrow \exp\left(z\Gamma_j\hat{A}^{j\dagger} + z\mu_j\hat{C}_{II}^{j\dagger} - h.c.\right)|\text{vac}\rangle \\ &= \exp\left(z\Gamma_j\hat{A}^{j\dagger} - h.c.\right)\exp\left(z\mu_j\hat{C}_{II}^{j\dagger} - h.c.\right)|\text{vac}\rangle \end{aligned} \quad (\text{C.3})$$

where $\hat{C}_{II}^{j\dagger}|\text{vac}\rangle = \sum_{\alpha\beta} \int d\omega_1 d\omega_2 \phi_{\alpha\beta}^j(\omega_1, \omega_2) \hat{a}_\alpha^j(\omega_1) \hat{a}_\beta^j(\omega_2) |\text{vac}\rangle \equiv |\psi\rangle_j$, and the factorization in the second line is possible because all non-vanishing pump mode operators commute with those of the downconverted photon spectra. The first term is the coherent state corresponding to the undepleted pump, and can be dropped to leave only the SPDC terms. Hence, the total state becomes:

$$|\Psi_{\text{SPDC}}\rangle = \exp\left(\mu_A\hat{C}_{II}^{A\dagger} - h.c.\right)\exp\left(z\mu_B\hat{C}_{II}^{B\dagger} - h.c.\right)|\text{vac}\rangle \quad (\text{C.4})$$

Taking the Taylor expansion of the exponentials to first order, this reduces to

$$\begin{aligned} |\Psi_{\text{SPDC}}\rangle &= \left(1 + \mu_A\hat{C}_{II}^{A\dagger}\right)\left(1 + z\mu_B\hat{C}_{II}^{B\dagger}\right)|\text{vac}\rangle \\ &= |\text{vac}\rangle + \mu_A|\psi\rangle_A + z\mu_B|\psi\rangle_B + z\mu_A\mu_B|\psi\rangle_A|\psi\rangle_B. \end{aligned} \quad (\text{C.5})$$

The amplitudes μ_A and μ_B can be used to account for unequal pair generation rates. It will be assumed that pumping and the conversion efficiency are equal in both paths so that $\mu_A = \mu_B$, and these factors are amalgamated into the BPAs. Keeping only the two-photon terms, the total SPDC state is then

$$|\psi_{\text{SPDC}}\rangle = |\psi\rangle_A + z|\psi\rangle_B, \quad (\text{C.6})$$

which is anti-bunched, path-entangled, and takes the same form as Equation(3.1).

Appendix D

Two-Photon Outcome Probabilities

Complete expressions for the output probabilities referred to by Equations (3.26)-(3.28) are listed below:

$$R_{AB} = \sum_{\alpha\beta} \int d\omega_1 d\omega_2 \left[\eta_\alpha(\omega_1) [1 - \eta_\beta(\omega_2)] |\phi_{\alpha\beta}^A(\omega_1, \omega_2)|^2 + [1 - \eta_\alpha(\omega_1)] \eta_\beta(\omega_2) |\phi_{\alpha\beta}^B(\omega_1, \omega_2)|^2 \right. \quad (\text{D.1}) \\ \left. + 2\text{Re} \left\{ e^{-i\theta} \phi_{\alpha\beta}^B(\omega_1, \omega_2) \phi_{\alpha\beta}^{A*}(\omega_1, \omega_2) e^{-i[\omega_1 + \omega_2]\tau} \sqrt{[1 - \eta_\alpha(\omega_1)] \eta_\beta(\omega_2) \eta_\alpha(\omega_1) [1 - \eta_\beta(\omega_2)]} \right\} \right],$$

$$R_{BA} = \sum_{\alpha\beta} \int d\omega_1 d\omega_2 \left[[1 - \eta_\alpha(\omega_1)] \eta_\beta(\omega_2) |\phi_{\alpha\beta}^A(\omega_1, \omega_2)|^2 + \eta_\alpha(\omega_1) [1 - \eta_\beta(\omega_2)] |\phi_{\alpha\beta}^B(\omega_1, \omega_2)|^2 \quad (\text{D.2}) \right. \\ \left. + 2\text{Re} \left\{ e^{-i\theta} \phi_{\alpha\beta}^B(\omega_1, \omega_2) \phi_{\alpha\beta}^{A*}(\omega_1, \omega_2) e^{-i[\omega_1 + \omega_2]\tau} \sqrt{\eta_\alpha(\omega_1) [1 - \eta_\beta(\omega_2)] [1 - \eta_\alpha(\omega_1)] \eta_\beta(\omega_2)} \right\} \right],$$

$$R_{AA} = \sum_{\alpha\beta} \int d\omega_1 d\omega_2 \left[\eta_\alpha(\omega_1) \eta_\beta(\omega_2) |\phi_{\alpha\beta}^A(\omega_1, \omega_2)|^2 + [1 - \eta_\alpha(\omega_1)] [1 - \eta_\beta(\omega_2)] |\phi_{\alpha\beta}^B(\omega_1, \omega_2)|^2 \quad (\text{D.3}) \right. \\ \left. - 2\text{Re} \left\{ e^{-i\theta} \phi_{\alpha\beta}^B(\omega_1, \omega_2) \phi_{\alpha\beta}^{A*}(\omega_1, \omega_2) e^{-i[\omega_1 + \omega_2]\tau} \sqrt{[1 - \eta_\alpha(\omega_1)] [1 - \eta_\beta(\omega_2)] \eta_\alpha(\omega_1) \eta_\beta(\omega_2)} \right\} \right],$$

$$R_{BB} = \sum_{\alpha\beta} \int d\omega_1 d\omega_2 \left[[1 - \eta_\alpha(\omega_1)] [1 - \eta_\beta(\omega_2)] |\phi_{\alpha\beta}^A(\omega_1, \omega_2)|^2 + \eta_\alpha(\omega_1) \eta_\beta(\omega_2) |\phi_{\alpha\beta}^B(\omega_1, \omega_2)|^2 \quad (\text{D.4}) \right. \\ \left. - 2\text{Re} \left\{ e^{-i\theta} \phi_{\alpha\beta}^B(\omega_1, \omega_2) \phi_{\alpha\beta}^{A*}(\omega_1, \omega_2) e^{-i[\omega_1 + \omega_2]\tau} \sqrt{\eta_\alpha(\omega_1) \eta_\beta(\omega_2) [1 - \eta_\alpha(\omega_1)] [1 - \eta_\beta(\omega_2)]} \right\} \right],$$

The normalization condition is now checked. Normalization requires $\sum_{pq} R_{pq} = 1$. Summing the above equations leads to

$$\begin{aligned} \sum_{pq} R_{pq} = \sum_{\alpha\beta} \int d\omega_1 d\omega_2 \left[\Upsilon_{\alpha\beta}(\omega_1, \omega_2) \left(|\phi_{\alpha\beta}^A(\omega_1, \omega_2)|^2 + |\phi_{\alpha\beta}^B(\omega_1, \omega_2)|^2 \right) \right. \\ \left. + 4\Xi_{\alpha\beta}(\omega_1, \omega_2, \tau) - 4\Xi_{\alpha\beta}(\omega_1, \omega_2, \tau) \right] \end{aligned} \quad (\text{D.5})$$

where

$$\Xi_{\alpha\beta}(\omega_1, \omega_2, \theta, \tau) = \text{Re} \left\{ e^{-i\theta} \phi_{\alpha\beta}^B(\omega_1, \omega_2) \phi_{\alpha\beta}^{A*}(\omega_1, \omega_2) e^{-i[\omega_1 + \omega_2]\tau} \sqrt{\eta_\alpha(\omega_1) \eta_\beta(\omega_2) [1 - \eta_\alpha(\omega_1)] [1 - \eta_\beta(\omega_2)]} \right\} \quad (\text{D.6})$$

and

$$\begin{aligned} \Upsilon_{\alpha\beta}(\omega_1, \omega_2) &= \eta_\alpha(\omega_1) \eta_\beta(\omega_2) + [1 - \eta_\alpha(\omega_1)] \eta_\beta(\omega_2) + \eta_\alpha(\omega_1) [1 - \eta_\beta(\omega_2)] + [1 - \eta_\alpha(\omega_1)] [1 - \eta_\beta(\omega_2)] \\ &= 2\eta_\alpha(\omega_1) \eta_\beta(\omega_2) - 2\eta_\alpha(\omega_1) \eta_\beta(\omega_2) + \eta_\alpha(\omega_1) - \eta_\alpha(\omega_1) + \eta_\beta(\omega_2) - \eta_\beta(\omega_2) + 1 \\ &= 1. \end{aligned} \quad (\text{D.7})$$

The terms containing $\Xi_{\alpha\beta}(\omega_1, \omega_2, \tau)$ cancel, and the expression simplifies to

$$\begin{aligned} \sum_{pq} R_{pq} &= \sum_{\alpha\beta} \int d\omega_1 d\omega_2 \left(|\phi_{\alpha\beta}^A(\omega_1, \omega_2)|^2 + |\phi_{\alpha\beta}^B(\omega_1, \omega_2)|^2 \right) \\ &= \sum_j \sum_{\alpha\beta} \int d\omega_1 d\omega_2 |\phi_{\alpha\beta}^j(\omega_1, \omega_2)|^2 \\ &= 1, \end{aligned} \quad (\text{D.8})$$

where the last line follows from the original BPA normalization condition given by Equation (3.2).

Appendix E

Maximal Contour for Cross-Polarized States

In Chapter 3.4.2, Equation 3.40 provided a general approximation to the IFPS separation probability P_S based on the central wavelength splitting ratios, in the case of co-polarized photon pair states. It is clear from Figure 3.9 that the contour $\eta^{(1)} + \eta^{(2)} = 1$ leads to maximal P_S . However, for cross-polarized states, the approximated P_S behaviour becomes a four-dimensional function of $\eta_\sigma^{(j)}$, where $j \in \{1, 2\}$ and $\sigma \in \{\text{TE}, \text{TM}\}$. The contour of maximal P_S is thus not straightforward to visualize, and must be discerned directly from the analytic expression for P_S .

In the case of co-polarized states, Equation 3.40 can be rewritten in the form $P_S = A+B+2\sqrt{AB}$ using the definitions $A = \eta^{(1)}[1-\eta^{(2)}]$ and $B = \eta^{(2)}[1-\eta^{(1)}]$. Note that this is equivalent to $P_S = (\sqrt{A}+\sqrt{B})^2$; setting $P_S = 1$ then leads to the simplification $\sqrt{A} + \sqrt{B} = 1$. This expression is self-consistent with the substitutions $[1 - \eta^{(2)}] = \eta^{(1)}$ in A and $[1 - \eta^{(1)}] = \eta^{(2)}$ in B , which convert it to $\eta^{(1)} + \eta^{(2)} = 1$.

For cross-polarized states, in the special case of maximal polarization entanglement, a simple expression for the maximal P_S contour can likewise be obtained. Beginning with the general Equations (3.26)-(3.35), the following assumptions are made: $\phi_{\alpha\beta}^A(\omega_1, \omega_2) = \phi_{\alpha\beta}^B(\omega_1, \omega_2) = \phi_{\alpha\beta}(\omega_1, \omega_2)$ (symmetric paths); $\phi_{\alpha\beta}(\omega_1, \omega_2) = \phi_{\beta\alpha}(\omega_1, \omega_2)$ (maximal polarization entanglement); and $\phi_{\alpha\beta}(\omega_1, \omega_2) = \delta(\omega - \omega_1)\delta(\omega' - \omega_2)\delta_{\alpha\alpha'}\delta_{\beta\beta'}/\sqrt{4}$ (delta-function spectral simplification), where $1/\sqrt{4}$ comes from normalization requirements. Letting $\eta_\sigma^{(j)}$ represent the directional coupler splitting ratio at the central

wavelength of photon j for polarization σ , the separation probability simplifies to

$$P_S = \frac{1}{2} \left(\eta_{\text{TE}}^{(1)} [1 - \eta_{\text{TM}}^{(2)}] + [1 - \eta_{\text{TE}}^{(1)}] \eta_{\text{TM}}^{(2)} + \eta_{\text{TM}}^{(1)} [1 - \eta_{\text{TE}}^{(2)}] + [1 - \eta_{\text{TM}}^{(1)}] \eta_{\text{TE}}^{(2)} \right) \\ + \sqrt{\eta_{\text{TE}}^{(1)} [1 - \eta_{\text{TM}}^{(2)}] [1 - \eta_{\text{TE}}^{(1)}] \eta_{\text{TM}}^{(2)}} + \sqrt{\eta_{\text{TM}}^{(1)} [1 - \eta_{\text{TE}}^{(2)}] [1 - \eta_{\text{TM}}^{(1)}] \eta_{\text{TE}}^{(2)}}. \quad (\text{E.1})$$

Defining $A = \eta_{\text{TE}}^{(1)} [1 - \eta_{\text{TM}}^{(2)}] / 2$, $B = [1 - \eta_{\text{TE}}^{(1)}] \eta_{\text{TM}}^{(2)} / 2$, $C = \eta_{\text{TM}}^{(1)} [1 - \eta_{\text{TE}}^{(2)}] / 2$, and $D = [1 - \eta_{\text{TM}}^{(1)}] \eta_{\text{TE}}^{(2)} / 2$, Equation (E.1) can be rewritten as $P_S = A + B + C + D + 2\sqrt{AB} + 2\sqrt{CD} = (\sqrt{A} + \sqrt{B})^2 + (\sqrt{C} + \sqrt{D})^2$. Maximal P_S is expected when $\eta_{\text{TE}}^{(1)} + \eta_{\text{TM}}^{(2)} = 1$ and $\eta_{\text{TM}}^{(1)} + \eta_{\text{TE}}^{(2)} = 1$ occur simultaneously; making these substitutions for $P_S = 1$ gives

$$\frac{1}{2} [\eta_{\text{TE}}^{(1)} + \eta_{\text{TM}}^{(2)}]^2 + \frac{1}{2} [\eta_{\text{TM}}^{(1)} + \eta_{\text{TE}}^{(2)}]^2 = 1 \quad (\text{E.2})$$

for the ideal contour. Hence, defining $\Sigma = [\eta_{\text{TE}}^{(1)} + \eta_{\text{TM}}^{(2)}]^2 / 2 + [\eta_{\text{TM}}^{(1)} + \eta_{\text{TE}}^{(2)}]^2 / 2$, the proximity of Σ to unity provides a metric for quantifying the splitting ratio anti-symmetry, analogous to role played by the sum $\eta^{(1)} + \eta^{(2)}$ for co-polarized states.

Bibliography

- [1] J. C. F. Matthews, A. Politi, A. Stefanov, and J. L. O'Brien. "Manipulation of multiphoton entanglement in waveguide quantum circuits." *Nature Photon.* **3**, 346 (2009).
- [2] M. F. Saleh, G. D. Giuseppe, B. E. A. Saleh, and M. C. Teich. "Photonic Circuits for Generating Modal, Spectral, and Polarization Entanglement." *IEEE Photon. J.* **2**, 736 (2010).
- [3] J. Chen, K. F. Lee, and P. Kumar. "Deterministic quantum splitter based on time-reversed Hong-Ou-Mandel interference." *Phys. Rev. A* **79**, 031804 (2007).
- [4] J. W. Silverstone, D. Bonneau, K. Ohira, N. Suzuki, H. Yoshida, N. Iizuka, M. Ezaki, C. M. Natarajan, M. G. Tanner, R. H. Hadfield, V. Zwiller, G. D. Marshall, J. G. Rarity, J. L. O'Brien, and M. G. Thompson. "On-chip quantum interference between silicon photon-pair sources." *Nature Photon.* **8**, 104 (2014).
- [5] S. V. Zhukovsky, L. G. Helt, P. Abolghasem, D. Kang, J. E. Sipe, and A. S. Helmy. "Bragg reflection waveguides as integrated sources of entangled photon pairs." *J. Opt. Soc. Am. B* **29**, 2516 (2012).
- [6] M. Thompson, A. Politi, J. Matthews, and J. O'Brien. "Integrated waveguide circuits for optical quantum computing." *IET Circ. Device Syst.* **5**, 94 (2011).
- [7] J. W. Fleming. "Dispersion in GeO₂-SiO₂ glasses." *Appl. Opt.* **23**, 4486 (1984).
- [8] S. Gehrsitz, F. K. Reinhart, C. Gourgon, N. Herres, A. Vonlanthen, and H. Sigg. "The refractive index of AlGaAs below the band gap: Accurate determination and empirical modeling." *J. Appl. Phys.* **87**, 7825 (2000).
- [9] P. Abolghasem, J. Han, B. J. Bijlani, A. Arjmand, and A. S. Helmy. "Highly Efficient Second-Harmonic Generation in Monolithic Matching Layer Enhanced AlGaAs Bragg Reflection Waveguides." *IEEE Photon. Technol. Lett.* **21**, 1462 (2009).

- [10] P. Abolghasem. *Phase-Matching Second-Order Optical Nonlinear Interactions using Bragg Reflection Waveguides: A Platform for Integrated Parametric Devices*. Ph.D. thesis, University of Toronto, Department of Electrical and Computer Engineering (2011).
- [11] R. T. Horn, P. Kolenderski, D. Kang, P. Abolghasem, C. Scarcella, A. D. Frera, A. Tosi, L. G. Helt, S. V. Zhukovsky, J. E. Sipe, G. Weihs, A. S. Helmy, and T. Jennewein. “Inherent polarization entanglement generated from a monolithic semiconductor chip.” *Sci. Rep.* **3**, 2314 (2013).
- [12] U. Peschel, T. Pertsch, and F. Lederer. “Optical Bloch oscillations in waveguide arrays.” *Opt. Lett.* **23**, 1701 (1998).
- [13] A. Einstein, B. Podolsky, and N. Rosen. “Can Quantum-Mechanical Description of Physical Reality Be Considered Complete?” *Phys. Rev.* **47**, 777 (1935).
- [14] J. S. Bell. “On the Einstein Podolsky Rosen Paradox.” *Physics* **1**, 195 (1964).
- [15] A. Aspect, P. Grangier, and G. Roger. “Experimental Tests of Realistic Local Theories via Bell’s Theorem.” *Phys. Rev. Lett.* **47**, 460 (1981).
- [16] A. Aspect, P. Grangier, and G. Roger. “Experimental Realization of Einstein-Podolsky-Rosen-Bohm Gedankenexperiment: A New Violation of Bell’s Inequalities.” *Phys. Rev. Lett.* **49**, 91 (1982).
- [17] C. K. Hong, Z. Y. Ou, and L. Mandel. “Measurement of Subpicosecond Time Intervals between Two Photons by Interference.” *Phys. Rev. Lett.* **59**, 2044 (1987).
- [18] X. Y. Zou, L. J. Wang, and L. Mandel. “Induced coherence and indistinguishability in optical interference.” *Phys. Rev. Lett.* **67**, 318 (1991).
- [19] J. D. Franson. “Two-photon interferometry over large distances.” *Phys. Rev. A* **44**, 4552 (1991).
- [20] T. B. Pittman, D. V. Strekalov, A. Migdall, M. H. Rubin, A. V. Sergienko, and Y. H. Shih. “Can Two-Photon Interference be Considered the Interference of Two Photons?” *Phys. Rev. Lett.* **77**, 1917 (1996).
- [21] D. V. Strekalov, T. B. Pittman, and Y. H. Shih. “What we can learn about single photons in a two-photon interference experiment.” *Phys. Rev. A* **57**, 567 (1998).
- [22] R. Horodecki, P. Horodecki, M. Horodecki, and K. Horodecki. “Quantum entanglement.” *Rev. Mod. Phys.* **81**, 865 (2009).

- [23] D. Bouwmeester, J.-W. Pan, K. Mattle, M. Eibl, H. Weinfurter, and A. Zeilinger. “Experimental quantum teleportation.” *Nature* **390**, 575 (1997).
- [24] Z. Zhao, T. Yang, Yu-Ao, A.-N. Zhang, and J.-W. Pan. “Experimental Realization of Entanglement Concentration and a Quantum Repeater.” *Phys. Rev. Lett.* **90**, 207901 (2003).
- [25] I. Afek, O. Ambar, and Y. Silberberg. “High-NOON States by Mixing Quantum and Classical Light.” *Science* **328**, 879 (2010).
- [26] M. Kacprowicz, R. Demkowicz-Dobrzański, W. Wasilewski, K. Banaszek, and I. A. Walmsley. “Experimental quantum-enhanced estimation of a lossy phase shift.” *Nature Photon.* **4**, 357 (2010).
- [27] V. Giovannetti, S. Lloyd, and L. Maccone. “Advances in quantum metrology.” *Nature Photon.* **5**, 222 (2011).
- [28] T. Ono, R. Okamoto, and S. Takeuchi. “An entanglement-enhanced microscope.” *Nat. Commun.* **4**, 2426 (2013).
- [29] M. A. Taylor, J. Janousek, V. Daria, J. Knittel, B. Hage, H.-A. Bachor, and W. P. Bowen. “Subdiffraction-Limited Quantum Imaging within a Living Cell.” *Phys. Rev. X* **4**, 011017 (2014).
- [30] Y. Israel, S. Rosen, and Y. Silberberg. “Supersensitive Polarization Microscopy Using NOON States of Light.” *Phys. Rev. Lett.* **112**, 103604 (2014).
- [31] O. Roslyak, C. A. Marx, and S. Mukamel. “Nonlinear spectroscopy with entangled photons: Manipulating quantum pathways of matter.” *Phys. Rev. A* **79**, 033832 (2009).
- [32] F. Schlawin, K. E. Dorfman, B. P. Fingerhut, and S. Mukamel. “Suppression of population transport and control of exciton distributions by entangled photons.” *Nat. Commun.* **4**, 1782 (2013).
- [33] F. Schlawin and S. Mukamel. “Two-photon spectroscopy of excitons with entangled photons.” *J. Chem. Phys.* **139**, 244110 (2013).
- [34] F. Schlawin and S. Mukamel. “Matter correlations induced by coupling to quantum light.” *Phys. Rev. A* **89**, 013830 (2014).
- [35] G. B. Lemos, V. Borish, G. D. Cole, S. Ramelow, R. Lapkiewicz, and A. Zeilinger. “Quantum imaging with undetected photons.” *Nature* **512**, 409 (2014).

- [36] C. H. Bennett and G. Brassard. “Quantum cryptography: Public key distribution and coin tossing.” *Proc. of IEEE International Conference on Computers, Systems and Signal Processing* **175**, 8 (1984).
- [37] H.-K. Lo and H. F. Chau. “Unconditional Security of Quantum Key Distribution over Arbitrarily Long Distances.” *Science* **283**, 2052 (1999).
- [38] N. Gisin, G. Ribordy, W. Tittel, and H. Zbinden. “Quantum cryptography.” *Rev. Mod. Phys.* **74**, 145 (2002).
- [39] V. Scarani, H. Bechmann-Pasquinucci, N. J. Cerf, M. Dušek, N. Lütkenhaus, and M. Peev. “The security of practical quantum key distribution.” *Rev. Mod. Phys.* **81**, 1301 (2009).
- [40] H.-K. Lo, M. Curty, and B. Qi. “Measurement-Device-Independent Quantum Key Distribution.” *Phys. Rev. Lett.* **108**, 130503 (2012).
- [41] W. K. Wootters and W. H. Zurek. “A single quantum cannot be cloned.” *Nature* **299**, 802 (1982).
- [42] M. Aspelmeyer, T. Jennewein, M. Pfennigbauer, W. R. Leeb, and A. Zeilinger. “Long-Distance Quantum Communication With Entangled Photons Using Satellites.” *IEEE J. Sel. Top. Quantum Electron.* **9**, 1541 (2003).
- [43] P. Villoresi, T. Jennewein, F. Tamburini, M. Aspelmeyer, C. Bonato, R. Ursin, C. Pernechele, V. Luceri, G. Bianco, A. Zeilinger, and C. Barbieri. “Experimental verification of the feasibility of a quantum channel between space and Earth.” *New J. Phys.* **10**, 033038 (2008).
- [44] X.-S. Ma, T. Herbst, T. Scheidl, D. Wang, S. Kropatschek, W. Naylor, B. Wittmann, A. Mech, J. Kofler, E. Anisimova, V. Makarov, T. Jennewein, R. Ursin, and A. Zeilinger. “Quantum teleportation over 143 kilometres using active feed-forward.” *Nature* **489**, 269 (2012).
- [45] D. F. Walls. “Squeezed states of light.” *Nature* **306**, 141 (1983).
- [46] V. Giovannetti, S. Lloyd, and L. Maccone. “Quantum-Enhanced Measurements: Beating the Standard Quantum Limit.” *Science* **306**, 1330 (2004).
- [47] K. Goda, O. Miyakawa, E. E. Mikhailov, S. Saraf, R. Adhikari, K. McKenzie, R. Ward, S. Vass, A. J. Weinstein, and N. Mavalvala. “A quantum-enhanced prototype gravitational-wave detector.” *Nature Phys.* **4**, 472 (2008).
- [48] M. Mehmet, T. Eberle, S. Steinlechner, H. Vahlbruch, and R. Schnabel. “Demonstration of a quantum-enhanced fiber Sagnac interferometer.” *Opt. Lett.* **35**, 1665 (2010).

- [49] H. Yonezawa, D. Nakane, T. A. Wheatley, K. Iwasawa, S. Takeda, H. Arao, K. Ohki, K. Tsumura, D. W. Berry, T. C. Ralph, H. M. Wiseman, E. H. Huntington, and A. Furusawa. “Quantum-Enhanced Optical-Phase Tracking.” *Science* **337**, 1514 (2012).
- [50] E. Knill, R. Laflamme, and G. J. Milburn. “A scheme for efficient quantum computation with linear optics.” *Nature* **409**, 46 (2001).
- [51] J. L. O’Brien. “Optical Quantum Computing.” *Science* **318**, 1567 (2007).
- [52] A. Aspuru-Guzik and P. Walther. “Photonic quantum simulators.” *Nature Phys.* **8**, 285 (2012).
- [53] X. song Ma, B. Dakic, W. Naylor, A. Zeilinger, and P. Walther. “Quantum simulation of the wavefunction to probe frustrated Heisenberg spin systems.” *Nature Phys.* **7**, 399 (2011).
- [54] S. Tanzilli, A. Martin, F. Kaiser, M. P. D. Micheli, O. Alibart, and D. B. Ostrowsky. “On the genesis and evolution of Integrated Quantum Optics.” *Laser Photon. Rev.* **6**, 115 (2011).
- [55] A. J. Shields. “Semiconductor quantum light sources.” *Nature Photon.* **1**, 215 (2007).
- [56] I. J. Luxmoore, R. Toro, O. D. Pozo-Zamudio, N. A. Wasley, E. A. Chekhovich, A. M. Sanchez, R. Beanland, A. M. Fox, M. S. Skolnick, H. Y. Liu, and A. I. Tartakovskii. “III-V quantum light source and cavity-QED on Silicon.” *Sci. Rep.* **3**, 1239 (2013).
- [57] Y.-M. He, Y. He, Y.-J. Wei, D. Wu, M. Atatüre, C. Schneider, S. Höfling, M. Kamp, C.-Y. Lu, and J.-W. Pan. “On-demand semiconductor single-photon source with near-unity indistinguishability.” *Nat. Nanotechnol.* **8**, 213 (2013).
- [58] C. L. Salter, R. M. Stevenson, I. Farrer, C. A. Nicoll, D. A. Ritchie, and A. J. Shields. “An entangled-light-emitting diode.” *Nature* **465**, 594 (2010).
- [59] M. Ghali, K. Ohtani, Y. Ohno, and H. Ohno. “Generation and control of polarization-entangled photons from GaAs island quantum dots by an electric field.” *Nat. Commun.* **3**, 661 (2012).
- [60] M. H. Rubin, D. N. Klyshko, Y. H. Shih, and A. V. Sergienko. “Theory of two-photon entanglement in type-II optical parametric down-conversion.” *Phys. Rev. A* **50**, 5122 (1994).
- [61] Z. Yang, M. Liscidini, and J. E. Sipe. “Spontaneous parametric down-conversion in waveguides: A backward Heisenberg picture approach.” *Phys. Rev. A* **77**, 033808 (2008).
- [62] J. Chen, X. Li, and P. Kumar. “Two-photon-state generation via four-wave mixing in optical fibers.” *Phys. Rev. A* **72**, 033801 (2005).

- [63] T. Suhara. “Generation of quantum-entangled twin photons by waveguide nonlinear-optic devices.” *Laser Photon. Rev.* **3**, 370 (2009).
- [64] S. Khasminskaya and W. H. P. Pernice. “A silicon nanowire factorable photon pair source.” *Opt. Quant. Electron.* **45**, 357 (2012).
- [65] J. B. Spring, P. S. Salter, B. J. Metcalf, P. C. Humphreys, M. Moore, N. Thomas-Peter, M. Barbieri, X.-M. Jin, N. K. Langford, W. S. Kolthammer, M. J. Booth, and I. A. Walmsley. “On-chip low loss heralded source of pure single photons.” *Opt. Express* **21**, 13522 (2013).
- [66] R. Horn, P. Abolghasem, B. J. Bijlani, D. Kang, A. S. Helmy, and G. Weihs. “Monolithic Source of Photon Pairs.” *Phys. Rev. Lett.* **108**, 153605 (2012).
- [67] M. Davanço, J. R. Ong, A. B. Shehata, A. Tosi, I. Agha, S. Assefa, F. Xia, W. M. J. Green, S. Mookherjea, and K. Srinivasan. “Telecommunications-band heralded single photons from a silicon nanophotonic chip.” *Appl. Phys. Lett.* **100**, 261104 (2012).
- [68] N. Matsuda, H. L. Jeannic, H. Fukuda, T. Tsuchizawa, W. J. Munro, K. Shimizu, K. Yamada, Y. Tokura, and H. Takesue. “A monolithically integrated polarization entangled photon pair source on a silicon chip.” *Sci. Rep.* **2**, 817 (2012).
- [69] L. Olislager, J. Safioui, S. Clemmen, K. P. Huy, W. Bogaerts, R. Baets, P. Emplit, and S. Massar. “Silicon-on-insulator integrated source of polarization-entangled photons.” *Opt. Lett.* **38**, 1960 (2013).
- [70] S. Krapick, H. Herrmann, V. Quiring, B. Brecht, H. Suche, and C. Silberhorn. “An efficient integrated two-color source for heralded single photons.” *New J. Phys.* **15**, 033010 (2013).
- [71] B. J. Bijlani, P. Abolghasem, and A. S. Helmy. “Semiconductor optical parametric generators in isotropic semiconductor diode lasers.” *Appl. Phys. Lett.* **103**, 091103 (2013).
- [72] F. Boitier, A. Orioux, C. Autebert, A. Lemaître, E. Galopin, C. Manquest, C. Sirtori, I. Favero, G. Leo, and S. Ducci. “Electrically Injected Photon-Pair Source at Room Temperature.” *Phys. Rev. Lett.* **112**, 183901 (2014).
- [73] S. V. Zhukovsky, L. G. Helt, D. Kang, P. Abolghasem, A. S. Helmy, and J. E. Sipe. “Generation of maximally-polarization-entangled photons on a chip.” *Phys. Rev. A* **85**, 013838 (2012).
- [74] A. Eckstein, A. Christ, P. J. Mosley, and C. Silberhorn. “Highly Efficient Single-Pass Source of Pulsed Single-Mode Twin Beams of Light.” *Phys. Rev. Lett.* **106**, 013603 (2011).

- [75] D. Kang, A. Pang, Y. Zhao, and A. S. Helmy. “Two-photon quantum state engineering in nonlinear photonic nanowires.” *J. Opt. Soc. Am. B* **31**, 1581 (2014).
- [76] P. Abolghasem, M. Hendrych, X. Shi, J. P. Torres, and A. S. Helmy. “Bandwidth control of paired photons generated in monolithic Bragg reflection waveguides.” *Opt. Lett.* **34**, 2000 (2009).
- [77] S. V. Zhukovsky, D. Kang, P. Abolghasem, L. G. Helt, J. E. Sipe, and A. S. Helmy. “Proposal for on-chip generation and control of photon hyperentanglement.” *Opt. Lett.* **36**, 3548 (2011).
- [78] A. Vallés, M. Hendrych, J. Svozilík, R. Machulka, P. Abolghasem, D. Kang, J. Bijlani, A. S. Helmy, and J. P. Torres. “Generation of polarization-entangled photon pairs in a Bragg reflection waveguide.” *Opt. Express* **21**, 10841 (2013).
- [79] A. Politi, M. J. Cryan, J. G. Rarity, S. Yu, and J. L. O’Brien. “Silica-on-Silicon Waveguide Quantum Circuits.” *Science* **320**, 646 (2008).
- [80] A. Laing, A. Peruzzo, A. Politi, M. R. Verde, M. Halder, T. C. Ralph, M. G. Thompson, and J. L. O’Brien. “High-fidelity operation of quantum photonic circuits.” *Appl. Phys. Lett.* **97**, 211109 (2010).
- [81] P. J. Shadbolt, M. R. Verde, A. Peruzzo, A. Politi, A. Laing, M. Lobino, J. C. F. Matthews, M. G. Thompson, and J. L. O’Brien. “Generating, manipulating and measuring entanglement and mixture with a reconfigurable photonic circuit.” *Nature Photon.* **6**, 45 (2012).
- [82] D. Bonneau, E. Engin, K. Ohira, N. Suzuki, H. Yoshida, N. Iizuka, M. Ezaki, C. M. Natarajan, M. G. Tanner, R. H. Hadfield, S. N. Dorenbos, V. Zwiller, J. L. O’Brien, and M. G. Thompson. “Quantum interference and manipulation of entanglement in silicon wire waveguide quantum circuits.” *New J. Phys.* **14**, 045003 (2012).
- [83] J. Wang, A. Santamato, P. Jiang, D. Bonneau, E. Engin, J. W. Silverstone, M. Lerner, J. Beetz, M. Kamp, S. Höfling, M. G. Tanner, C. M. Natarajan, R. H. Hadfield, S. N. Dorenbos, V. Zwiller, J. L. O’Brien, and M. G. Thompson. “Gallium arsenide (GaAs) quantum photonic waveguide circuits.” *Opt. Commun.* **327**, 49 (2014).
- [84] D. Bonneau, M. Lobino, P. Jiang, C. M. Natarajan, M. G. Tanner, R. H. Hadfield, S. N. Dorenbos, V. Zwiller, M. G. Thompson, and J. L. O’Brien. “Fast Path and Polarization Manipulation of Telecom Wavelength Single Photons in Lithium Niobate Waveguide Devices.” *Phys. Rev. Lett.* **108**, 053601 (2012).

- [85] L. Sansoni, F. Sciarrino, G. Vallone, P. Mataloni, A. Crespi, R. Ramponi, and R. Osellame. “Polarization Entangled State Measurement on a Chip.” *Phys. Rev. Lett.* **105**, 200503 (2010).
- [86] A. Crespi, R. Ramponi, R. Osellame, L. Sansoni, I. Bongioanni, F. Sciarrino, G. Vallone, and P. Mataloni. “Integrated photonic quantum gates for polarization qubits.” *Nat. Commun.* **2**, 566 (2011).
- [87] B. J. Smith, D. Kundys, N. Thomas-Peter, P. G. R. Smith, and I. A. Walmsley. “Phase-controlled integrated photonic quantum circuits.” *Opt. Express* **17**, 13516 (2009).
- [88] A. Politi, J. C. F. Matthews, and J. L. O’Brien. “Shor’s Quantum Factoring Algorithm on a Photonic Chip.” *Science* **325**, 1221 (2009).
- [89] A. Peruzzo, M. Lobino, J. C. F. Matthews, N. Matsuda, A. Politi, K. Poulios, X.-Q. Zhou, Y. Lahini, N. Ismail, K. Wörhoff, Y. Bromberg, Y. Silberberg, M. G. Thompson, and J. L. O’Brien. “Quantum Walks of Correlated Photons.” *Science* **329**, 1500 (2010).
- [90] W. H. P. Pernice, C. Schuck, O. Minaeva, M. Li, G. Goltsman, A. Sergienko, and H. Tang. “High-speed and high-efficiency travelling wave single-photon detectors embedded in nanophotonic circuits.” *Nat. Commun.* **3**, 1325 (2012).
- [91] G. Reithmaier, S. Lichtmanecker, T. Reichert, P. Hasch, K. Müller, M. Bichler, R. Gross, and J. J. Finley. “On-chip time resolved detection of quantum dot emission using integrated superconducting single photon detectors.” *Sci. Rep.* **3**, 1901 (2013).
- [92] R. H. Hadfield. “Single-photon detectors for optical quantum information applications.” *Nature Photon.* **3**, 696 (2009).
- [93] P. G. Kwiat, K. Mattle, H. Weinfurter, A. Zeilinger, A. V. Sergienko, and Y. Shih. “New High-Intensity Source of Polarization-Entangled Photon Pairs.” *Phys. Rev. Lett.* **75**, 4337 (1995).
- [94] P. G. Kwiat, E. Waks, A. G. White, I. Appelbaum, and P. H. Eberhard. “Ultrabright source of polarization-entangled photons.” *Phys. Rev. A* **60**, R773 (1999).
- [95] A. Orioux, X. Caillet, A. Lemaître, P. Filloux, I. Favero, G. Leo, and S. Ducci. “Efficient parametric generation of counterpropagating two-photon states.” *J. Opt. Soc. Am. B* **28**, 45 (2011).
- [96] Z. Y. Ou and L. Mandel. “Observation of Spatial Quantum Beating with Separated Photodetectors.” *Phys. Rev. Lett.* **61**, 54 (1988).

- [97] C. Liang, K. F. Lee, M. Medic, P. Kumar, R. H. Hadfield, and S. W. Nam. “Characterization of fiber-generated entangled photon pairs with superconducting single-photon detectors.” *Opt. Express* **15**, 1322 (2007).
- [98] X. Li, L. Yang, X. Ma, L. Cui, Z. Y. Ou, and D. Yu. “All-fiber source of frequency-entangled photon pairs.” *Phys. Rev. A* **79**, 033817 (2009).
- [99] M. Medic, J. B. Altepeter, M. A. Hall, M. Patel, and P. Kumar. “Fiber-based telecommunication-band source of degenerate entangled photons.” *Opt. Lett.* **35**, 802 (2010).
- [100] N. Zhao, L. Yang, and X. Li. “Passive optical switching of photon pairs using a spontaneous parametric fiber loop.” *Opt. Lett.* **37**, 1220 (2012).
- [101] H. Jin, F. Liu, P. Xu, J. Xia, M. Zhong, Y. Yuan, J. Zhou, Y. Gong, W. Wang, and S. Zhu. “On-Chip Generation and Manipulation of Entangled Photons Based on Reconfigurable Lithium-Niobate Waveguide Circuits.” *Phys. Rev. Lett.* **113**, 103601 (2014).
- [102] M. O. Scully and M. S. Zubairy. *Quantum Optics*. Cambridge University Press (1997).
- [103] C. Gerry and P. Knight. *Introductory Quantum Optics*. Cambridge University Press (2004).
- [104] M. Hillery. “An Introduction To The Quantum Theory of Nonlinear Optics.” *Acta Physica Slovaca* **59**, 1 (2009).
- [105] G. S. Agarwal. *Quantum Optics*. Cambridge University Press, 1 edition (2012).
- [106] P. Kok and B. W. Lovett. *Introduction to Optical Quantum Information Processing*. Cambridge University Press (2010).
- [107] V. V. Dodonov. “Nonclassical states in quantum optics: a squeezed review of the first 75 years.” *J. Opt. B* **4**, R1 (2002).
- [108] T. S. Humble and W. P. Grice. “Effects of spectral entanglement in polarization-entanglement swapping and type-I fusion gates.” *Phys. Rev. A* **77**, 022312 (2008).
- [109] S. Barnett. *Quantum Information*. Oxford University Press (2009).
- [110] S. Parker, S. Bose, and M. B. Plenio. “Entanglement quantification and purification in continuous-variable systems.” *Phys. Rev. A* **61**, 032305 (2000).
- [111] S. Hill and W. K. Wootters. “Entanglement of a Pair of Quantum Bits.” *Phys. Rev. Lett.* **78**, 5022 (1997).

- [112] W. K. Wootters. “Entanglement of Formation of an Arbitrary State of Two Qubits.” *Phys. Rev. Lett.* **80**, 2245 (1998).
- [113] Z. Y. Ou. “Temporal distinguishability of an N-photon state and its characterization by quantum interference.” *Phys. Rev. A* **74**, 063808 (2006).
- [114] W. P. Grice and I. A. Walmsley. “Spectral information and distinguishability in type-II down-conversion with a broadband pump.” *Phys. Rev. A* **56**, 1627 (1997).
- [115] Y.-H. Kim and W. P. Grice. “Quantum interference with distinguishable photons through indistinguishable pathways.” *J. Opt. Soc. Am. B* **22**, 493 (2005).
- [116] C. Liu, J. F. Chen, S. Zhang, S. Zhou, Y.-H. Kim, M. M. T. Loy, G. K. L. Wong, and S. Du. “Two-photon interferences with degenerate and nondegenerate paired photons.” *Phys. Rev. A* **85**, 021803 (2012).
- [117] M. J. Holland and K. Burnett. “Interferometric detection of optical phase shift at the Heisenberg limit.” *Phys. Rev. Lett.* **71**, 1355 (1993).
- [118] B. E. A. Saleh and M. C. Teich. *Fundamentals of Photonics*. Wiley, 2 edition (2007).
- [119] A. Yariv and P. Yeh. *Photonics: Optical Electronics in Modern Communications*. Oxford University Press, 6 edition (2006).
- [120] H. F. Taylor and A. Yariv. “Guided Wave Optics.” *Proc. IEEE* **62**, 1044 (1974).
- [121] A. Yariv. “Coupled-Mode Theory for Guided-Wave Optics.” *IEEE J. Quant. Electron.* **9**, 919 (1973).
- [122] M. Kawachi. “Silica waveguides on silicon and their application to integrated-optic components.” *Opt. Quant. Electron.* **22**, 391 (1990).
- [123] A. Rai and G. S. Agarwal. “Possibility of coherent phenomena such as Bloch oscillations with single photons via W states.” *Phys. Rev. A* **79**, 053849 (2009).
- [124] P. Abolghasem, J.-B. Han, D. Kang, B. J. Bijlani, and A. S. Helmy. “Monolithic Photonics Using Second-Order Optical Nonlinearities in Multilayer-Core Bragg Reflection Waveguides.” *IEEE J. Sel. Top. Quantum Electron.* **18**, 812 (2012).
- [125] A. Takagi, K. Jinguji, and M. Kawachi. “Wavelength characteristics of (2x2) optical channel-type directional couplers with symmetric or nonsymmetric coupling structures.” *J. Lightwave Technol.* **10**, 735 (1992).

- [126] R. Chakraborty, J. Biswas, and S. Lahiri. “Analysis of directional coupler electro-optic switches using effective-index-based matrix method.” *Opt. Commun.* **219**, 157 (2003).
- [127] J. Fekete, D. Rieländer, M. Cristiani, and H. de Riedmatten. “Ultranarrow-Band Photon-Pair Source Compatible with Solid State Quantum Memories and Telecommunication Networks.” *Phys. Rev. Lett.* **110**, 220502 (2013).
- [128] M. M. Fejer, G. A. Magel, D. H. Jundt, and R. L. Byer. “Quasi-Phase-Matched Second Harmonic Generation: Tuning and Tolerances.” *IEEE J. Quant. Electron.* **28**, 2631 (1992).
- [129] S. J. B. Yoo, R. Bhat, C. Caneau, and M. A. Koza. “Quasi-phase-matched second-harmonic generation in AlGaAs waveguides with periodic domain inversion achieved by wafer-bonding.” *Appl. Phys. Lett.* **66**, 3410 (1995).
- [130] J. D. Joannopoulos, P. R. Villeneuve, and S. Fan. “Photonic crystals: putting a new twist on light.” *Nature* **386**, 143 (1997).
- [131] B. J. Bijlani. *Monolithic integration of active and second-order nonlinear functionality in Bragg reflection waveguides*. Ph.D. thesis, University of Toronto, Department of Electrical and Computer Engineering (2011).
- [132] B. R. West and A. S. Helmy. “Dispersion tailoring of the quarter-wave Bragg reflection waveguide.” *Opt. Express* **14**, 4073 (2006).
- [133] A. S. Helmy. “Phase matching using Bragg reflection waveguides for monolithic nonlinear optics applications.” *Opt. Express* **14**, 1243 (2006).
- [134] D. Kang and A. S. Helmy. “Generation of polarization entangled photons using concurrent type-I and type-0 processes in AlGaAs ridge waveguides.” *Opt. Lett.* **37**, 1481 (2012).
- [135] L. B. Soldano and E. C. M. Pennings. “Optical multi-mode interference devices based on self-imaging: principles and applications.” *J. Lightwave Technol.* **13**, 615 (1995).
- [136] O. Wallner, W. R. Leeb, and P. J. Winzer. “Minimum length of a single-mode fiber spatial filter.” *J. Opt. Soc. Am. A* **19**, 2445 (2002).
- [137] A. F. Milton and W. K. Burns. “Mode coupling in optical waveguide horns.” *IEEE J. Quant. Electron.* **QE-13**, 828 (1977).
- [138] Y. Fu, T. Ye, W. Tang, and T. Chu. “Efficient adiabatic silicon-on-insulator waveguide taper.” *Photon. Res.* **2**, A41 (2012).

- [139] F. Bloch and A. Siegert. “Magnetic Resonance for Nonrotating Fields.” *Phys. Rev.* **57**, 522 (1940).
- [140] R. Regener and W. Sohler. “Loss in low-finesse Ti:LiNbO₃ optical waveguide resonators.” *Appl. Phys. B* **36**, 143 (1985).
- [141] L. S. Yu, Q. Z. Liu, S. A. Pappert, P. K. L. Yu, and S. S. Lau. “Laser spectral linewidth dependence on waveguide loss measurements using the Fabry-Pérot method.” *Appl. Phys. Lett.* **64**, 536 (1994).
- [142] A. D. Rossi, V. Ortiz, M. Calligaro, L. Lanco, S. Ducci, V. Berger, and I. Sagnes. “Measuring propagation loss in a multimode semiconductor waveguide.” *J. Appl. Phys.* **97**, 073105 (2005).
- [143] D. N. Klyshko. “Use of two-photon light for absolute calibration of photoelectric detectors.” *Sov. J. Quantum Electron.* **10**, 1112 (1981).
- [144] S. V. Polyakov and A. L. Migdall. “High accuracy verification of a correlated-photon-based method for determining photon-counting detection efficiency.” *Opt. Express* **15**, 1390 (2007).
- [145] M. Liscidini and J. E. Sipe. “Stimulated Emission Tomography.” *Phys. Rev. Lett.* **111**, 193602 (2013).
- [146] T. Pertsch, P. Dannberg, W. Elflein, A. Bräuer, and F. Lederer. “Optical Bloch Oscillations in Temperature Tuned Waveguide Arrays.” *Phys. Rev. Lett.* **83**, 4752 (1999).
- [147] R. Morandotti, U. Peschel, J. S. Aitchison, H. S. Eisenberg, and Y. Silberberg. “Experimental Observation of Linear and Nonlinear Optical Bloch Oscillations.” *Phys. Rev. Lett.* **83**, 4756 (1999).
- [148] Y. Bromberg, Y. Lahini, and Y. Silberberg. “Quantum and Classical Correlations in Waveguide Lattices.” *Phys. Rev. Lett.* **105**, 263604 (2010).
- [149] C. Thompson, G. Vemuri, and G. S. Agarwal. “Quantum physics inspired optical effects in tight-binding lattices: Phase-controlled photonic transport.” **84**, 214302 (2011).
- [150] M. A. Nielsen and I. L. Chuang. *Quantum Computation and Quantum Information*. Cambridge University Press (2000).